École Doctorale des **Sciences de la Matière, du Rayonnement et de l'Environnement**

Unité de recherche **UMET**

Thèse présentée par **Tomasz Stasiak**

Soutenue le 17 Décembre 2020

En vue de l'obtention du grade de docteur de l'Université de Lille

Discipline **Physique et Science des matériaux**

High Entropy Alloys with improved mechanical properties

Alliages à Haute Entropie à propriétés mécaniques améliorées

Composition du jury

Éric Fleury	Rapporteur	Professeur	Université de Lorraine
Thierry Gloriant	Rapporteur	Professeur	INSA Rennes
Anna Fraczkiewicz	Présidente du jury	Directrice de recherche	Mines Saint-Étienne
Franck Tancret	Examinateur	Professeur	Université de Nantes
Zhao Huvelin	Examinatrice	Ingénieur d'études et de recherche	ONERA Châtillon
Corinne Nouvellon	Examinatrice	Project leader	Materia Nova, Mons, Belgique
Catherine Cordier	Directrice de thèse	Maître de Conférences	Université d'Artois, (IUT Béthune)
Matthieu Touzin	Co-encadrant	Maître de Conférences	Université de Lille
Franck Béclin	Invité	Maître de Conférences	Université de Lille

Thèse réalisée au sein de l'Unité Matériaux et Transformations - UMR 8207 cofinancé par l'Université de Lille (50 %) et la Région Hauts-de-France (50 %)

Acknowledgements

In the beginning, I would like to express my most profound sense of gratitude to my supervisor, Dr. Catherine Cordier, for accepting me as a doctoral student at the UMET laboratory as well as for her time and help during the last three years. Without her experience and knowledge in metallurgy, this work could not have been done. Equally important, I would like to thank my co-supervisors, Dr. Franck Béclin and Dr. Matthieu Touzin. Their help and suggestions were essential during my work. I would like to acknowledge the Université de Lille and Hauts-de-France region for co-financing my doctoral scholarship.

I would like to thank the reviewers of my thesis, Prof. Éric Fleury and Prof. Thierry Gloriant, as well as Prof. Anna Fraczkiewicz, who accepted to be the president of the jury. Additionally, I would like to express my gratitude to other jury members for participation in defense of my thesis: Dr. Zhao Huvelin, Dr. Corinne Nouvellon, and Prof. Franck Tancret.

Working at UMET laboratory was a valuable experience, mostly thanks to people I have met during my stay. I want to thank all my colleagues from UMET and the University of Lille for their help and assistance. I want to mention a few people:

- Dr. Ahmed Addad for guidance during SEM and TEM observations;
- Dr. Rémy Besson for important remarks during meetings;
- Prof. Olivier Tougait for the help with arc melting;
- Dr. Qier Wu for help with the compression tests at room temperature;
- Damien Creton and Jocelyn Golek for their help in sample preparation;
- Adeline Marin for the maintenance of the sintering device;
- Corinne Henry and Isabelle Samain for their help with all administrative documents.

I would express my gratitude to all my friends from Warsaw, Poland, and other countries, who supported me throughout my life. Without them, hard work during my thesis would be more difficult. Many thanks should go to my office colleagues, who often change (ten people for the period of my thesis), but always were friendly and helpful. I want to thank especially Mourtada Aly Sow, who shared with me the office for the last two years and worked in the field of high entropy alloys like me. The endless mutual discussions and his help during research experiments were invaluable.

Finally, I would like to thank my family, especially my parents and my aunt Halina, who supported me throughout life. Without their help, successes during my Ph.D. work would not be possible.

Abstract

High Entropy Alloys (HEAs) are a new type of multicomponent alloys. They contain at least five elements with the content of each between 5 and 35 at. %. The high configuration entropy, which is the source of the name of the whole family of alloys, together with other parameters, such as mixing enthalpy, atomic size difference, electronegativity difference, or valence electron concentration, stabilize a solid solution instead of complex intermetallic compounds. Promising properties and interesting microstructures focus the attention of the scientific community to HEAs.

In this work, the novel Al-Cr-Fe-Mn-Mo high entropy alloy family was studied. The microstructural and chemical analyses were performed by XRD, Mössbauer spectrometry, SEM, TEM, EDX, EBSD. In the first stage, parametric approach calculations were carried out to optimize the chemical composition of the alloy. The selected compositions were prepared by mechanical alloying in different devices. The optimized conditions that ensure maximum chemical homogeneity of powder and the small contamination from balls and vial materials were chosen. In most of the powders, two bcc phases form during mechanical alloying with the lattice parameters about 3.13 Å (bcc#1) and 2.93 Å (bcc#2). The heat treatment of powder results in several phase transformations (e.g., the formation of the χ phase). The annealing at 950 °C for 1 h promotes the significant increase of volume fraction of the bcc#2 phase, while the bcc#1 and χ disappear. Nevertheless, small fractions of carbides and oxides were found.

The bulk samples were fabricated by hot press sintering of the optimized mechanically alloyed powders. The conditions of consolidation were evaluated and optimized to promote the formation of the bcc phase and reduce the formation of carbides and oxides resulting from the contamination during mechanical alloying and sintering. The optimized bulk samples present a major disordered body-centered cubic phase (> 95 % of volume fraction) with a lattice parameter of 2.92 Å and a very small fraction of carbides (M_6C, $M_{23}C_6$) and oxides (Al_2O_3). The bcc phase is stable after annealing at 950 °C for 10 h. Moreover, the alloy presents very high hardness up to 950 HV_{2N}. The compression tests of the optimized bulk sample from room temperature to 800 °C reveal promising properties, especially between 600 and 700 °C. The alloy shows brittle behavior between room temperature and 400 °C. However, the alloy starts to demonstrate some degree of plasticity at 500 °C. At 600 °C, the yield strength is 1022 MPa, while strain to failure is about 22 %.

Keywords: High Entropy Alloy, Powder Metallurgy, Mechanical Alloying, Microstructural Observation, Chemical Composition, Mechanical Properties.

Résumé

Les Alliages à Haute Entropie (AHEs ou HEAs en anglais) sont un nouveau type d'alliages multi-élémentaires. Ils contiennent au moins cinq éléments de teneur comprise entre 5 et 35 at %. L'entropie de configuration élevée, qui est une raison du nom de cette famille d'alliages, ainsi que d'autres paramètres, tels que l'enthalpie de mélange, la différence de taille atomique, la différence d'électronégativité ou la concentration d'électrons de valence, stabilisent une solution solide plutôt que des composés intermétalliques. L'attention de la communauté scientifique a été attirée par les propriétés prometteuses et les microstructures intéressantes des HEAs.

Dans ce travail, une nouvelle famille de HEAs Al-Cr-Fe-Mn-Mo a été étudiée. Les analyses microstructurales et chimiques ont été menées par DRX, spectrométrie Mössbauer, MEB, MET, EDX, EBSD. Dans un premier temps, des calculs basés sur une approche paramétrique ont été réalisés pour optimiser la composition chimique. Les compositions sélectionnées ont été préparées par mécanosynthèse dans différents types broyeurs. Les conditions optimisées garantissant une homogénéité chimique maximale de la poudre et une faible contamination par les matériaux des billes et des jarres ont été déterminées. Deux phases cubique centrée (cc) se forment pendant la mécanosynthèse avec les paramètres de maille 3,13 Å (cc#1) et 2,93 Å (cc#2). Le traitement thermique de la poudre entraîne plusieurs transformations de phase (la formation de la phase χ). Le recuit à 950 °C/1 h favorise l'augmentation de la fraction volumique de la phase cc#2, tandis que les cc#1 et χ disparaissent. Néanmoins, de petites fractions de carbures et d'oxydes ont été trouvées.

Les échantillons massifs ont été fabriqués par frittage à chaud des poudres mécanosynthétisées. Les conditions de consolidation ont été évaluées et optimisées pour favoriser la formation de la phase cc et réduire la formation de carbures et d'oxydes résultant de la contamination. Les échantillons massifs optimisés présentent une phase majoritaire cubique centrée (> 95 % volumique) avec un paramètre de maille de 2,92 Å et une très petite quantité de carbures (M_6C, $M_{23}C_6$) et d'oxydes (Al_2O_3). La phase cc est stable après recuit à 950 °C pendant 10 h. De plus, l'alliage présente une dureté très élevée jusqu'à 950 HV_{2N}. Les essais de compression de l'échantillon massif optimisé, entre la température ambiante et 800 °C, révèlent des propriétés prometteuses, en particulier entre 600 et 700 °C. L'alliage présente un comportement fragile entre la température ambiante et 400 °C. Cependant, l'alliage commence à démontrer un certain degré de plasticité à 500 °C. À 600 °C, la limite d'élasticité est de 1022 MPa, tandis que la déformation à la rupture est d'environ 22 %.

Mots clés : Alliage à Haute Entropie, Métallurgie des Poudres, Mécanosynthèse, Observation Microstructurale, Composition Chimique, Propriétés Mécaniques.

Table of Contents

Introduction

Traditional alloys contain one or two main elements and usually a small fraction of alloying elements. In 2004, the publication of two papers by Cantor *et al.* [1] and Yeh *et al.* [2] broke this paradigm. The new concept of High Entropy Alloys (HEAs) was born. HEAs are multicomponent alloys that contain at least five metallic elements in close to equiatomic ratios (usually between 5 and 35 at. %) [2–4]. The second definition defines HEAs as alloys having configurational entropy greater than 1.5 R (R- gas constant), which was a source of HEAs' name [3,4]. The high configurational entropy was believed to stabilize solid solutions and to prevent the formation of intermetallic compounds [4]; however, other parameters, such as mixing enthalpy or atomic size difference, play an essential role too. These novel multicomponent alloys quickly gained the interest of the scientific community, thanks to promising properties, surprisingly simple microstructure, and almost infinity of original compositions.

One of the first reported HEA is CrMnFeCoNi equiatomic alloy (known as Cantor alloy). The alloy mentioned above, which was studied extensively in the past 15 years, crystallizes into a single fcc solid solution [1,5]. The exceptional properties of Cantor alloy, such as an increase of yield strength and ductility with decreasing temperature [6], confirm the promising future of the whole high entropy alloys family. HEAs often present interesting properties beyond high strength and ductility, which in many cases, surpass traditional alloys. The promising properties of different HEAs were shown in many recent papers: high creep resistance (fcc matrix and $L1_2$ precipitates [7,8]), excellent mechanical resistance at high temperatures (refractory bcc alloys [9]), irradiation resistance (fcc, fcc+bcc, bcc, or bcc refractory alloys [10,11]), good weldability (fcc+hcp phases [12]), and resistance to corrosion (fcc [13,14]) or hydrogen embrittlement (fcc phases [15,16]).

The almost infinite number of new possible compositions makes it impossible to study all HEAs systems experimentally. The basic tool to choose an alloy system and optimize its composition is the well-established parametric approach [4,17]. The calculation of parameters (such as mixing enthalpy, mixing entropy, atomic size difference, electronegativity difference, valence electron concentration, or omega parameter which is evaluated by the combining effects of enthalpy and entropy of mixing)) enables to predict structure for selected composition. Although the parametric approach results are not always in agreement with the experimental findings, it is still the first-choice tool to quickly analyze a new system. In recent years, Calculation of Phase Diagrams (CALPHAD) becomes a very common way to predict the phase composition of alloys. In-depth studies in CALPHAD are especially needed in the field of high entropy alloys. The development of the HEAs database (TCHEA) by Thermo-Calc Software Company is a significant progress in the prediction of the phase structure of HEAs [18]. For example, Thermo-Calc, coupled with TC-python, could be an effective tool in the investigation of phases stability and screening to discover new HEAs [19]. However, the calculation results for new non-experimentally studied systems are not totally reliable, and CALPHAD cannot replace the experimental research.

The most common way of fabrication of bulk high entropy alloys is melting, followed by casting. The liquid route of HEA processing presents some disadvantages, e.g., may lead to dendritic segregation, which is generally desired to be avoided. Powder metallurgy techniques, such as mechanical alloying (MA) followed by sintering, are becoming more and more popular, which results in a significant increase in the number of publications in the field [20,21]. The considerable advantages of mechanical alloying followed by sintering are the possibility to obtain nanocrystalline grains without segregation and a more efficient mixing of the elements. For alloys with a large difference in melting temperatures of constituent elements, powder metallurgy is particularly preferred. The main drawbacks are contaminations (during MA and sintering) and generally a small amount of produced powder [4].

The main objective of this work is to prepare a novel high entropy alloy with a single-phase structure by powder metallurgy techniques. Ideally, the bulk samples should present a single multi-element disordered body-centered cubic phase and high mechanical strength. The study focuses on the optimization of fabrication parameters and the careful analysis of the microstructure of produced powder and bulk samples. The mechanical properties were investigated by the micro-indentation and the compression tests at different temperatures up to 800 °C.

The Al-Cr-Fe-Mn-Mo high entropy alloy family, prepared by powder metallurgy techniques, was studied. Powder metallurgy (mechanical alloying, followed by hot-press sintering) was chosen due to the presence of the elements with the significantly different melting temperatures, i.e., aluminum and molybdenum. Senkov *et al.* [22] published some promising information (melting temperature, phase composition, Young modulus, etc.) obtained by CALPHAD calculations about the equiatomic AlCrFeMnMo HEA. The first experimental results for this system were published by our group during this work. Three compositions of HEAs based on the parametric approach and preliminary experimental results were selected. The milling was performed in different mills to find optimized conditions. The mechanically alloyed powders, in most of the studied conditions, present two disordered bcc phases. The annealings of mechanically alloyed powders were performed to study thermal stability. The most promising results reveal one primary bcc phase and a small fraction of carbides and oxides. The optimization of sintering parameters allowed to produced samples with a high-volume fraction of bcc (> 98 vol. %) and a small fraction of carbides (M_6C, $M_{23}C_6$) and oxide (Al_2O_3) resulting from the contamination. The bulk samples are characterized by high hardness and high compressive strength.

This thesis is divided into seven chapters to present the results obtained during three years clearly. The first and the second chapter consist of the literature review and the experimental procedures, respectively. The third chapter deals with the design and optimization of a new HEA composition, describing the calculation by the parametric approach. In the two next chapters, the information about mechanical alloying (the optimization of MA, the structure of powder, and its thermal stability) could be found. The sixth chapter consists of microstructural results of bulk samples. The last chapter deals with the mechanical properties of sintered samples. In the end, the conclusions and perspectives are presented.

In this thesis, detailed microstructural studies of powder and bulk HEAs after different conditions (mechanical alloying, annealing, sintering) were performed. Nevertheless, many phenomena occurring in the Al-Cr-Fe-Mn-Mo are not fully understood; therefore, further studies are needed. However, the result obtained in the frame of this thesis, such as optimization of the chemical composition or the mechanical alloying conditions, allowed the UMET laboratory and the University of Lille to launch other projects such as the Allihentrop Interreg project consisting of the fabrication and characterization of coatings of alloys from the Al-Cr-Fe-Mn-Mo family.

1. Literature review

1.1. High Entropy Alloys

1.1.1. Definition of HEA

The consensus among the scientific community regarding the definition of high entropy alloy does not exist. The two most common definitions describe HEAs as alloys containing at least five metallic elements in close to equiatomic ratios (between 5 and 35 %) or alloys having configurational entropy greater than 1.5 R (R is the gas constant, 8.314 J mol^{-1} K^{-1}) [2–4]. Nevertheless, the 4-element multicomponent alloys are often named as high entropy alloys in the literature. The name of HEA, introduced in one of the first publications dealing with this kind of alloys [2], is related to high configurational entropy, which could be easily calculated using the following equation [4]:

$$\Delta S_{conf} = -R\sum_{i=1}^{n} c_i ln c_i \tag{1.1}$$

where R is the gas constant, n is the number of components, and c_i is the atomic fraction of the ith component. The calculation for equiatomic composition shows that configurational entropy increases with the increasing number of elements (Fig. 1-1) and is equal to 1.61 R for the 5-element equiatomic alloy. However, the calculation of entropy requires that alloy has a single value of entropy (entropy could change with increasing temperature), and atoms occupy random positions in the lattice, which is not common in metallic solutions, even at the melting temperature [23].

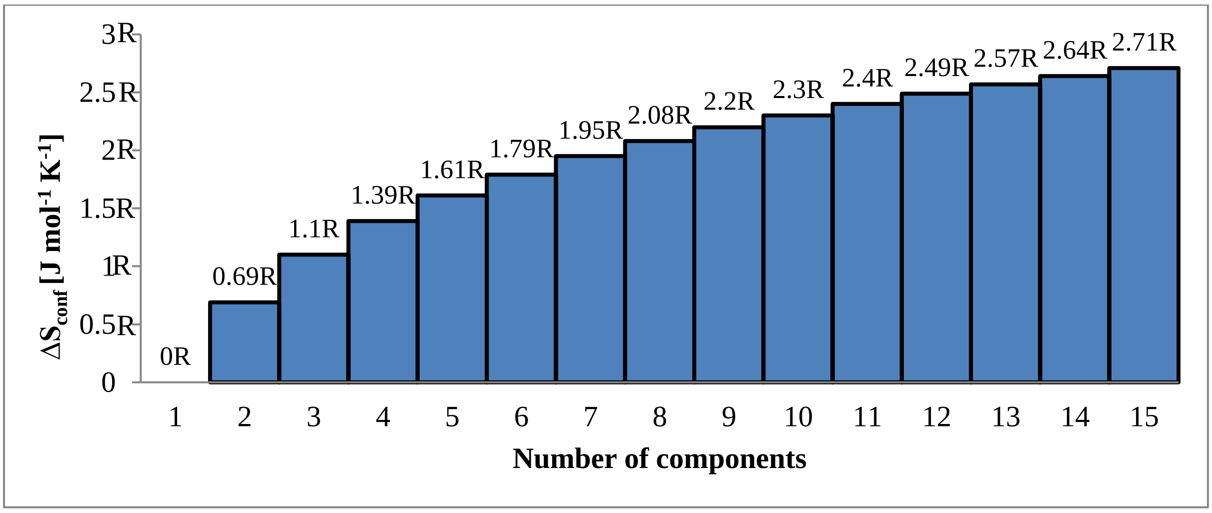

Figure 1-1. Configurational entropies of equiatomic alloys as a function of the number of components.

Some researchers (e.g., [24]) insist that only single solid solution multicomponent alloys can be considered as HEA. To describe multicomponent alloys regardless of the number and the type of phases or the entropy value, new names, such as complex concentrated alloys (CCAs), compositionally complex alloys (CCAs), multi-principal element alloys (MPEAs) or baseless alloys, have appeared [5,23]. However, the term high entropy alloy is still commonly used in the literature to describe all types of multicomponent alloys, and it seems that this catchy name endures [5].

1.1.2. High Entropy Alloy concept

In the early years of the study of high entropy alloys, the concept of four core effects (high-entropy, lattice distortion, sluggish diffusion, and cocktail effects) was introduced [25]. Nowadays, after several years of research in the field of multicomponent alloys, a large amount of data enables to make some verifications of the four core effects concept [23,26,27].

The high-entropy effect was the founding concept of the whole family of HEAs. The Gibbs free energy, which is given by the equation below, controls the phase formation in alloys [4].

$$\Delta G_{mix} = \Delta H_{mix} - T\Delta S_{mix} \tag{1.2}$$

where ΔG_{mix} is the Gibbs free energy of mixing, ΔH_{mix} is the enthalpy of mixing, T is the temperature at which elements are mixed, and ΔS_{mix} is the entropy of mixing (predominantly configurational entropy). The competition between $T\Delta S_{mix}$ and ΔH_{mix} governs the phase formation. Thermodynamic equilibrium is achieved when the Gibbs free energy is the lowest for given pressure and temperature. Multi-element solid solution phases present medium negative ΔH_{mix} and high ΔS_{mix} [4]. Hence, high configurational entropy was believed to stabilize the solid solution and prevent the formation of intermetallic compounds. The last research showed that many alloys, considered as HEAs, are not a single-phase; hence, the high configurational entropy is not the only factor to stabilize the solid solution. For example, configuration entropy increases with an increasing number of elements in equiatomic alloys; however, equiatomic alloys with 16 or 20 elements are not a single-phase [1]. Moreover, it should be noted that the choice of elements to produce HEAs is not random, and thus, the high entropy concept is not verified for all elements. Most of the HEAs consist of 3d transition metals, so it is not surprising that fcc and bcc are the most common phases, and therefore, it could be concluded that the high configurational entropy is not the sole factor to stabilize solid solution [26]. The study of alloys in as-cast (possible non-equilibrium microstructures) conditions also contributes to the increased number of single-phase HEAs because annealing leads, in many cases, to produce multi-phase structures [26]. Pickering *et al.* [28] showed that long-term exposure of the most studied fcc single-phase Cantor alloy (CoCrFeMnNi), triggered the formation of chromium-rich σ phase (tetragonal structure with lattice parameters of $a \approx 8.8$ Å and $c \approx 4.5$ Å). Many other HEAs decompose after prolonged annealing [27]. It can be concluded that the high configurational entropy plays a role in the stabilization of solid solution; however, it is not the only criterium to obtain a single-phase alloy. The mixing enthalpy seems to play also an important role [26,27].

The sluggish diffusion effect, due to great fluctuation of lattice potential energy between the lattice sites in HEAs, was proposed by Yeh in 2006 [25]. The previously obtained results, such as high recrystallization temperatures, the easy formation of nanocrystals (even in the as-cast state), were related to the sluggish diffusion. Tsai *et al.* [29] confirmed experimentally the sluggish diffusion in Co–Cr–Fe–Mn–Ni HEA family. However, other studies (e.g., Dąbrowa *et al.* [30]) showed that sluggish diffusion is not present in all HEA systems. Despite many publications in the field of diffusion, the consensus has not been achieved. It seems that the diffusion in HEAs is slower than average, compared to materials with the same crystal structure; however, it is not the slowest [26].

The lattice distortion effect is the result of different sizes of HEAs constituent atoms, which cause strains. It is believed that the impact is more severe in HEAs than in traditional alloys. Hence, it contributes significantly to the following properties: hardness increase, reduction of thermal and electrical conductivity and its temperature dependence [23]. However, the experimental measurements of the lattice distortion seem to be very challenging and have received the least attention among the four core effects [26]. The lattice distortion is usually evaluated using the difference in radii of constituent elements, which gives only approximate values (e.g., vary depending on the structure) [26]. The experimental studies, including high-resolution TEM images, neutron scattering, have not unambiguously proved the severe lattice distortion hypothesis [26,27]. More in-depth studies should be conducted to evaluate the severe lattice distortion effect and its contribution to the HEAs properties.

The cocktail effect was introduced by Ranganathan [31]. It means that the final properties of alloys are not just the sum of constituent elements properties, but are also the result of unexpected synergies between them [23]. Hence, HEAs properties cannot be easily predictable. The cocktail effect is not a hypothesis but has a significant influence on HEAs studies [23,26].

Based on data obtained during the studies of HEAs, it could be concluded that the four core effects influence on structure and properties is not as important as it was believed [26,27]. The high configurational entropy does not play a dominant role in the stabilization of solid solutions (other parameters as enthalpy should be considered). The diffusion rate in HEAs is usually slower than average, but it is not the slowest. The lattice distortion due to the atomic size difference should be better quantified [23,26,27].

1.1.3. Common HEA compositions

Many high entropy alloys have been developed during the last 15 years of research in this field. For the 13 most common elements in the design of HEAs, there are 7099 possible equiatomic compositions (from 5 to 13 elements) [2]. The number of publications on HEAs increases at an exponential rate (Fig. 1-2). HEAs can be divided into two main groups: single-phase HEAs and multiphase HEAs (usually named CCAs, compositionally complex alloys). HEAs and CCAs can be divided into the following categories based on constituent elements (Fig. 1-3): 3d transition metal, refractory metal, 4f transition metal, light metal, bronzes and brasses HEAs/CCAs [32]. Each node in Figure 1-3 represents an alloy, while lines connecting nodes show sharing elements (at least one) with other alloys.

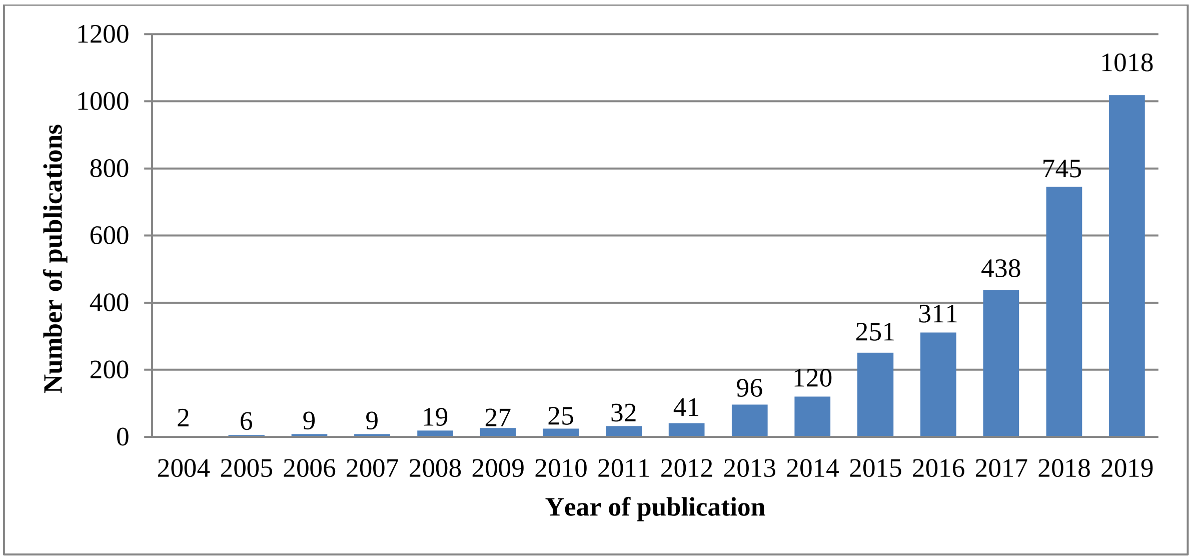

Figure 1-2. Number of publications on High Entropy Alloys from 2004 to 2019 (results based on Scopus analysis).

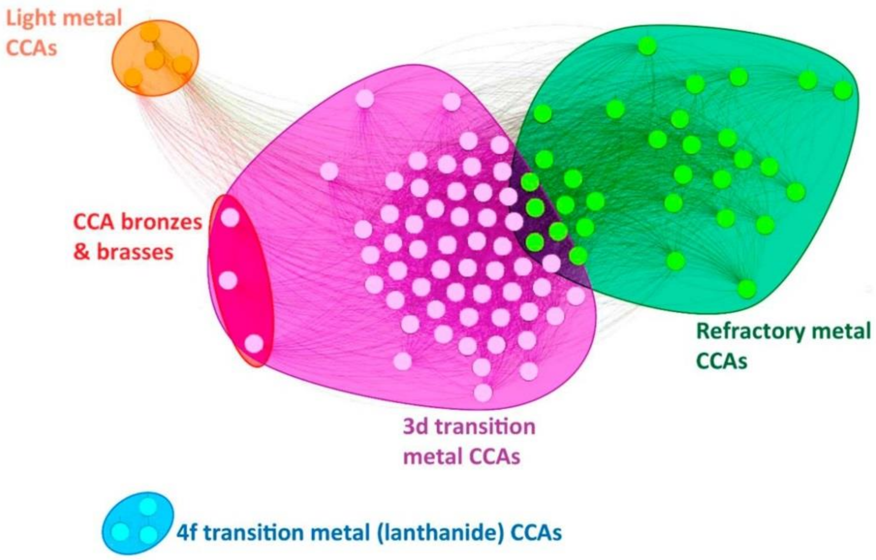

Figure. 1-3. Alloy network of 110 equiatomic HEAs/CCAs showing five main categories. Dots represent alloys, lines represent sharing one or more elements. Reproduced with permission from Elsevier [32].

3d transition metal HEAs are definitely the biggest family, mainly based on aluminum, cobalt, chrome, copper, iron (the most common element), manganese, nickel, titanium, and vanadium [23,32]. The large majority of single phase fcc alloys belongs to this family [23]. A good example could be the first introduced HEA, CoCrFeMnNi [1]. Some alloys with elements mostly from 3d transition metal family present bcc structure, e.g., AlFeTiCrZnCu [33], or $Al_xCoCrFeNi$ ($x > 1$) (bcc/B2) [10,34–36]. The properties of many 3d transition metal HEAs are very promising, e.g., tensile strength and ductility [32].

The refractory metal HEAs (RHEAs) are the second-largest family mainly based on hafnium, molybdenum, niobium, tantalum, titanium, vanadium, tungsten, zirconium and usually sharing some elements from the 3d transition metal group. This family is characterized by a wide range of melting temperatures (1855 – 3422 °C) and density (4.5 - 19.4 g cm^{-3}) [23]. Refractory HEAs present promising mechanical and oxidation resistance at high temperatures [23,32]. A good example could be the $Nb_{25}Mo_{25}Ta_{25}W_{25}$ or $V_{20}Nb_{20}Mo_{20}Ta_{20}W_{20}$ alloy, both single bcc phase, developed by Senkov *et al.* [9].

Other families of HEAs are significantly smaller than 3d transition and refractory metals. The 4f transition metal HEAs (lanthanide or rare-earth HEAs) is a completely isolated family, which does not share elements with other families. The examples of alloys are DyErGdHoLuScTbY and DyGdHoLaTbY, both single-phase with the hexagonal close-packed structure [37]. The light metal HEAs are a small family of alloys based on the following elements: aluminum, beryllium, lithium, magnesium, scandium, silicon, tin, titanium, and zinc [23]. Many low-density elements are toxic or very reactive. Therefore, the choice of possible composition is very limited [32]. Moreover, these elements present a wide range of melting points, which makes it difficult to prepare alloys by the liquid route. Mechanical alloying seems to be a preferred way to fabricate these alloys, e.g., the $Al_{20}Li_{20}Mg_{10}Sc_{20}Ti_{30}$ compositions (density, $\rho = 2.67$ g cm^{-3}) was developed by mechanical alloying [38]. The high hardness and low density could make the light metal HEAs an attractive choice for some application, e.g., in the aerospace industry. The bronzes and brasses HEAs (contain tin and zinc, respectively) is a very small group of alloys that could be included in the 3d transition metal family due to the significant content of manganese or nickel [32]. The best example of possible compositions are alloys from the Al-Cu-Mn-Ni-Sn-Zn family, which in certain conditions could exceed the mechanical properties of traditional bronzes and brasses [39]. Besides family included in Figure 1-3, HEAs containing boron, carbon, or nitrogen should be mentioned. The alloys consist mainly of 3d transition or refractory metals; however, the additions of boron, carbon, or nitrogen could significantly affect microstructure and properties [23]. Hence, some authors created this separate group. Moreover, the relatively new family of HEAs based on precious metals is not included in Figure 1-3. An example could be AuCuNiPdPt, which crystallizes in a single fcc structure [40]. The precious HEAs could be used for catalysis applications [23].

An alternative classification of HEAs could be based on the structure. The first evident classification is the crystalline and amorphous alloys. The crystalline alloys could be later divided into single or multi-phase. The phases formed in HEAs could be simple disordered (e.g., bcc, fcc), simple ordered phases (e.g., B2, $L1_2$), or complex ordered phases (e.g., sigma or Laves phases) [23].

Despite the development of many HEAs, the most investigated alloy is still the single fcc phase equiatomic CoCrFeMnNi alloy, which was introduced in 2004 by Cantor *et al.* [1]. Though crystallization after melting into the fcc structure, the Cantor alloy decomposes after prolonged annealing [28,41]. Nevertheless, CoCrFeMnNi is still considered as the typical high-entropy alloy. Thorough years, alloys with modified Cantor composition appeared. The alloys with removed one or two elements from CoCrFeMnNi have been tested by Wu *et al.* [42]. It was shown strength and ductility increase with decreasing temperature for some compositions. The non-equiatomic compositions were developed to produce twinning-induced plasticity [43] or transformation induced plasticity [44]. Another example of a commonly studied system is the TiZrHfNbTa refractory alloy. It crystallizes in a single bcc structure and exhibits tensile ductility at room temperature [5]. In alloys without refractory metals in the composition, the occurrence of bcc is less common. The Al-Co-Cr-Cu-Fe-Ni system is also one of the most investigated in recent years. It consists of fcc#1, fcc#2 (rich in copper), and bcc/b2 phases with volume fraction depending on the composition [45]. The $Al_xCoCrFeNi$ ($x = 0 – 1.5$) family is also frequently studied [10,34–36,46]. The structure changes significantly with the increasing content of aluminum, i.e. single fcc structure ($Al_{0.1}CoCrFeNi$) [10], fcc + ordered B2 ($Al_{0.75}CoCrFeNi$) [35], bcc (lattice parameter, a = 2.88 Å) + B2 ($Al_{1.5}CoCrFeNi$) [10,36].

1.1.4. Mechanical Properties

The properties of HEAs vary significantly depending on the chemical composition; however, based on the available data from the literature, remarkable properties of HEAs can be listed. The mechanical properties have been studied most thoroughly. Fig. 1-4a shows that the best 3d transitions HEAs/CCAs (filling the space between titanium alloys and steels) are equivalent, considering density, in uniaxial tension to the best traditional alloys such as aluminum alloys [32]. Moreover, refractory alloys are expected to present better properties at high temperatures than many conventional alloys. In terms of yield strength vs. Young’s modulus (Fig. 1-4b), refractory HEAs/CCAs, surpass significantly traditional alloys as well as other HEAs/CCAs. Fig. 1-4 shows that many HEAs/CCAs can equal mechanical properties of conventional alloys or even exceed them in some conditions. Taking into consideration the relatively short time of research in the field of HEAs, the properties should be further improved in the near future.

One of the best-known properties of CoCrFeMnNi alloy is the simultaneous increase of its strength and ductility with decreasing temperature from room temperature to 77 K (liquid nitrogen) [6,47]. Moreover, the high value of fracture toughness ($K_{JIc} \sim 220$ MPa $m^{1/2}$) is preserved when decreasing the temperature to 77 K [6]. Gludovatz *et al.* [6], in a frequently cited paper, concluded that remarkable fracture toughness at cryogenic temperature is the effect of nanotwinning occurring at low temperatures. The nanotwinning (plasticity mechanism), which increases the tensile ductility, and high strength at cryogenic temperature, enables the preservation of high fracture toughness at low temperatures.

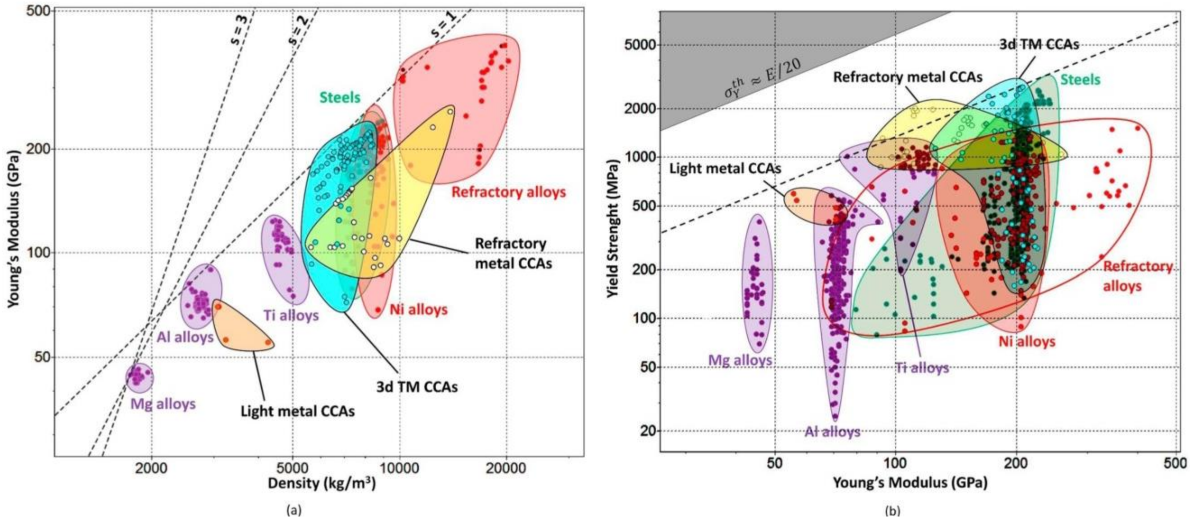

Figure. 1-4. a) Young's modulus vs. density of traditional alloys and HEAs/CCAs, dashed lines show performance indices of mechanical properties in (alloys above performance lines present better performance than alloys below): uniaxial tension (s=1), beam bending (s=2), panel bending (s=3); b) Yield strength vs. Young's modulus of traditional alloys and HEAs/CCAs. Reproduced with permission from Elsevier [32].

Other remarkable mechanical properties of HEAs are high tensile strength at high temperature and creep resistance. The $Ni_{47.9}Al_{10.2}Co_{16.9}Cr_{7.4}Fe_{8.9}Ti_{5.8}Mo_{0.9}Nb_{1.2}W_{0.4}C_{0.4}$ alloy consists of γ matrix (fcc) and γ′ precipitates ($L1_2$), similarly to widely known superalloys [7]. Hence, HEAs with γ + γ′ structure are named high entropy superalloys. The alloy mentioned above presents a yield strength (800 MPa) above 800 °C comparable with some conventional nickel-based superalloys and greater than other HEAs. Moreover, creep resistance of this alloy is similar to some first-generation conventional nickel-based superalloys [7]. The high entropy superalloys are in the early stage of development, and it seems that their properties could be significantly improved soon. The $Al_{0.5}CoCrCuFeNi$ alloy (fcc and $L1_2$ structures) also presents high creep resistance; however, it was measured by nanoindentation experiment (as many other HEAs), which is not totally reliable [8]. The $Al_xCoCrFeNi$ family with bcc/B2 structure (x = 1.12 or x = 1.33) presents high compressive strength (yield strength 1350–1400 MPa) and high hardness ($HV_{0.5}$ = 517 – 527); however, the plastic deformation is limited (14-17 %) [34].

Examples of good mechanical properties of alloys with a single disordered bcc structure are refractory HEAs - $V_{20}Nb_{20}Mo_{20}Ta_{20}W_{20}$ and $Nb_{25}Mo_{25}Ta_{25}W_{25}$ [9,48]. These alloys show very high hardness: 535 HV for the $V_{20}Nb_{20}Mo_{20}Ta_{20}W_{20}$ and 454 HV for the $Nb_{25}Mo_{25}Ta_{25}W_{25}$ [48]. Moreover, both alloys present very high compressive yield strength at room temperature, 1246 MPa ($V_{20}Nb_{20}Mo_{20}Ta_{20}W_{20}$), and 1058 MPa ($Nb_{25}Mo_{25}Ta_{25}W_{20}$); however, the plastic deformation is very limited (1.5 – 2 %). At higher temperatures, the yield strength is also very promising, e.g., at 1000 °C is 548 MPa and 842 MPa with a fracture strain of 19 % for the $Nb_{25}Mo_{25}Ta_{25}W_{20}$ and $V_{20}Nb_{20}Mo_{20}Ta_{20}W_{20}$ alloys, respectively (Fig. 1-5a,b) [9]. The plastic deformation of alloys increases significantly compared to the tests at room temperature. At the temperatures above 800 °C, the yield strengths of both refractory high entropy alloys exceed those of common superalloys (e.g., Inconel 718, Haynes 320) significantly, and decrease slowly with increasing testing temperature (Fig. 1-5c). Hence, the refractory HEAs could be the promising candidates in similar applications as traditional superalloys. However, the high density of the alloys, 13.75 g/cm^3 for the $Nb_{25}Mo_{25}Ta_{25}W_{25}$, and 12.36 g/cm^3 for the $V_{20}Nb_{20}Mo_{20}Ta_{20}W_{20}$ could be a significant disadvantage of the refractory HEAs [48].

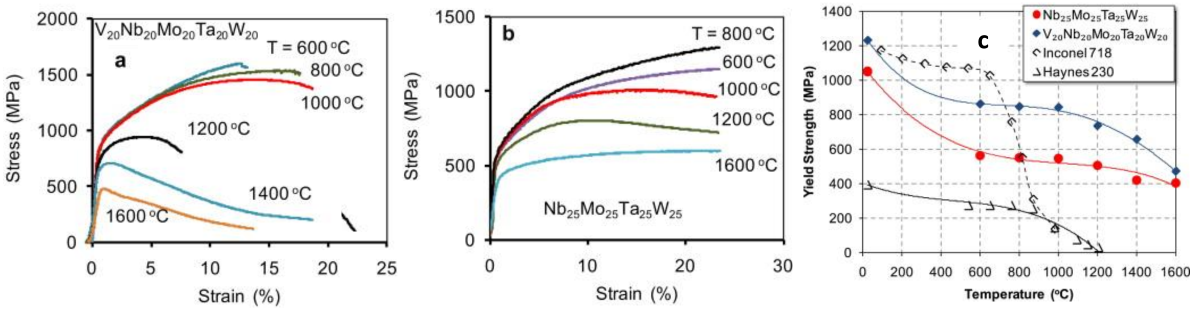

Figure 1-5. Mechanical properties of refractory HEAs: compressive engineering stress-strain curves for the $V_{20}Nb_{20}Mo_{20}Ta_{20}W_{20}$ (a) and $Nb_{25}Mo_{25}Ta_{25}W_{25}$ (b) alloys; c) comparison of yield strength of two refractory HEAs and two superalloys at different temperatures [9].

1.1.5. Other properties

The mechanical properties of developed HEAs are already promising; however, it seems that it will be difficult to replace the conventional alloys in many applications due to the high cost of many HEAs and often not significantly superior mechanical properties compared to superalloys, steels, etc. Thereby, the development of HEAs should be focused on good mechanical properties coupled with exceptional functional properties [5]. Hence, functional properties also gained considerable attention. The irradiation resistance of HEAs studied by El-Atwani *et al.* [11] showed that $W_{38}Ta_{36}Cr_{15}V_{11}$ refractory HEA (single bcc structure) presents negligible hardening with no dislocation loops after irradiation of 8 displacements per atom (dpa), which proves exceptional irradiation resistance of this composition. Xia *et al.* [10] and Yang *et al.* [35] revealed that $Al_{0.1}CoCrFeNi$ (single fcc structure) presents better irradiation resistance than frequently used nuclear materials. Corrosion is a significant problem in many industrial environments; hence, the corrosion resistance of HEAs is also frequently studied. Chou *et al.* [13] showed good corrosion resistance of the $Co_{1.5}CrFeNi_{1.5}Ti_{0.5}Mo_{0.1}$ HEA (single fcc structure), in which molybdenum addition plays an important role by increasing the critical pitting temperature and the pitting potential. The superior resistance to corrosion of the $Al_{0.3}CoCrFeNi$ HEA (single fcc structure), than conventional alloy, was revealed by Shi *et al.* [14]. The CoCrFeMnNi alloy (single fcc structure) presents very high hydrogen embrittlement resistance during a tensile test at cryogenic temperature. It is thanks to a gradient of nanotwins structure arising during deformation due to a gradient of charged hydrogen [15,16].

1.1.6. Processing routes

High entropy alloys, as conventional alloys, are prepared by many different routes (Fig. 1-6). The fabrication methods can be divided into three groups based on the state of the elements during mixing.

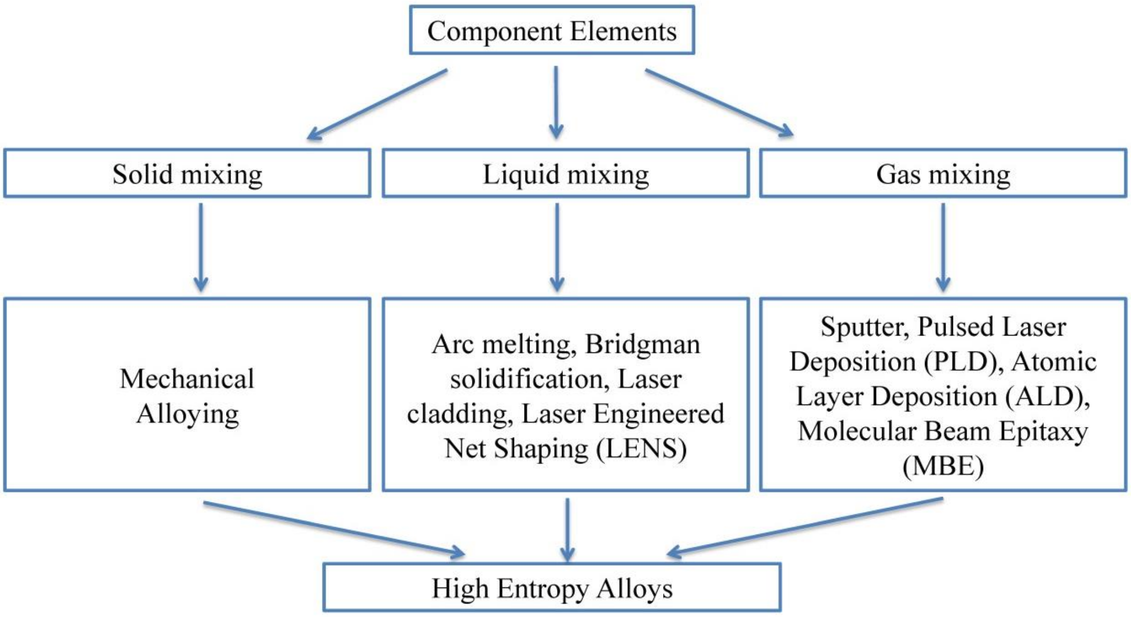

Figure 1-6. Processing routes of High Entropy Alloys [4].

The liquid path, especially arc melting or induction melting, is the most common method of fabrication of HEAs [4,17,49]. Usually, an alloy is melted and solidified at least five times to provide chemical homogeneity of the sample. The liquid route enables to prepare relatively easy and quickly a large quantity of the alloy. The high temperatures during arc melting may cause evaporation of some elements, e.g., manganese [49]. Other disadvantages of the liquid route are the formation of a dendritic structure with chemical segregation, the formation of non-equilibrium phases, porosities, cracks [4]. The Bridgman solidification method is used to produce single-crystal HEAs [4]. The Laser Engineered Net Shaping (LENS) technique enables to rapidly fabricate many chemical compositions by using a highpowered laser beam into the metal powders [36,49]. The gas routes of HEAs processing, such as pulsed laser deposition, are commonly used to produce thin films [4].

The solid processing of HEAs consists of the milling of elemental powders to obtain alloyed powders. The mechanical alloying (MA) was initially developed by Benjamin in 1970 [50]. The main advantages of MA are the absence of segregation problems, the possible mixing of elements with largely different melting temperatures, the extended solid solubility, or the easiness to obtain nanocrystalline materials [4,49]. The main disadvantage of mechanical alloying is the frequently occurring contamination by carbon, oxygen, etc. However, the contamination could lead to the formation of carbides and oxides, which can increase the mechanical resistance of an alloy or induce its brittleness. The source of contamination could be the materials of the balls and the vial, the process control agent (PCA), or the milling atmosphere [4]. Moreover, mechanically alloyed powder has to be consolidated, by sintering, to obtain bulk material. During sintering, grain growth is usually observed, and contamination from die can occur [49,51]. Nevertheless, the advantages of MA outweigh the disadvantages, and thus mechanical alloying is a common method to obtain metallic alloys for the last 50 years. The first paper on mechanically alloyed HEA was published in 2008 by Varalakshmi *et al.* [33]. It deals with the preparation of nanocrystalline, single-phase bcc AlFeTiCrZnCu HEA. Since then, reviews on HEAs prepared by powder metallurgy have been published [20,21,52,53]. In recent years, the number of published papers on HEAs MA has increased significantly (Fig. 1-7).

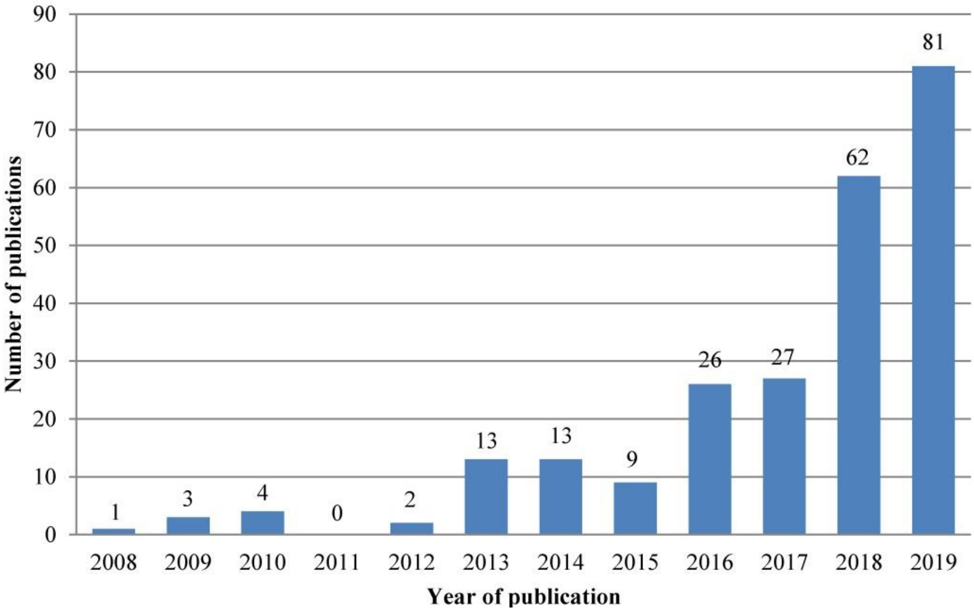

Figure 1-7. Number of publications on High Entropy Alloys prepared by mechanical alloying from 2008 to 2019 (results based on the Scopus analysis).

1.1.7. Potential applications

High entropy alloys have been studied for more than 15 years. Other commonly used materials, such as superalloys, have been studied for a more significant amount of time; thus, the identified applications of HEAs are rather limited. Some high entropy superalloys or refractory high entropy alloys can replace conventional superalloys in some applications in the aerospace or energy industries [4,7]. The Cantor alloy is a potential candidate for cryogenic applications [6,47]. HEAs (with fcc structure) could be used as a binder for WC to obtain higher fracture toughness [54]. Hard coatings, such as (AlCrNbSiTiV)N (single fcc structure), could find their applications in milling or cutting tools [4,55]. The (Al,Cr,Nb,Y,Zr)N thin film (NaCl-type single solid solution) is a promising protective coating for applications in aggressive environments [56]. The (AlCrTaTiZr)N HEA (fcc and amorphous structure) is a promising candidate for diffusion barrier in microelectronics [57]. The $W_{38}Ta_{36}Cr_{15}V_{11}$ (single bcc structure) can be used in applications under irradiation conditions [11]. George *et al.* [5] suggested that to find the potential applications for HEA, research should be focused on coupling outstanding functional properties with good mechanical properties. Moreover, the cost of many HEAs is higher than many traditional alloys; therefore, the HEAs have to reveal significantly better properties to be used in the industry for the given application.

1.2. Design of a new composition

1.2.1. Parametric approach

The number of possible compositions of HEAs is almost infinite. Hence, the experimental studies should be preceded by a theoretical calculation to choose the chemical compositions which could form alloys with the microstructures as simple as possible. The parametric approach was introduced to give help to predict the structure and find single-phase HEAs [4,17,58,59]. This empiric approach consists of the calculation of the following parameters: mixing entropy, mixing enthalpy, atomic size difference, electronegativity difference, valence electron concentration, and omega (which combines the effects of the melting temperature and mixing entropy and enthalpy). The limit values of these parameters to form HEA have been obtained from the literature.

The mixing entropy consists of four components, such as configurational entropy, vibrational entropy, magnetic dipole, and electronic randomness [4]. To simplify the calculations, only configurational entropy is usually considered due to its predominant value over other contributions [2]. The configuration entropy (ΔS_{conf}) is calculated using the following formula [4,59]:

$$\Delta S_{conf} = -R\sum_{i=1}^{n} c_i ln c_i \qquad (1.3)$$

where R is the gas constant, n is the number of components, and c_i is the atomic fraction of the ith component. Despite the lack of consensus on HEA definition, it is usually mentioned that HEAs should possess configurational entropy higher than 1.5 R. Medium entropy alloys (MEAs) and low entropy alloys (LEAs) possess configurational entropy between 1.0 R and 1.5 R, and lower than 1.0 R, respectively [4]. It was believed that configurational entropy plays a crucial role in the stabilization of the solid solution; however, as it was mentioned in Subsection 1.1.2. “High entropy alloy concept”, other parameters are also important.

The mixing enthalpy (ΔH_{mix}) is a very important parameter in the prediction of the solid solution vs. intermetallic compounds or amorphous phases. It is calculated using the following formula [4,59]:

$$\Delta H_{mix} = \sum_{i=1;j\neq i}^{n} 4\Delta H_{AB}^{mix} c_i c_j \qquad (1.4)$$

where ΔH_{AB}^{mix} is the mixing enthalpy for the binary liquid AB alloys, n is the number of components, c_i and c_j are the atomic fractions of the ith and jth components, respectively. To form HEA, i.e., a solid solution, ΔH_{mix} should be in the range between -10 and 5 kJ/mol [17,59]. For lower values of the mixing enthalpy, bulk metallic glass or intermetallic compounds could form (Fig. 1-8), while for higher values, the alloy could not form [4,59].

The atomic size difference (δ) has a crucial role in the formation of solid solution phases instead of intermetallics or amorphous phases. It could be calculated using the formula below [59]:

$$\delta = \sqrt{\sum_{i=1}^{n} c_i \left(1 - \frac{r_i}{\sum_{i=1}^{n} c_i r_i}\right)^2} \tag{1.5}$$

where r_i is the atomic radius and c_i is the atomic fraction of the ith element, n is the number of components. In general, as it could be seen in Fig. 1-8 and Fig. 1-9, the atomic size difference should be below 6.6 %. However, between 5.0 and 6.6 %, a solid solution or an ordered solid solution may form, depending on alloy’s composition [17]. A δ value higher than 6.6 % prevents in all cases, the formation of a solid solution in multicomponent alloys [17,59].

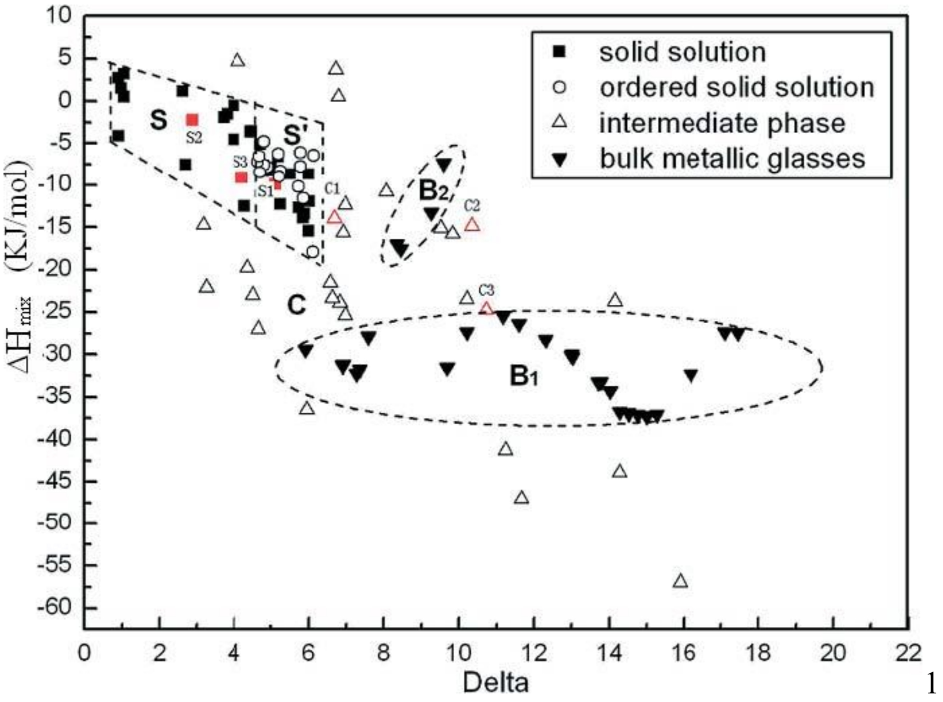

Figure 1-8. Ability to form a solid solution, an ordered solid solution, an intermediate phase (e.g. precipitation of intermetallic compounds), or a bulk metallic glass from a multicomponent composition based on the relationship between the mixing enthalpy and delta (atomic size difference). Reproduced with permission from John Wiley and Sons [59].

The electronegativity difference ($\Delta\chi$) between constituent elements has an important influence on the phase formation. It could be calculated using the following formula [58]:

$$\Delta\chi = \sqrt{\sum_{i=1}^{n} c_i(\chi_i - \sum_{i=1}^{n} c_i\chi_i)^2} \tag{1.6}$$

where χ_i is the Pauling electronegativity and c_i is the atomic fraction of the ith element, n is the number of components. The electronegativity difference should be below 0.175 to form a solid disordered solution in HEA; however, some molybdenum-containing HEAs with a much higher electronegativity present a solid solution structure [60]. Moreover, some HEAs, with an electronegativity difference well below 0.175, contain intermetallic compounds (Fig. 1-9) [60]. Hence, the Δχ should be considered only as guidance and not as a strict criterion of phase formation.

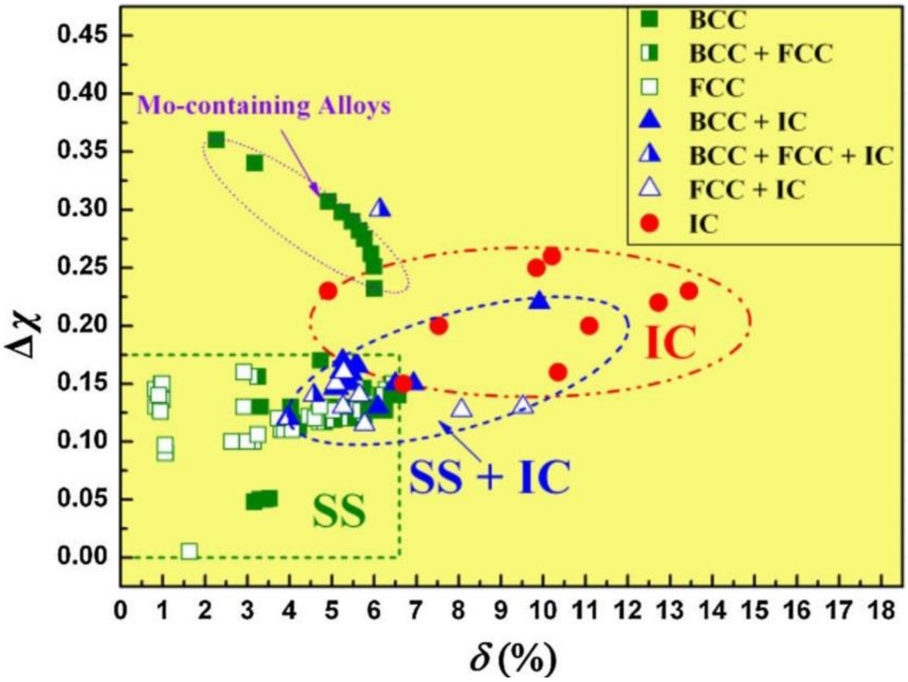

Figure 1-9. Plot of the prediction of structures formation in HEAs based on the relationship between the electronegativity difference (Δχ) and the atomic size difference (δ) (experimental data). Reproduced with permission from Springer Nature [60].

The valence electron concentration (VEC) is a useful criterion to predict bcc or fcc formation for a given composition of HEA. It is calculated using the following formula [58,61]:

$$VEC = \sum_{i=1}^{n} c_i(VEC)_i \tag{1.7}$$

where $(VEC)_i$ is the valance electron concentration of the ith element and c_i is the atomic fraction of the ith element, n is the number of components. To form a pure bcc structure, VEC should be below 6.87, while to form a pure fcc structure, VEC should be higher than 8.00 (Fig. 1-10). Between the values mentioned above, HEAs have a two-phase structure (bcc+fcc). The validity of the VEC criterion has been verified mainly for transition metals

HEAs; hence, an additional work should be done to confirm this rule for all HEA systems [4]. Moreover, some exceptions, as CrCuFeMnNi, have been found [61].

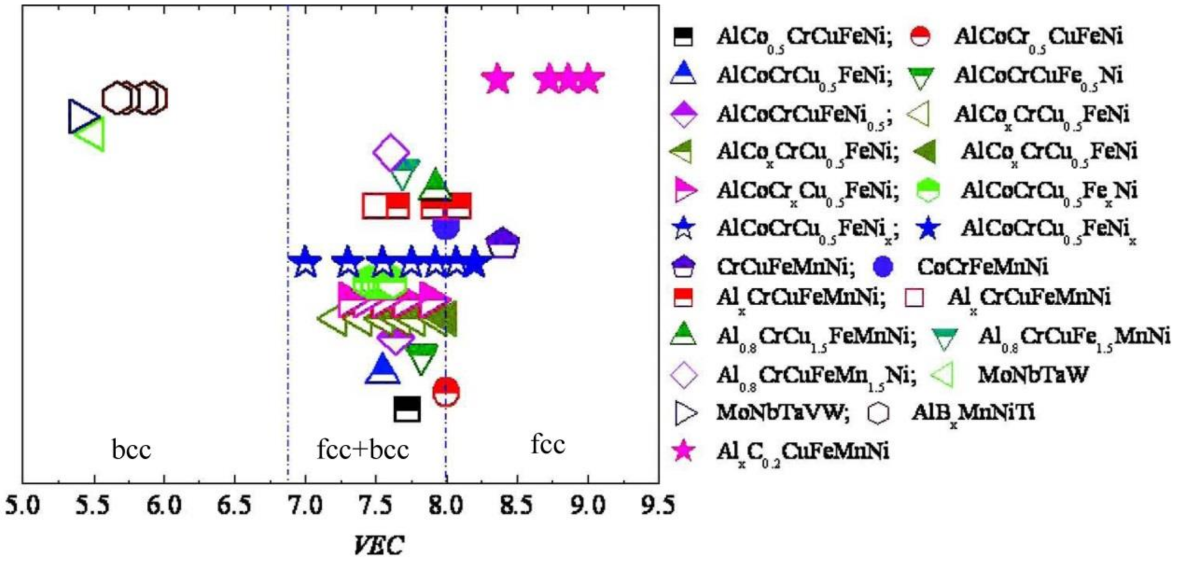

Figure 1-10. Relationship between VEC and phase stability of HEA systems. Completely filled, half-filled, and non-filled symbols represent alloys with fcc phases only, alloys with a mixture of bcc and fcc, and alloys with fcc, respectively. Reproduced with permission from AIP Publishing [61].

The Omega (Ω) parameter combines three parameters: mixing entropy ΔS_{mix} (mostly configurational), mixing enthalpy (ΔH_{mix}), and average melting temperature of the alloy (T_m). It is calculated using the formula below [4,17,60]:

$$\Omega = \frac{T_m \Delta S_{mix}}{|\Delta H_{mix}|} \tag{1.8}$$

where the average melting temperature of the alloy is defined as follows:

$$T_m = \sum_{i=1}^{n} c_i (T_m)_i \tag{1.9}$$

where c_i is the atomic fraction the ith component, n is the number of components. Zhang *et al.* [17] suggested that to form solid solution phases, the Ω should be higher than 1.1. Smaller values of Ω facilitate the formation of intermetallics or amorphous phases [4].

Despite the simplicity and relatively good correlation with the experimental data, the parametric approach has significant limitations. The ranges for parameters to form HEA vary, depending on the publication, because there is no convincing fundamental explanation based on the physical basis [27]. Moreover, data, which is used for the creation and validation of the parametric approach, is mainly based on the as-cast microstructures [27]. The as-cast microstructures are usually non-equilibrium and depend on cooling rates. The equilibrium state may be significantly different. Nevertheless, the parametric approach is still widely used to predict the crystal structure of HEAs.

1.2.2. CALPHAD calculations

The parametric approach is an easy and primary tool to select composition and predict the phase structure of HEAs. A more sophisticated method is CALPHAD (**CAL**culation of **PHA**se **D**iagrams). The CALPHAD method uses binary and ternary diagrams obtained by experiments as input data. However, when experimental data is not available, data collected from first-principle calculation is used. The optimized input data is extrapolated to generate a thermodynamic description of the multi-component system. The as-generated database should be further optimized by the calculation of Gibbs energies to obtain a reliable phase diagram for multi-component alloy [4]. The scheme of procedures used in the CALPHAD approach is shown in Fig. 1-11.

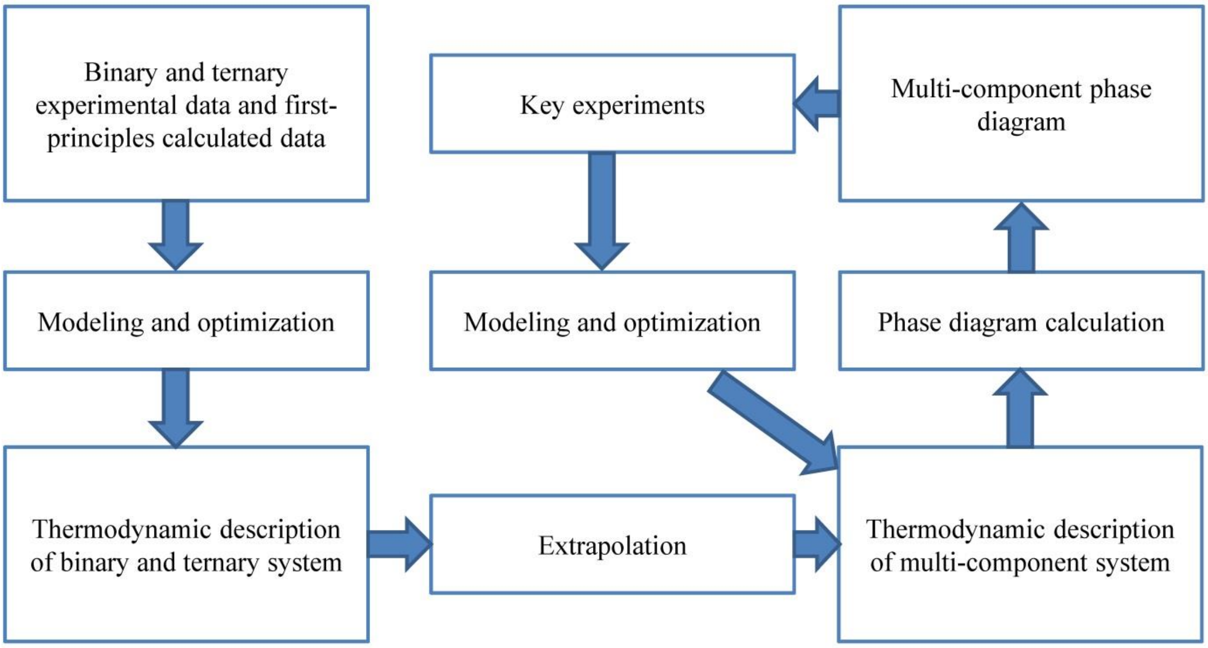

Figure 1-11. Procedures used in the CALPHAD approach to obtain a thermodynamic description of a HEA system [4].

The frequently used CALPHAD software packages are ThermoCalc, MTDATA, Pandat, and FactSage [4,62]. The database for high entropy alloys (TCHEA for Thermo-Calc [18] and PanHEA for Pandat) has been developed recently. The CALPHAD method is now a common tool to quickly predict the phase composition of HEAs; however, obtained data is not always consistent with the experimental results [27,62]. It was found that the prediction of intermetallic phases is very problematic in CALPHAD approach; however, it is crucial for designing structural materials [27]. CALPHAD is rarely used to design a new system of HEAs. More often, it is used to slightly modify the chemical composition of already existing, or chosen by the parametric approach, HEA system to obtain single-phase regions (or other interesting domains) [62]. It is usually done by calculating pseudo-binary or pseudo-ternary diagrams. Nevertheless, the screening studies, as [22] by Senkov *et al.*, have also been performed. The screening and phase stability studies are often conducted using Thermo-Calc software coupled with TC-python software [19]. Gorsse *et al.* [62] suggested that the CALPHAD screening for new compositions should be improved by better descriptions of the Gibbs energy curves for near equiatomic compositions of HEAs (more information from ternary) and by coupling CALPHAD with design tools, such as data mining, physicochemical criteria, as well with optimization techniques.

1.2.3. Al-Cr-Fe-Mn-Mo system by CALPHAD

In recent years, many potential compositions of HEAs have been analyzed by CALPHAD. Senkov *et al.* [22] presented 157 promising equiatomic alloys after screened over one hundred thousand 3 to 6 component alloys by the CALPHAD method using Pandat Software. Among the listed HEAs, the AlCrFeMnMo equiatomic composition presents interesting properties (Table 1-1). The alloy consists of a single bcc phase at the melting temperature (T_m) of 1600 °C. The structure of the AlCrFeMnMo HEA is a bcc phase and the intermetallic $AlMo_3$ (primitive cubic structure, space group: Pm-3n (No. 223), lattice parameter a= 4.95 Å [63]) at room temperature up to 1041 °C (T_{use} = the maximum use temperature). The alloy presents relatively low density (ρ) and high Young's modulus (E) compared to other studied HEAs. The promising results encourage studying AlCrFeMnMo HEA experimentally.

Table 1-1. Results of calculation of AlCrFeMnMo equiatomic alloy [22].

Alloy	T_m [°C]	T_{use} [°C]	Phases at 600 °C	ρ [g/cm^3]	E [GPa]
AlCrFeMnMo	1600	1041	Bcc + $AlMo_3$	7.0	213

1.3. Powder metallurgy of High Entropy Alloys

1.3.1. General overview

As it was mentioned earlier, the powder metallurgy of high entropy alloys develops quickly in recent years. The term "Powder metallurgy" brings together a few different techniques, which can be divided according to powder preparation and consolidation methods. The various powder metallurgy routes to produce bulk samples of HEA, without taking into account the additive manufacturing, are shown in Figure 1-12.

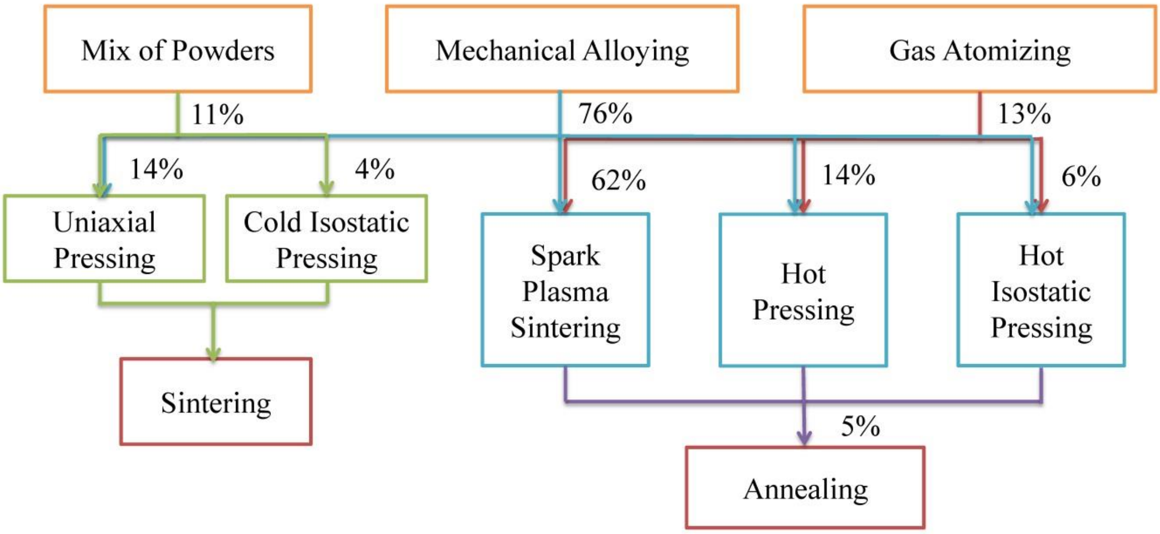

Figure. 1-12. Powder metallurgy fabrication routes of bulk HEAs (the percentage share of each method is indicated) [21].

Based on data published in 2019 by Torralba *et al.* [21], the mechanical alloying is by far the most common route of preparation of HEA powder. The gas atomization is an alternative method to prepared alloyed powder. The third possibility is to use a mixture of pure metal powder, which is consolidated without any pre-alloying (no contamination as during mechanical alloying). The most common sintering method is spark plasma sintering (SPS). The advantage of SPS is a short sintering time to attain near full density; thus, the grain growth is limited [64]. Hot press sintering (HP) and hot isostatic pressing are also commonly used methods. Another possibility is the uniaxial pressing and cold isostatic pressing. The cold-pressed powder is then sintered without applying any pressure to obtain bulk samples. The disadvantages of the last two methods are grain growth due to higher temperature and longer time to obtain near full density (e.g., 93.5 % [65]). Nevertheless, those routes are used in the industrial production of traditional powder metallurgy materials due to a lower cost and easier processing [21]. The other less common method (not included in Fig. 1-12), such as powder extrusion [66] or shock wave compaction [67], should be mentioned. Despite not being a classical powder metallurgy method, additive manufacturing of HEAs, which needs an elemental or pre-alloyed powder, develops rapidly in recent years [68]. Powders are also required to produce HEA coatings [69]. The powder metallurgy of HEAs is a vast topic. In the next subsections, the most common HEAs fabrication techniques, such as mechanical alloying, gas atomization, hot-press sintering, and spark plasma sintering, are discussed.

1.3.2. Mechanical alloying

Mechanical alloying enables solid-state processing of alloys. The solid-state reactions are induced mechanically by the collisions of milling media (usually balls) with introduced powders (diffusion couples) in the milling device [50,70]. During mechanical alloying, the repetitive cold welding, fracturing, and cold rewelding of mixed powders occur. The scheme of the evolution of the powder microstructure during MA is shown in Figure 1-13 based on the example of a mixture of titanium and iron powders.

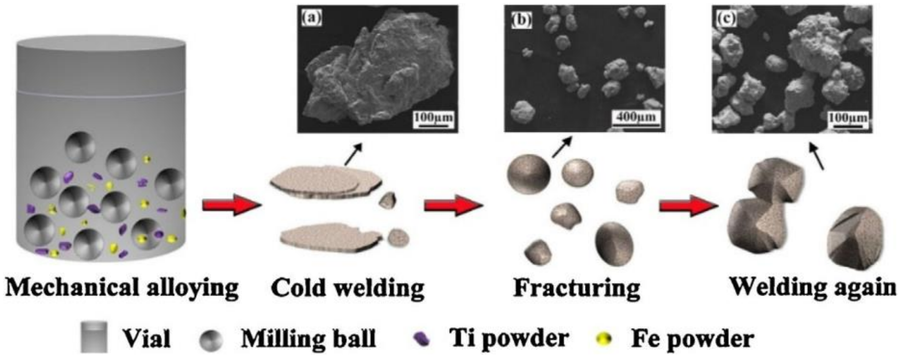

Figure. 1-13. Schematic diagram of the evolution (microstructure) of metallic powders (for example, Ti and Fe) during mechanical alloying. Reproduced after Xu *et al.* [71] under a Creative Commons license (https://creativecommons.org/licenses/by-nc-nd/4.0/).

The solid-state powder metallurgy helps to overcome casting segregation, which is a common problem in cast metallic materials [4,49]. Moreover, easiness to obtain nanocrystalline structure, extended solid solubility, and synthesis of elements with significantly different melting points are also beneficial [4,20,49,70]. MA can be performed in many different types of mills, e.g., vibratory, planetary, attritor, centrifugal ball mills [70]. Various parameters, which affect the final powder microstructure, are shown in Figure 1-14. The choice of milling media is crucial because it could be a source of severe contamination due to balls and vial wear. A suitable material of the milling media should be chosen based on the hardness, brittleness, and chemical composition of the powder to be milled. The atmosphere, commonly argon, is also a crucial factor in MA. The presence of residual oxygen could lead to the formation of oxides. The contamination source could also be the process control agent (PCA), which is usually added to prevent agglomeration of particles, or even the dust [70]. Hence, the most important disadvantage of mechanical alloying is contamination, which can result from different factors.

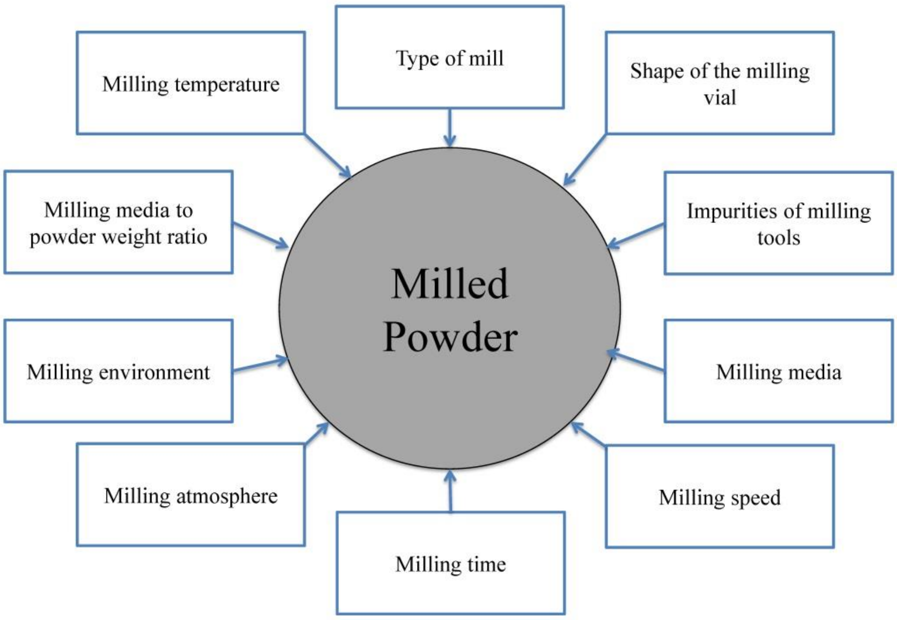

Figure 1-14. Main factors which affect the final microstructure of milled powders [70].

Mechanical alloying is used to prepare a wide range of powders such as Oxide Dispersed Strengthened (ODS) alloys, intermetallic compounds, nanocomposites, various nanomaterials, or metallic glasses [70]. The first article about mechanically alloyed HEA was published by Varalakshmi *et al.* in 2008 [33], only four years after the first publications on HEAs [1,2]. Nowadays, mechanical alloying is by far the most common route of fabrication of alloyed HEAs powder [21]. It is due to undeniable advantages, which are even more critical for HEAs because multicomponent alloys could present a high difference of melting temperatures between elements, and the risk of casting segregation is higher than in traditional alloys.

HEAs are commonly synthesized in planetary mills (e.g., [33,67,80–86,72–79]); however, MA in shaker rod mill [87], or in vibrational mill SPEX [38,88–91] were also conducted. Process control agents, such as toluene [33,72,75,76,81,86], methanol [74], stearic acid [77], N-heptane [79,83–85] and gasoline [82], were especially used for milling in the planetary mills. Moreover, the combination of dry milling and wet milling was employed [76,92]. Processing in SPEX was conducted without PCA [38,90] or in methanol [88,89,91]. In vibrational mills, the risk of sticking of the powder particles to the walls of the vial is much lower than in planetary mill due to the high energy frontal impacts; therefore, PCA is not always needed. The most of millings are performed at room temperature under argon atmosphere; however, millings at cryogenic temperatures were also carried out [38]. Different types of vial and balls materials were used e.g., tungsten carbide [33,72,77,86], zirconia [67,73], hardened steel [74,75,80–82,88,90] or stainless steel [38,76,78,79,83–85]. The most common ball to powder weight ratios were 5:1 (mainly in SPEX, e.g., [88,89]), 10:1 [33,67,82,84,86,90,91,72–77,80,81], 13:1 [78], 15:1 [79,83,85] or 20:1 [38]. The MA time and speed depend mainly on the chosen composition and factors listed above. The typical total time is between 15 and 40 h to obtain a solid solution; longer milling could increase the possibility of contamination [20]. The mechanical activation, which could be described as a non-completed mechanical alloying (shorter time and less energy in milling), was also successfully studied for the elaboration of high entropy alloys [93]. The most abundant papers on MA of HEAs deal with the evolution of the microstructure during milling.

Mechanical alloying usually produces metastable phases. MA is known to extend solid solubility; hence, the probability of obtaining a single solid solution is higher than for other fabrication methods [20]. Many alloys present single bcc (e.g., [74,81]) or fcc (e.g., [87,94]) after MA; however, sintering or annealing often leads to the formation of multiphase structure. Multiphase compositions, especially dual-phase, e.g., a mixture of bcc and fcc, are also common for mechanically alloyed HEAs [20]. Subsequent sintering also frequently leads to phase transformations. It should be noted that the phase structure after MA and sintering is sometimes different than observed in samples prepared by the liquid route [20]. Milling could also lead to the formation of an amorphous phase [95], or even total amorphization of an alloy [96].

Despite promising results on mechanically alloyed HEAs, the contamination problem is the biggest challenge [21,52]. The contamination sources were usually identified as balls and vials [73,77,79–81,84–86], the process control agent [74,76,79,81–86], or the atmosphere [74,78,83,85]. The contamination could lead to the formation of carbides, oxides, or significantly change the final composition of powder [20,21]. Vaidya *et al.* [86] carefully investigated the elaboration of CoCrFeMnNi HEA by powder metallurgy techniques. In the mechanically alloyed powder, XRD diffraction revealed a major fcc phase and small peaks corresponding to tungsten carbides. The presence of WC is attributed to the erosion of balls and vials (both made of WC) during milling. In particular, chromium, due to its bcc structure and high melting point, is believed to cause significant erosion damage. After heat treatment and sintering, the WC peaks disappeared (probably due to low fraction), and peaks attributed to carbide Cr_7C_3 appeared. Moreover, microscopic observations revealed the presence of two types of oxides. The authors discussed the source of carbon (to form Cr_7C_3) and the initiation moment of the carbide appearance. The conducted Atom Probe Tomography (APT) analysis showed that the formation of chromium-rich carbide started during mechanical alloying (Fig. 1-15). It is in opposition to the general belief that carbides formation is initiated during annealing or sintering. Vaidya *et al.* [86] suggested that toluene, used as process control agent, is the primary source of carbon. The results presented above confirmed that the contamination, which is difficult to manage, is a huge challenge in mechanical alloying of high entropy alloys.

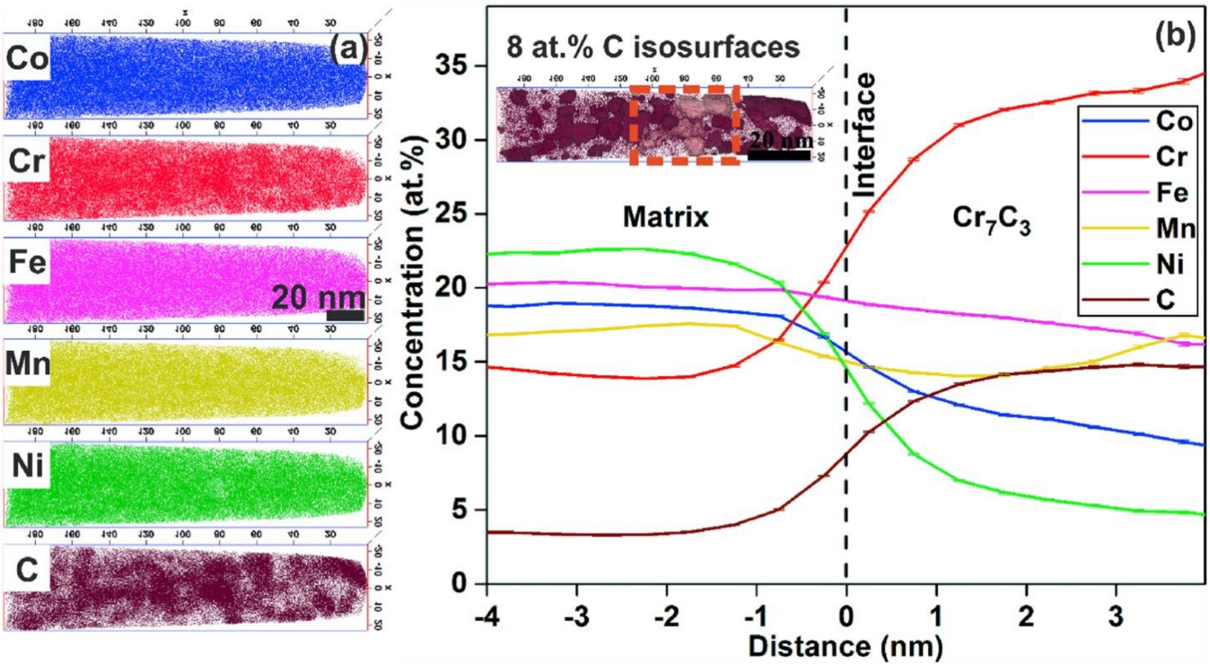

Figure. 1-15. Atom probe tomography analysis: a) distribution of elements in CoCrFeMnNi powder after 15h MA, b) proximity histogram, obtained from the dotted box, revealing the presence of chromium carbide. Reproduced with permission from Elsevier [86].

1.3.3. Gas atomization

The gas atomization is an alternative route for the preparation of alloyed HEAs powders [21]. The atomization technique is classified as powder metallurgy; however, in opposition to mechanical alloying, it is not a solid-state method. It consists of three main stages: the melting of starting material, the disintegration of melt into small droplets and its solidification [97]. The fast cooling rate generally prevents the formation of segregation. The gas atomized powder usually has a spherical shape with a smooth surface [70]. The process itself is cleaner than mechanical alloying [66]. The main disadvantages of the atomization are a very high cost and limited possibility of preparation of alloys with largely different melting temperatures of constituent elements [70]. The HEA powders are usually atomized in argon [46,66] or nitrogen [98]. Moreover, liquid atomization in water, which is a cheaper method than gas atomization, was performed [99]. Liquid atomization should be only limited to alloys with a low affinity to oxygen [97]. The atomized HEA powders are rather used in additive manufacturing than in conventional sintering [21].

1.3.4. Hot-Press sintering

The hot-press sintering (HP) is one of the consolidation methods from the family of hot compaction processes to obtain full density product [97]. It is a solid-state process, where the temperature and external pressure act together. Mechanisms, such as plastic yielding, creep (power law and diffusional), grain boundary sliding, play an essential role in the process. The contribution of each mechanism depends on several factors, i.e., temperature, pressure, time, materials and their microstructure, etc. [70,97]. Temperature, by increasing atomic motion in the powder, increases the sinterability of the sample; thus, it should be set at least above 0.5 T_m, more often between 0.7 and 0.9 T_m [70]. The value of pressure is usually limited up to 100 MPa because of the low mechanical resistance of the graphite dies [97]. The paper about the simulation of hot press sintering of HEA has been published [100]. The schematic illustration of the hot-press sintering device is shown in Fig. 1-16.

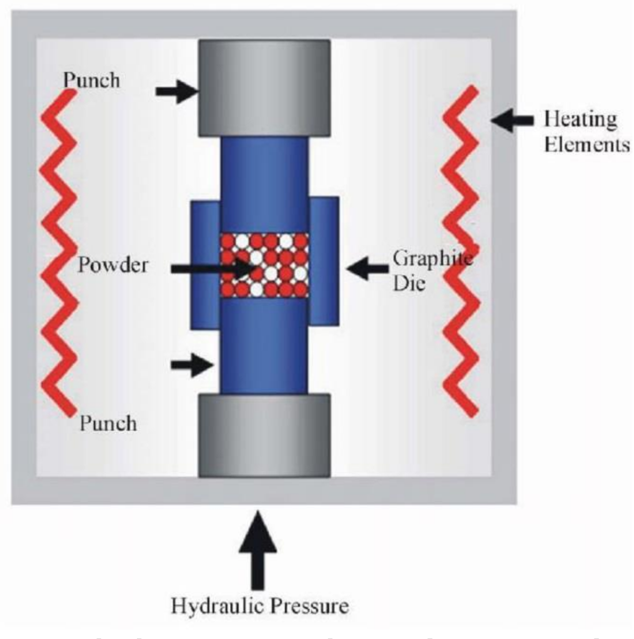

Figure 1-16. Scheme showing the hot-pressing technique device. Reproduced after Moustafa *et al.* [101] under a Creative Commons license (https://creativecommons.org/licenses/by-nc-nd/4.0/).

Despite not being the most common powder consolidation technique, the hot-press sintering is widely used to produce bulk HEAs [21]. The mechanically alloyed powders are usually sintered under vacuum (VHPS – vacuum hot press sintering) [79,83,85,87,102]; nevertheless, in some papers, information about the atmosphere is missing, e.g., [103]. The mechanically alloyed powder is generally loaded into a graphite die, which enables processing at high temperature, and then sintered applying uniaxial pressure and temperature simultaneously. The most frequently used range of the sintering temperature for HEAs is between 700 and 1000 °C, while the pressure is between 30 and 50 MPa [79,83,85,87,102]. The standard sintering time is 1 or 2 h.

In their review, Vaidya *et al.* [20] listed many single-phase HEAs after mechanical alloying, that became multiphase after sintering or annealing. The mechanical alloying, as it was mentioned earlier, could extend solid state and thus produces supersaturated phases. These metastable phases often undergo a transformation during annealing or sintering. The second reason for the formation of new phases is contamination. Contamination could occur during mechanical alloying and sintering, mainly by oxygen and carbon [20]. The contamination by carbon from graphite die during hot-press sintering of HEAs is rarely discussed in the literature [51]. The emphasis is usually put on the contamination during mechanical alloying. Nevertheless, the carbon diffusion from graphite die is a problem not only limited to the surface, especially for small samples. The oxygen contamination could occur during MA and the subsequent sintering due to residual oxygen in the furnace chamber. It can lead to the formation of oxides, e.g., Al_2O_3, $TiMnO_3$,…, during sintering [83,85].

Cheng *et al.* [79] investigated CoCrFeNiMn HEA prepared by mechanical alloying followed by vacuum hot-press sintering. The mechanically alloyed powder (45 h) consists of a major fcc phase and a small fraction of bcc phase (Fig 1-17a). The vacuum hot-press sintered sample presents a major fcc phase, precipitates of carbides $M_{23}C_6$ (M corresponds to chromium, iron, and manganese) and σ phase (tetragonal structure) (Fig.1-17b). The minor bcc phases disappeared in favor of precipitates during sintering. Carbon, which is needed to form carbides, was introduced during MA from the process control agent (N-heptane), and balls and vial material. The bulk samples, sintered at 800 °C, present promising mechanical properties, i.e., compressive yield strength of 1483 MPa, strain-to-failure of 13.3 %, and hardness of 472 HV.

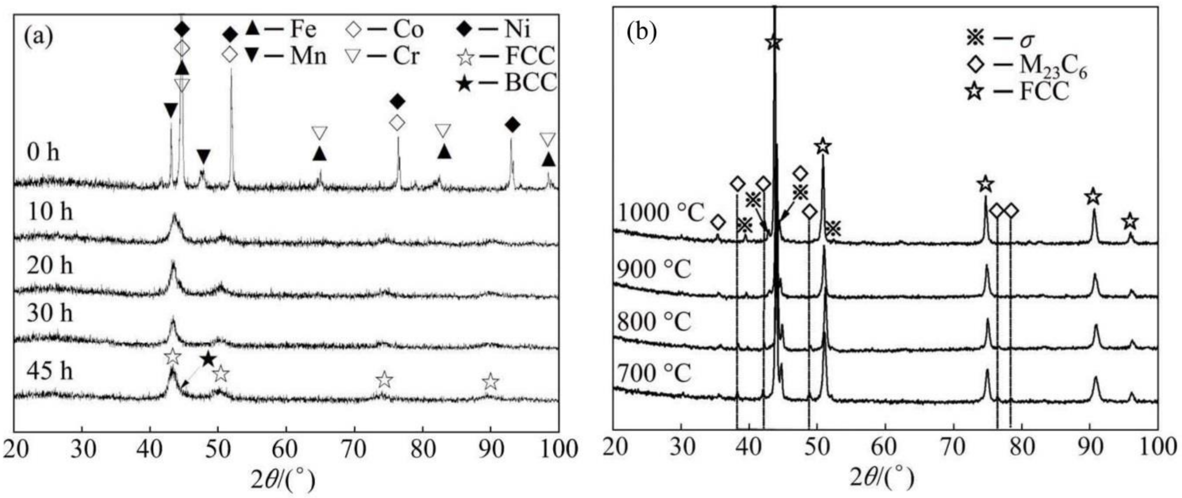

Figure 1-17. XRD patterns of CoCrFeMnNi High Entropy Alloy: a) mechanically alloyed powders after different milling time, b) consolidated alloys at different sintering temperatures. Reproduced with permission from Elsevier [79].

Cheng *et al.* [85] also studied $FeCoCrNiMnAl_x$ with different contents of aluminum (x from 0 to 1). As-milled powders presented a dual-phase fcc/bcc structure. The sintered samples revealed fcc structure for alloys with no aluminum or $FeCoCrNiMnAl_{0.1}$, while higher contents (x>0.1) of aluminum lead to the formation of fcc + bcc structure. The bulk samples contain a small fraction of $M_{23}C_6$ and M_7C_3 carbides. The carbon sources were the process control agent and the balls and vials material. The small quantity of Al_2O_3 in the form of 20 nm-diameter particles was found in alloys containing aluminum. The oxygen was probably absorbed during MA or sintering. The microstructure of the alloy with no aluminum consists of coarse grains (>1 µm) (Fig. 1-18a) and fine grains (100-200 nm) (Fig. 1-18b). The chemical compositions and lattice parameters of coarse and fine fcc grains are similar. Authors suggested that the formation of carbides can hinder diffusion; hence, the presence of fine fcc grains occurs. The bulk samples show promising mechanical properties. Hardness and compressive strength increase with increasing Al content, up to 684 HV_{10N} and 2406 MPa, respectively.

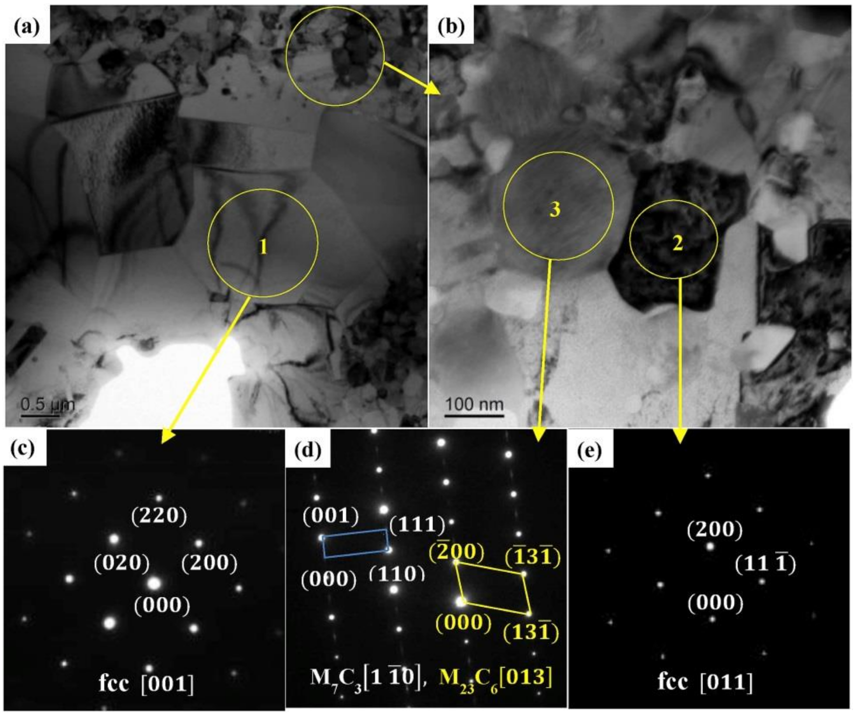

Figure 1-18. TEM BF images and SAED patterns of sintered CoCrFeMnNi High Entropy Alloy: a) TEM BF image of coarse grain region, b) TEM BF image of fine-grained region, c) SAED patterns of fcc coarse grain, d) SAED patterns of two carbides – M_7C_3 and $M_{23}C_6$, e) SAED patterns of fcc fine grain. Reproduced with permission from Elsevier [85].

The results concerning hot-press sintered HEAs showed the great potential of this technique. The hot-pressing could produce samples, which microstructure consists of fine grains, with high mechanical properties. Nevertheless, the different sources of contamination constitute the main problems.

1.3.5. Spark plasma sintering

Spark plasma sintering (SPS) is a common sintering method of nanocrystalline or fine-grained materials. SPS presents many similarities with hot-press sintering; however, the heating method is entirely different. The powder placed in the graphite die is heated by Joule effect [70]. The heating rate and cooling rate are very fast, up to 1800 °C/min. The dwell time in SPS is usually between 5 and 20 min. A short time coupled with fast heating/cooling rates promotes densification and prevents grain growth. Moreover, according to one hypothesis, the intervals of direct current, which create spark impact pressure, spark plasma, an electrical field diffusion effect, and joule heating, lead to clean and activate the surface of powder [70].

Spark plasma sintering is the most common route of the consolidation of HEA powders [21]. SPS of HEAs is usually carried out in the range of temperatures between 900 and 1100 °C [73,74,76,81,84,86,92,94,104], rarely at higher temperatures e.g. 1400 °C [78].

The common pressures employed are 30 MPa [75,78,81,104], 50 MPa [60,63,80] and 60 MPa [74,86]. Short time of consolidation is preferred, usually between 3 and 10 min [73,74,76,78,81,86,92,94,104]. SPS is usually performed under vacuum [75,94,104] or argon [73,84] atmosphere. As it was mentioned earlier, spark plasma sintering prevents significant grain growth during consolidation; nevertheless, grain size increases compared to the initial mechanically alloyed powder. Joo *et al.* [73] observed that grains of CoCrFeMnNi HEA increase from about 11 nm after MA to 0.28 µm and 1.87 µm after SPS at 900 and 1100 °C, respectively. Hence, the bulk alloys should not be considered as nanocrystalline anymore.

Fu *et al.* [104] studied the sintering of $Al_{0.6}$NiFeCrCo and $Al_{0.6}$NiFeCr mechanically alloyed HEA powders by spark plasma sintering and hot-press sintering. The metastable structure of MA powders consists of a major bcc and a minor fcc phase. During sintering, phase transformations occurred. Samples after SPS and HP consist of a major fcc and a minor bcc phase. No significant differences between structures produced by SPS and HP have been observed. The contamination problems have not been discussed; nevertheless, neither carbide nor oxide peaks are present in the XRD patterns. SPS samples exhibit slightly higher density (less porosity) than samples prepared by HP. Authors explained that mass transport during SPS is enhanced by an increase of point defect concentration and their mobility due to the presence of an electric field. Compression tests and hardness measurements revealed some differences in the mechanical properties of alloys consolidated by SPS vs. HP. For $Al_{0.6}$NiFeCrCo, yield strength (σ_y) and hardness are slightly higher, while compressive strength (σ_{max}) and strain to failure (ε_f) are lower for the SPS than for the HP sample (Table 1-2, Fig. 1-19). The authors suggested that higher compressive strength of the HP sample is related to larger grains (longer time of consolidation by HP than by SPS), which can facilitate the intergranular accumulation of dislocations and thus obtain the stronger strain-hardening effect. However, the $Al_{0.6}$NiFeCr alloy sintered by SPS presents higher compressive and yield strength than HP alloy, but lower strain to failure.

Table 1-2. Mechanical properties obtained from the compression test and hardness measurements [104].

Alloy	Sintering	σ_y [MPa]	σ_{max} [MPa]	ε_f [%]	$HV_{0.3}$
$Al_{0.6}$NiFeCrCo	SPS	1870	2150	10.6	594
$Al_{0.6}$NiFeCrCo	HP	1830	2298	10.8	570
$Al_{0.6}$NiFeCr	SPS	1607	1992	11.2	552
$Al_{0.6}$NiFeCr	HP	1420	1948	13.5	431

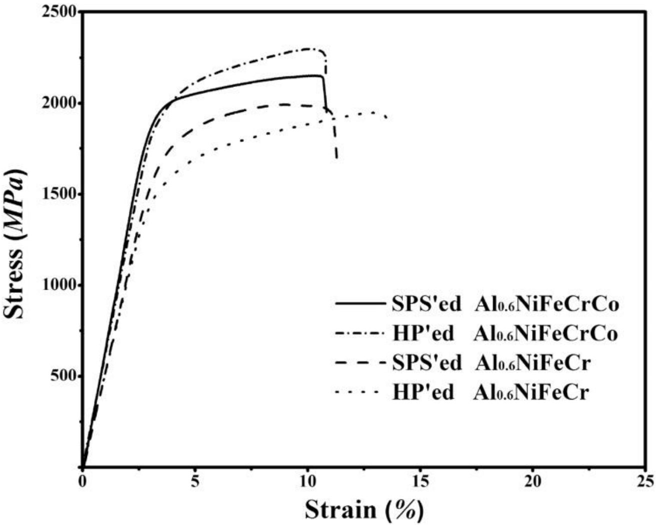

Figure 1-19. Compressive room temperature stress-strain curves of sintered HEAs. Reproduced with permission from Elsevier [104].

The study conducted by Fu *et al.* [104] showed that for some HEAs composition, e.g., $Al_{0.6}NiFeCrCo$, SPS is not an obviously superior method over hot-press sintering. Despite that most of HEAs are sintered by SPS, HP also presents excellent potential in powder metallurgy of high-entropy alloys.

1.4. Conclusions and objectives

In this literature review, a general overview of HEAs, methods of designing new compositions, and powder metallurgy processing have been presented. High entropy alloys (or compositionally complex alloys, or multi-component alloys depending on definition and nomenclature) have changed metallurgy by showing the almost infinite potential of multi-component alloys with compositions close to equiatomic. The increase in the number of publications in this field is exponential.

HEAs usually present a simpler structure than expected. The explanation of solid solution stabilization by high configurational entropy is often undermined; nevertheless, it is not fully understood [23,26,27]. It was suggested that many parameters, such as mixing enthalpy or atomic size difference, play an essential role too [26,27]. HEAs could be classified into a few categories, depending on the constituent elements; the 3d transition metal and refractory metal HEAs are the most common ones [32]. The promising mechanical properties, which were already revealed for serval compositions, could be combined with excellent functional properties to compete with currently used traditional materials for some applications [5]. The liquid route of processing (melting and casting) is the most common, although powder metallurgy, mainly mechanical alloying, which presents many advantages, develops rapidly [21].

The design of new HEA compositions provides many challenges. The number of potential compositions is almost infinite; hence, it is not possible to study all systems experimentally. The basic tool to design multi-component compositions is the parametric approach [4,17,58,59]. Although the parametric approach is not an ideal tool to predict phase structure, it is widely used to choose the alloy’s components and their ratios. The CALPHAD method, which is also a common way to design HEAs, can be used to screen many potential HEAs [22] or, more often, to slightly modify the composition obtained by the parametric approach to produce desired structure [62]. Both approaches, having important limitations, are essential tools in the search for new HEAs.

The powder metallurgy of HEAs develops rapidly due to its undeniable advantages, such as the absence of dendritic segregation, the extended solid solubility, the possibility of preparation of alloys with a significant difference in melting points of constituent elements, the nanocrystalline microstructure [4,20,49,70]. Many promising compositions with single bcc or fcc phases and multiphase structures with nano-size grains were prepared by mechanical alloying [20]. The main disadvantage is the contamination by carbon and oxygen coming from the vials and balls materials, and process control agent [20,21]. The contamination could change the final powder composition significantly and cause the formation of carbides and oxides. However, in some cases, the formation of carbides and oxides could be beneficial from the mechanical resistance point of view. The consolidation of mechanically alloyed powders is generally done by spark plasma sintering method or other solid-state consolidation processes such as hot-press sintering [21]. During sintering, metastable phases produced by MA undergo phase transformations, which often lead to a multiphase structure. Moreover, the contamination induced during MA and sintering could lead to the formation of oxides, carbides, etc. [20]. Nevertheless, the optimization of mechanical alloying and sintering enables to master the phenomena of contamination and obtain the target composition with a very small fraction of phases resulting from the contamination. The sintering methods usually preserve relatively fine-grained microstructure, which results in improved mechanical properties. Many published papers present interesting and promising results of HEAs prepared by powder metallurgy techniques; hence these fabrication methods are worth of interest.

The purpose of this thesis is to produce a new high entropy alloy with high mechanical properties by the powder metallurgy technique. The equiatomic composition was taken from the list of promising candidates for HEA, obtained by CALPHAD calculations by Senkov *et al.* [22]. However, the chosen system was not experimentally studied prior to this thesis. The equiatomic composition was optimized using the parametric approach and based on first experimental results. To produce bulk HEA, mechanical alloying, followed by hot-press sintering, was chosen. The mechanical alloying was chosen to prevent casting segregation and eventual evaporation of elements due to the significant difference in melting temperatures. Hot-press sintering was chosen to consolidate mechanically alloyed powders while maintaining fine grains. The structure, microstructure, and mechanical properties were analyzed.

2. Experimental procedures

In this chapter, the procedures to choose the HEA chemical composition and the fabrication methods of powder and bulk samples are discussed. Moreover, the characterization methods of microstructure, thermal stability, and mechanical properties are presented.

2.1. Choice of HEA composition

The Al-Cr-Fe-Mn-Mo system, which had not been experimentally studied yet, was chosen using a parametric approach (presented in detail in the Literature review in subsection "1.2.1. Parametric approach"). The parametric approach consists of calculating several parameters such as the mixing enthalpy, the mixing entropy, the atomic size difference, the valance electron concentration, and omega (combining effects of melting temperature, the enthalpy, and entropy of mixing). A careful literature review of novel HEA compositions was also conducted. In particular, the paper by Senkov *et al.* [22], evaluating many equiatomic alloys by CALPHAD calculations caught our attention. Our focus was to choose a HEA system, which presents a promising structure (primary bcc phase) according to CAPLHAD and parametric approach predictions, and good mechanical properties, mainly high strength and hardness. The data to calculate parameters was taken from the literature. Takeuchi *et al.* [105] calculated mixing enthalpy of binary systems using Miedema's macroscopic model. The results were used to calculate the mixing enthalpy of HEA. The atomic radii (to calculate the atomic size difference) and electronegativity (to calculate the electronegativity difference) were taken from a paper by Senkov *et al.* [106] and from an article by Fang *et al.* [107], respectively.

2.2. Alloy preparation

2.2.1. Mechanical alloying

Alloyed powders were prepared by mechanical alloying (MA) of elemental powders which were purchased commercially from the Goodfellow Company. The particle size and purity are listed in Table 2-1.

Table. 2-1. Particle size and purity of elemental powders.

	Al	**Cr**	**Fe**	**Mn**	**Mo**
Particle size [µm]	<15	38-45	<60	<45	<350
Purity [wt. %]	>99.0	>99.0	>99.0	>99.5	>99.9

The mechanical alloying was performed at room temperature, using the following three devices: a planetary mill RETSCH PM-100 and two different vibrational mills SPEX 8000 and CryoMill. During the initial stage of this study, the milling time was optimized as a function of obtained results (homogeneity, contamination). The detailed information about milling time and speed is presented in the chapter “4. Mechanical alloying of HEA powder”. The milling parameters are listed in Table 2-2. Milling time breaks were applied to prevent the temperature rise (MA performed at room temperature) due to balls-vial-powder collisions. The duration of the interruptions was chosen from preliminary tests carried out separately for each device. To avoid confusion in this thesis, only the effective milling time (without breaks) is indicated. The balls and vials for all mills were made of hardened steels. The ball-to-powder weight ratio was 10:1; however, the number of balls, their size, and the vial volume depend on the mill (see Table 2-2). The stearic acid ($C_{18}H_{36}O_2$) was added as process control agent for milling in planetary mill RETSCH to prevent powder agglomeration on vial and balls surface during MA. The MA in vibrational mills was carried out without the addition of a process control agent because the frontal impacts in vibration mills cause less risk of sticking powder to the walls of the vial. All manipulations with powder before milling, including weighing, were performed in a glove box under argon atmosphere. The vials filled with powder were hermetically closed under argon atmosphere.

Table 2-2. Optimized mechanical alloying parameters for milling in RETSCH, CryoMill, and SPEX devices.

Parameter	RETSCH PM-100	CryoMill	SPEX 8000
Rotation speed or frequency	300 rpm	15/20/25 Hz	18 Hz
Milling cycle (milling time/break time)	30 min / 15 min	90 min / 5 min	60 min / 30 min
Number and size of balls	3 balls (Φ = 20 mm) and 6 balls (Φ = 10 mm)	2 balls (Φ = 10 mm)	2 balls (Φ = 10 mm)
Average weight of balls	105 g	12 g	12 g
Ball-to-powder weight ratio	10:1	10:1	10:1
Vial volume	125 ml	50 ml	50 ml
Process control agent	2 wt.% of stearic acid	—	—

2.2.2. Annealing

The MA powders were annealed under vacuum in sealed quartz tubes or under argon in an atmosphere-controlled furnace. In the second case, powders were placed in an alumina crucible. The annealing in quartz tube was performed in a Nabertherm furnace, while the annealing under argon was carried out in a Centorr Vacuum Industries furnace (a secondary vacuum was obtained in the graphite chamber before the introduction of argon). The annealing was conducted with heating and cooling rates of 10 °C/min. The annealing time (at the chosen temperature) was 1 h.

2.2.3. Hot press sintering

The consolidation by hot press sintering was chosen to produce bulk samples. The MA powder was placed into a 10-mm-diameter graphite die (radius, r = 5 mm). For the easier removal of sintered samples, graphite foils were placed between the walls of die, punches, and the powder. Simple calculations were made to find the weight of needed powder (m_{powder}) to produce sintered samples of 5 mm height (h) (the samples of 7 to 8 mm of height were also sintered for compression tests). The bulk sample density (ρ_{bulk}), calculated on the basis of the density of the pure elements (Table 2-3), is between 6.59 and 7.05 g cm^{-3}, depending on the chemical composition. It is the reason why the ρ_{bulk} value of 7.00 g cm^{-3} was adopted to simplify the calculations. The volume of the sintered sample (V_{bulk}) was calculated using the following formula:

$$V_{bulk} = \pi \cdot r^2 \cdot h = \pi \cdot (0.5\ \text{cm})^2 \cdot 0.5\ \text{cm} = 0.39\ \text{cm}^3 \tag{2.1}$$

where r and h are defined in the above text, and the needed powder weigh (m_{powder}) using the formula below:

$$m_{powder} = \rho_{bulk} \cdot V_{bulk} = 7.00\ \text{g cm}^{-3} \cdot 0.39\ \text{cm}^3 = \mathbf{2.73\ g} \tag{2.2}$$

Table 2-3. Densities of pure elements.

Element	Density [g/cm^3]
Al	2.70
Cr	7.19
Fe	7.87
Mn	7.21
Mo	10.28

It should be noted that one mechanical alloying cycle in SPEX or CryoMill produces only 1 to 1.2 g of powder. Thus, three millings are needed for the sintering of a sample of 5 mm in height. As the contamination during MA could vary slightly between different cycles, special attention was given to mix powders issued from different millings before introducing it into the die.

The hot-press sintering of powder was performed under argon or vacuum in a high-temperature Centorr Vacuum Industries furnace coupled with an Instron 4507 press. The heating and cooling rates were 10 °C/min, which is a common rate for hot-press sintering. The pressure was 80 MPa (force, F = 6280 N); this is the maximum value acceptable for graphite die. The sintering time was 1 h or 2 h to densify samples without causing a significant grain growth. The sintering was performed in the temperature range between 950 and 1250 °C (chosen based on the DSC and powder annealing results). As a first stage of the heating procedure, an annealing at 400 °C for 30 min was carried out under vacuum (<1.5 Pa) to degas the powder while avoiding phase transformations. After this first step, the argon is introduced into the furnace chamber before the second temperature ramp-up to the sintering temperature. The cycle of sintering is schematically shown in Fig. 2-1.

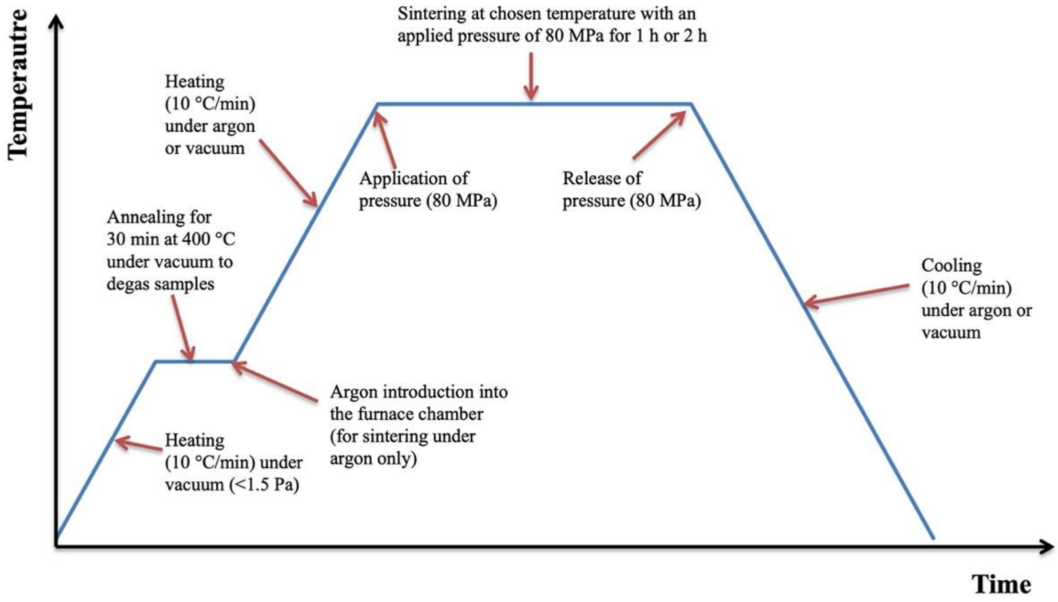

Figure 2-1. Schematic representation of the sintering cycle.

Moreover, one sample was prepared by arc melting to verify the possibility of the preparation of the alloy from the Al-Cr-Fe-Mn-Mo family by the liquid route. The selected mechanically alloyed powder was pre-sintered at 600 °C for 1 h under argon atmosphere (load 80 MPa). The consolidated sample was arc melted in a Bühler Compact Arc Melter MAM-1 under argon partial pressure.

2.3. Material characterization

2.3.1. Structural and microstructural characterizations of MA powders

The structural and microstructural characterizations of MA powders were carried out by X-ray diffraction (XRD), Mössbauer spectrometry (MS), Scanning Electron Microscope equipped with Energy-Dispersive X-ray spectroscopy (SEM-EDX), and Transmission Electron Microscope with EDX (TEM-EDX) (only on selected powders). The XRD analyses were performed using X'PERT Pro Philips – Panalytical operating at 40 kV and 20 mA equipped with a cobalt tube. The average value of the $\lambda_{\mathrm{KalphaCo}}$ (1.79026 Å) was calculated based on the $\lambda_{\mathrm{Kalpha1Co}}$ (1.78897 Å) and the $\lambda_{\mathrm{Kalpha2Co}}$ (1.79285 Å). The $\lambda_{\mathrm{KbetaCo}}$ (1.62079 Å) is not visible due to an iron filter. Data were acquired in a continuous mode at the rate of 0.03° /min with the range (2θ) between 20 and 120°. Beam masks of 10 mm and fixed divergence and anti-scatter slits of 1° were used in the exit of the cobalt tube. A 1° slit was placed before the detector. Mössbauer spectrometry was conducted at room temperature, using a ^{57}Co (Rh) source and Aries-Wissel devices. Deconvolution of Mössbauer spectra was performed using Lorentzian shape peaks and iron as reference to determine the Mössbauer parameters. The parameters, such as Hyperfine Field (HF), peak Width (W), Isomer Shift (IS), Quadrupole Splitting (QS), and the relative Amount of each iron environment (A) were calculated.

SEM observations were performed on non-polished and polished mechanically alloyed powders by SEM JEOL JSM-7800F equipped with EDX. The as-milled powders were bonded to a carbon tape. The investigations were conducted using the secondary electron signal (15 kV) to determine particle size, shape, and surface appearance. The MA powders were also hot mounted using a Struers CitoPress-1 device for 210 s at 180 °C under 250 bar pressure in PolyFast resin and polished by SiC grinding papers P320-P4000 using water as lubricant, and then the final polishing was done using diamond pastes up to 0.25 µm. The SEM observations (secondary (SE) and backscattered electron (BSE) signals) coupled with EDX analyses were performed at an acceleration voltage range between 5 kV and 20 kV to observe the surface features and evaluate the MA powders chemical homogeneity.

The selected powders for TEM characterization were prepared by focused ion beam (FIB) (powders analyzed by TEM Titan) or by traditional method. The conventional method consists of mixing the MA powder with M-bond adhesive. The mixture was left for at least 24 h to cure thoroughly. Then, the powder was roughly polished by SiC papers (P2400 and

P4000) to reduce the thickness down to about 50 µm. Subsequently, the polished sample was glued to a copper TEM support grid. Final thinning was performed using ion mill – Gatan Duo Mill. TEM analyses were carried out using a TEM FEI Tecnai G2–20 twin at 200 kV or a TEM FEI Titan Themis at 300 kV, both equipped with EDX. Bright-field images and STEM mode images with EDX maps were acquired.

2.3.2. Thermal stability of MA powders

The thermal stability of the powders was investigated by analyzing their structure and microstructure after annealing under vacuum (quartz tube) or argon atmosphere by XRD, SEM-EDX, and Mössbauer spectrometry. The preparation methods and analysis parameters were the same as for non-heat treated powders (Subsection 2.2.1.). Moreover, Differential Scanning Calorimetry (DSC) was performed to determine phase transformation temperatures in selected samples. The analysis was performed on mechanically alloyed powders using a Netzsch DSC 404C device. The MA powder, about 10 mg (accuracy of ± 0.01 mg), was inserted into an alumina crucible. Then, DSC was carried out under constant high-pure argon flow with the heating and cooling rates of 10 °C/min from room temperature up to 1480 °C. Two cycles of heating and cooling were performed. Before the series of tests on HEA powders, the DSC device was calibrated using the enthalpy and melting temperatures of elements such as indium, tin, bismuth, zinc, aluminum, silver, and gold. The baseline scans were performed before each measurement.

2.3.3. Density measurements of sintered samples

The density of the sintered samples was determined according to the Archimedes principle. The measurements were carried out in air and ethanol using a Mettler Toledo balance. The density (ρ_{BA}) was calculated using the following formula:

$$\rho_{BA} = \frac{A}{A-B}\left(\rho_{ethanol} - \rho_{air}\right) + \rho_{air} \tag{2.3}$$

where A is the weight of the sample in air, B is the weight of the sample in ethanol, $\rho_{ethanol}$ = 0.790 g cm^{-3}, ρ_{air} = 0.001225 g cm^{-3}.

2.3.4. Structural and microstructural characterizations of bulk samples

The structural and microstructural characterizations of bulk samples were carried out by XRD, SEM-EDX, TEM-EDX, and Electron BackScatter Diffraction (EBSD). The parameters of the analyses presented in this thesis are the result of an optimization. The XRD was performed using the same device and parameters as MA and annealed powders, except the use of a 5 mm beam mask due to the smaller size of bulk samples. For SEM-EDX, the samples were cut to be analyzed in cross-sections. Then, the samples were hot mounted and polished (SiC papers P80-P4000 and diamond pastes up to 0.25 µm). The SEM observations (secondary and backscattered electron signals) coupled with EDX analyses were performed at 5-20 kV using SEM JEOL JSM-7800F to analyze the homogeneity of the chemical composition.

The initial preparation procedure of EBSD samples was similar to SEM samples. However, after polishing using 0.25 µm diamond paste, the samples were polished in a Buehler VibroMet 2 with OP-S NonDry colloidal silica suspension for three cycles of 20 minutes to obtain a better surface quality. Final preparation was done using a Fischione Instruments' Model 1061 SEM Mill by ion milling for 20 minutes at 5 kV. Subsequently, the prepared sample was immediately introduced into the SEM chamber to limit the oxidation and contamination of the surface. EBSD was conducted in SEM JEOL JSM-7800F equipped with an EBSD Oxford Instrument (hkl Nordlys Max^2 detector). Before the EBSD experiments, the CIF files (Crystallographic Information File) were created based on the information about the supposed phases from XRD and SEM-EDX investigations. Then, the CIF files were entered into Aztec HKL software. The step size of the analysis was set to 40 nm. The processing of obtained data was carried out using Aztec HKL software, followed by ATEX software [108]. The EBSD mapping was performed to determine the mean grain size and phase ratio. The analyses were performed in the center of the samples, far from the contact surface with graphite die during sintering.

The sintered samples for TEM observations, taken from areas far from the surface, were prepared by using focus ion beam (FIB) or ion milling. The samples for ion milling were cut into small pieces from sintered samples and then mechanically polished to the thickness of about 100 µm. The thinned samples were glued on a copper TEM support grid. The final thinning was conducted using a Gatan Precision Ion Polishing System (PIPS) until the formation of a hole in the center. TEM analyses were performed using a TEM FEI Tecnai G2–20 twin at 200 kV or a TEM FEI Titan Themis at 300 kV, both equipped with EDX. Bright-field images with corresponding SAED patterns in different orientations were performed to confirm the presence of phases. STEM mode images with EDX maps were also acquired.

Moreover, DSC of the selected sintered sample was performed up to 1480 °C using similar conditions as for the powder samples (Subsection 2.2.2.). The sample after the DSC experiment was analyzed by SEM-EDX and XRD.

2.3.4. Mechanical properties

The mechanical properties of sintered samples were evaluated by micro-indentation and compression tests. The Vickers micro-hardness measurements were carried out using a CSM Instruments Micro-Hardness Tester. The analyses were carried out in the center of the samples under loads of 0.5 N, 0.75 N, 1 N, 2 N, 5 N, 9 N to assess the influence of the load on the micro-hardness value. The dwell time was 10 s. At least 15 measurements for each sample and load were performed. The distance between indents was at least three diagonal lengths. The obtained data were analyzed using the Oliver-Pharr method [109]. Besides hardness, Young's moduli were determined from the indentation curves.

The compression tests were performed on cylindrical samples (diameter, d=3 mm; height, h=4.5 mm). Samples were cut from the sintered samples (d=10 mm, h=7-8 mm) using an Electrical Discharge Machining (EDM) to obtain 3 mm-diameter cylinders. The cut cylinders were hot mounted and then polished using a Struers Tegramin-30 automatic polishing machine to reduce the height to 4.5 mm and ensure the surface parallelism. The polishing surface was changed every two minutes. The final polishing was performed using a 3 μm diamond paste to obtain sufficient surface quality. The compression tests at room temperature were carried out in the air with a strain rate of 10^{-3} s^{-1} using an Instron 8031 machine. The test was continued until the fracture of the sample. The fracture surface of samples tested at room temperature was analyzed by SEM-SE. The compression tests at higher temperatures (400, 500, 600, 650, 700, 800 °C) were performed using an Instron 4507 press coupled with a high-temperature Centorr Vacuum Industries furnace with a strain rate of 10^{-3} s^{-1}. The samples were heated up to the test temperature with a rate of 10 °C/min under argon atmosphere and held for 5 minutes before testing. The testing was performed until the fracture of the sample or reaching true strain of about 32 %, depending on the temperature.

3. Design and optimization of a new High Entropy Alloy composition

In this chapter, the parametric approach calculation for three compositions from the Al-Cr-Fe-Mn-Mo HEA family is presented. This approach allowed a quick verification and optimization of the chemical composition in order to increase the probability of producing a single bcc phase. The results of the calculation of parameters, defined in Subsection 1.2.1., are presented in Table 3-1.

Table 3-1. Summary of parametric approach calculations for alloys from the Al-Cr-Fe-Mn-Mo family.

Parameter	« HEA »	20%Al, 20%Cr, 20%Fe, 20%Mn, 20%Mo	22.5%Al, 22.5%Cr, 28% Fe, 20%Mn, 7%Mo	19%Al, 22%Cr, 34%Fe, 19%Mn, 6%Mo
Enthalpy of mixing [kJ/mol] (ΔH_{mix})	$-10< \Delta H_{mix} <5$	-6.56	-8.30	-7.39
Entropy of mixing [J/(K·mol)] (ΔS_{mix})	> 12.47	13.38	12.77	12.47
Atomic size difference [%] (δ)	< 6.6	5.45	5.87	5.78
Electronegativity difference ($\Delta\chi$)	<0.175	0.220	0.162	0.156
Valence electron concentration (VEC)	<6.87 (to form bcc)	6.00	6.09	6.30
Omega (Ω) ($\Omega = \frac{T_m \Delta S_{mix}}{\lvert\Delta H_{mix}\rvert}$)	>1.1	3.81	2.64	2.93

3.1. Equiatomic composition

Our initial focus was to choose a HEA with a single bcc phase to produce an alloy with improved mechanical properties. The bcc structure usually presents a high mechanical resistance and a sufficient ductility at high temperatures. The Al-Cr-Fe-Mn-Mo family was chosen during the Master internship of Surya Nilamegam Kumaran [110]. Elements such as iron, manganese, and chromium were chosen first; thus, they are frequently used in many HEAs, and the cost of their powders is relatively low. In addition, chromium should increase the corrosion resistance of the alloy. The other two elements were chosen from a group of elements such as aluminum, cobalt, nickel, molybdenum, titanium, silicon, vanadium, zinc, and zirconium, based on the parametric approach (especially, valence electron concentration to form bcc structure) and based on the availability of the powders in the laboratory. Moreover, the promising results by CALPHAD screening studies published by Senkov *et al.* [22], which are discussed in the “Literature review” of this thesis, confirm that the Al-Cr-Fe-Mn-Mo system is a good candidate for experimental studies. The investigated system is new; hence, the CALPHAD results could not be completely reliable due to limited information in databases. The parametric approach calculations were done carefully to check and optimize the composition of HEA from the Al-Cr-Fe-Mn-Mo family to promote the formation of a solid solution and prevent intermetallic compounds.

The parameters calculated for the equiatomic composition are in a good range of values, except for the electronegativity difference. The enthalpy of mixing, which is very important in phase prediction, is between values for which most alloys form solid solution [17]. The entropy of mixing is superior to the widely accepted 1.5 R (R= gas constant = 8.314 J K^{-1} mol^{-1}; 1.5 R = 12.47 J K^{-1} mol^{-1}) value [4], thus, whether or not the entropy plays a dominant role in the stabilization of a single solid solution, this composition can be classified as HEA. The atomic size difference is lower than the critical value of 6.6 %. However, it was shown that alloys with the range of 5.0-6.6 % could form solid solution phases, either intermetallic compound. δ below 5.0 % significantly limits the formation of ordered phases [59]. The electronegativity difference of the equiatomic composition is too high compared to the value found in the literature (0.175) [60]. Although some molybdenum-containing alloys with higher electronegativity difference present a single bcc structure, it seems that large calculated electronegativity difference can favor the formation of intermetallic compounds [60]. The valence electron concentration of equiatomic has the value to form a bcc. It is in agreement with general intuition; four of five elements (except aluminum) present bcc structure; moreover, aluminum is known to stabilize the bcc phase [61]. Furthermore, the omega parameter is definitely in the perfect range to form a solid solution.

3.2. Optimization using parametric approach

The large electronegativity difference of the equiatomic alloy could lead to the formation of undesirable intermetallic compounds. The influence of each element on the electronegativity difference was carefully investigated. Molybdenum presents the highest electronegativity among components and contributes significantly to the large electronegativity difference of the alloy. Hence, the only way was to reduce the molybdenum concentration and increased the content of other elements. After many calculations, it was decided that molybdenum will be reduced to 7 at. %, while the content of iron, aluminum, chromium will be increased, and the manganese content will be kept constant. The iron content will be increased most significantly due to the low cost of iron powder. The optimized composition (22.5% Al, 22.5% Cr, 28% Fe, 20% Mn, 7% Mo) presents all parameters in a good range for solid solution formation, including the electronegativity difference, which is well below the critical value (see Table 3-1). Nevertheless, it should be mentioned that the entropy of mixing decreased slightly; the highest value is always achieved for equiatomic concentrations of atoms. The atomic size difference and valence electron concentration increase their value, which could not be beneficial to form a single solid solution. The CALPHAD calculations for the optimized composition using Thermo-Calc software with TCHEA2 database were performed in collaboration with Dr. Peter Klaver from TU Delft. The results show a multiphase structure at room temperature, i.e., two bcc B2 phases, σ phase, and intermetallic compound type Cr_3Si (A15). The CALPHAD calculation due to limitations of databases could be considered only as an indication and not as reliable result.

The composition (19% Al, 22% Cr, 34% Fe, 19% Mn, 6% Mo) developed based on experimental results (named experimentally optimized, it will be discussed in the next chapters), was verified by the parametric approach. All parameters are in good range to form a solid solution; the electronegativity difference is even lower than in optimized alloy (22.5% Al, 22.5% Cr, 28% Fe, 20% Mn, 7% Mo) (see Table 3-1). On the other hand, the atomic size difference and the valence electron concentration values are higher than in equiatomic alloy, which is generally not beneficial for the formation of a solid solution. The mixing entropy of the experimentally optimized composition (19% Al, 22% Cr, 34% Fe, 19% Mn, 6% Mo) has exactly the limit value for the HEA.

3.3. Discussion and summary

Two compositions, equiatomic and optimized (22.5% Al, 22.5% Cr, 28% Fe, 20% Mn, 7% Mo), were selected for experimental investigation. Moreover, the composition (19% Al, 22% Cr, 34% Fe, 19% Mn, 6% Mo, named experimentally optimized), determined experimentally and verified by the parametric approach, was also chosen for further studies. The parametric approach made it possible to check quickly, by simple calculations, the probability of the formation of a single solid solution phase in selected HEAs from the Al-Cr-Fe-Mn-Mo system. Nevertheless, it should be noted that the ranges of values to form HEA and solid solutions phases are based on experimental results for other multicomponent systems; in other words, the fundamental, convincing explanation of the parametric approach based on a physical basis does not exist [27]. All three compositions could probably form a solid solution. However, the vast electronegativity difference of equiatomic alloy could be a problem; therefore, it could lead to the formation of intermetallic phases.

4. Mechanical alloying of HEA powder

In this chapter, the mechanical alloying of three compositions of HEAs powders are discussed. The investigations concerning the structure, the microstructure, the chemical homogeneity, and the contamination, depending on milling conditions, allowed the optimization of the mechanical alloying parameters and the choice of powders for further research to prepare bulk samples. The list of the powder samples prepared by mechanical alloying is shown in Table 4-1 to present the results clearly (more details in Appendix - Names of samples).

Table 4-1. List of powder samples prepared by mechanical alloying.

Name of sample	Initial composition of powder (at. %)	Milling conditions
P-EQ-S16h	20% Al, 20% Cr, 20% Fe, 20% Mn, 20% Mo	SPEX 16 h
P-EQ-S32h	20% Al, 20% Cr, 20% Fe, 20% Mn, 20% Mo	SPEX 32 h
P-EQ-S64h	20% Al, 20% Cr, 20% Fe, 20% Mn, 20% Mo	SPEX 64 h
P-EQ-RFe-S32h	22.2% Al, 22.2% Cr, 11.2% Fe, 22.2% Mn, 22.2% Mo	SPEX 32 h
P-EQ-NFe-S32h	25% Al, 25% Cr, 25% Mn, 25% Mo	SPEX 32 h
P-EQ-R70h	20% Al, 20% Cr, 20% Fe, 20% Mn, 20% Mo	RETSCH 70 h
P-EQ-R70hS1h	20% Al, 20% Cr, 20% Fe, 20% Mn, 20% Mo	RETSCH 70 h + SPEX 1 h
P-EQ-R70hS2h	20% Al, 20% Cr, 20% Fe, 20% Mn, 20% Mo	RETSCH 70 h + SPEX 2 h
P-EQ-R70hS4h	20% Al, 20% Cr, 20% Fe, 20% Mn, 20% Mo	RETSCH 70 h + SPEX 4 h
P-EQ-C32h-15Hz	20% Al, 20% Cr, 20% Fe, 20% Mn, 20% Mo	CryoMill (15 Hz) 32 h
P-EQ-C32h-20Hz	20% Al, 20% Cr, 20% Fe, 20% Mn, 20% Mo	CryoMill (20 Hz) 32 h
P-EQ-C32h	20% Al, 20% Cr, 20% Fe, 20% Mn, 20% Mo	CryoMill (25 Hz) 32 h
P-EQ-C64h	20% Al, 20% Cr, 20% Fe, 20% Mn, 20% Mo	CryoMill (25 Hz) 64 h
P-EQ-C32hS8h	20% Al, 20% Cr, 20% Fe, 20% Mn, 20% Mo	CryoMill (25 Hz) 32 h + SPEX 8 h
P-EQ-RFe-C32hS8h	22.2% Al, 22.2% Cr, 11.2% Fe, 22.2% Mn, 22.2% Mo	CryoMill (25 Hz) 32 h + SPEX 8 h
P-O-S32h	22.5% Al, 22.5% Cr, 28% Fe, 20% Mn, 7% Mo	SPEX 32 h
P-O-C32h	22.5% Al, 22.5% Cr, 28% Fe, 20% Mn, 7% Mo	CryoMill (25 Hz) 32 h
P-O-C32hS8h	22.5% Al, 22.5% Cr, 28% Fe, 20% Mn, 7% Mo	CryoMill (25 Hz) 32 h + SPEX 8 h
P-OE-S32h	19% Al, 22% Cr, 34% Fe, 19% Mn, 6% Mo	SPEX 32 h

4.1. Chemical homogeneity, contamination and phase composition of MA powders

4.1.1. Equiatomic powder

Firstly, the mechanical alloying of equiatomic composition in three different mills was studied. The combination of different successive millings was also evaluated. As a result, optimal milling conditions are proposed.

4.1.1.1. SPEX

In the first stage of this investigation, millings in SPEX for 16, 32, and 64 h of starting equiatomic composition were performed (P-EQ-S16h, P-EQ-S32h and P-EQ-S64h, respectively). The XRD analyses show the formation of two bcc phases (called bcc#1 and bcc#2) for all studied processing times. It should be noted that the intensity of bcc#1 and bcc#2 peaks are quite similar (Fig. 4-1), which suggests that both volume fractions are very close. In Table 4-2, the lattice parameters of formed structures, which present rather close values after different milling times, and final overall chemical compositions of powders are shown. The SEM-BSE (Fig. 4-2) and EDX analyses reveal non-milled particles of molybdenum and iron in powder milled for 16 h. The milling time of 32 h and 64 h produced rather homogenous powders. The composition of each bcc phase cannot be determined at the SEM scale due to the nanocrystalline grain size. Nevertheless, the bcc#1 lattice parameter is close to the lattice parameter of pure molybdenum, so that phase is probably enriched by molybdenum. The bcc#2 lattice parameter is close to that of pure iron and chromium. For all studied mechanical alloying conditions, the powder is severely contaminated by iron due to the wear of balls and vial. Without surprise, the contamination increases with the milling time and the contamination for milling during 64 h is the highest. In the literature, the iron contamination from the erosion of steel balls and vial during milling of HEA in the SPEX device was also found [111]. The SEM observations of non-polished milled (P-EQ-S32h) powder show agglomeration of small particles (Appendix A, Fig. A1a). The size of the majority of particles is between 3 and 5 µm, although 10 µm particles could also be easily found. The surface is rugged, which proves that shocks during milling in SPEX are highly energetic.

The mechanical alloying in SPEX presents advantages (homogeneity of powder) and disadvantages (contamination). The 16 h and 64 h milling were abandoned due to insufficient homogeneity (especially non-milled particles of molybdenum) and very high contamination by iron, respectively. Nevertheless, the powders highly contaminated by iron present the parameters in good range to form HEA except for the electronegativity difference. The 32 h milling was retained for further investigation. However, to obtain a final composition not too enriched in iron, the amount of iron powder that was initially introduced into the vial was reduced.

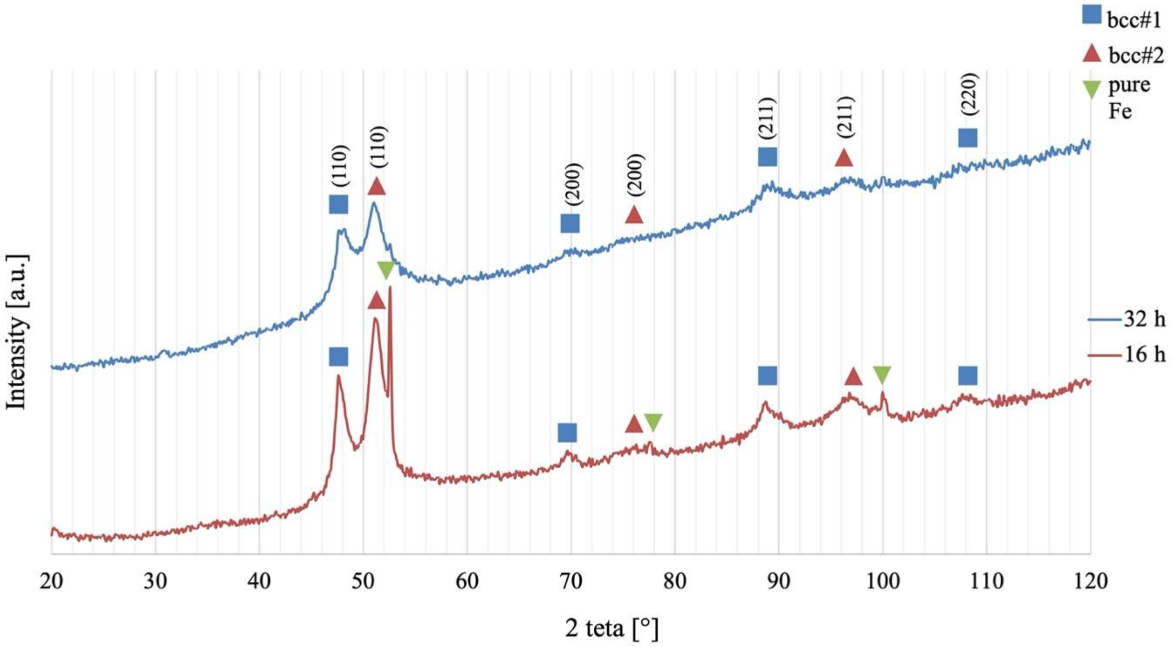

Figure 4-1. XRD pattern of the equiatomic powder after milling in SPEX for 16 h (P-EQ-S16h) and 32 h (P-EQ-S32h).

Table 4-2. Summary of MA results of the equiatomic powder milled in SPEX.

Sample	Final composition and homogeneity	Lattice parameters	
		bcc#1	bcc#2
P-EQ-S16h	17% Al, 18% Cr, 33% Fe, 16% Mn, 16% Mo (heterogeneous; non-alloyed Mo particles)	3.14 Å	2.93 Å
P-EQ-S32h	17% Al, 19% Cr, 29% Fe, 18% Mn, 17% Mo (homogeneous)	3.13 Å	2.94 Å
P-EQ-S64h	16% Al, 16% Cr, 37% Fe, 15% Mn, 16% Mo (homogeneous)	3.13 Å	2.96 Å

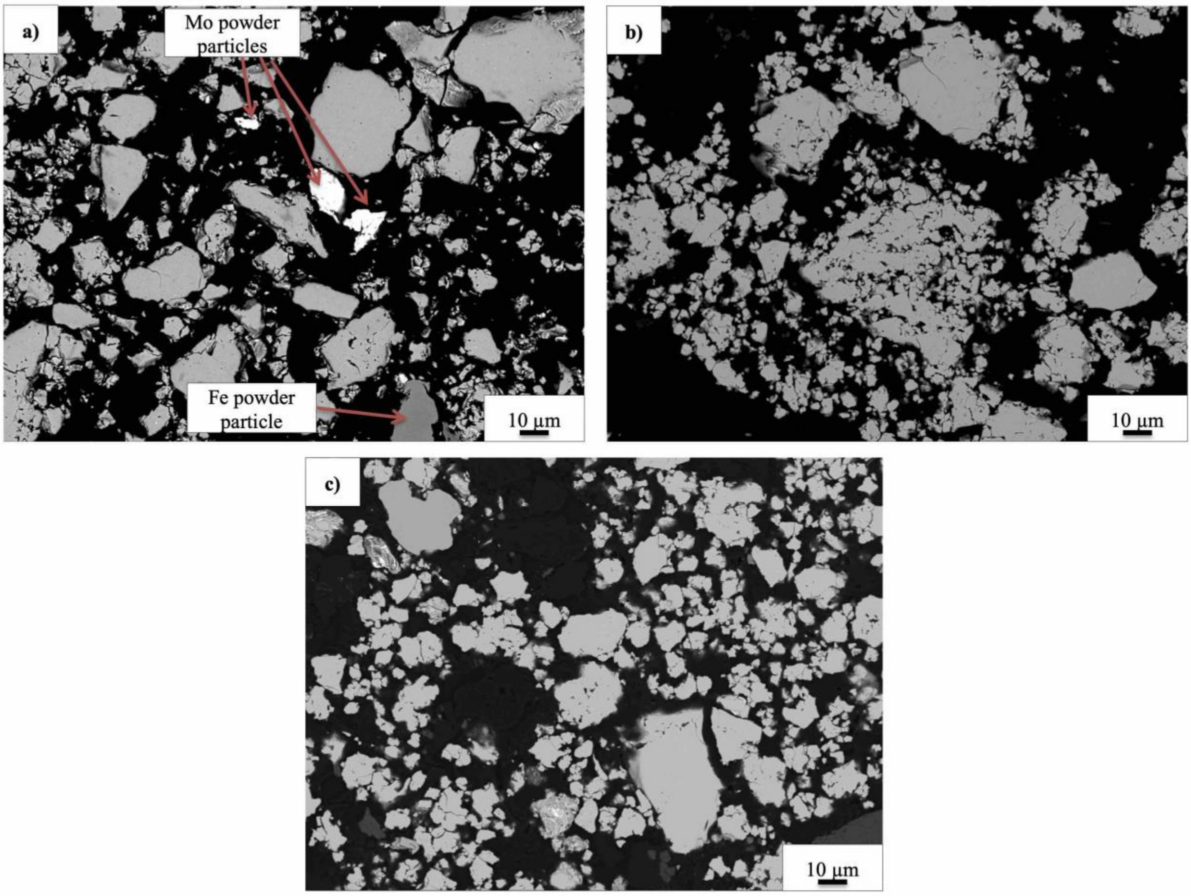

Figure 4-2. SEM-BSE images of the equiatomic powder after milling in SPEX a), P-EQ-S16h, b) P-EQ-S32h, c) P-EQ-S64h.

Powders with reduced content of iron (22.2% Al, 22.2% Cr, 11.2% Fe, 22.2% Mn, 22.2% Mo, P-EQ-RFe-S32h) and without iron (25% Al, 25% Cr, 25% Mn, 25% Mo, P-EQ-NFe-S32h) in their starting composition were also tested to produce an alloy with a final equiatomic composition, including iron (coming from balls and vial). The results after 32 h of milling show homogeneous microstructure at the SEM scale (nevertheless, some iron particles were found); however, the content of iron in alloyed particles is higher than 20 at. % (see Appendix A, Figs. A2 and A3, Table A1). It means that the relative increase of iron concentration for both alloys is unexpectedly much higher than for the starting equiatomic powder. A possible explanation is a higher concentration of molybdenum and chromium (both highly hard) in the initial powder composition, which probably causes a more significant erosion of balls and vials materials. Moreover, the pure molybdenum particles are much larger than other powders and thus contribute to wear even more significantly. The erosion of steel balls and vial and resulting iron contamination is a common problem in the MA process [77,80,111]. The contamination phenomenon is difficult to control during mechanical alloying of target equiatomic composition in SPEX. Both powders consist of two bcc phases with lattice parameters similar to those found in the quinary alloy without reduced iron content in the starting composition (Table A1). It should be noted that all parameters except for the electronegativity difference are in good range to form HEA. These results show that SPEX mill produces homogeneous powders (initially equiatomic and with reduced iron) at the SEM scale but massively contaminated by iron coming from balls and vials. Hence, the milling in other devices should be considered to find optimal conditions for the preparation of equiatomic powder.

The XRD analysis of the P-EQ-S32h, P-EQ-RFe-S32h, and P-EQ-NFe-S32h reveals two bcc phases, while the Mössbauer spectrometry (performed at 20 °C) shows iron environments centered between -2 et 2 mm/s (Figure 4-3). It unveils that there is only a small amount of magnetic iron environment. The spectra are relatively similar for the three powders; however, an evolution is revealed on the left side of spectra with decreasing iron content. The hyperfine parameters of the iron environments obtained after the deconvolution of spectra using the Lorentzian function with iron as a reference, to quantitatively and qualitatively analyze results, are shown in Table A2. These iron environments were numbered from site 1 to site 12. Depending on the sample, the amount of the magnetic environment is between 14.5±4.50 % and 5.52±2.25 %. This magnetic contribution does not come from two bcc phases; it is the effect of not fully completed alloying or the iron contamination from the milling media. The presence of iron environments in the sample without iron in the initial composition (P-EQ-NFe-S32h) confirms the contamination from balls and vial material found by EDX measurements. The bcc phases are characterized by iron environments of doublet and singlet types. Each environment of non-magnetic iron is described by the Mössbauer parameters such as Isomer Shift (IS), Quadrupole Splitting (QS), peak Width (W), and the relative Amount of each iron environment (A). The values of IS and QS vary slightly depending on the chemical composition of the bcc phases and their ratio. It is impossible to associate each doublet and singlet to the bcc#1 or bcc#2 phase because no single-phase mechanically alloyed powder was produced in this study. Taking into account only the non-magnetic iron environments, it could be noted that the amount of site 5 increases, while the amount of sites 6, 9, and 12 decreases with decreasing initial iron content. The evolution of sites 7 and 8 is less evident.

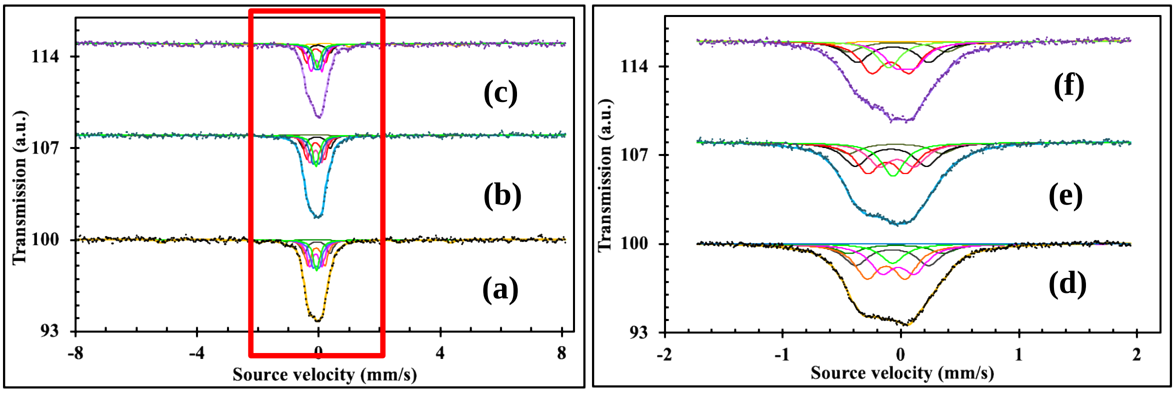

Figure 4-3. Mössbauer spectra of the P-EQ-S32h (a, d), P-EQ-RFe-S32h (b, e), and P-EQ-NFe-S32h (c, f) powders alloyed in SPEX for 32 h.

4.1.1.2. RETSCH

The starting equiatomic composition was also prepared by using a planetary mill - RETSCH PM-100. The initial conditions, chosen during the Master thesis internship of Surya Nilamegam Kumaran [110], consisted in a milling for 70 h at 300 rpm (P-EQ-R70h). The powder processed at these conditions is not chemically homogeneous (Fig. A5a) - manganese, molybdenum, and chromium-rich areas were observed; however, only low contamination by iron from balls and vial materials was detected (Table A3). The idea was to optimize mechanical alloying for the purpose of obtaining a homogeneous and non-contaminated powder. The milling in a planetary mill for 70 h, followed by a short homogenization in SPEX (e.g., 1, 2, or 4 h), was chosen as an optimization attempt. The results (Fig. A5) show that a milling for 70 h in RETSCH mill followed by a homogenization in SPEX for 4 h (optimized conditions, P-EQ-R70hS4h) produce a homogeneous powder at the SEM scale. The intensity of bcc#1 XRD peaks (a = 3.14 Å) is surprisingly dominant over those of bcc#2 (a = 2.87 Å), which presents a decrease of lattice parameter as a function of the increasing homogenization time in SPEX (Fig. A4, Table A3). Nevertheless, small peaks corresponding to non-alloyed manganese are still present, which is surprising considering the low manganese melting temperature and therefore, an expected fast alloying rate. However, a slower alloying rate of manganese than elements with higher melting temperatures was also found by Joo *et al.* [73]. The SEM-SE observation of non-polished powders reveal a significant difference in surface, shape, and size of particles compared to powders milled in SPEX. The particles milled in RETSCH for 70 h (P-EQ-R70h, Fig. A1b) are more spherical, smaller, less agglomerated, and their surface is flat compared to powder mechanically alloyed in SPEX for 32 h (P-EQ-S32h, Fig. A1a). The results for powder milled in optimized conditions (P-EQ-R70hS4h, Fig. A1c) are between millings only in SPEX or RETSCH. It confirms that shocks in RETSCH are less energetic than in SPEX. TEM observations were carried out to evaluate grain size and chemical homogeneity of particles after milling in optimized conditions. In Figure 4-4, nanometric grains (about 20 nm) and compositional uniformity are revealed at the scale of the analysis. Due to problems with the powder preparation for TEM observations, the electron diffraction was not performed to confirm the phase structure. The exact chemical composition of constituent phases was not measured due to the limited resolution of EDX analysis. The coupling of milling in RETSCH (70 h) and SPEX (4 h) enables the production of a relatively homogeneous and slightly contaminated (by iron) equiatomic powder.

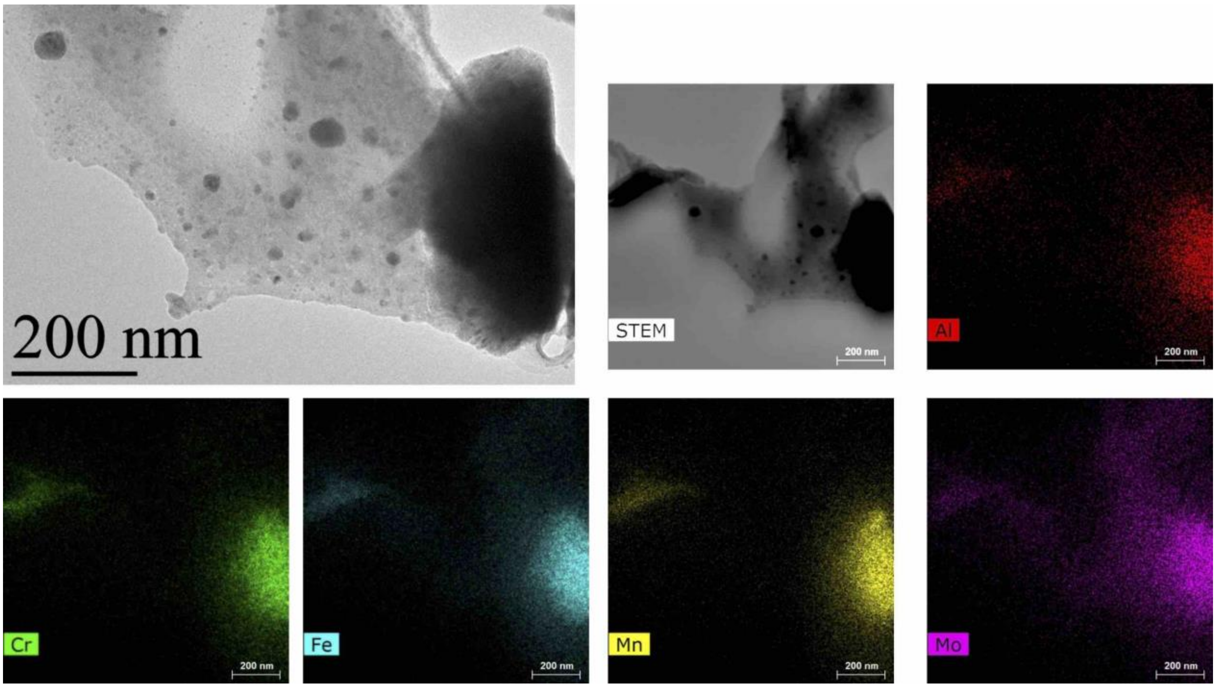

Figure 4-4. TEM bright-field image and corresponding STEM-EDX mapping of powder particles of P-EQ-R70hS4h sample.

The Mössbauer spectra of the alloys with the equiatomic content of elements introduced to the vial before milling in the planetary mill RETSCH are centered between -2 and 2 mm/s (Figure 4-5), it is similar to the powder mechanically alloyed in SPEX (Subsection 4.1.1.1). The magnetic contribution varies between 16.23±1.81 % for milling in RETSCH for 70 h and 9.40±0.41 % for milling in RETSCH for 70 h, followed by SPEX for 4 h (Table A4). It can be the effect of the homogenization in the vibration mill (SPEX), which is in good agreement with the results obtained by SEM-EDX. Comparing spectra c and d in Fig. 4-5, it could be found that the center of the spectrum gets closer due to the milling in SPEX. Non-magnetic environments (sites 5-9) are still noticed. The additional milling in SPEX for 4 h is associated with a decrease of the relative intensity of phases in the non-magnetic sites 5 and 6 (3 to 5 %) and an increase of sites 7, 8, and 9 (1 to 2 %).

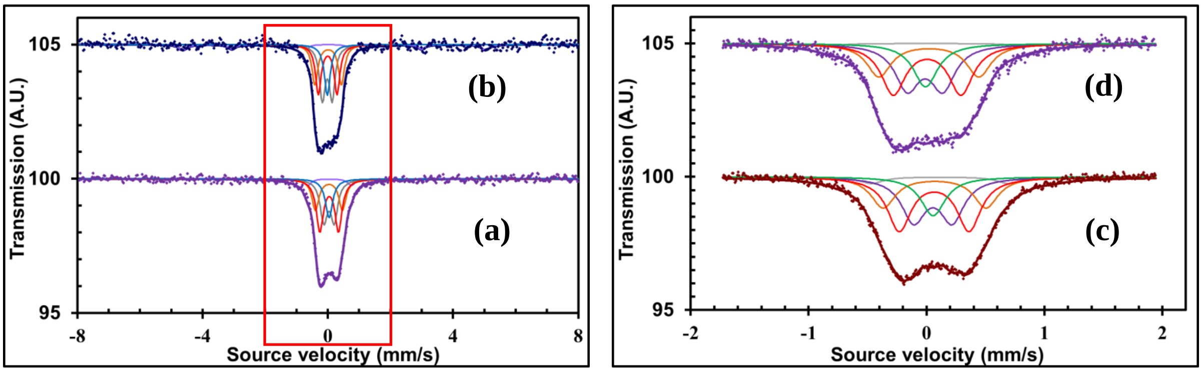

Figure 4-5. Mössbauer spectra of powders: P-EQ-R70h (a, c) and P-EQ-R70hS4h (b, d).

4.1.1.3. CryoMill at room temperature

The powder with equiatomic ratio of elements before milling was also mechanically alloyed in a CryoMill device at room temperature. Initially, the effects of operating frequency (15, 20, and 25 Hz) and time (32 and 64 h) were investigated. Microstructure analysis results (Appendix A, Fig. A6 and A7, Table A5) reveal that powder homogeneity increases with increasing milling frequency. The XRD of powder milled for 32 h at 15 Hz (P-EQ-C32h-15Hz) presents peaks of pure elements instead of bcc phases (Fig. A6). The patterns for the highest frequency show the formation of two bcc phases. On the other hand, it is shown that even after milling for 64 h at 25 Hz (P-EQ-C64h), the powder is not completely homogeneous at the SEM scale; however, the powder is not contaminated by iron. The observation of non-polished powder reveals a spherical shape and smooth surface of particles (Fig. A1d), which confirms that shocks in CryoMill are less energetic than in SPEX. Hence, a similar strategy of optimization of powder homogeneity, as for planetary device, was tested. The milling time in CryoMill was set to 32 h at 25 Hz, followed by homogenization in SPEX for 1, 2, 4, 8 h. The powder milled in CryoMill for 32 h at 25 Hz (P-EQ-C32h) seems to be less homogeneous than the powder milled in RETSCH for 70 h (P-EQ-R70h); therefore, only homogenization for 8 h in SPEX (P-EQ-C32hS8h) produces a rather homogeneous powder. However, the milling in SPEX for 8 h introduces significant contamination by iron (Fig. A8 and A9, Table A6). Hence, the composition with reduced iron content (22.2% Al, 22.2% Cr, 11.2% Fe, 22.2% Mn, 22.2% Mo) was studied (P-EQ-RFe-C32hS8h). The mechanical alloying in CryoMill for 32 h followed by milling in SPEX for 8 h produces a rather homogeneous powder with the almost equiatomic composition. It should also be noted that other optimization cycles, for starting equiatomic composition, were tested, e.g., 8 h CryoMill + 8 h SPEX + 8 h CryoMill + 8 h SPEX (and also 8 h SPEX + 8 h CryoMill + 8 h SPEX + 8 h CryoMill). The homogeneity increases compared to mechanical alloying in CryoMill for 32 h, but the contamination is found to be very high, i.e., 16% Al, 19% Cr, 31% Fe, 17% Mn, 17% Mo, but the parameters (except the electronegativity difference) are in good range to form HEA. To my best knowledge, no paper dealing with the mechanical alloying of HEA powder in the CryoMill device at room temperature has been published yet. It seems that ball shocks in that mill do not produce enough energy to homogenize powder fully; for this reason, the milling should be conducted rather at cryogenic temperature in this device.

Powders milled in CryoMill are not completely homogeneous because they are composed of magnetic particles, whose Mössbauer peaks positions are shown by arrows in Figure 4-6, and non-magnetic particles peaks which shows doublets and a single peak centered between -2 and 2 mm/s. The content of magnetic phase is 30.54 % after milling in CryoMill (P-EQ-C32h), while the content of magnetic phase decreases to 25.00 % after additional milling in SPEX for 8 h (P-EQ-C32hS8h) (Table A7). The more violent milling in SPEX changes the general appearance of the spectra because of the contamination from the milling media by iron and the homogenization of the alloyed powder. However, both alloys (P-EQ-C32hS8h and P-EQ-RFe-C32hS8h), regardless of the amount of iron introduced to the vial, present the similar spectrum appearance after milling in the CryoMill for 32 h, followed by milling in SPEX for 8 h. The analysis of Mössbauer parameters of iron environments shows that additional milling in the SPEX for 8 h has an effect on the sites 9 and 12 (their amount goes from 17.5 to 25.6 %) in alloy with 20 % of iron initially introduced. The amount of the sites 9+12 increases from 16.5 to 25.6 % when the initial iron content introduced to the vial increases form 11.2 and 20 %. Hence, these sites (9 and 12) could be associated with the iron atoms with more iron neighbors.

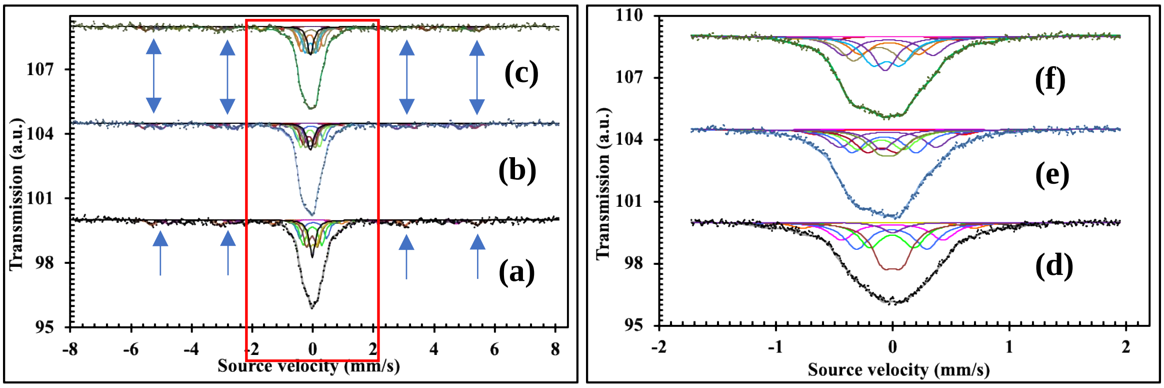

Figure 4-6. Mössbauer spectra of powders: P-EQ-C32h (a, d), P-EQ-C32hS8h (b, e), and P-EQ-RFe-C32hS8h (c, f).

4.1.2. Optimized powder

As the next step of the study, the composition (22.5% Al, 22.5% Cr, 28% Fe, 20% Mn, 7% Mo) optimized thanks to the parametric approach calculation (lower electronegativity difference), was also prepared by mechanical alloying in SPEX and CryoMill devices.

4.1.2.1. SPEX

Based on the results obtained for the alloy with the equiatomic content of elements introduced in the vial, a milling in SPEX for 32 h of the optimized composition was initially performed (P-O-S32h). The milled powder is homogeneous at the SEM scale (Fig. 4-7b), which is similar to the P-EQ-S32h sample. The SEM-SE observations of the non-polished powder reveal agglomerated particles with a rugged surface, which confirms the high energy of shocks in SPEX (Fig. A1e). However, the powder is surprisingly only slightly contaminated by iron. The final average composition, measured by SEM-EDX, is 22% Al, 22% Cr, 30% Fe, 19% Mn, 7% Mo, which is close to the composition of the powder before the milling, and the parameters present good values to form HEA. The much lower contamination by iron is attributed to the significantly lower molybdenum content (7 at. % compared to 20 at. %). Molybdenum particles cause heavy wear of steel balls and vial, due to larger particle size and high hardness. The milled powder consists of two bcc phases: minor bcc#1 (a = 3.13 Å) and major bcc#2 (a = 2.93 Å) (Fig. 4-7a). The lattice parameters are similar to those found for the equiatomic composition.

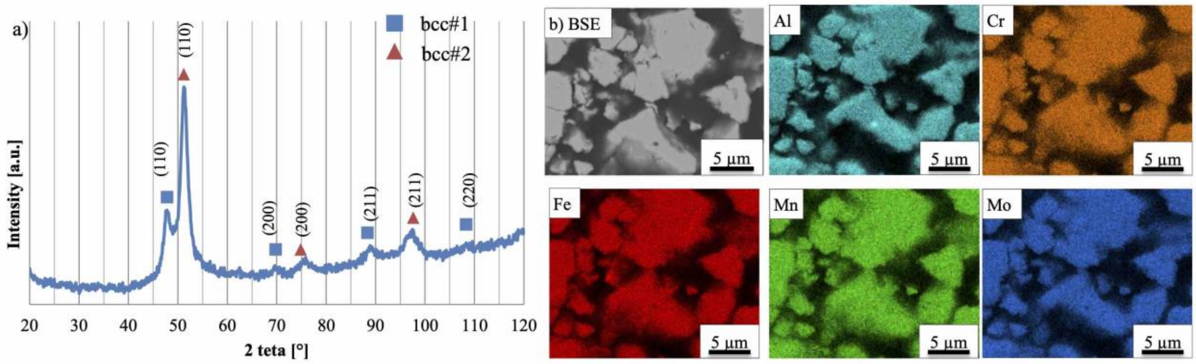

Figure 4-7. Analysis of the P-O-S32h powder after milling: a) XRD pattern, b) SEM-EDX mapping.

TEM images and EDX analyses at high magnification of a MA powder sample prepared by FIB were performed to study the chemical composition of the present phases. It is revealed that powder consists of two regions that differ in terms of chemical composition (Fig. 4-8). The matrix, which is associated with the bcc#2 phase, contains all chemical elements. The phase significantly enriched in molybdenum is attributed to bcc#1 due to the close lattice parameter between bcc#1 phase and pure molybdenum. Moreover, some small regions enriched in chromium were also found. The exact concentrations of elements are not indicated, because of limited EDX resolution and the too large sample thickness.

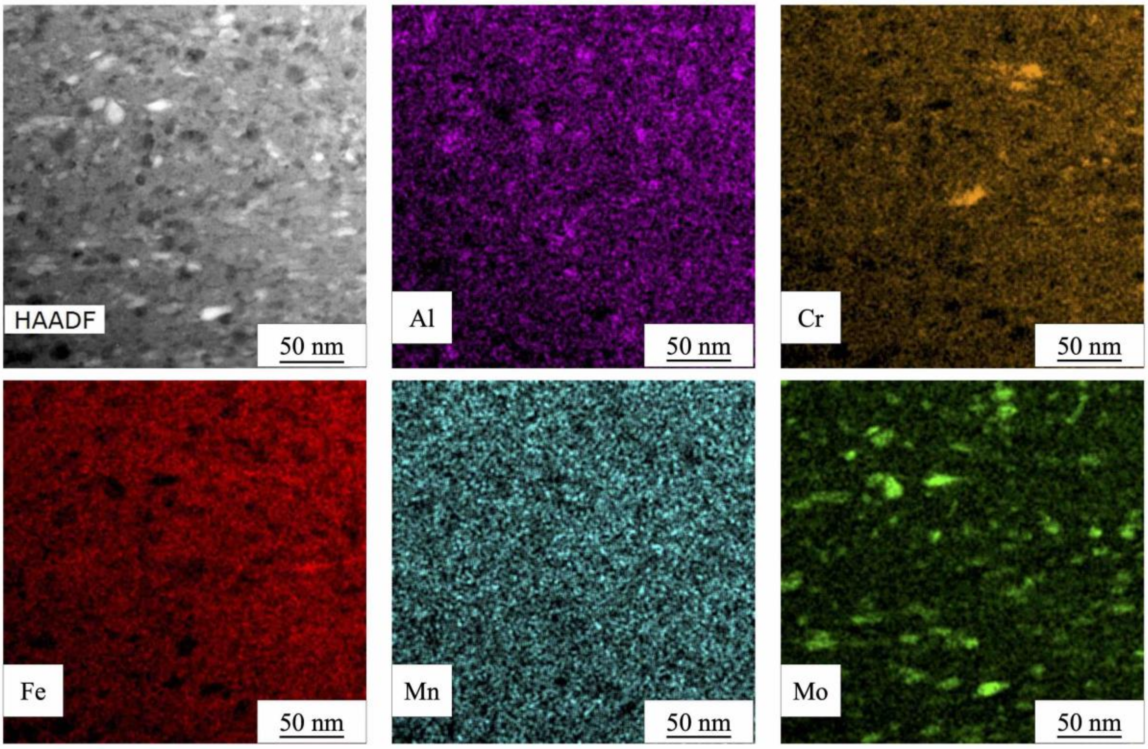

Figure 4-8. STEM high magnification HAADF image and corresponding EDX mapping of the powder mechanically alloyed – P-O-S32h.

In opposition to the equiatomic composition, the milling of the optimized powder in SPEX for 32 h seems to be an optimal condition because the milled powder presents a two bcc phase structure with good chemical homogeneity at the SEM scale and a limited contamination by iron.

4.1.2.2. CryoMill

The milling of the optimized powder in CryoMill was also performed for 32 h at 25 Hz (P-O-C32h). The powder, similarly, to the equiatomic one (P-EQ-C32h), is contamination-free but not homogeneous. Hence, a homogenization for 8 h in SPEX was also conducted (P-O-C32hS8h). Both powders consist of two bcc phases with lattice parameters similar to powders alloyed in other conditions. The homogeneity of particles increases, but it seems less homogeneous than for the milling in SPEX for 32 h (Fig. A10 and A11, Table A8). Small contamination by iron was detected. The SEM-SE observations of non-polished powders reveal spherical particles with a flat surface, which proves that shocks in CryoMill are much less energetic than in SPEX (Fig. A1f). The milling in CryoMill for this composition was abandoned because the mechanical alloying in SPEX for 32 h provides much more promising results in terms of homogeneity and limited contamination.

According to the Mössbauer spectrometry results, the magnetic contribution (showed by the arrows in Figure 4-9) is higher for the optimized powder milled in the CryoMill (54.5 %) compared to the powder milled in the SPEX (12.9 %) for the same duration (32 h). Hence, for the powder milled in CryoMill, there is 54.5 % of magnetic phase and 45.5 % of non-magnetic phase (Table A9). This sample is not homogeneous because it contains 21.64 % of the iron environments only with iron atoms as the first and second neighbors (while the total iron content is only about 28 %). The preferred route to synthesized homogeneous optimized powder (22.5% Al, 22.5% Cr, 28% Fe, 20% Mn, 7% Mo) is milling in SPEX. The same iron sites characterize two powders milled in SPEX and CryoMill; only their amount varies in the function of the milling device and the real iron content. The spectrum of the P-O-S32h is very promising since it is relatively symmetrical and shows only 12.9 % of magnetic phase. Hence, the powder milled in SPEX is homogeneous because the local order around the iron atoms is similar to the whole alloy. These results are in good agreement with the SEM results (Fig. 4-7b), which shows homogeneous particles. The XRD results (Fig. 4-7a and Fig. A10) reveal two bcc phases. At this stage of the study, it is impossible to find which sites from 5 to 9 and 12 come from the bcc#1 or the bcc#2.

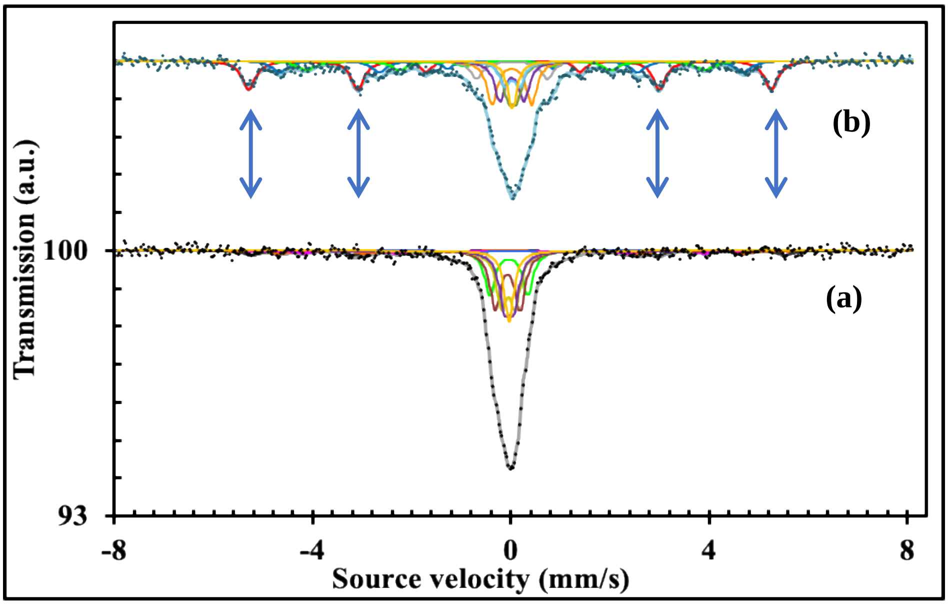

Figure 4-9. Mössbauer spectra of the optimized composition mechanically alloyed in SPEX for 32 h: a) P-O-S32h and b) P-O-C32h.

4.1.3. Experimentally optimized powder

Finally, the mechanical alloying of the experimentally optimized powder (19% Al, 22% Cr, 34% Fe, 19% Mn, 6% Mo) was performed (P-OE-S32h). The MA was carried out in SPEX for 32 h, based on previous results of the optimized composition (22.5% Al, 22.5% Cr, 28% Fe, 20% Mn, 7% Mo). The powder is homogeneous at the SEM scale (Fig. 4-10b) and only slight contamination by iron is detected. The final composition is 18% Al, 21% Cr, 37% Fe, 18% Mn, 6% Mo, close to the starting composition. The parameters are in good range to form HEA, except the mixing entropy, which is slightly too low. The alloy consists of two bcc phases (Fig. 4-10a): minor bcc#1 (a = 3.13 Å) and major bcc#2 (a = 2.91 Å). The similar values of lattice parameters are found there for the other analyzed compositions. The MA in other conditions was not performed because milling in SPEX for 32 h produced a rather promising powder in terms of homogeneity, formed phases, and contamination.

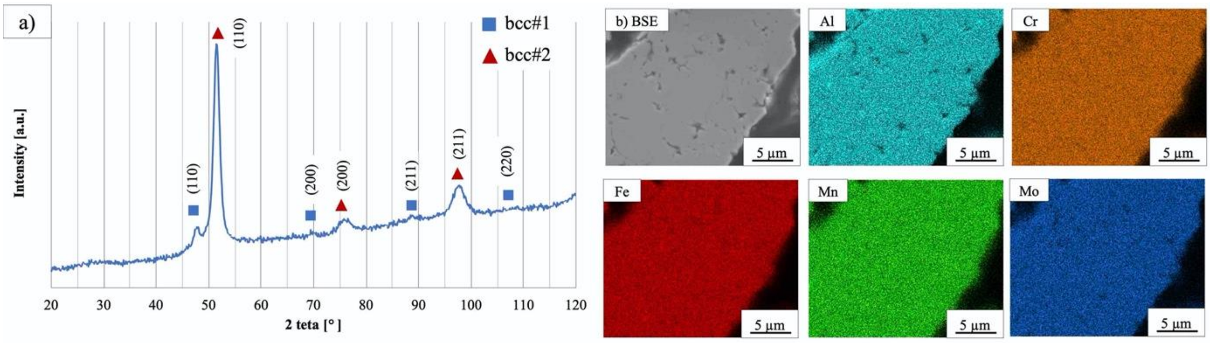

Figure 4-10. Analysis of the experimentally optimized powder after milling - P-OE-S32h.

The Mössbauer spectra in the range of 8 mm/s of the P-O-S32h and P-OE-S32h powders alloyed in SPEX for 32 h (Fig. 4-11 a and b) show only a small amount of magnetic phase (9.4 to 12.9 %) while a majority of the spectra are localized between -2 and 2 mm/s (Fig. 4-11 c and d). The local order around iron atoms in both powders is comparable. Nevertheless, the spectra of the P-OE-S32h sample are more symmetrical (Fig 4-11 b and d), which is related to a higher amount of the bcc#2 compared to bcc#1 (it is in agreement with the XRD results shown in Fig. 4-10). Comparing the obtained parameters (Tables A9 and A10) with the powder annealed at 950 °C for 1 h (Subsection 5.2.1.), the site 12 could be associated with the presence of the χ phase clusters (cluster or local nuclei of χ phase before the appearance of this phase detectable by XRD).

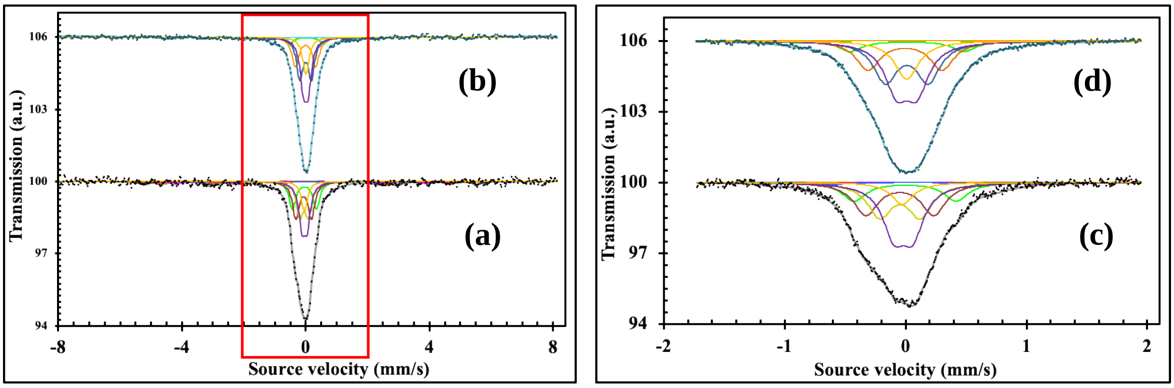

Figure 4-11. Mössbauer spectra of the powders after mechanical alloying: P-O-S32h (a, c) and P-OE-S32h (b, d)

4.2. The contamination phenomenon

The contamination is an important disadvantage of the mechanical alloying process. The pollution, as it is mentioned in the literature review, comes from various ways. The most significant source seems to be the wear of balls and vial, which depends on the material of which they are made. In this study, only hardened steel milling media were tested. It was shown that the contamination also depends on the milling device. The ball-vial-powder shocks in RETSCH and CryoMill are less energetic than in SPEX. The particles milled in SPEX are less spherical, and their surface is more rugged than after mechanical alloying in the two other devices. Less energetic shocks also result in a lower chemical homogeneity of powders for a given milling time. However, milling in RETSCH or CryoMill introduces only a very limited (or even no) iron contamination, while after mechanical alloying in SPEX, the contamination seems to be inevitable. In the literature, the iron contamination of HEA powder from balls and vial material in SPEX was also reported by Derimow *et al.* [111]. The introduction of iron into HEA powder from milling media was also detected in planetary mills [77,80]. The contamination problems of HEA powder prepared in CryoMill at room temperature are not known due to a lack of articles dealing with the mechanical alloying in this type of mill. Moreover, in this study, it was shown that the initial composition of HEA powder could present a significant impact on the contamination during milling. The powder with the equiatomic content of elements introduced to the vial before MA is much more contaminated by iron after milling in SPEX than the optimized alloys 22.5% Al, 22.5% Cr, 28% Fe, 20% Mn, 7% Mo and 19% Al, 22% Cr, 34% Fe, 19% Mn, 6% Mo. It is probably related to the difference in molybdenum content. The molybdenum particles are much bigger than the other particles. Moreover, pure molybdenum presents very high hardness [112]. It is believed that hard elements with large particles cause significant erosion of balls and vials. It should be noted that other components, such as carbon [79,81,84,85] and alloying elements form steel, could be introduced in small fractions, which are much more difficult to detect by typical characterization methods, especially in MA powders.

Besides balls and vials materials, another significant source of contamination is the process control agent. The millings in SPEX and CryoMill were carried out without a PCA. However, the addition of a process control agent, e.g., stearic acid ($C_{18}H_{36}O_2$), for mechanical alloying in the planetary device (RETSCH) is necessary. Stearic acid could be a source of carbon or oxygen [113]. In the literature, it could be found that the effect of contamination from a PCA is often not visible after mechanical alloying due to the small fraction of carbides or their amorphous structure. The carbides usually form after annealing or sintering of MA powders [74,76,79,81,82,85,113]; therefore, the heat-treated powders should be studied carefully. However, Vaidya *et al.* [86] showed by Atom Probe Tomography analysis that the formation of carbides could occur during milling due to carbon coming from the PCA. The other contamination source could be the atmosphere during mechanical alloying. The millings were performed under argon atmosphere; however, leaks during long time milling seem to be impossible to prevent. The accidental introduction of oxygen during mechanical alloying was found in many papers [78,83,85]. It often results in the formation of oxides after annealing. The contamination during the weighing of raw powders (e.g., dust) and then during the preparation of samples for investigation is not negligible [70]. Finally, despite the high purity of used powders, the powders are not completely pure; thus, some minor contaminations, difficult to detect, can also be introduced.

The contamination during MA is a very complex problem and seems to be inevitable. However, a careful investigation of the produced powder and then the right choice of optimized conditions enabled, in this study, to synthesize a powder with limited contamination at least by iron. Moreover, many effects of accidentally introduced elements during milling, such as carbides or oxides, are visible only after annealing; therefore, the annealed powders should be studied carefully. The contamination by carbon and oxygen could also present some beneficial effects on the properties of bulk materials. Precipitates (carbides and oxides) can pin the grain boundaries and thus prevent grain growth during annealing. This effect, coupled with high hardness of carbides and oxide, could improve significantly the mechanical properties.

4.3. Discussion and summary

In this thesis, the mechanical alloying of three compositions from the Al-Cr-Fe-Mn-Mo HEA family was studied. The main target of this stage of the study was to prepare chemically homogeneous powders with disordered bcc phases. A special attention was given to limit contamination, especially iron, coming from the wear of balls and vial material. It was found that the homogeneity and contamination depend on the milling device and also on the chosen chemical composition.

The milling in SPEX produces homogenous powder at the SEM scale; however, a significant contamination by iron was detected, especially for the powder with equiatomic content of elements introduced to the vial before mechanical alloying. The smaller iron pollution for both optimized powders is attributed to a lower molybdenum content, which is, due to high hardness and large particle size, responsible for the significant wear of balls and vial material. The milling in CryoMill and RETSCH do not produce homogeneous powders, even after prolonged mechanical alloying for 64 or 70 h. However, the contamination by iron is still very limited regardless to the studied composition. It can be concluded that shocks in SPEX have much higher energy. Therefore, it results in easiness to obtain a homogeneous powder but also facilitates the wear of balls and vial material. This was also confirmed by observation of non-polished powders. The surface of particle milled in SPEX is more rugged than in RETSCH or CryoMill, which proves a more severe character of shocks in SPEX.

All sufficiently long millings produce two disordered bcc phases in the three compositions. The $AlMo_3$ intermetallic compound, predicted in the equiatomic composition by CALPHAD by Senkov *et al.* [22], and σ phase or intermetallic compound type Cr_3Si (A15), predicted by our CALPHAD studies, were not found in any studied powders. The lattice parameter of the bcc#1 phase is between 3.12 and 3.14 Å, which is close to the pure molybdenum. Similar peaks in a molybdenum containing HEA powder, attributed to non-alloyed pure molybdenum, were found by other authors [114]. However, in the present study, it is believed that these peaks could be attributed to the multi-element bcc#1 phase, enriched in molybdenum. Avila-Rubio *et al.* [91] found a bcc phase with a similar lattice parameter (a = 3.14 Å) enriched in molybdenum after mechanical alloying in SPEX of powder from the AlCoFeNiMoTi and AlCoFeNiMo systems. The TEM-EDX analysis cannot unambiguously prove the presence of pure molybdenum or bcc#1. Moreover, the width of peaks is quite large (even in CryoMill) with slightly different lattice parameters depending on the composition or milling conditions, which could be an argument in favor of the existence of the bcc#1 phase instead of non-milled pure molybdenum. The alloying rate in mechanical alloying depends predominantly on the melting temperature of elements, i.e., the components with lower melting temperature form alloy usually more quickly [90]. For the Al-Cr-Fe-Mn-Mo HEA system, the theoretical alloying order is as following Al ➔ Mn ➔ Fe ➔ Cr ➔ Mo. It could contribute to the formation of the bcc#1 (rich in molybdenum) due to the slow dissolution of molybdenum in the bcc#2 phase. However, the alloying rate could not explain the presence of manganese peaks after processing of equiatomic composition in the planetary mill for 70 h. The slower alloying rate of manganese than other elements with higher melting temperatures was also observed by Joo *et al.* [73]. The lattice parameter of the bcc#2 phase is in the range from 2.87 to 2.96 Å. This lattice parameter is close to those of pure iron and chromium. A similar lattice parameter (a = 2.88 Å) of the bcc phase was found in other HEA – AlCoCrFeNi [36]. The intensity of XRD peaks of both bcc structures depends on milling and chemical composition. For the equiatomic alloy, the amount of the bcc#1 phase is usually higher than the bcc#2 phase; however, milling in SPEX (especially for 32 h) causes a significant increase of the bcc#2. It is believed that the rise of homogeneity causes an increase of bcc#2 volume fraction and a decrease of the bcc#1. For optimized powders, 22.5% Al, 22.5% Cr, 28% Fe, 20% Mn, 7% Mo and 19% Al, 22% Cr, 34% Fe, 19% Mn, 6% Mo, the amount of bcc#1 phase is much lower than that of bcc#2, which proves that the bcc#1 phase (and therefore its volume fraction) is related to molybdenum content. TEM at high magnification coupled with EDX mapping of P-O-S32h confirms the presence of two predominant bcc phases – bcc#2 with all introduced elements and bcc#1 significantly enriched in molybdenum. These results are in perfect agreement with XRD results.

The optimized milling conditions, based on these results, were decided for each of the chosen compositions. The powders selected for the thermal stability analyses and the verification of the potential formation of carbides or oxides after annealing due to the contamination during MA stage are listed in Table 4-3. It should be noted that, despite significant electronegativity difference, the equiatomic composition was also chosen for further studies because it is the flagship composition of the Al-Cr-Fe-Mn-Mo HEA family. Nevertheless, the optimized alloys present more promising results, i.e., lower electronegativity and significant predominance of the bcc#2 over the bcc#1 phase. Hence, it is more likely that these compositions form single bcc after annealing or sintering.

Table 4-3. Mechanically alloyed powders chosen for further investigations with their chemical compositions (at. %).

Powder	Initial composition	Milling conditions	Final composition
P-EQ-R70hS4h	20% Al, 20% Cr, 20% Fe, 20% Mn, 20% Mo	RETSCH 70 h + SPEX 4 h	18% Al, 20% Cr, 24% Fe, 19% Mn, 19% Mo
P-O-S32h	22.5% Al, 22.5% Cr, 28% Fe, 20% Mn, 7% Mo	SPEX 32 h	22% Al, 22% Cr, 30% Fe, 19% Mn, 7% Mo
P-OE-S32h	19% Al, 22% Cr, 34% Fe, 19% Mn, 6% Mo	SPEX 32 h	18% Al, 21% Cr, 37% Fe, 18% Mn, 6% Mo

5. Thermal stability of HEA powder

In this chapter, the thermal stability of the selected alloyed powders is discussed. The mechanically alloyed powders present a metastable structure, hence the interest to study their thermal stability. The results of differential scanning calorimetry are analyzed to choose the temperature of annealing to study the phase transformations. The annealed powders were investigated carefully to determine appropriate sintering temperatures.

5.1. Differential scanning calorimetry

The Differential Scanning Calorimetry (DSC) was performed to study the phase transformations in mechanically alloyed powders under argon atmosphere. The DSC of the optimized powder (P-O-S32h) reveals several phase transitions (Fig. 5-1). A first endothermic peak appears at T_1 (around 50 °C) only during the first cycle of heating. It is related to the evaporation of substances adsorbed during mechanical alloying. Subsequently, the slow exothermic region between T_1 (50 °C) and T_2 (400 °C) could be associated with three phenomena, such as the reorganization of the dislocations, the increase of the crystallite size, and the relaxation of the internal stresses resulting from the mechanical alloying process. A similar tendency was observed on the DSC curves in the literature [76,82,115]. The small bump, just below T_2, can be considered as an artifact since a similar bump was found on the baseline scan. The endothermic region between T_2 and T_3 (724 °C) is attributed to the diffusion of elements. The exothermic peak at T_3 that occurs only during the first heating seems to be related to a phase transformation. This phase transformation has to be investigated by annealing of the powder, which will be discussed later (Subsection 5.2.1.). The endothermic phenomenon between T_3 and T_5 (987 °C) is assigned to the atomic diffusion, probably chromium and molybdenum. The exothermic peak at 879 °C (T_4) could be related to the other phase formation. The endothermic peaks at T_6 (1286 °C) and T_7 (1445 °C), which are present during the first and the second heating, are attributed to the melting of two phases and will be discussed later (Subsections 5.2.1. and 6.4.1.). During the second heating, the temperatures of T_6 and T_7 are slightly higher, which can be related to small changes in the chemical composition of the different phases due to partial evaporation of elements such as aluminum or manganese.

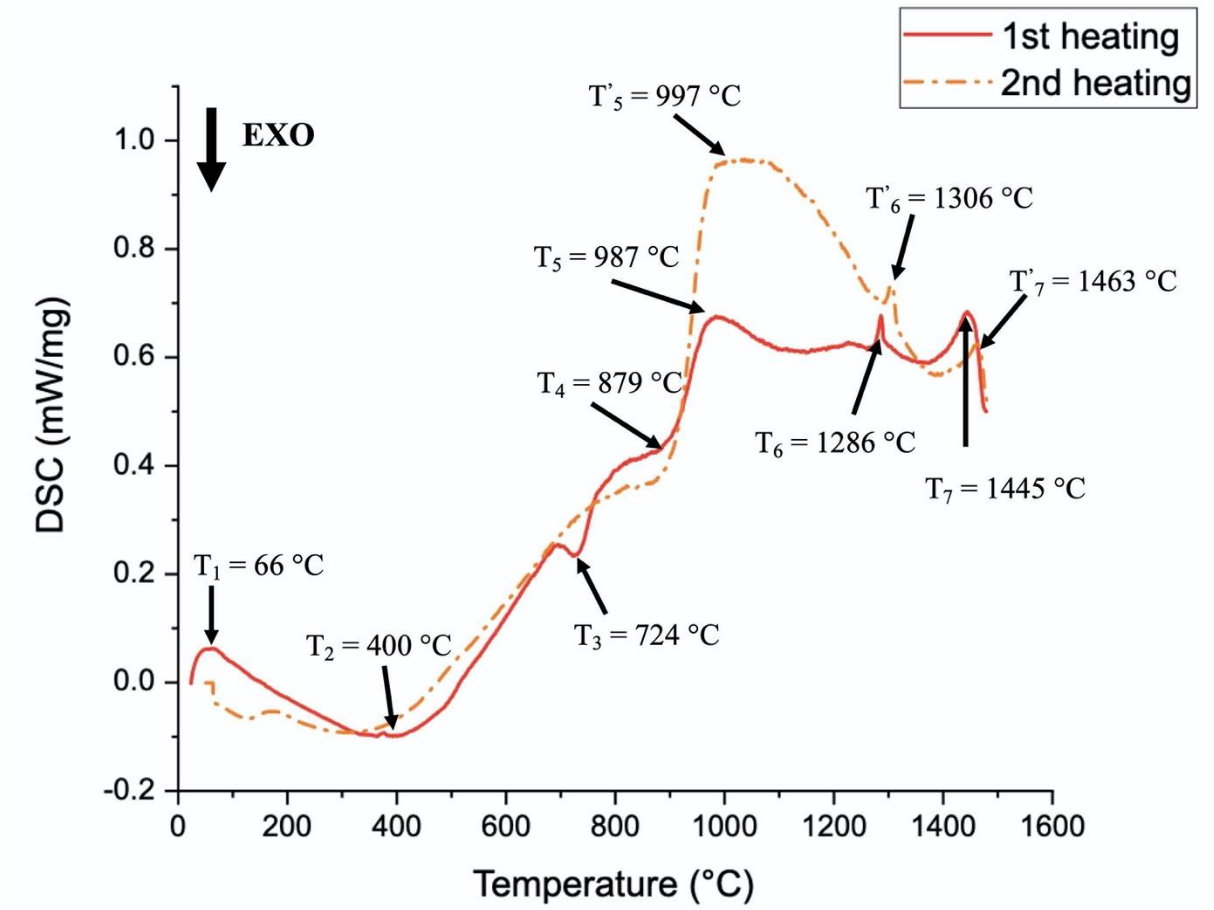

Figure 5-1. DSC curves (2 cycles of heating) of the P-O-S32h mechanically alloyed powder.

The DSC of the P-EQ-R70hS4h mechanically alloyed powder was also performed (Fig. 5-2). The analyses reveal mostly similar phase transformations to those observed for the optimized powder (P-O-S32h) (Fig. 5-1). The phenomena up to T_3 are the same as in Fig. 5-1. The temperature of T_3 is slightly higher, 753 °C for the P-EQ-R70hS4h sample compared to 724 °C for the optimized powder (P-O-S32h). It could be related to the difference in chemical composition, especially the higher content of molybdenum. The T_4 temperature (895 °C) is close to the T_4 temperature in the optimized alloy (879 °C). The T_5 (994 °C) value is similar to that found for the P-O-S32h alloy, while T_6 (1270 °C) is slightly lower. The peak at T_7 is not visible in Fig. 5-2. It can be a result of the higher content of molybdenum, which has a very high melting temperature and therefore increases the melting point of the alloy significantly, above the DSC range of analysis. The DSC results of both powders reveal similar phase transformations. The annealing of three different HEA powder compositions was performed to clearly identify and characterize the phases formed at the temperatures found by DSC (see Subsection 5.2.).

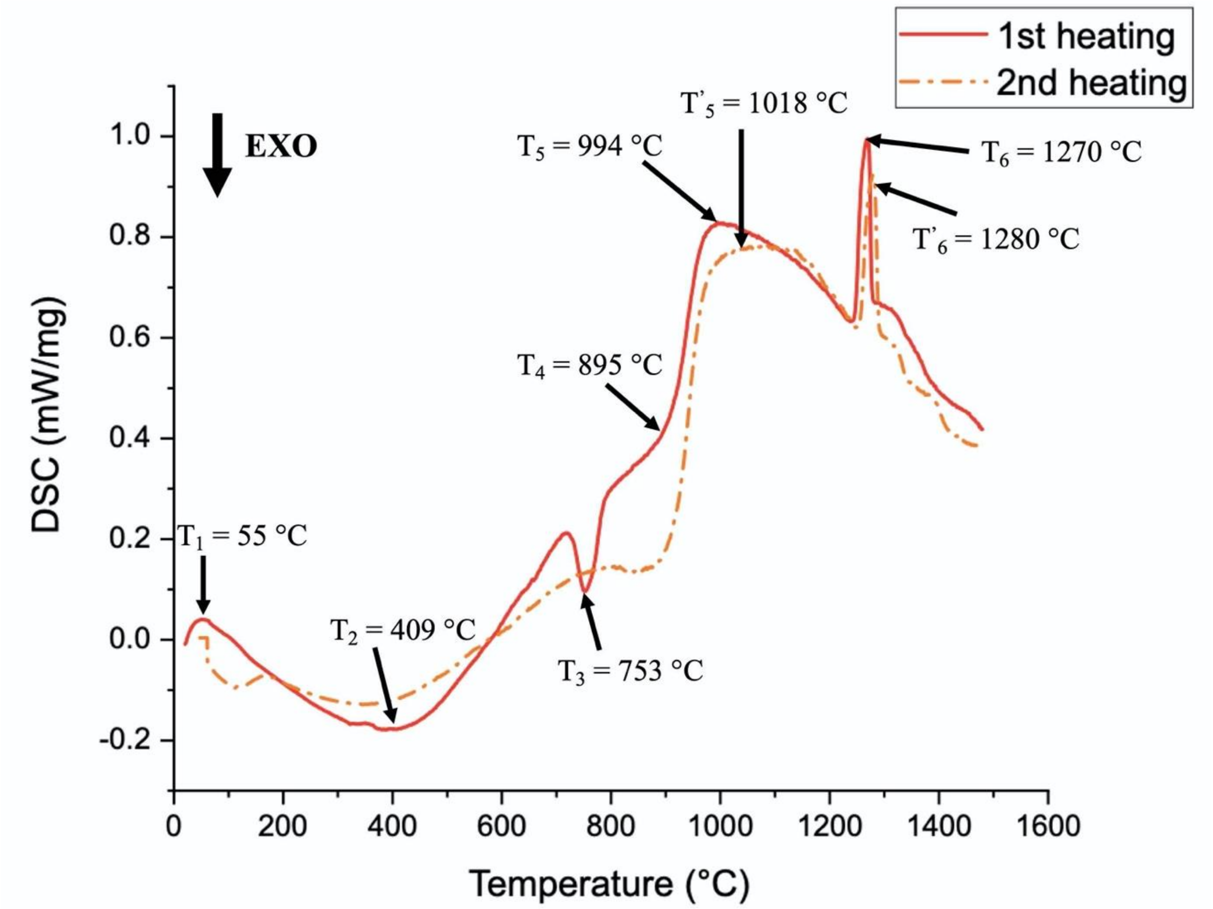

Figure 5-2. DSC curves (2 cycles of heating) of the P-EQ-R70hS4h mechanically alloyed powder.

5.2. Annealing of mechanically alloyed powders

The list of powders annealed in sealed quartz tubes under vacuum is shown in Table 5-1. to present the results clearly (more details in Appendix - Names of samples).

Table 5-1. List of the powder samples annealed under vacuum.

Name of the annealed powder	Name of the MA powder	Annealing conditions
A-O-S32h-500	P-O-S32h	500 °C for 1 h
A-O-S32h-650		650 °C for 1 h
A-O-S32h-800		800 °C for 1 h
A-O-S32h-950		950 °C for 1 h
A-EQ-R70hS4h-850	P-EQ-R70hS4h	850 °C for 1 h
A-EQ-R70hS4h-950		950 °C for 1 h
A-OE-S32h-950	P-OE-S32h	950 °C for 1 h

5.2.1. Optimized powder

XRD and SEM observations of annealed optimized composition (P-O-S32h, 22.5% Al, 22.5% Cr, 28% Fe, 20% Mn, 7% Mo) powder were carried out to determine the crystallographic structure of the phases formed (Figs. 5-3 and 5-4, and Table 5-2). The annealing at 500 °C/1h (A-O-S32h-500) was chosen to verify the phase composition slightly above the temperature (T_2) and below the temperature (T_3) obtained from the DSC curves (Fig. 5-1). The duration of 1 h seems to be sufficient for the incubation to transform phases. The alloy presents the same phase structure (two bcc) as after MA; therefore, the powder is stable up to this temperature of heat treatment. However, small changes in lattice parameters of both bcc phases were detected (Table 5-2), they could be related to slightly different chemical compositions of phases. The SEM-BSE images (Fig. 5-4a) reveal similar microstructure as MA powder. It is consistent with DSC results (Fig. 5-1), which show no phase transformation in this temperature range.

The annealing at 650 °C/1h (A-O-S32h-650) was performed to evaluate the possibility of the occurrence of the phase transformation, found by DSC at temperature T_3 (724 °C), at a lower temperature due to a longer time. The XRD results after annealing at 650 °C/1h reveal the disappearance of bcc#1, the decrease of the intensity of bcc#2 peaks, and the formation of the χ phase (Fig. 5-3). The χ phase (space group: I- 43m (217), sometimes classified as a type $M_{18}C$ carbide) is an intermetallic phase, which rarely forms in HEA [116] but more commonly in molybdenum-containing steels [117–120]. Thus, the exothermic peak at T_3 (724 °C) in the DSC curve (Fig. 5-1), is attributed to the formation of the χ phase. The peak at T_3 appears only during the first heating; therefore, it is believed that phases which are more stable than the χ phase will form at a higher temperature. The transformation temperature found by DSC is much higher compared to the annealing results. It could be due to the incubation time needed to form the χ phase. The heat treatment of the sample at 650 °C/1h enables the transformation, which occurs at a higher temperature in DSC at the heating rate of 10 °C/min. The SEM-BSE images (Fig. 5-4b) do not reveal significant changes in the microstructure in comparison to the powder annealed at 500 °C. It could be due to the small grain size and the close chemical composition between bcc#2 and χ phases.

The annealing at 800 °C (A-O-S32h-800) was performed to analyze the structure above the phase transformation at T_3. The XRD pattern after annealing at 800 °C/1h (Fig. 5-3) reveals the presence of the χ phase, an increase of the peak intensity of bcc#2, and the formation of a small fraction of type M_6C carbides (space group: Fd-3m (227)). In the literature, it could be found that a close link between the M_6C carbide and the χ phase exists; therefore, they can substitute each other depending on the conducted heat treatment or they can exist in equilibrium [120]. The M_6C carbides are reported to form in some mechanically alloyed HEAs [87,114]. The carbon, needed to form carbides, was probably introduced during mechanical alloying from balls and vial material. The SEM-BSE observations (Fig. 5-3c) reveal three different chemical contrasts. The SEM-EDX analyses (Fig. B1) show that major light grey regions have a composition close to the initial one, with a slight increase in molybdenum and a decrease in aluminum. These regions are attributed to the χ phase. The dark grey areas, enriched in iron, are associated with bcc#2. The EDX line scans confirmed a small difference in chemical composition between bcc#2 and χ phases. This could be a reason for the impossibility to distinguish these phases after heat treatment at 650 °C for 1 h. The small white precipitates, significantly enriched in molybdenum, are M_6C carbides. The results are in agreement with DSC results. The exothermic peak T_4 at 879 °C could be associated with the formation of M_6C carbides which, due to higher incubation time, occurs at a lower temperature than found by DSC. The endothermic phenomenon above T_4 could be assigned to the diffusion of elements to increase the volume fraction of molybdenum rich M_6C carbides.

The XRD results for the powder annealed at 950 °C for 1 h (A-O-S32h-950) show the disappearance of the χ phase and the increase of the peak intensity of the M_6C carbide (Fig. 5-3). Moreover, the bcc#2 phase, whose lattice parameter is similar to annealings at lower temperatures (Table 5-2), becomes definitely the dominant phase. Peaks corresponding to the type $M_{23}C_6$ carbide (space group Fm-3m (225)) are detected. The $M_{23}C_6$ carbide, commonly rich in chromium, forms in many mechanically alloyed HEA [79,81,82,84,85,113]. Some very smalls peaks of Al_2O_3 are also noticed. It is the effect of the oxidation due to residual oxygen in quartz ampoule. The SEM-BSE image (Fig. 5-4d) shows three different chemical contrasts. Based on the EDX mapping (Fig. B2), the major dark grey regions are attributed to the bcc#2 phase. The small light grey precipitates are assigned to $M_{23}C_6$ chromium-rich carbides. The white spots are associated with M_6C molybdenum-rich carbides. The Al_2O_3 particles, due to small grain size and low volume fraction, were not detected by SEM. The results are in agreement with DSC (Fig. 5-1). The M_6C carbides form at T_4. The endothermic process up to T_5 (987 °C), is attributed to the diffusion of elements, i.e., to increase the volume fraction of carbides (M_6C and then $M_{23}C_6$), and meanwhile to increase the volume fraction of bcc#2 phase. The peak related to the formation of the $M_{23}C_6$ carbide was not detected, probably due to the small fraction of this carbide initially formed or to the superposition of endothermic phenomenon with the small exothermic peak of the $M_{23}C_6$ formation. Moreover, it seems that the peak at T_6 (1286 °C) could be the melting point of $M_{23}C_6$ carbides. An almost similar melting temperature (1310 °C) was found by Yurkova *et* *al.* [82]. The peak at T_7 (1445 °C) represents the melting of the bcc#2 phase. The powder, recuperated after DSC experiments, seems to be completely melted, which confirms the fusion of the alloy during the rise of temperature up to 1480 °C. The powder annealed at 950 °C for 1 h (A-O-S32h-950) presents a very promising microstructure with the major bcc#2 phase and only a small fraction of carbides and oxide.

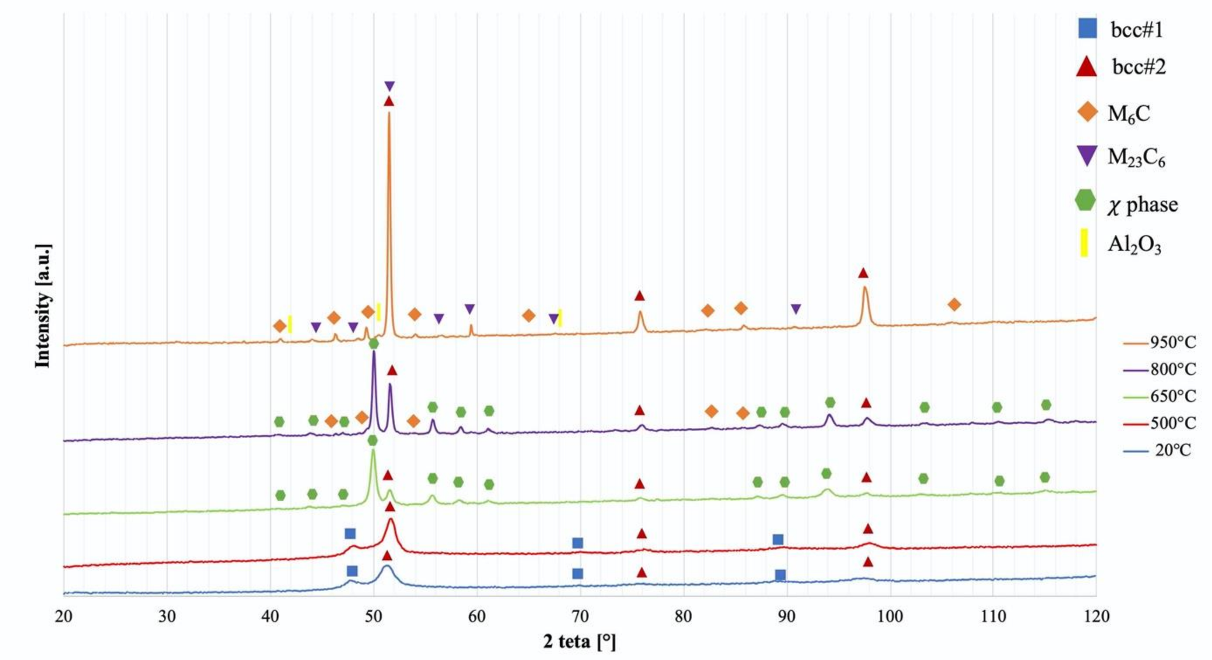

Figure 5-3. XRD patterns of the P-O-S32h powder annealed at different temperatures for 1 h: 20 °C (P-O-S32h), 500 °C (A-O-S32h-500), 650 °C (A-O-S32h-650), 800 °C (A-O-S32h-800), 950 °C (A-O-S32h-950).

Table 5-2. Lattice parameter values of phases of the annealed P-O-S32h powder.

Sample	Lattice parameter [Å]				
	bcc#1	bcc#2	χ phase	M_6C	$M_{23}C_6$
P-O-S32h	3.13	2.93	---	---	---
A-O-S32h-500	3.11	2.90	---	---	---
A-O-S32h-650	---	2.91	8.98	---	---
A-O-S32h-800	---	2.91	8.97	11.14	---
A-O-S32h-950	---	2.91	---	11.15	10.68

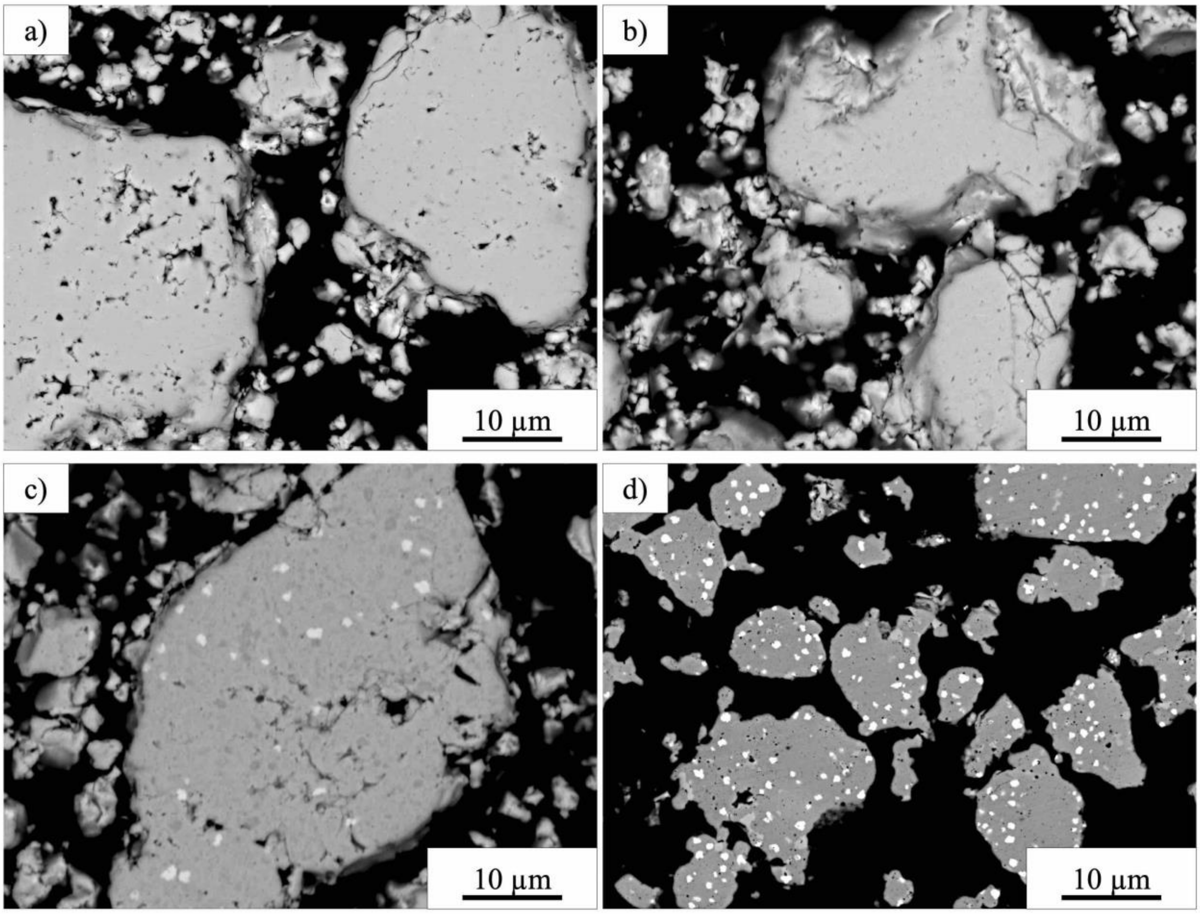

Figure 5-4. SEM-BSE images of the P-O-S32h powder after annealing: a) A-O-S32h-500, b) A-O-S32h-650, c) A-O-S32h-800, and d) A-O-S32h-950.

The comparison of the XRD (Fig. 5-3) and the Mössbauer results (Fig. 5-5) of the annealed powders allows to attribute the 7, 8, 9, and 12 sites to the bcc#2 phase, while the 5 and 6 sites are associated to the bcc#1 phase. The χ phase is characterized by two iron sites of QS = 0.95 mm/s and 0.70 mm/s. Therefore, according to the Mössbauer results, the non-annealed mechanically alloyed P-O-S32h powder sample presents mainly a two-phase structure with 34.43 % of bcc#1, 62.42 % of bcc#2 and 3.14 % of magnetic residue (Table B1). The spectrum related to the non-magnetic iron environments is broad and not perfectly symmetrical. The annealing at 500 °C for 1 h (A-O-S32h-500) results in a decrease in the amount of magnetic residue and bcc#1, while the amount of bcc#2 increases (80.59 %). After annealing at 950 °C for 1 h, there is no more bcc#1 phase. The spectrum is symmetrical and centered at 0 mm/s. The volume fraction of χ phase is 4.82 %, the bcc#2 phase fraction is between 70.84 and 95.18 %, and the carbide ratio is between 0 and 24.34 % (the sum of the bcc#2 and carbides is 95.18 %).

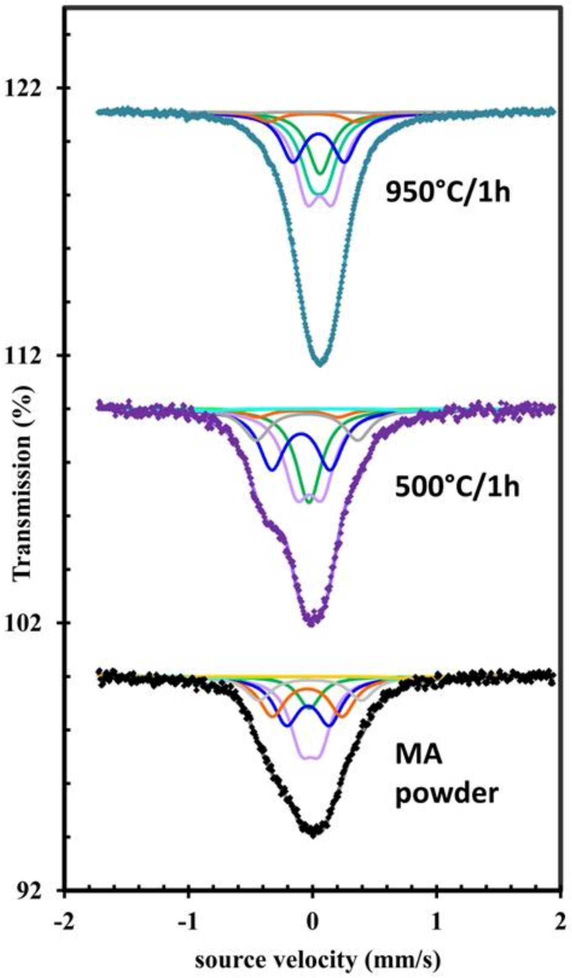

Figure 5-5. Mössbauer spectra of the P-O-S32h mechanically alloyed powder and annealed at 500 °C/1h (A-O-S32h-500) and 950 °C/1h (A-O-S32h-950).

5.2.2. Equiatomic powder

The annealing of the P-EQ-R70hS4h powder at 850 °C (A-EQ-R70hS4h-850) and 950 °C was also performed. The XRD after heat treatment at 850 °C/1h reveals the formation of the χ phase and M_6C carbide (Fig. 5-6b). The bcc#1 phase, which is present after MA (Fig. 5-6a), disappears completely, similarly as for the annealing of the optimized alloy (Fig. 5-3). The peaks of non-milled pure manganese also disappear, which shows the dissolution of manganese in the χ or bcc#2 phase. The peaks of the bcc#2 phase present a very low intensity (lower than for the optimized alloy; A-O-S32h-800). After annealing at 850 °C, the bcc#2 lattice parameter increases slightly to 2.91 Å (Table 5-3), which is similar to the value found in the annealed optimized powder (Table 5-2). The SEM-BSE image (Fig. 5-6e) reveals a white-grey compositional contrast. It seems that all three present phases (bcc#2, χ, and M_6C) have small grain size (< 200 nm); therefore, the distinction between them using SEM images is very challenging. The EDX mapping and line scan (Fig. B3 in appendix) show regions enriched and depleted in molybdenum. The high, medium and low content of molybdenum could be attributed to M_6C, χ phase, and bcc#2 phase, respectively. The volume fraction of M_6C seems to be much higher than for the optimized alloy (22.5% Al, 22.5% Cr, 28% Fe, 20% Mn, 7% Mo). The annealing at 950 °C/1h (A-EQ-R70hS4h-950) reveals the presence of major bcc#2 phase, with similar lattice parameter (2.91 Å) as after annealing 850 °C (A-EQ-R70hS4h-850) (Fig. 5-6c, Table 5-3). The χ phase disappears completely. The intensity of M_6C peaks increases compared to 850 °C, and small peaks of $M_{23}C_6$ appear (Fig 5-6c). The SEM-BSE image reveals (Fig. 5-6f) three contrasts: dark grey (bcc#2), light grey ($M_{23}C_6$, enriched in chromium), white (M_6C, enriched in molybdenum). The results present great similarity with the optimized powder after annealing; however, the volume fraction of carbides is higher. It could be related to the higher content of carbon due to the use of the stearic acid as of process control agent for the milling in planetary mill – RETSCH and high content of molybdenum in equiatomic powder. The lattice parameters of carbides (Table 5-3) are similar to those found in the optimized powder after heat treatment (Table 5-2). The results are in good agreement with DSC (Fig. 5-2). The peak at T_3 (753 °C) is associated with the formation of the χ phase. The peak at T_4 (895 °C) is related to the formation of M_6C carbide. The endothermic process between T_4 and T_5 (994 °C) is related to the diffusion of elements to increase the volume fraction of the M_6C, then $M_{23}C_6$ carbides and bcc#2 phase. The peak of the formation of the $M_{23}C_6$ carbide is not visible. It could be related to the small peak due to the initial small volume fraction of this carbide or to the superposition of the endothermic phenomenon with the small exothermic peak. The peak at T_6 (1270 °C) is assigned to the melting of $M_{23}C_6$, which occurs at a slightly lower temperature than for the optimized powder. The fusion of the bcc#2 phase occurs probably above analysis range due to the higher content of molybdenum, which significantly increases the melting temperature.

Table 5-3. Lattice parameter values of phases of the P-EQ-R70hS4h powder after annealing.

Sample	Lattice parameter [Å]					
	bcc#1	bcc#2	Mn bbc	χ phase	M_6C	$M_{23}C_6$
P-EQ-R70hS4h	3.14	2.87	8.92	---	---	---
A-EQ-R70hS4h-850	---	2.91	---	8.99	11.15	---
A-EQ-R70hS4h-950	---	2.91	---	---	11.15	10.66

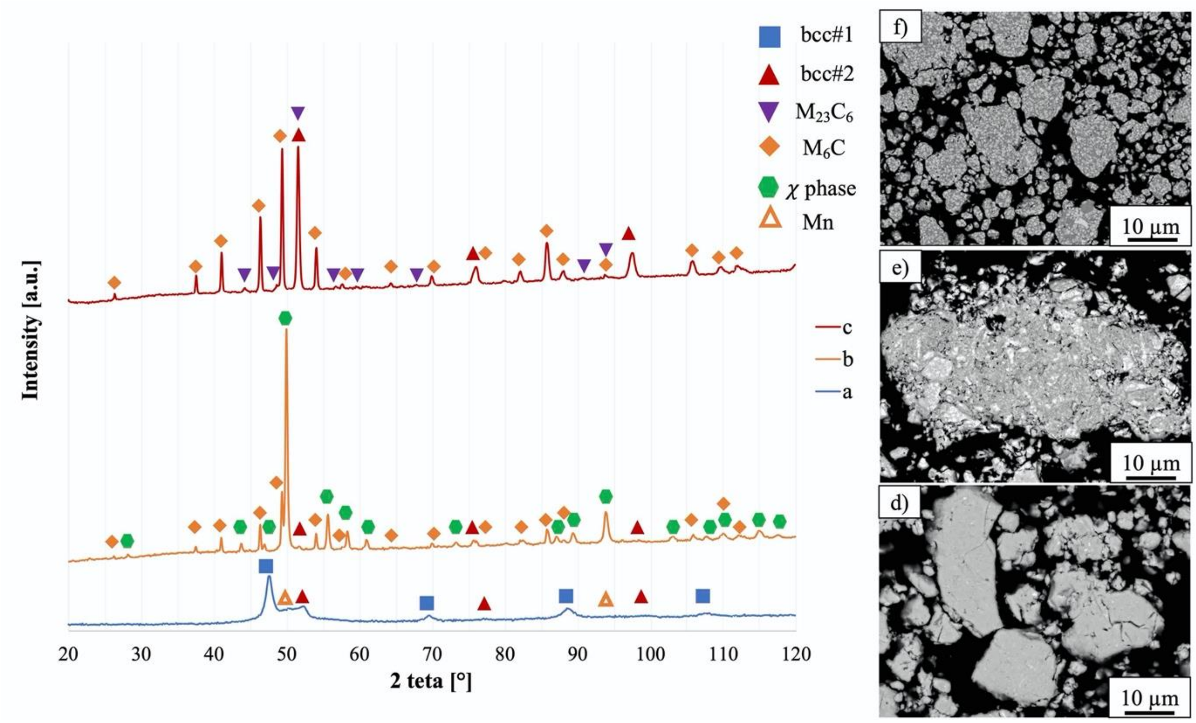

Figure 5-6. Analysis of the P-EQ-R70hS4h after annealing: a) XRD pattern of the P-EQ-R70hS4h powder, b) XRD pattern of the A-EQ-R70hS4h-850 powder, c) XRD pattern of the A-EQ-R70hS4h-950 powder, d) SEM-BSE image of the P-EQ-R70hS4h powder, e) SEM-BSE image of the A-EQ-R70hS4h-850 powder, f) SEM-BSE image of the A-EQ-R70hS4h-950 powder.

The Mössbauer results show that the P-EQ-R70hS4h powder after mechanical alloying is not entirely homogeneous; the volume fraction of magnetic iron-rich phase is about 10 %. The central part of the spectrum is broad and non-symmetrical (Fig. 5-7a, c). The annealing at 850 °C for 1 h (A-EQ-R70hS4h-850) leads to the disappearance of the magnetic phase (Table B2 in appendix). The spectrum becomes more symmetrical and the bcc#1 phase disappears (Fig. 5-7b, d).

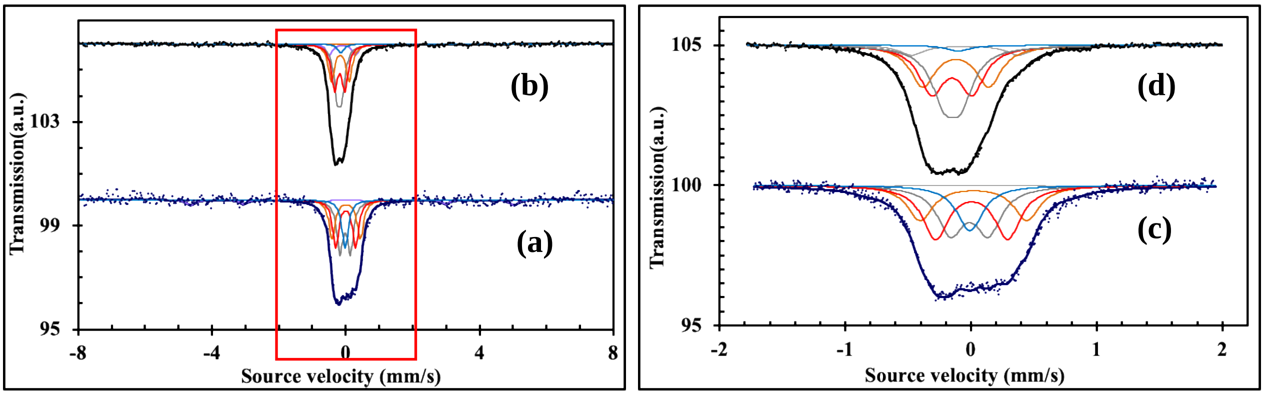

Figure 5-7. Mössbauer spectra of the P-EQ-R70hS4h and A-EQ-R70hS4h-850 powders.

5.2.3. Experimentally optimized powder

The annealing of the experimentally optimized powder (P-OE-S32h, 19% Al, 22% Cr, 34% Fe, 19% Mn, 6% Mo) was also carried out. The XRD results after annealing at 950 °C for 1 h (A-OE-S32h-950) show the disappearance of the bcc#1 phase (Fig. 5-8a, b). The major bcc#2 phase, the χ phase (also the quite high intensity of peaks), and small fractions of M_6C and $M_{23}C_6$ are detected. The lattice parameter of the bcc#2 phase is comparable to its value before annealing (Table 5-4). The SEM-BSE image (Fig. 5-8d) reveals four chemical contrasts: dark grey (bcc#2), two different light grey (χ and $M_{23}C_6$), and white spots (M_6C). The EDX mapping (Fig. B4) confirms the high-volume fraction of the χ phase enriched in molybdenum. The presence of the χ phase after heat treatment at 950 °C (A-OE-S32h-950) is very unexpected. It is quite unlikely that it is only related to the carbon content as carbon pollution is expected to be similar to that of the P-O-S32h powder. However, it cannot be excluded entirely since the contamination is a random process. The presence of the χ phase could also be related to the different chemical composition (e.g. higher iron content, lower aluminum content), which could sufficiently promote the shift of phase transformation temperature.

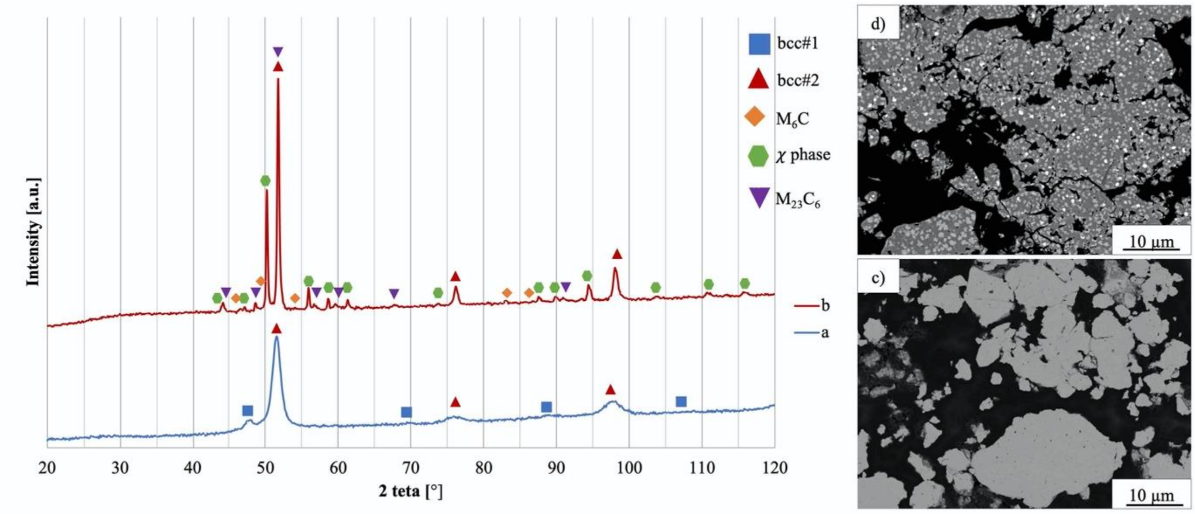

Figure 5-8. Analysis of the experimentally optimized powder. XRD patterns of a) P-OE-S32h, b) A-OE-S32h-950. SEM-BSE images of the c) P-OE-S32h, d) A-OE-S32h-950.

Table 5-4. Lattice parameter values of phases in P-OE-S32h and A-OE-S32h-950 powders.

Sample	Lattice parameter [Å]				
	bcc#1	bcc#2	χ phase	$M_{23}C_6$	M_6C
P-OE-S32h	3.13	2.91	---	---	---
A-OE-S32h-950	---	2.90	8.95	10.66	11.15

According to Mössbauer spectrometry results (Fig. 5-9, Table B3), the non-annealed P-OE-S32h powder is more homogeneous (major bcc#2 phase and minor bcc#1) than after the annealing at 950 °C for 1 h (A-OE-S32h-950) (bcc#2, χ phase, carbides), which is very surprising compared with other analyzed compositions. The Mössbauer spectra are broader, less symmetrical, and the number of different iron sites increases after the annealing. It is in good agreement with the XRD results (Fig. 5-8), which shows the multiphase structure after the heat treatment.

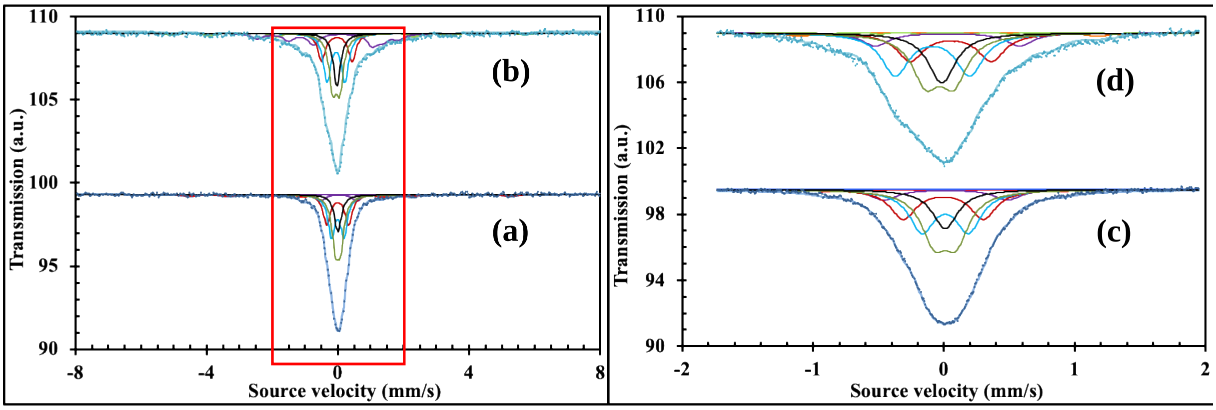

Figure 5-9. Mössbauer spectra of the experimentally optimized powder: P-OE-S32h (a, c) and A-OE-S32h-950 (b, d).

5.3. Discussion and summary

The annealing of mechanically alloyed powders is a necessary step before the sintering of powders. In this study, the complex phase transformations occurring in the powders were studied by performing heat treatments of three HEA compositions. The DSC analyses reveal several phase changes and their temperature.

The powder with the optimized composition (P-O-S32h) presents several phase transformations during annealing. The melting temperature of the major bcc#2 phase was determined at 1445 °C by DSC analysis. The heat treatment at a lower temperature (e.g., 650 or 800 °C for 1 h) leads to the disappearance of the bcc#1 phase and the formation of a high-volume fraction of the intermetallic χ phase. Further annealing, at a higher temperature, leads to the gradual disappearance of the χ phase, the formation of the molybdenum-rich M_6C (and also chromium-rich $M_{23}C_6$) and the increase of the amount of the bcc#2 phase. The transformation between the χ phase and M_6C was also suggested in the literature [120,121]. Indeed, there is a close link between these phases [120]. The χ phase, firstly described by Andrews [122], is generally not desirable, especially due to its brittleness [116,121]. A microstructure made of the major bcc phase with carbide precipitates seems to be much more beneficial. The disappearance of the χ phase and the formation of the M_6C and the increase of the volume fraction of bcc#2 should be studied further in the future to better understand this phenomenon. Vaidya *et al.* [123] found that in the CoCrFeMnNiV HEA, carbon and oxygen contaminations introduced during mechanical alloying and sintering could prevent the formation of tetragonal σ phase, commonly observed in the cast and homogenized alloy, and favor the formation of carbides and oxides, which could be more beneficial in terms of ductility. The authors explain that the formation of carbides and oxides, enriched in chromium and vanadium, leads to depletion of the main fcc phase in these elements. Therefore, the required composition to form the σ phase is not reached. It could not be excluded that the formation of carbides and oxides after annealing at a higher temperature in this study prevents the presence of the χ phase. Carbides, such as M_6C [87,114] or $M_{23}C_6$ [79,81,82,84,85,113], are commonly found in many HEA prepared by powder metallurgy. Carbon, which plays obviously a key role in the formation of carbides, also could dissolve, in smaller amounts, in the χ phase. The presence of large holes in the crystal structure allows the dissolution of carbon in the χ phase [120]. Hence, carbon contamination, introduced during mechanical alloying, can significantly affect the microstructure and the properties after annealing or sintering. The source of carbon for the milling in SPEX mill is the steel of balls and vial; the pollution could also come from materials used to weigh and prepare the mixture of powders or even from dust [70]. The contamination during mechanical alloying is inevitable; however, appropriate heat treatment could lead to the formation of carbides, which are more beneficial for mechanical properties than the brittle χ phase. Dealing with the phase transformations during the annealings of powder, the most interesting is the increase of the volume fraction of bcc#2 phase after the annealing at 950 °C compared to 800 °C, while the χ phase disappears. It should be further studied in the future. The composition of the bcc#2 phases was not measured precisely due to the small grain size of annealed powder; however, based on the presence of other phases (carbides and χ), it is sure that the chemical composition of bcc#2 phase varies depending on the heat treatment. The composition of bcc#2 is discussed more detailed in bulk samples in the next chapter. Nevertheless, it could be concluded that the powder annealed at 950 °C for 1 h (A-O-S32h-950) consists of a dominant bcc#2 phase and a small fraction of carbides (M_6C and $M_{23}C_6$).

The DSC curves of the P-EQ-R70hS4h and P-O-S32h alloys are similar with slightly shifted temperatures of phase transformations. The heat treatment of the P-EQ-R70hS4h powder, at 850 °C for 1 h, leads to the disappearance of the bcc#1 phase and the dissolution of pure manganese. Moreover, the dramatic decrease of peaks intensity of the bcc#2 phase, the formation of a high-volume fraction of the χ phase, and the M_6C carbide rich in molybdenum are observed. After the heat treatment at 950 °C for 1 h, the complete disappearance of the χ phase is found similarly to the A-O-S32h-950 annealed powder. The intensity of the bcc#2 peaks increases significantly as well as the peaks of the M_6C. Moreover, small peaks of the $M_{23}C_6$ appear. The high amount of carbides could be the effect of higher contamination in carbon, especially from stearic acid (process control agent) during mechanical alloying in the planetary mill. The high content of molybdenum, which is a strong carbide former [124], could drastically increase the ability to form the M_6C carbide, which is usually enriched in molybdenum [87,114]. Moreover, carbon could dissolve in the χ phase [120]; however, the high content of carbon could lead to an easier transformation of the χ phase into the M_6C carbide, which contains a higher content of carbon. The high content of molybdenum also seems to be preferred to form either the χ phase or the molybdenum rich M_6C carbide instead of a disorder multi-element bcc phase. The typical chemical formula of the χ phase in steels is $Fe_{36}Cr_{12}Mo_{10}$ [119]. Furthermore, the large electronegativity difference of equiatomic alloy could facilitate the formation of intermetallic compounds instead of a disorder bcc phase.

The annealing of the P-OE-S32h powder shows somewhat surprising results. The χ phase is present after heat treatment at 950 °C for 1 h (P-OE-S32h-950). There are two possible reasons for that. The small change of chemical composition, compared to the P-O-S32h powder, could result in the shift of temperature of the χ phase transformation to M_6C to a higher temperature. The lower content of molybdenum, which is a carbide former, stronger than chromium [124], can hinder the formation of molybdenum-rich carbide M_6C. The second reason could be smaller contamination by carbon for the P-OE-S32h compared to the P-O-S32h powder. Both alloys were fabricated by the same processing in SPEX for 32 h; hence, the decrease of pollution is unlikely. However, contamination is a random process, which cannot be fully controlled. Maybe, a small change in the chemical composition could affect the contamination by carbon.

In conclusion, the P-O-S32h powder mechanically alloyed in SPEX for 32 h was chosen for sintering experiments. The alloy presents a major bcc#2 phase (a = 2.91 Å) and a small fraction of carbide precipitates after annealing at 950 °C/1h (A-O-S32h-950). Moreover, it should be noted that at this temperature, no harmful χ phase was detected. The very promising feature of this powder is the high-volume fraction of disordered bcc#2. A more detailed study of bcc#2 is conducted on the bulk samples and presented in the next chapter. It seems that this alloy, with similar microstructure after sintering, could present very promising mechanical properties (e.g., high hardness and strength). The equiatomic powder shows a significant electronegativity difference, which could be beneficial to stabilize intermetallic compounds after sintering. Moreover, the alloy with equiatomic content of elements introduced to the vial (P-EQ-R70hS4h) presents much higher carbon contamination and high molybdenum content, which is a strong carbide former [124]. Both aspects lead to the formation of a high-volume fraction of carbides after annealing and probably even higher after sintering due to the contact with graphite die. The P-OE-S32h powder consists of a harmful χ phase despite having parameters in the good range, which shows that this composition, prepared in SPEX, could not be a promising candidate for obtaining an alloy with excellent mechanical properties after sintering.

6. Structure and microstructure of the bulk samples

Mainly the sintering of the optimized powder mechanically alloyed in SPEX for 32 h (P-O-S32h) was performed due to its promising microstructure (i.e., major bcc and a small fraction of carbides) obtained after thermal treatment. Three sintering temperatures were selected: 950, 1100, and 1250 °C. The lowest sintering temperature (950 °C) was chosen to prevent the formation of the χ phase, while the highest sintering (1250 °C) was selected to be below the melting points (measured by DSC of MA powder, Subsection 5.1.) of the $M_{23}C_6$ carbide (1286 °C) and the bcc#2 phase (1445 °C). The list of sintered samples is shown in Table 6-1. to present the results clearly (more details in Appendix - Names of samples).

Table 6-1. List of sintered samples.

Name of sintered samples	Name of MA powder	Sintering conditions
S-O-S32h-S950-1hV	P-O-S32h	950 °C for 1 h under vacuum
S-O-S32h-S950-1hA		950 °C for 1 h under argon
S-O-S32h-S950-2hA		950 °C for 2 h under argon
S-O-S32h-S1100-2hA		1100 °C for 2 h under argon
S-O-S32h-S1250-2hA		1250 °C for 2 h under argon
S-EQ-R70hS4h-S950-1hA	P-EQ-R70hS4h	950 °C for 1 h under argon
S-OE-S32h-S950-1hA	P-OE-S32h	950 °C for 1 h under argon

6.1. Structure of sintered optimized alloy

The XRD analyses of consolidated P-O-S32h powders reveal a significant influence of the sintering temperature on the phase formation (Fig. 6-1). All samples sintered at 950 °C present a somewhat similar structure, i.e., a major bcc#2 phase and carbides (predominant M_6C and lower volume fraction of $M_{23}C_6$) (Fig. 6-1a, b, and c). The phase ratios of different phases were not estimated by the XRD due to the impossibility to know the peak intensity of the pure new multi-element bcc#2 phase and pure multi-metallic carbides. The present phases are in agreement with the results of the A-O-S32h-950 annealed powder presented in Subsection 5.2.1. The lattice parameters of the phases are close to be found in the heat-treated powder (Table 6-2). The lattice parameters of carbides are slightly different depending on the sample. It could be due to possible differences in the composition of the metallic part of carbides and the difficulty of measuring the position of peaks because of their low intensity. The XRD result of the S-O-S32h-S1100-2hA sample reveals the presence of the bcc#2 phase similar to the samples sintered at 950 °C; however, the volume fraction of $M_{23}C_6$ carbide increases while the amount of the M_6C carbide decreases. The $M_{23}C_6$ is the predominant carbide after sintering at this temperature. Some barely noticeable peaks of Al_2O_3 appear, which could be due to the residual presence of oxygen in the furnace chamber or due to the contamination by oxygen during mechanical alloying. The lattice parameter of the bcc#2 phase is slightly smaller than the one found in the samples sintered at 950 °C. The results of the S-O-S32h-S1250-2hA sample show the presence of the major bcc#2 phase without substantial change of lattice parameter compared to the samples sintered at lower temperatures (Table 6-2). It should be noted that a small fraction of the powder has melted during sintering at 1250 °C for 2 h. This powder is kept inseparably glued to the die and punch and therefore was not analyzed. This could be related to a partial fusion of $M_{23}C_6$ carbide. The DSC analysis (see Subsection 5.1.) shows the $M_{23}C_6$ melting temperature at 1286 °C; however, a longer incubation time and higher carbon content could probably slightly decrease the melting temperature. The major carbide $M_{23}C_6$ and a smaller volume fraction of M_6C are present, which is similar to the S-O-S32h-S1100-2hA sample. The low peaks of Al_2O_3 are also noticed, which is due to the high affinity of aluminum to oxygen. It should be noted that the χ phase, which was found after annealing of powder at 650 and 800 °C for 1 h (A-O-S32h-650 and A-O-S32h-800, see Subsection 5.2.1.), was not detected in any sintered samples. The presence of the intermetallic $AlMo_3$ or σ phase or the intermetallic type Cr_3Si (A15), which were predicted by CALPHAD calculations by Senkov et al. [22] and by our calculations, were not confirmed by XRD.

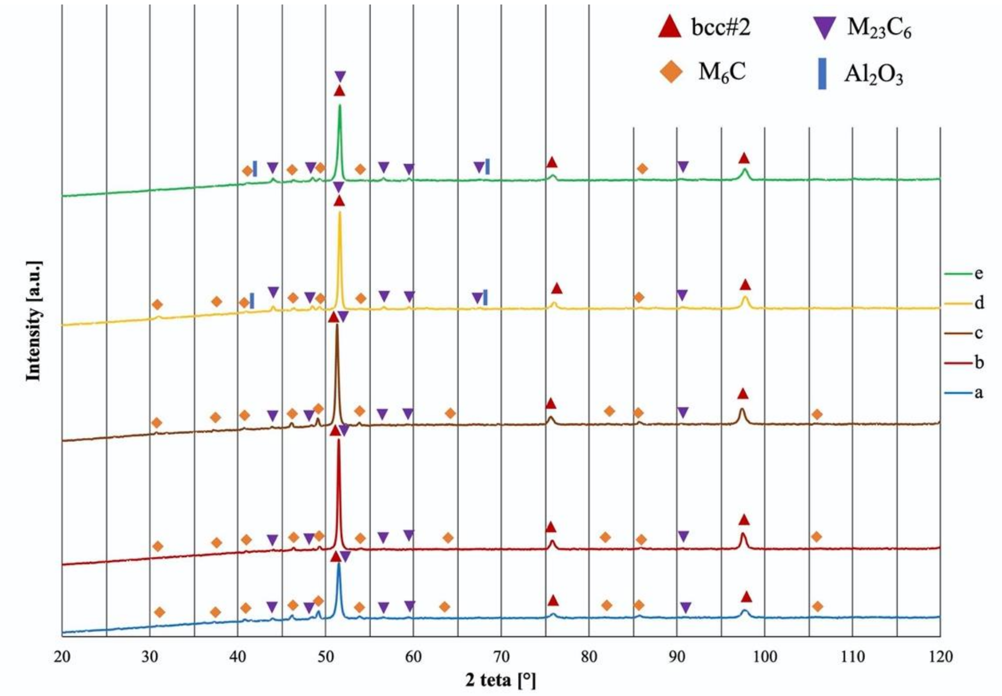

Figure 6-1. XRD patterns of the sintered optimized alloy: a) S-O-S32h-S950-1hV, b) S-O-S32h-S950-1hA, c) S-O-S32h-S950-2hA, d) S-O-S32h-S1100-2hA, e) S-O-S32h-S1250-2hA.

Table 6-2. Lattice parameters of phases formed during sintering of the P-O-S32h powder.

Sample	Lattice parameters [Å]		
	bcc#2	M_6C	$M_{23}C_6$
S-O-S32h-S950-1hV	2.92	11.17	10.69
S-O-S32h-S950-1hA	2.92	11.16	10.68
S-O-S32h-S950-2hA	2.92	11.18	10.69
S-O-S32h-S1100-2hA	2.91	11.16	10.67
S-O-S32h-S1250-2hA	2.91	11.15	10.68

6.2. Microstructure of sintered optimized alloy

6.2.1. Scanning electron microscopy with EDX analysis

The SEM analyses were performed in the central region of the cross-section of samples and in the areas close to the sample surface, which was in contact with graphite foils during sintering and therefore, could present different microstructure.

6.2.1.1. Areas in the center of the cross-sections of samples

SEM-BSE analyses (Fig. 6-2) reveal significant differences in microstructure between studied samples. The exact chemical composition of phases was measured by TEM-EDX and is presented in Subsection 6.2.3. The bcc#2 (dark grey contrast) is the major phase in all sintered samples, which is in agreement with the XRD results (see Subsection 6.1.) and confirms the findings of the A-O-S32h-950 annealed powder (see Subsection 5.2.1.). The χ, $AlMo_3$, and other intermetallics are not present in the sintered samples.

The samples sintered at 950 °C (Fig. 6-2a-c) consist, besides the major bcc#2 phase, of carbides M_6C and $M_{23}C_6$. The light precipitates significantly enriched in molybdenum (Fig. 6-3 and Figs. C1 and C2) are associated with the M_6C carbide, which is usually molybdenum-rich in the literature [87,114]. The M_6C carbide is predominant in all samples sintered at 950 °C; however, its distribution varies significantly depending on the region of analysis. It is believed that it is related to the randomness of the contamination phenomena during mechanical alloying. The powder particles are contaminated by a different amount of carbon during MA. It seems that the atmosphere, either vacuum or argon, does not play an important role in the microstructure of the sintered sample at 950 °C. Argon is an inert gas and thus does not react with powder during sintering. The longer sintering time could probably enhance the diffusion of carbon from graphite die and therefore promotes the formation of carbides [51]. The small fraction of the $M_{23}C_6$ carbide, which is often chromium-rich according to the literature [51,73,79,81–83,85,113], is also revealed by EDX analyses (Fig. 6-3 and Figs. C1 and C2). The presence of Al_2O_3 could not be unambiguously confirmed by SEM-EDX studies. The zones enriched in aluminum, visible in Fig. 6-3, could be related to an artifact (presence of holes – porosity), to the presence of alumina or both phenomena simultaneously. Analyses with better resolution, such as EBSD or TEM, were conducted to confirm the formation of Al_2O_3 (Subsections 6.2.2. and 6.2.3.3.). The formation of Al_2O_3 [74,85] or other oxides [78,83,125] is a common phenomenon in sintered HEAs. The porosity is also frequently observed in sintered samples [79,83,87,104].

SEM analyses of the S-O-S32h-S1100-2hA sample reveal a significantly different microstructure (Fig. 6-2d). Nevertheless, the bcc#2 phase is still predominant. The molybdenum-rich M_6C carbide almost disappeared after sintering at 1100 °C (Fig. C3). The major carbide is the chromium-rich $M_{23}C_6$. In the literature, the M_6C is believed to be more stable at higher levels of temperature than the $M_{23}C_6$ carbide [126]. However, in this study, other effects could enhance the transformation of the M_6C into the $M_{23}C_6$ carbide. The M_6C seems to be formed from the χ phase (enriched in molybdenum). As mentioned earlier, in the literature, the close link between the M_6C carbide and the χ phase was suggested. The sintering at 1100 °C enables faster diffusion of carbon from the graphite die towards the sample, which could enhance the transformation because $M_{23}C_6$ contains more carbon than M_6C. Moreover, the overall higher content of chromium than molybdenum could be beneficial in the formation of the chromium-rich $M_{23}C_6$ carbide. The zones enriched in aluminum in Fig. C3 suggest the formation of Al_2O_3, further analyses by EBSD and TEM were conducted to confirm the phenomenon. The volume fraction of black spots, which are related to porosity, seems to be higher for the S-O-S32h-S1100-2hA sample (Fig. 6-2d), than for samples sintered at 950 °C (Fig. 6-2a-c). It could be related to the coalescence at higher temperatures of the nano-porosity that existed already in samples consolidated at lower temperatures or to the formation of new pores (due to release of oxygen from the powder particles) or even to the extraction loss of alumina particles during polishing or to the phenomenon related to the thermal stresses.

SEM analyses of the S-O-S32h-S1250-2hA sample (Fig. 6-2e) reveal some similarities with the S-O-S32h-S1100-2hA sample. The volume fraction of the bcc#2 phase seems to decrease slightly compared to the S-O-S32h-S1100-2hA sample. The content and grain size of the predominant chromium-rich $M_{23}C_6$ carbides are much larger, which could be related to the faster diffusion of carbon from the graphite die during sintering at this temperature. The volume fraction of the molybdenum-rich M_6C carbide is still very low. It should be noted that the content of molybdenum in the $M_{23}C_6$ is higher than in the matrix bcc#2 phase (it is discussed in detailed based on the TEM-EDX analyses in Subsections 6.2.3.1. and 6.2.3.2.). The regions enriched in aluminum are much larger than in samples sintered at a lower temperature, suggesting a significant alumina formation (Fig. 6-4). The phenomena resulting in the visibility of many black spots, such as coalescence of nano-porosity, formation of new pores due to thermal stresses, are more important at 1250 °C. The volume fractions of phases were analyzed by EBSD and discussed in Subsection 6.2.2. The compositions of phases were measured by TEM-EDX and discussed in Subsection 6.2.3.

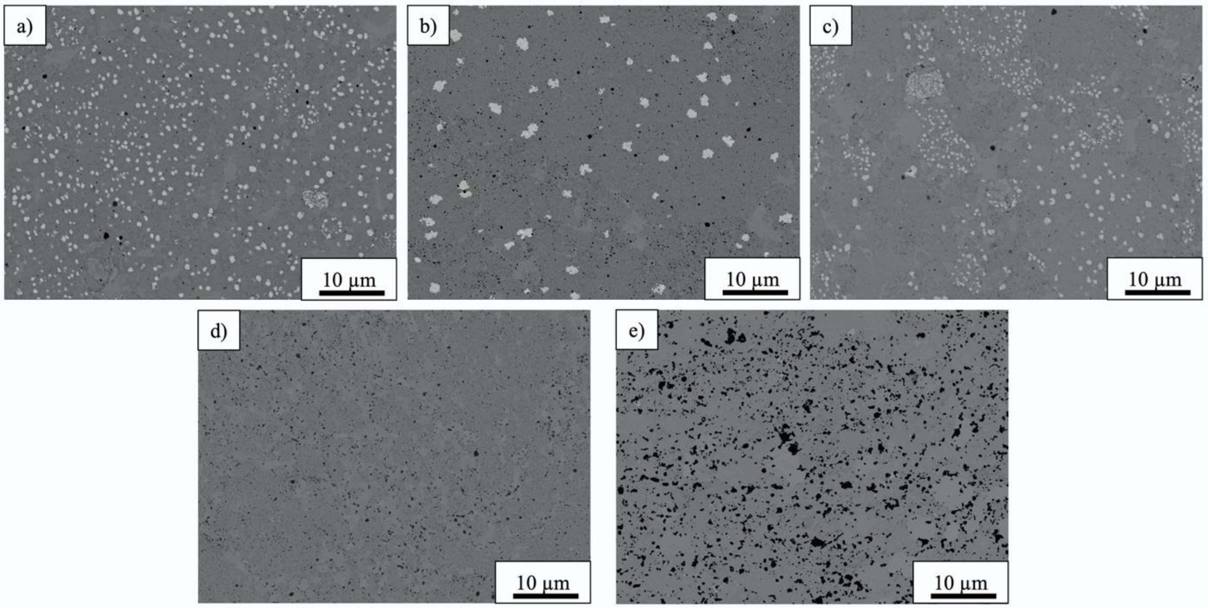

Figure 6-2. SEM-BSE images of the cross-section center in the optimized alloy samples sintered under different conditions: a) S-O-S32h-S950-1hV, b) S-O-S32h-S950-1hA, c) S-O-S32h-S950-2hA, d) S-O-S32h-S91100-2hA e) S-O-S32h-S1250-2hA.

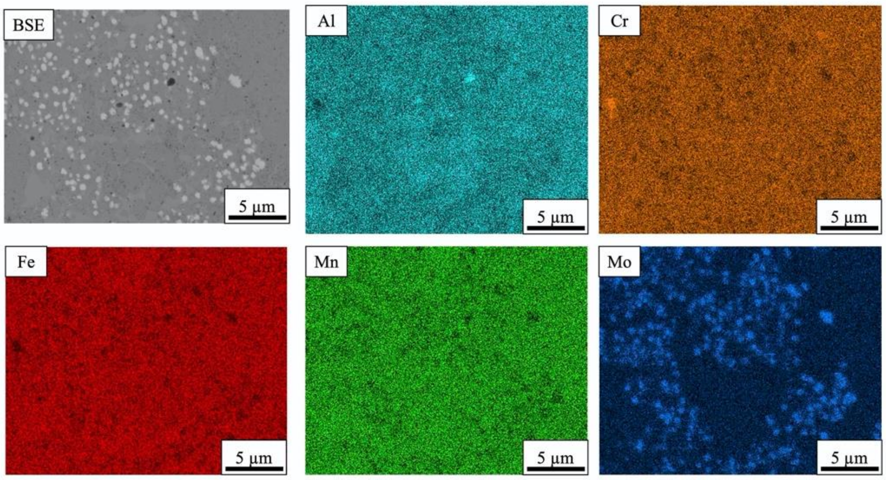

Figure 6-3. SEM-BSE image with corresponding EDX mapping in the central area of the S-O-S32h-S950-2hA sample.

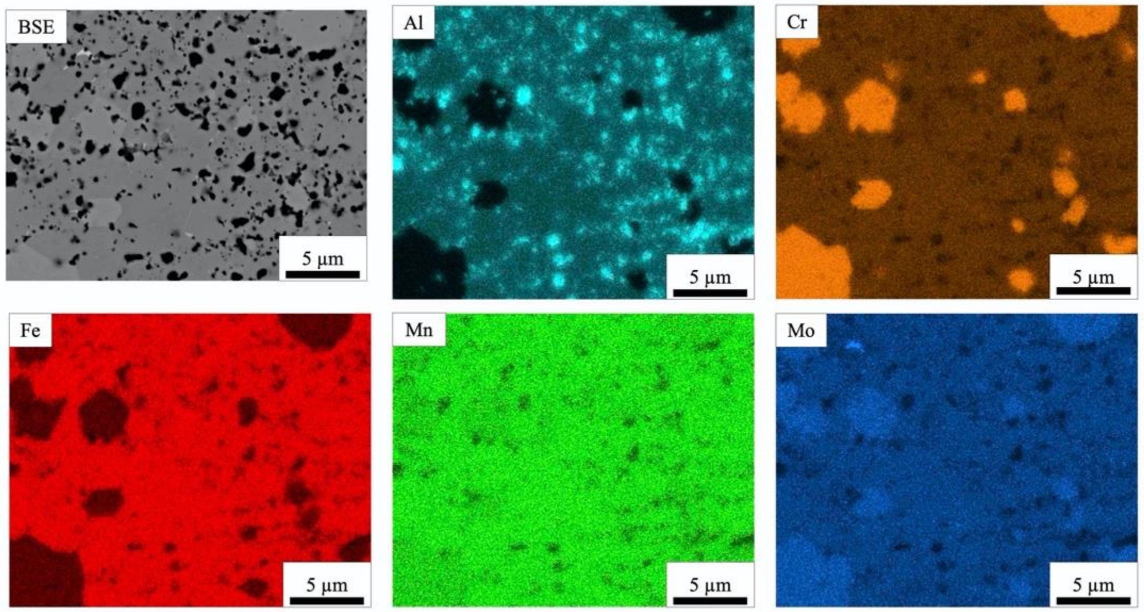

Figure 6-4. SEM-BSE image with corresponding EDX mapping in the central area of the S-O-S32h-S1250-2hA sample.

6.2.1.2. Areas close to the surface of samples

The analyses of regions close to the surface, which were in contact with the graphite die during sintering, were also conducted. The severe contamination by carbon in these regions was reported in the literature [51,73]. In this study, Figure 6-5 reveals a significantly higher volume fraction of carbides close to the surface than in the central region of each sample (Fig. 6-2). The volume fraction of carbides decreases gradually from the surface towards the center of the sample. The strict boundary between surface and core does not exist; however, the region with a significant amount of carbides was estimated up to 80 µm from the surface for the S-O-S32h-S950-1hV sample (Fig. 6-5b) and a few hundred microns (300 – 400 µm) for the S-O-S32h-S1100-2hA sample (Fig. 6-5c, d).

The analyses of the samples sintered at 950 °C reveal the formation of high-volume fraction of both carbides (Fig. 6-5a, b, Fig. 6-6, Figs. C4, and C5). In the central region, the predominant carbide is molybdenum-rich M_6C, while in the surface region, both carbides (M_6C and $M_{23}C_6$) present a somewhat similar volume fraction because of the effect of the high carbon content due to the diffusion from the graphite die. The sufficiently high carbon content enables the formation of both carbides simultaneously, including $M_{23}C_6$, which needs a higher amount of carbon than M_6C.

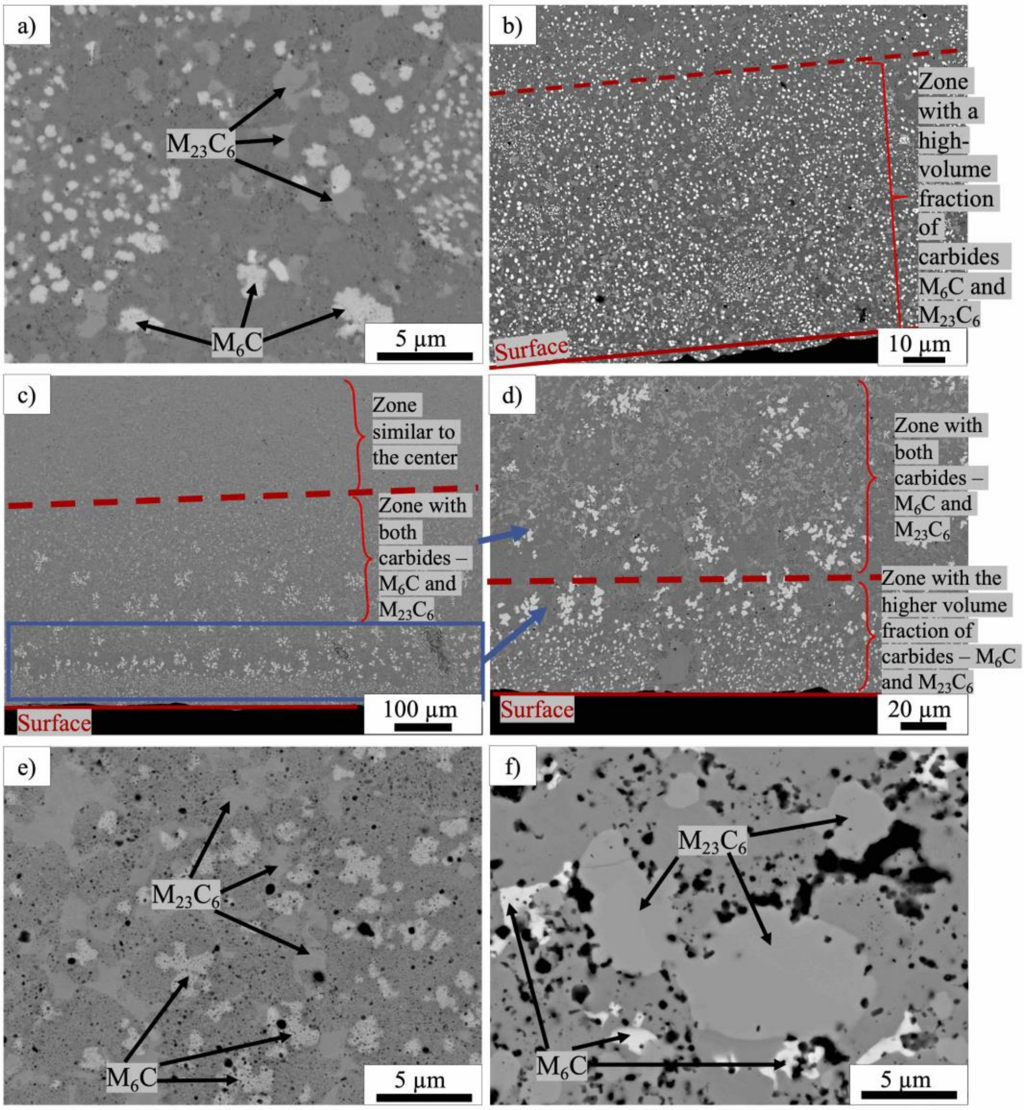

Figure 6-5. SEM-BSE images revealing carbides in areas close to the surface in the sintered samples: a) S-O-S32h-S950-2hA, b) S-O-S32h-S950-1hV (low magnification), c and d) S-O-S32h-S1100-2hA (low magnification), e) S-O-S32h-S1100-2hA, f) S-O-S32h-S1250-2hA.

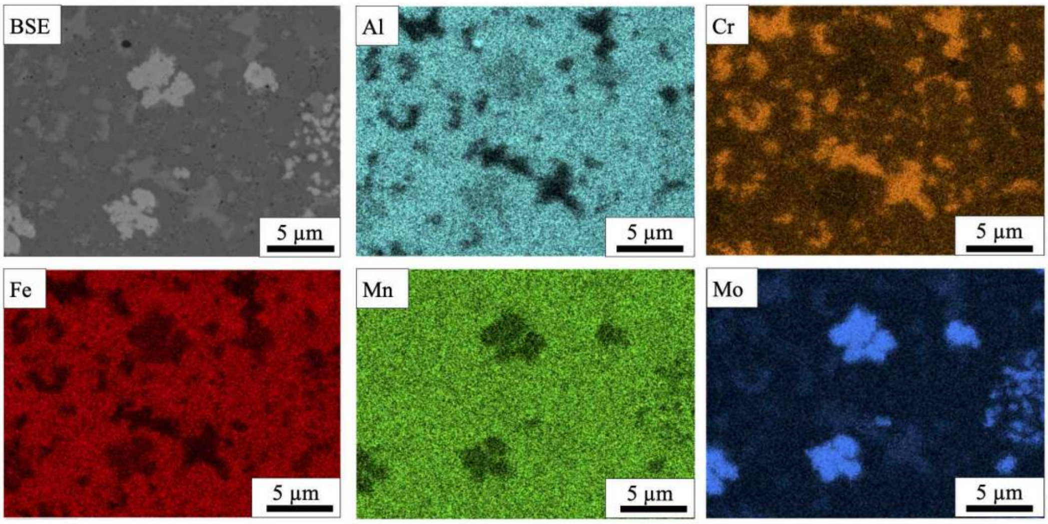

Figure 6-6. SEM-BSE image with corresponding EDX mapping showing region close to the surface of the S-O-S32h-S950-2hA sample.

The region close to the surface of the S-O-S32h-S1100-2hA sintered sample presents similarities with that of the samples sintered at 950 °C. Both types of carbides (M_6C and $M_{23}C_6$) are present (Fig. 6-5e). However, the region with a high fraction of both types of carbides is much larger than for the samples sintered at 950 °C. In Figure 6-5c and d, the zones with a decreasing amount of the molybdenum-rich M_6C carbide towards the sample core could be noticed. However, the predominant carbide seems to be the chromium-rich $M_{23}C_6$ (Fig. C6), even in the very first zone in the vicinity of the surface. Nevertheless, the volume fraction of the molybdenum-rich M_6C carbide is much higher than in the central region of the sample. The reason for the coexistence of both carbides is similar as for the samples consolidated at 950 °C. The diffusion of carbon is much easier at a higher consolidation temperature, and consequently, the zone with a high fraction of both types of carbides is significantly larger. The sufficient carbon content enables the formation of the $M_{23}C_6$ without the destruction of the M_6C.

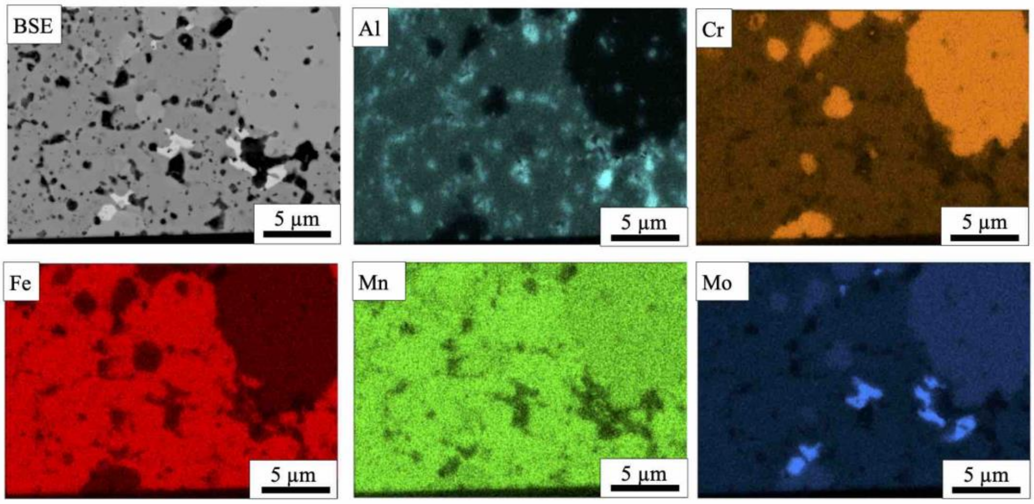

Figure 6-7. SEM-BSE image with corresponding EDX mapping showing region close to the surface of the S-O-S32h-S1250-2hA sample.

The region close to the surface of the S-O-S32h-S1250-2hA sample presents similarities with other sintered samples, i.e., both carbides (M_6C and $M_{23}C_6$) are present in a high-volume fraction (Fig. 6-5f). It is related to high contamination by carbon in these regions, which favors the coexistence of the M_6C and $M_{23}C_6$ carbides. The large grains of chromium-rich $M_{23}C_6$ are dominant over smaller grains of the molybdenum-rich M_6C (Fig. 6-7). The presence of black spots, attributed to the porosity and Al_2O_3, is similar to the central region of the sample. The analysis of areas close to the surface brings interesting insights into the phenomenon of carbon contamination coming from the graphite die. In the literature dealing with the sintering of HEAs, the contamination in the close to the surface region is not often discussed [79,85]. Nevertheless, it should be noted that areas with a significantly higher volume fraction of carbides are relatively small compared to the whole volume of the sample and the multi-element bcc#2 phase is also always present close to the surface. Therefore, all other studies focused on the core part.

6.2.2. Electron backscatter diffraction analysis

The EBSD analyses were conducted to determine the grain size in sintered samples, to confirm the phases detected by XRD, and to calculate their volume fractions. The spatial resolution of the EBSD can be considered about a few dozen nanometers, which is much better compared with the micrometer resolution of the SEM-EDX. In other words, the EBSD analyses provide more accurate data about phase ratio and its distributions.

The EBSD phase images (Fig. 6-8) show results with good agreement with XRD and SEM. The most predominant phase in all bulk samples is the multi-element bcc#2. The volume fraction of bcc#2 is above 95 % for samples consolidated at 950 and 1100 °C, and slightly lower for the sample sintered 1250 °C due to an easier diffusion of carbon at a higher temperature, and therefore, an increase of the carbide volume fraction (Table 6-3). The predominant carbide after consolidation at 950 °C is the molybdenum-rich M_6C carbide, even though a few chromium-rich grains of $M_{23}C_6$ were detected (Fig. 6-8a, b). The slight difference of volume fractions of carbides and bcc#2 between the samples consolidated at 950 °C (Table 6-3) is rather the effect of the randomness of the contamination during mechanical alloying than the result of sintering conditions (atmosphere or duration). The predominant carbide after consolidation at 1100 and 1250 °C is the chromium-rich $M_{23}C_6$ (Table 6-3), while only a very few grains of the M_6C carbide were detected (Fig. 6-8c, d). It confirms the XRD and SEM results, which show that M_6C transforms into $M_{23}C_6$ at higher temperatures. The presence of fine grains of alumina was detected in all bulk samples; however, the significant increase of its volume fraction occurs during sintering at 1250 °C (S-O-S32h-S1250-2hA). The higher temperature leads to an easier formation of Al_2O_3 from residual oxygen in the furnace chamber and introduced during mechanical alloying. In the literature, the formation of nanosized Al_2O_3 occurred during the sintering of mechanically alloyed HEAs by hot-press sintering at 900 °C [85] or by SPS at 1100 °C [74]. The porosity is present in all consolidated samples. The nano-porosity, which is difficult to detect even by EBSD, is undoubtedly present in the samples sintered at 950 °C. During the sintering at higher temperatures, grains grow at the same time as pores grow. It results in more visible pores after consolidation at 1100 °C (Fig. 6-8c). The coalescence of the porosity is particularly visible after sintering at 1250 °C (Fig. 6-8d), which is also revealed by SEM observations (Subsection 6.2.1.). The pore coalescence during sintering was also reported in the literature [127].

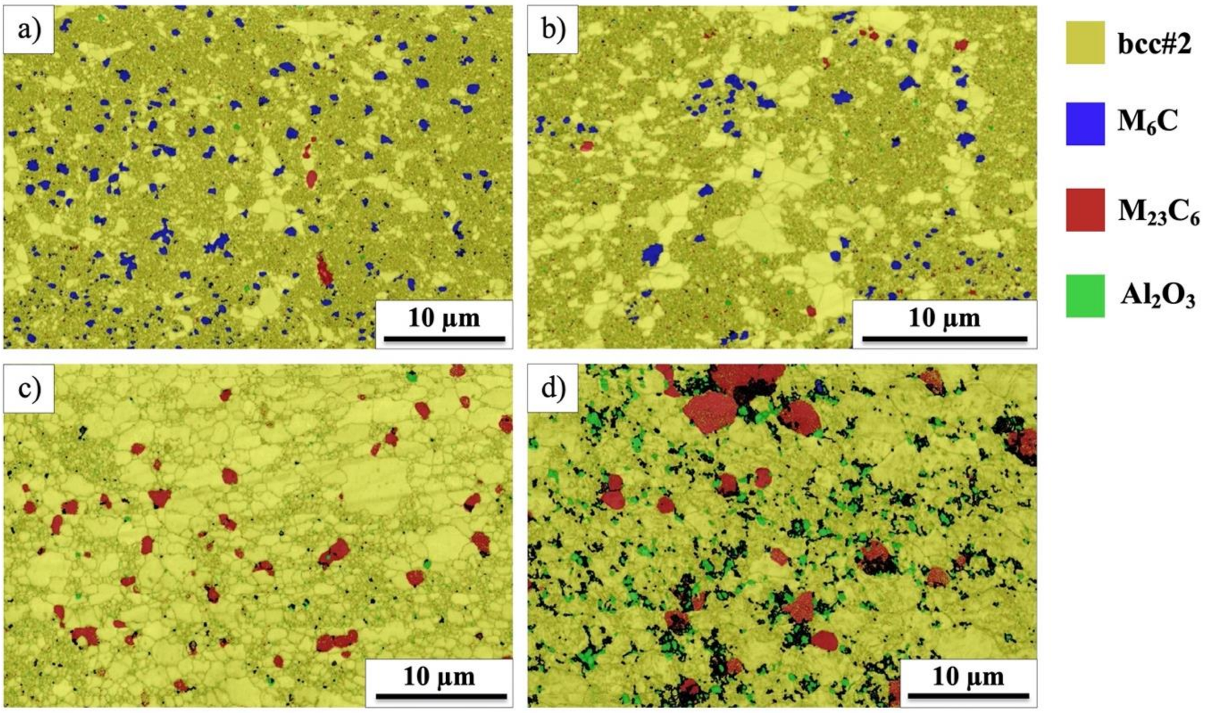

Figure 6-8. EBSD phase images of the optimized alloy sintered samples: a) S-O-S32h-S950-1hV, b) S-O-S32h-S950-2hA, c) S-O-S32h-S1100-2hA, d) S-O-S32h-S1250-2hA.

The grain size of phases, especially of the multi-element bcc#2 phase and the $M_{23}C_6$ chromium-rich carbide, varies significantly depending on the sintering conditions (temperature). In brief, a higher consolidation temperature causes an increase in grain size (Fig. 6-9). The mean grain size of bcc#2 in the samples S-O-S32h-S950-1hV and S-O-S32h-S950-2hA is almost similar (Table 6-3). On the other hand, the observation of EBSD phase images (Fig. 6-8a, b) could lead to the misleading impression that grains of the S-O-S32h-S950-2hA sample (Fig. 6-8b) are bigger than those of the S-O-S32h-S950-1hV sample (Fig. 6-8a). The detailed analysis of the grain size distribution showed in Fig. 6-10, reveals that in the S-O-S32h-S950-2hA sample, some grains grow rapidly and thus easily catch our attention. The vast majority of grains of both samples are so small that their outline cannot be seen on the EBSD phase map. Moreover, the S-O-S32h-S950-2hA sample presents a higher volume fraction of the smallest grains (0-0.20 µm), which contributes significantly to balance the influence of bigger grains (> 0.61 µm) on the mean grain size. Hence, the duration of sintering at 950 °C, either 1 or 2 h, has no essential effect on the mean grain size. The more significant abnormal grain growth observed in the S-O-S32h-S950-2hA sample could be related to a lower volume of nanosized carbides in the analyzed area. Carbides could play an essential role in inhibiting grain growth [73,94].

Table 6-3. Summary of the EBSD results of the optimized sintered alloy: mean grain size, standard deviation, and phase ratio.

Sample	Phase	Mean grain size [µm]	Standard deviation [µm]	Volume fraction [%]
S-O-S32h-S950-1hV	bcc#2	0.23	0.11	95.65
	M_6C	0.29	0.15	3.91
	$M_{23}C_6$	0.25	0.14	0.35
	Al_2O_3	0.25	0.11	0.09
S-O-S32h-S950-2hA	bcc#2	0.22	0.13	98.34
	M_6C	0.27	0.16	1.03
	$M_{23}C_6$	0.20	0.08	0.39
	Al_2O_3	0.23	0.12	0.24
S-O-S32h-S1100-2hA	bcc#2	0.43	0.36	96.79
	M_6C	0.00	0.00	0.00
	$M_{23}C_6$	0.38	0.29	2.98
	Al_2O_3	0.24	0.13	0.22
S-O-S32h-S1250-2hA	bcc#2	0.51	0.68	88.91
	M_6C	0.27	0.13	0.03
	$M_{23}C_6$	0.58	0.71	5.82
	Al_2O_3	0.27	0.12	5.25

The grain size of the M_6C carbide is similar for the sintering temperatures of 950 °C (1 or 2 h) and 1250 °C (Table 6-3). Nevertheless, it should be noted that above 950 °C, the M_6C carbide is mostly replaced by the $M_{23}C_6$, and therefore its volume fraction is too low to make a firm conclusion. The $M_{23}C_6$ carbide grains grow with increasing consolidation temperature from 0.20 µm to 0.58 µm (Fig. 6-9). Furthermore, at the sintering at 1250 °C, a relatively high phase ratio of large grains (> 1.21 µm) of the chromium-rich carbide was detected (Fig. 6-10). The grain size of Al_2O_3 in all sintered samples is similar – about 0.25 µm. The alumina grains do not grow, but their volume fraction increases significantly with temperature (Table 6-3). The oxide particles, similar to carbides, can inhibit grain growth by the Zener pinning effect [73,125].

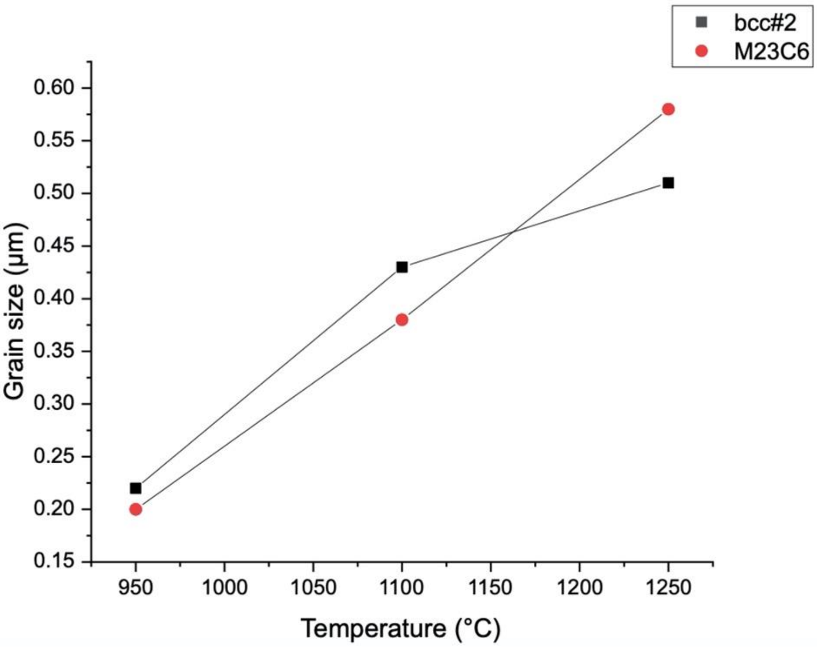

Figure 6-9. Grain size of the bcc#2 phase and the $M_{23}C_6$ carbides in the optimized alloy samples as a function of the sintering temperature for 2 h.

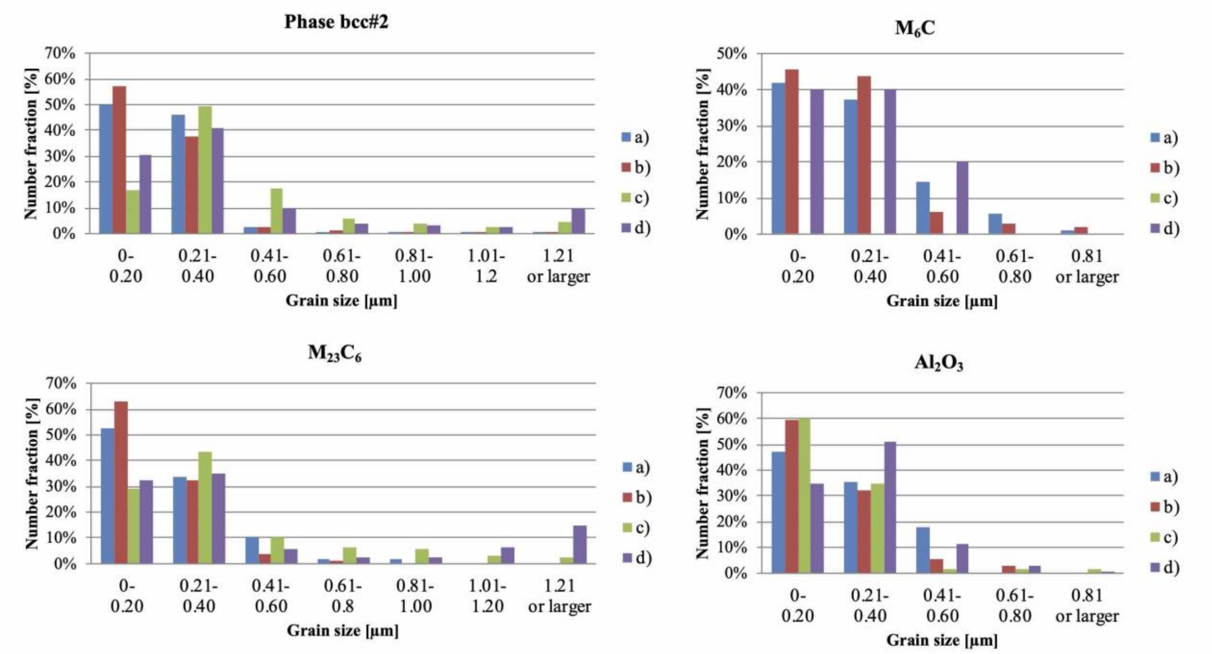

Figure 6-10. Histograms of grain size of phases (bcc#2, M_6C, $M_{23}C_6$, Al_2O_3) in the optimized sintered alloy: a) S-O-S32h-S950-1hV, b) S-O-S32h-S950-2hA, c) S-O-S32h-S1100-2hA, d) S-O-S32h-S1250-2hA.

6.2.3. Transmission electron microscopy analysis

TEM observations were performed to confirm the crystallographic structure of phases found by XRD and EBSD, as well as to evaluate the grain size. Moreover, TEM-EDX analyses were carried out to measure the chemical composition of each phase precisely thanks to a better resolution than SEM-EDX.

The observations of the S-O-S32h-S950-1hV alloy (Fig. 6-11a) show a phase composition in good agreement with results based by other techniques. The presence of molybdenum rich M_6C carbides and the multi-element bcc#2 phase was confirmed and will be discussed in detail later. Most of the grains are very small (< 200 nm); however, a few significantly larger grains (up to 1 µm) were detected. It is the effect of abnormal grain growth. The phenomenon is also revealed by EBSD (Subsection 6.2.2.). The observations of the S-O-S32h-S1100-2hA sample show a significant grain growth (Fig. 6-11b). The predominant phase is bcc#2. The grains of molybdenum-rich M_6C carbide disappeared almost completely, while the grains of chromium-rich $M_{23}C_6$ carbide formed. The pores become bigger and, therefore, much more visible on the images. The observations of the S-O-S32h-S1250-2hA reveal further grain growth. The multi-element bcc#2 phase is still predominant; however, big grains of the chromium-rich $M_{23}C_6$ carbides could be easily found. The pores are much bigger than for other sintered samples. Small grains of alumina could be easily detected. TEM results are in good agreement with XRD, SEM, EBSD results.

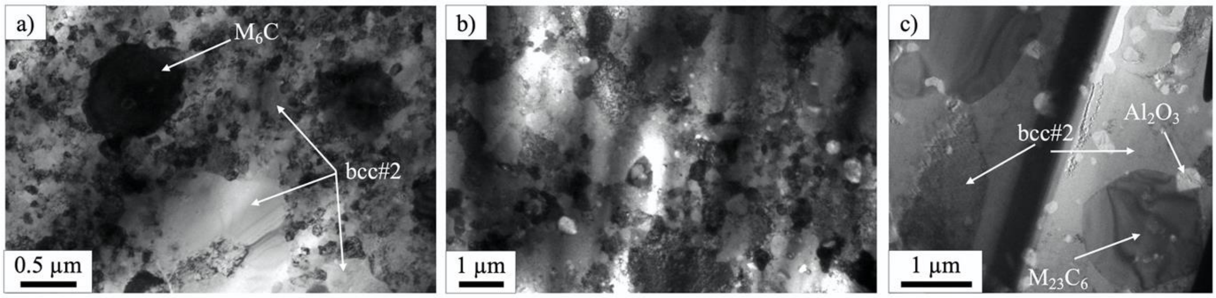

Figure 6-11. TEM bright-field images of the structure of the sintered optimized alloy: a) S-O-S32h-S950-1hV, b) S-O-S32h-S1100-2hA, c) S-O-S32h-S1250-2hA.

The STEM image with corresponding EDX mapping of the S-O-S32h-S950-1hV sample (Fig. 6-12) is in good agreement with SEM and EBSD analyses (Subsections 6.2.1. and 6.2.2., respectively). The molybdenum-rich precipitates attributed to M_6C carbide are present. The multi-element bcc#2 phase, which consists of all alloy elements, is the predominant phase. The distribution of elements in grains of bcc#2 phase is rather homogenous. Some very small regions enriched in chromium could be related to the chromium-rich $M_{23}C_6$ carbides.

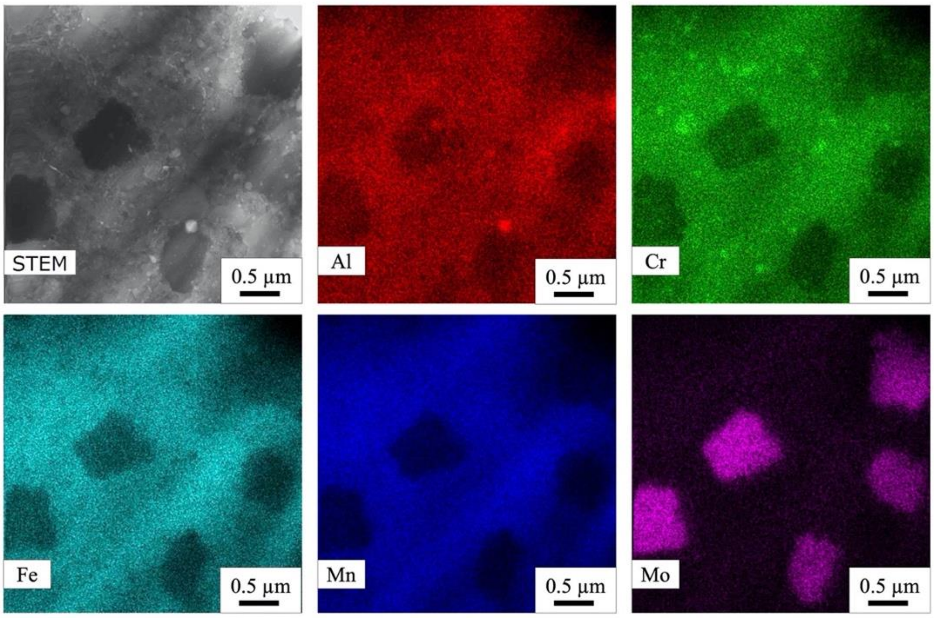

Figure 6-12. STEM image and corresponding EDX mapping of the S-O-S32h-S950-1hV sample.

6.2.3.1. Major body centered cubic phase

The bcc#2 with lattice parameter 2.91–2.92 Å is the predominant phase in all sintered samples from the optimized powder (P-O-S32h) according to the XRD results. The SAED patterns were acquired to confirm the bcc structure of the major phase. The TEM-EDX was performed to measure the chemical composition of the bcc#2 accurately.

SAED patterns of bcc#2 grains of the S-O-S32h-S950-1hV alloy were performed in three zone axis (ZA) ([111], [001], [101]). The patterns were analyzed in the Zero-Order Laue Zone (ZOLZ) and in the First-Order Laue Zone (FOLZ) to confirm the body-centered cubic structure of the major phase undoubtedly. Data were analyzed using the “Atlas of Electron Diffraction Zone-Axis Patterns” [128]. Based on the results of ZOLZ shown in Fig. 6-13, coupled with FOLZ shown in Fig. C7, it could be concluded that the major phase presents a bcc structure. It is in perfect agreement with the XRD results of annealed powder (Subsection 5.2.1.) and bulk samples (Subsection 6.1.). The TEM-SAED analyses confirm a similar bcc#2 lattice parameter as the one determined by XRD; however, the values calculated from the electron diffraction present significantly larger error than calculated based on the XRD. Therefore, the exact values are not listed here. Convergent-Beam Electron Diffraction (CBED) and Precession Electron Diffraction (PED) should be carried out carefully to confirm the space group of the phase [129,130]. Both techniques proved to be very challenging for the investigated sample (small grain size and multiphase structure) and hence were not performed in this study. However, based on the space group of pure iron, chromium, and molybdenum, which are the major elements in the bcc#2 phase, the most probable space group is $Im\bar{3}m$ (229), which is compatible with TEM results.

The average composition of bcc#2 grains, based on data showed in Table 6-4 and EDX analyses of random bcc#2 grains (at least ten not shown here), is $Al_{19}Cr_{22}Fe_{34}Mn_{19}Mo_6$. The chemical composition varies slightly between the grains. Based on the above results, the mechanical alloying and annealing of a powder of initial 19% Al, 22% Cr, 34% Fe, 19% Mn, 6% Mo composition, corresponding to the bcc#2 phase, were performed. This composition is named as experimentally optimized. The purpose was to prepare the powder in which chemical composition ensures the formation of a single bcc structure. The results of MA and thermal stability of the powder are discussed in Subsection 4.1.3. and 5.2.3., respectively.

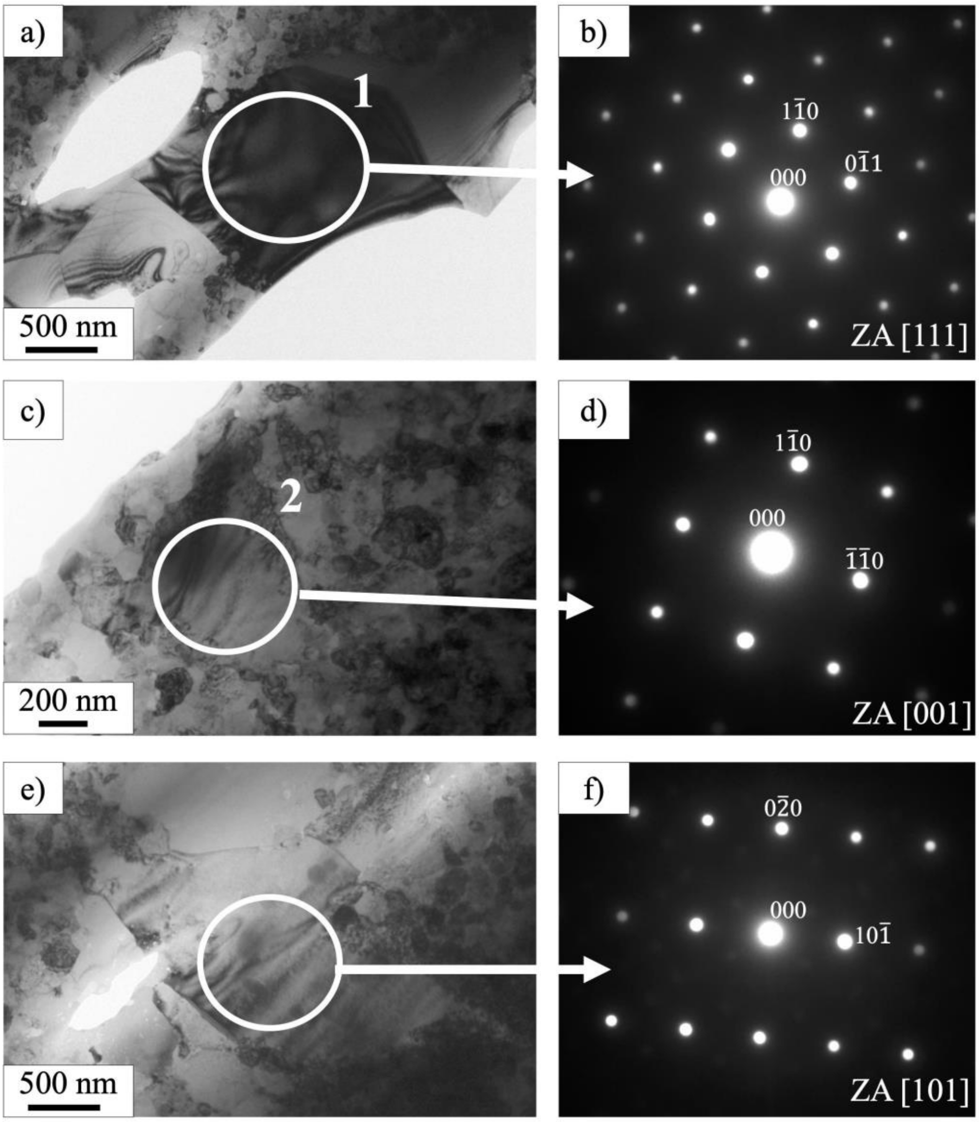

Figure 6-13. TEM bright-field images of bcc#2 grains (a, c, e) with corresponding SAED patterns (b, d, f) of the S-O-S32h-S950-1hV sample in three zone axis (ZA).

Table 6-4. Chemical composition of bcc#2 grains shown in Fig. 6-13 measured by TEM-EDX.

Region	Composition [at. %]				
	Al	Cr	Fe	Mn	Mo
1	19	21	34	19	7
2	19	22	34	19	6

TEM analyses of the bcc#2 phase in the S-O-S32h-S1100-2hA sample (Fig. 6-14) confirm the body-centered cubic structure with a similar lattice parameter as the one obtained by XRD. The chemical composition of the bcc#2 grain, shown in Figure 6-14, measured by EDX is $Al_{18}Cr_{20}Fe_{34}Mn_{20}Mo_8$, which is close to the composition of the bcc#2 grains of the sample sintered at the lower temperature (S-O-S32h-S950-1hV). The slight decrease of aluminum and chromium could be attributed to the formation of a higher volume fraction of chromium-rich $M_{23}C_6$ carbide and alumina.

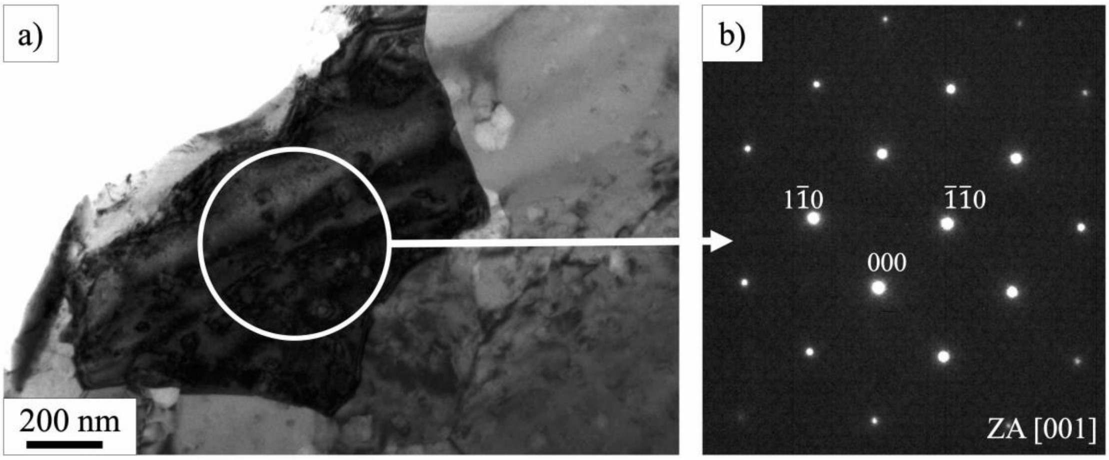

Figure 6-14. TEM bright-field image of bcc#2 grain with the corresponding SAED pattern of the S-O-S32h-S1100-2hA sample.

The analyses of the bcc#2 phase in the S-O-S32h-S1250-2hA sample (Fig. 6-15) confirm the body-centered structure of the predominant phase with similar lattice parameter to those measured by XRD in the sample sintered at 1250 °C and found in other bulk samples. The composition of the bcc#2 grain showed in Fig. 6-15 measured by EDX is $Al_{18}Cr_{14}Fe_{44}Mn_{19}Mo_5$. The significant increase of iron content in the bcc#2 phase is the effect of the decrease of other elements. The formation of a higher volume fraction of alumina and chromium-rich $M_{23}C_6$ carbide leads to the reduction of aluminum and chromium content, respectively. The molybdenum content in the $M_{23}C_6$ carbide is higher than in the bcc#2 phase (it is discussed later), and, as a consequence, the molybdenum content is lower in the bcc#2 phase. A decrease of the manganese to iron ratio is probably the result of the sublimation of manganese during sintering, which is more significant at 1250 °C than at lower temperatures. The manganese sublimation during sintering was also observed in the literature [131,132].

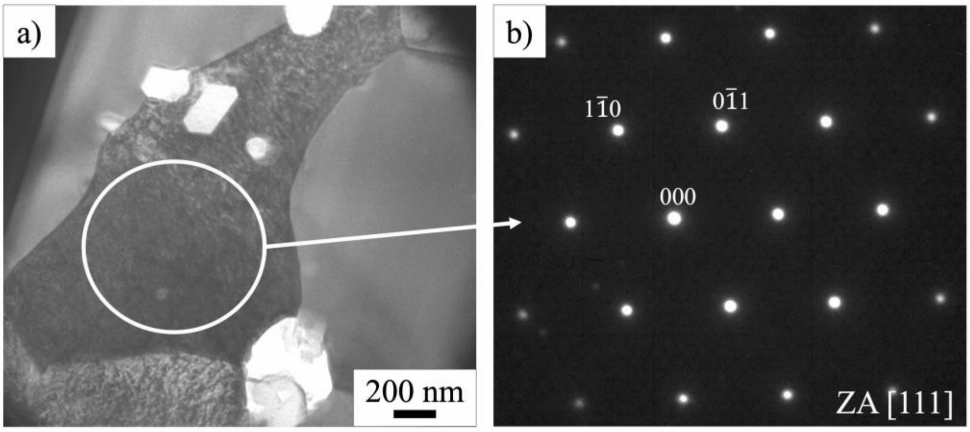

Figure 6-15. TEM bright-field image of the bcc#2 grain with the corresponding SAED pattern of the S-O-S32h-S1250-2hA sample.

6.2.3.2. Carbides precipitates

Two types of carbides were found using XRD, SEM, and EBSD in bulk samples. The molybdenum-rich M_6C carbide is present mainly in samples sintered at 950 °C, while the chromium-rich $M_{23}C_6$ is present particularly after sintering at 1100 and 1250 °C. The chemical composition of multi-element carbides was measured using TEM-EDX (without quantifying carbon). SAED patterns were acquired to confirm the crystallographic structure of carbides.

TEM analyses, coupled with SAED, confirm the face-centered cubic structure of the M_6C carbide (Fig. 6-16a, b). The lattice parameter is about 11.15 Å. It is in good agreement with XRD results of annealed powder (Subsection 5.2.1.) and bulk samples (Subsection 6.1.). TEM-EDX reveals a high content of molybdenum in the carbides in the S-O-S32h-S950-1hV sample; however, other elements are also present (Table 6-5). After sintering at higher temperatures (S-O-S32h-S1100-2hA and S-O-S32h-S1250-2hA), only a few small grains of M_6C were found (Fig. 6-16c); nonetheless, the composition is relatively similar to found in the samples consolidated at a lower temperature (Table 6-5).

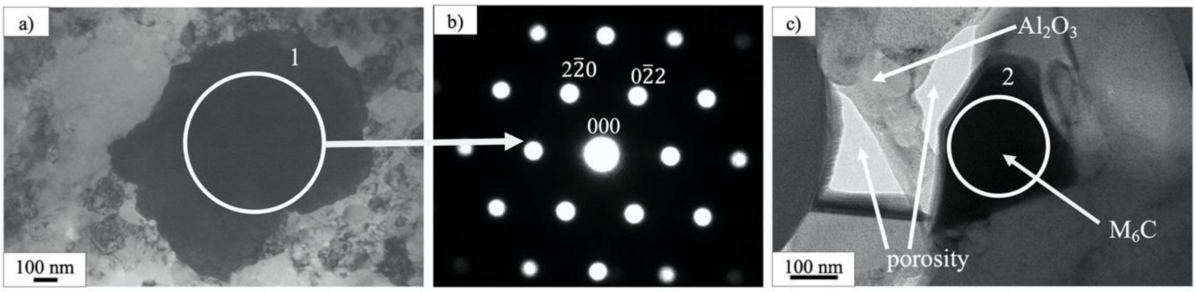

Figure 6-16. TEM analyses of M_6C carbide: a) TEM bright-field image of an M_6C grain of the S-O-S32h-S950-1hV sample, b) SEAD pattern of M_6C in ZA [111], c) TEM bright-field image of an M_6C grain of the S-O-S32h-S1250-2hA sample.

Table 6-5. Chemical composition (without quantifying carbon) of M_6C grains showed in Fig. 6-16 measured by TEM-EDX.

Region	Composition [at. %]				
	Al	Cr	Fe	Mn	Mo
1	15	13	19	9	44
2	11	12	27	10	40

Analyses of the chromium-rich $M_{23}C_6$ carbide were also carried out. In the S-O-S32h-S950-1hV sample, only a small fraction of the $M_{23}C_6$ was found. Hence, the investigations were focused on samples consolidated at higher temperatures (1100 and 1250 °C). TEM images, together with SAED patterns, confirm the face-centered cubic structure of the $M_{23}C_6$ carbide with a lattice parameter of about 10.68 Å (Fig. 6-17). The results are in good agreement with XRD investigations (Subsection 6.1.). The TEM-EDX reveals a high chromium content, while the presence of aluminum is almost negligible in the $M_{23}C_6$ carbides (Table 6-6). The molybdenum content is generally slightly higher than in the bcc#2 phase.

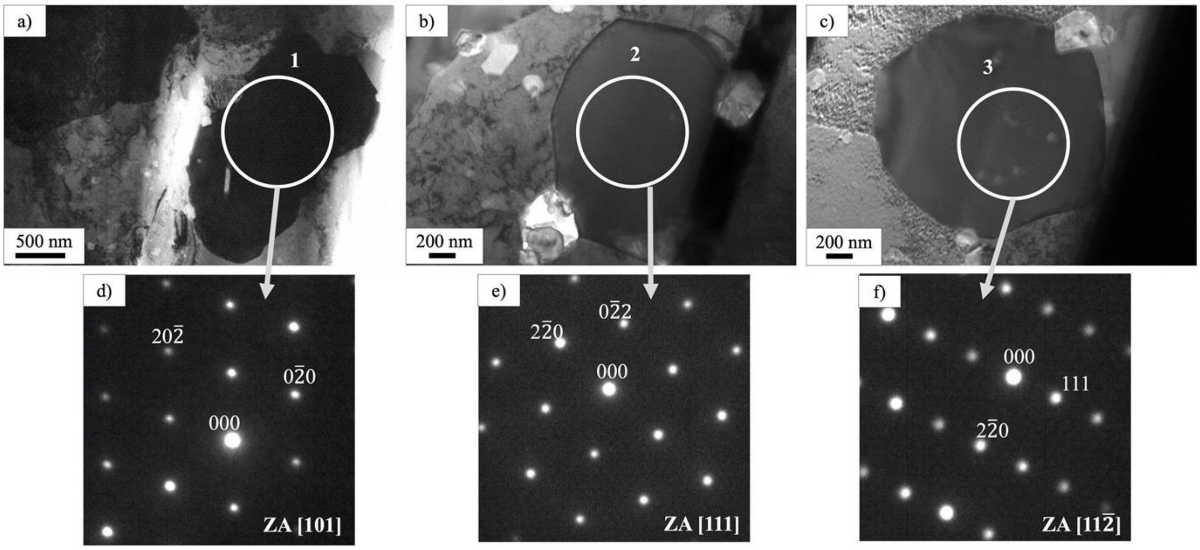

Figure 6-17. TEM analyses of the $M_{23}C_6$ carbide: bright-field images of grains in the sintered optimized alloy a) S-O-S32h-S1100-2hA, b) and c) S-O-S32h-S1250-2hA; corresponding SAED patterns d) in ZA [101] f) in ZA [111] e) in ZA $[11\bar{2}]$.

Table 6-6. Chemical composition (without quantifying carbon) of $M_{23}C_6$ grains showed in Fig. 6-17 measured by TEM-EDX.

Region	Composition [at. %]				
	Al	Cr	Fe	Mn	Mo
1	3	62	11	14	10
2	1	57	18	14	10
3	1	59	19	15	6

6.2.3.3. Alumina

A small fraction of alumina was detected by EBSD in the samples sintered at 950 and 1100 °C. EBSD reveals a slightly higher amount of Al_2O_3 in the sample consolidated at

1250 °C (S-O-S32h-S1250-2hA), so it was easier to detect and analyze it using TEM. In this sample, nanometric grains of alumina (between 200 and 400 nm) were found (Fig. 6-18). As mentioned earlier, alumina particles are also present in many sintered HEAs [74,85]. The high affinity between aluminum and oxygen (residual in the furnace chamber or introduced during mechanical alloying) leads to the formation of Al_2O_3. No other type of oxides was detected in the bulk samples sintered form the P-O-S32h powder. Many pores were found in the vicinity of alumina particles (Fig. 6-18). It could be related to three different phenomena. The coalescence of nano-porosity, which exists in samples sintered at 950 °C. The grains grow with increasing sintering temperature at the same rate as pores grow, and therefore, the porosity is more visible for the sample consolidated at 1250 °C. The second phenomenon could be the loss of brittle alumina particles during the preparation of samples for TEM and other experimental techniques such as SEM and EBSD. The third phenomenon could be related to thermal stresses. Furthermore, all phenomena could act simultaneously.

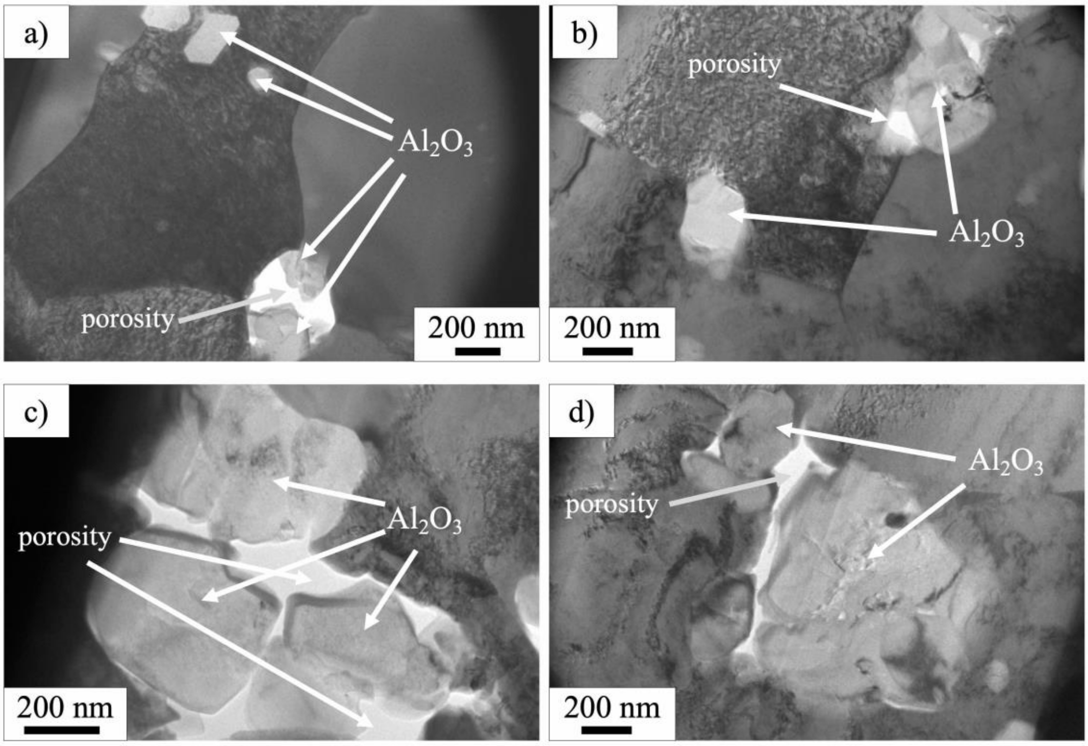

Figure 6-18. TEM bright-field images of Al_2O_3 grains (a, b, c, d) in the S-O-S32h-S1250-2hA.

The compositions of phases measured by TEM-EDX are presented in Table 6-7. The analyzes show quite a large range of chemical composition of bcc#2 depending on the sintering conditions. The iron content increases significantly for the highest studied sintering temperature. The chromium content decreases considerably in the S-O-S32h-S1250-2hA due to a relatively high-volume fraction of the chromium-rich $M_{23}C_6$ carbide in this sample. The compositions of carbides (M_6C and $M_{23}C_6$) also vary slightly, especially the iron content.

Table 6-7. Average compositions of phases based on TEM-EDX analyses (without quantifying carbon and oxygen).

Phase	Sintering temperature (sample)	Phase composition
Bcc#2	950 °C (S-O-S32h-S950-1hV)	$Al_{19}Cr_{22}Fe_{34}Mn_{19}Mo_6$
	1100 °C (S-O-S32h-S1100-2hA)	$Al_{18}Cr_{20}Fe_{34}Mn_{20}Mo_8$
	1250 °C (S-O-S32h-S1250-2hA)	$Al_{18}Cr_{14}Fe_{44}Mn_{19}Mo_5$
M_6C	950 °C (S-O-S32h-S950-1hV)	$Al_{15}Cr_{13}Fe_{19}Mn_9Mo_{44}$
	1250 °C (S-O-S32h-S1250-2hA)	$Al_{11}Cr_{12}Fe_{27}Mn_{10}Mo_{40}$
$M_{23}C_6$	1100 °C (S-O-S32h-S1100-2hA)	$Al_3Cr_{62}Fe_{11}Mn_{14}Mo_{10}$
	1250 °C (S-O-S32h-S1250-2hA)	$Al_1Cr_{58}Fe_{19}Mn_{14}Mo_8$

6.3. Density

The density measurements were performed using Archimedes' principle. The theoretical densities were calculated based on the densities of pure elements (listed in Subsection 2.1.3.). The composition of each sample was measured using large areas SEM-EDX mapping (oxygen and carbon were not quantified). SEM-EDX results present relatively high errors, especially for the five-element multicomponent alloy. In addition, the chemical composition could vary depending on the analyzed area of the sample, mainly due to a heterogeneous distribution of carbides and oxides. Hence, the ratio of measured density to theoretical density should be considered as an indication of densification rather than a strict value comparable between samples.

The results shown in Table 6-8 reveal good densification (> 97.0 %) of produced samples. In the literature, some relative densities of mechanically alloyed HEA powders sintered using hot press sintering could be found, e.g., 97.3 % for $Al_{0.6}$NiFeCrCo and 94.2 % $Al_{0.6}$NiFeCr alloy [104]. The relative density of SPSed samples are for example 96.8 % for NbMoTaWVTi [78] and 95 % for CoCrFeNi [114]. The measured densities of sintered optimized powder (P-O-S32h) vary around 6.55 g/cm^3. The variation of the ratio of measured density to theoretical density seems insignificant for samples sintered at 950 and 1100 °C. Moreover, a longer time of sintering (2 h) at 950 °C did not result in a higher density. A slightly lower density is observed for the sample sintered at 1250 °C (S-O-S32h-S1250-2hA). It might seem to be related to the porosity, which is visible on EBSD and TEM images. However, the increase in the visibility of porosity revealed by TEM and EBSD is much higher than the slight decrease in density showed by Archimedes measurements. Hence, it could be concluded that the porosity visible on EBSD and TEM images is mainly the result of the coalescence of the nano-porosity already present in samples and the loss of alumina particles during preparation. The slight decrease in density of the S-O-S32h-S1250-2hA sample could also be the effect of a higher volume fraction of alumina, which has low density – 3.99 g/cm^3.

Table 6-8. Density of sintered samples measured by the Archimedes' method.

Sample	Sintered sample final composition	Theoretical density (ρ_T) [g/cm^3]	Measured density (ρ_{BA}) [g/cm^3]	ρ_{BA}/ ρ_T [%]
S-O-S32h-S950-1hV	21%Al, 22%Cr, 30%Fe, 19%Mn, 8%Mo	6.70	6.61	98.6
S-O-S32h-S950-1hA	20%Al, 23%Cr, 30%Fe, 19%Mn, 8%Mo	6.74	6.62	98.2
S-O-S32h-S950-2hA	22%Al, 22%Cr, 30%Fe, 18%Mn, 8%Mo	6.66	6.53	98.0
S-O-S32h-S1100-2hA	21%Al, 23%Cr, 30%Fe, 19%Mn, 7%Mo	6.67	6.59	98.8
S-O-S32h-S1250-2hA	21%Al, 23%Cr, 31%Fe, 18%Mn, 7%Mo	6.68	6.48	97.0

6.4. Thermal stability of sintered optimized alloy

The optimized powder (P-O-S32h) consolidated at 950 °C reveals a promising microstructure, i.e., fine grain size, a small fraction of carbides, and oxides, as well as a predominant multi-element bcc#2 phase. Hence, the thermal stability of the S-O-S32h-S950-1hV sample was studied.

6.4.1. Differential scanning calorimetry

Differential scanning calorimetry analyses of the S-O-S32h-S950-1hV sintered sample (Fig. 6-19) reveal significant differences, especially during the first cycle of heating with DSC analyses of mechanically alloyed powder (P-O-S32h) (Subsection 5.1.). The curve of the first heating is rather flat compared to MA powders. Two endothermic peaks appear at T_1 (528 °C) and T_2 (879 °C). The endothermic peaks at T_3 (1297 °C) and T_4 (1461 °C) are in a close range of temperature as similar peaks found in mechanically alloyed powders, and therefore could be attributed to the same phenomena. The T_3 peak is related to the melting of the chromium-rich $M_{23}C_6$ carbide (similar to the temperature found by Yurkova *et al.* [82]), while the T_4 peak is assigned to the fusion of the major multi-element bcc#2 phase. The curve of the second heating presents more similarities with the results of MA powders. The long endothermic phenomenon, form 300 °C up to about 1000 °C, could be related to the diffusion. The peak of the melting of the $M_{23}C_6$ carbide (T_3) is bigger during the second heating than the first one, so the carbide volume fraction undeniably increased. Hence, the long endothermic process is probably a diffusion of chromium to form $M_{23}C_6$ carbides. The temperatures of melting peaks (T_3 and T_4) are slightly higher during the second heating. This shift could be the effect of slight changes of phase chemical compositions due to the partial evaporation of aluminum and manganese. A similar phenomenon was noticed in the analyses of mechanically alloyed powders.

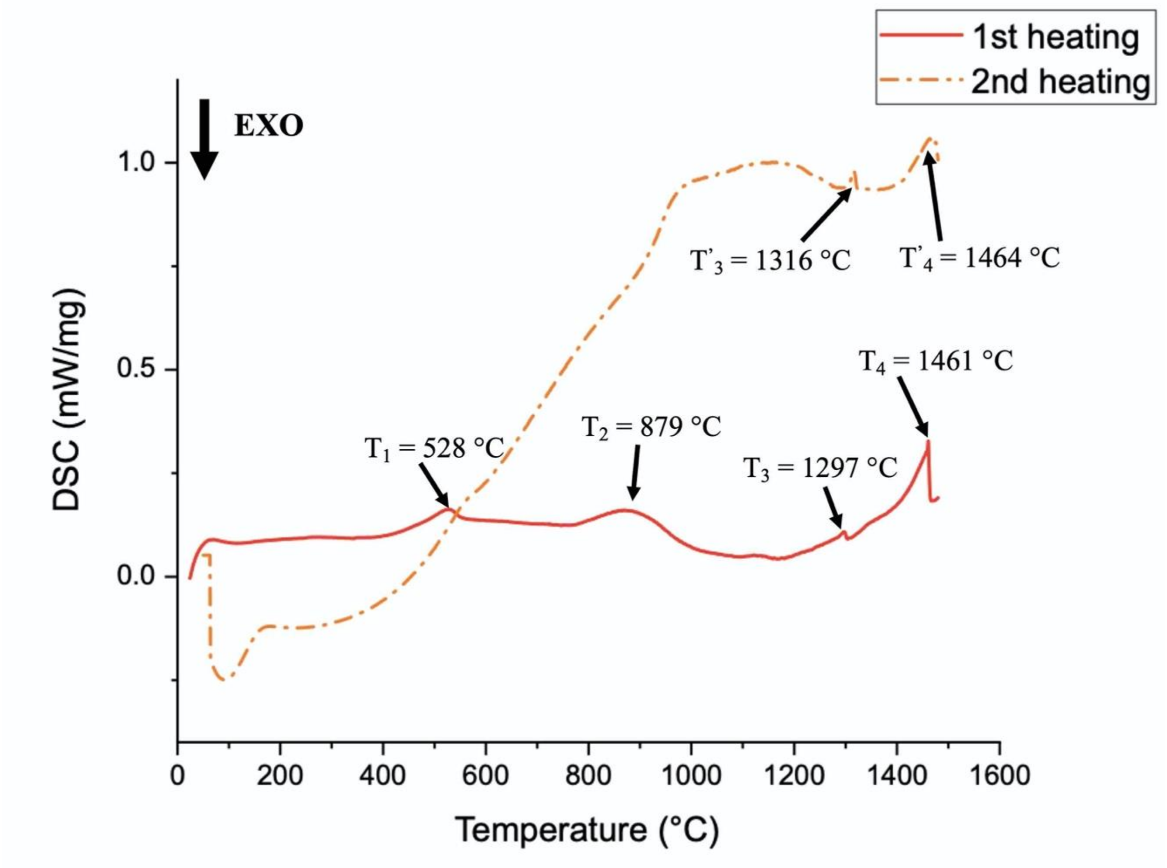

Figure 6-19. DSC curves (2 cycles of heating) of the S-O-S32h-S950-1hV sintered sample.

The sample placed in the DSC crucible was a small cuboid (about 40 mg) cut from the center of the sintered sample. After the experiment, the alloy was in the form of a sphere, which proves the sample fusion. The microstructure of the obtained sphere was investigated by SEM-BSE-EDX. The SEM-BSE image at low magnification (Fig. 6-20a) reveals large regions of major bcc#2 phase of a few hundreds of microns and a network of precipitates. SEM-EDX analyses show a high content of iron in the main bcc#2 phase (Table 6-9). A similar phenomenon is observed in the S-O-S32h-S1250-2hA sample (Subsection 6.2.3.1.). It could be the effect of the sublimation of manganese and the formation of molybdenum and chromium-rich carbides. Nevertheless, it should be noted that the content of chromium is higher, and manganese is lower in the major phase after the DSC experiment than in the bcc#2 phase after sintering at 1200 °C. The sublimation of manganese is significantly higher in DSC at 1480 °C. The volume fraction of carbides is certainly lower due to the smaller carbon contamination of sample for DSC (lower diffusion of carbon from graphite die during sintering at 950 °C) than sintered at 1250 °C, which results in a higher content of chromium in the major phase. Figure 6-20b (higher magnification) and Figure 6-21 show at least two types of precipitates in the network – chromium and molybdenum rich. The SEM-EDX mapping reveals a higher concentration of carbon in the precipitates. The SEM-EDX is not designed to measure carbon content quantitatively in alloys; however, it could reveal a difference between phases. The chromium-rich regions are assigned to the carbide, probably to the $M_{23}C_6$ (based on the sintered sample results). However, the presence of other chromium-rich carbides, e.g., M_7C_3, which was found in other sintered HEAs [83,85,86,133], could also be possible. The XRD analysis (not shown here) reveals the bcc phase with a lattice parameter of 2.91 Å. However, due to the small sample size and low intensity of peaks, the identification of carbides peaks is not possible. There are some composition differences (see areas 3 and 4 in Fig. 6-20b and Table 6-9) between chromium-rich regions. The “M” in $M_{23}C_6$ formula could contain a different concentration of elements such as chromium, iron, manganese, and molybdenum for the studied system. The slightly different compositions of the $M_{23}C_6$ carbide are also revealed in sintered samples (Table 6-6). The molybdenum-rich regions are attributed to M_6C. The chemical composition of these carbides (area 5 in Fig. 6-20b and Table 6-9) is close to found in sintered samples (Table 6-5). However, the wide variation of the M_6C composition, even wider than for $M_{23}C_6$, was suggested in the literature [134]. The network of carbides (M_6C and $M_{23}C_6$) on the grain boundaries was reported, for example, in superalloys after age-hardening heat treatment [135]. In addition to carbides, very few molybdenum-manganese precipitates were noticed (Fig. 6-21). Surprisingly, only a few alumina particles are present after melting in DSC under a constant flow of argon (maximum temperature 1480 °C), compared to 5.25 % volume fraction in the S-O-S32h-S1250-2hA sample. Therefore, the formation of Al_2O_3 in the sintered sample should be more related to the residual oxygen in the furnace chamber (sintering) than to oxygen introduced during mechanical alloying.

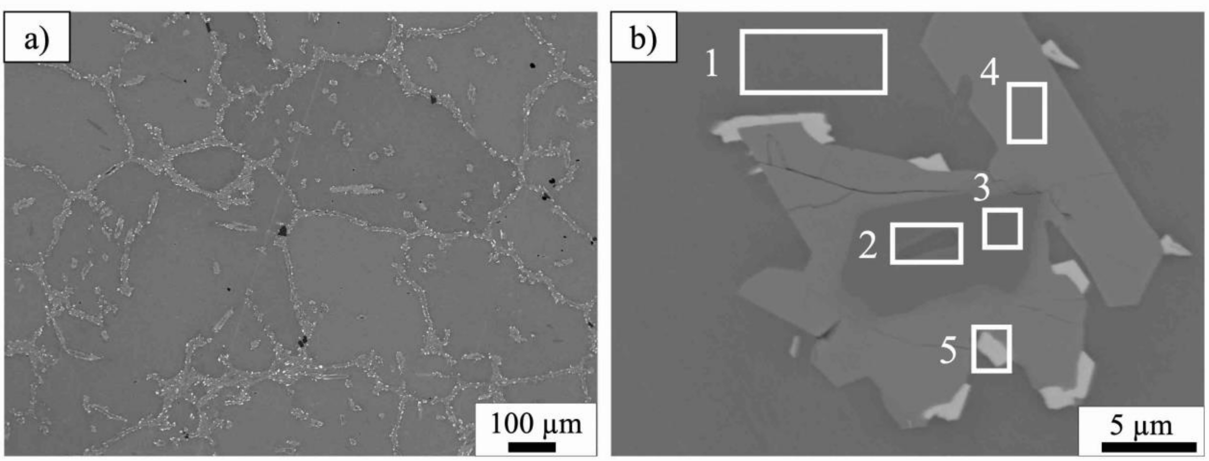

Figure 6-20. SEM-BSE images of the S-O-S32h-S950-1hV sintered sample and then melted in DSC during 2 cycles up to 1480 °C: a) low magnification, b) high magnification.

Table 6-9. Chemical composition (without quantifying carbon and oxygen) of regions highlighted in Fig. 6-20b.

Region	Composition [at. %]				
	Al	Cr	Fe	Mn	Mo
1	20	19	39	15	7
2	23	19	39	14	5
3	0	76	8	8	8
4	1	64	13	10	12
5	14	14	23	8	41

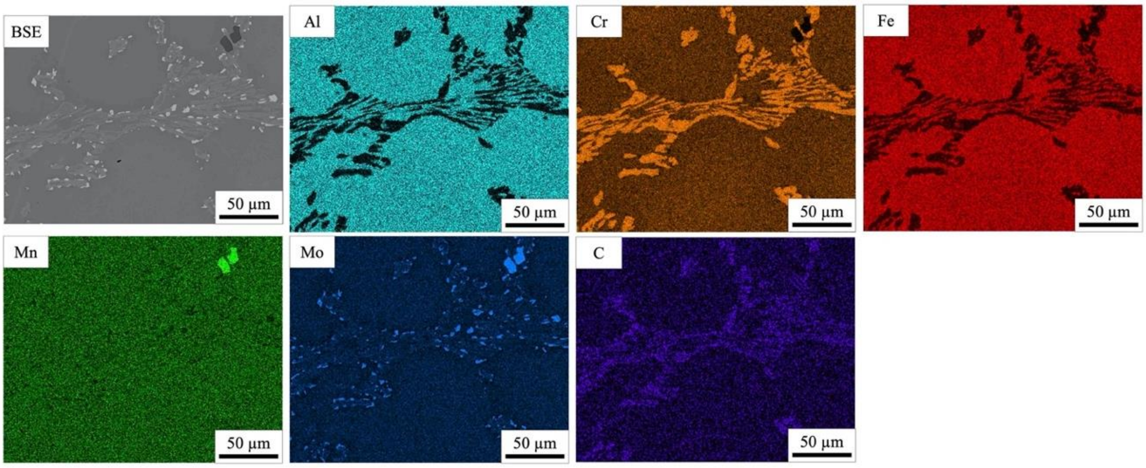

Figure 6-21. SEM-EDX mapping of precipitates in the S-O-S32h-S950-1hV sintered sample and then melted in DSC during 2 cycles up to 1480 °C.

6.4.2. Annealing of the sintered sample

The S-O-S32h-S950-1hV sintered sample was annealed for 10 h at 950 °C under argon to verify the phase stability. The microstructure revealed by SEM-BSE images (Fig. 6-22) is close to the microstructure of the S-O-S32h-S950-1hV sample (Subsection 6.2.1.1., Fig. 6-2a). The major bcc#2 phase coexists with predominant molybdenum-rich M_6C carbides and a smaller fraction of chromium-rich $M_{23}C_6$ carbides (Fig. 6-22b). The chemical composition of the bcc#2 phase is $Al_{21}Cr_{21}Fe_{32}Mn_{20}Mo_6$, which is similar to the composition of the bcc#2 in the samples sintered at 950 °C. The TEM observations show grain growth after annealing (Fig. 6-23a, b) compared to the non-heat-treated sample (Subsection 6.2.3., Fig. 6-11a). Nevertheless, a large majority of the grains is below 300 nm of diameter. SEAD pattern confirmed the M_6C structure of molybdenum-rich grains (Fig. 6-23d). The chemical composition of the M_6C (Fig. 6-23c) is very close to found in the non-annealed sample (Subsection 6.2.3.2., Table 6-5). The analyses show good thermal stability after 10 h of annealing at 950 °C of the structure produced during sintering.

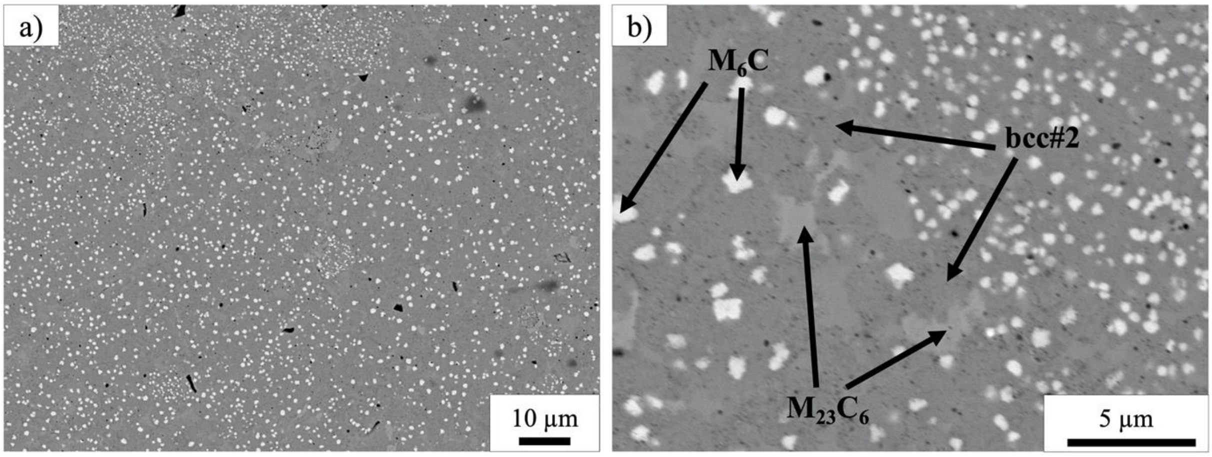

Figure 6-22. SEM-BSE images of the S-O-S32h-S950-1hV sintered sample and then annealed at 950 °C for 10 h under argon: a) low magnification, b) high magnification.

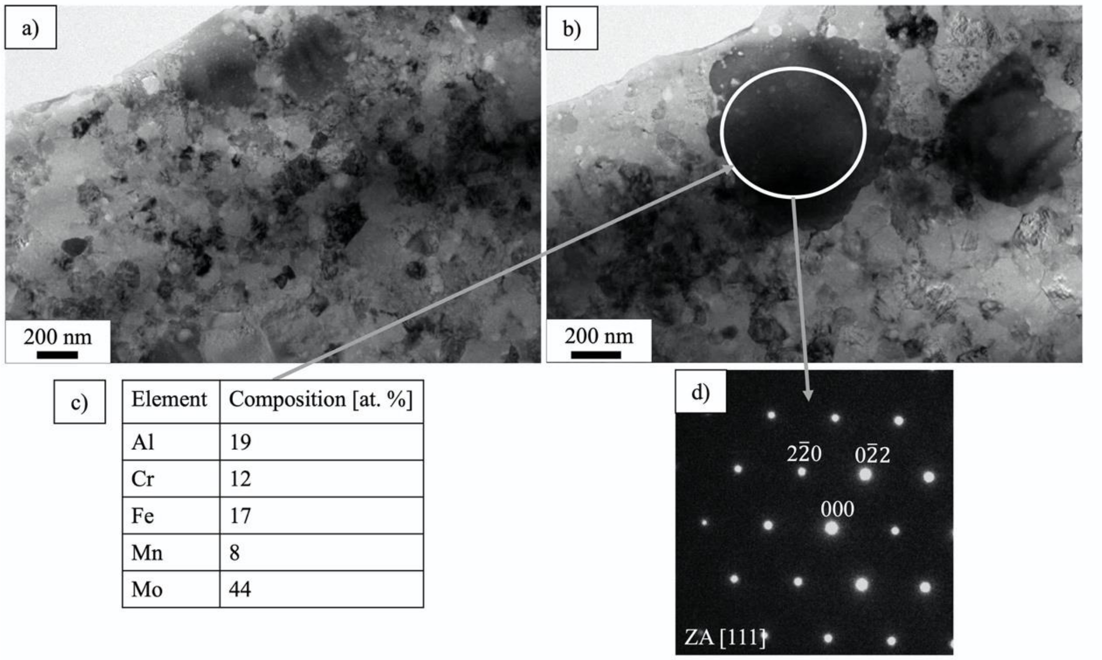

Element	Composition [at. %]
Al	19
Cr	12
Fe	17
Mn	8
Mo	44

Figure 6-23. TEM observations of the S-O-S32h-S950-1hV sintered sample and then annealed at 950 °C for 10 h under argon: a) TEM bright-field image of a general view of the structure, b) TEM bright-field image of molybdenum rich M_6C grain, c) chemical composition of M_6C grain (without quantifying carbon), d) SAED pattern of M_6C grain.

6.5. Arc melting preparation of optimized alloy

The P-O-S32h powder was pre-sintered at 600 °C for 1 h under argon (load 80 MPa). The consolidated sample was placed in the furnace chamber, and then arc melted under argon partial pressure. As mentioned earlier (Subsection 1.1.5.), the arc melting is not a preferred processing route for alloys with a high difference of melting temperatures of constituent elements, such as the Al-Cr-Fe-Mn-Mo family. However, in this study, the arc melting was performed on pre-sintered mechanically alloyed powder to prevent the presence of pure elements with a large gap of fusion temperatures. Nevertheless, the high temperature could lead to the evaporation or sublimation of elements, e.g., manganese [49]. However, some studies revealed a successful preparation of the alloy with a relatively high difference of melting temperatures of elements by arc melting, e.g., CoCrFeMnNi alloy with addition of 16 at. % of molybdenum [136]. In this study, arc melting was performed to check if evaporation occurs and evaluate the final microstructure. The sample after arc melting consists of three separate parts named A, B, and C in Figure 6-24. Each piece was carefully investigated to determine its microstructure.

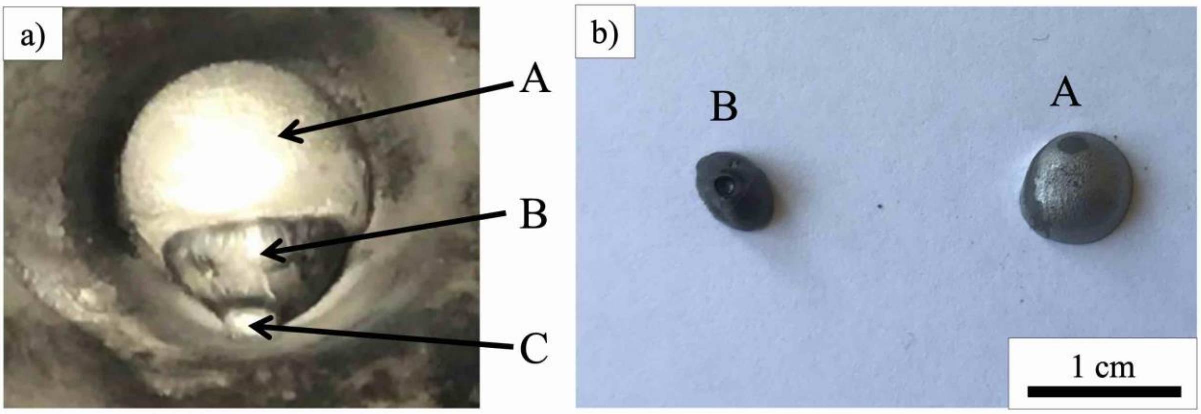

Figure 6-24. Sample of the P-O-S32h powder pre-sintered at 600 °C for 1 h under argon after arc melting. Three separate parts (A, B, C).

The biggest part of the arc melted sample is A (Fig. 6-24). The XRD (Fig. C8) reveals the largely predominant presence of the bcc#2 phase with a lattice parameter of a = 2.93 Å. Some small peaks were also detected. Their intensities are lower than the carbides peaks in the sintered samples; thus, it is very difficult to distinguish them from background noise and identify undoubtedly the corresponding phases. These peaks might be probably related to the carbides, such as $M_{23}C_6$ or M_7C_3; however, more detailed investigations should be carried out in the future. The SEM-BSE observations (Fig. 6-25a) show a similarity in the microstructure with the melted sample obtained after DSC experiment (Subsection 6.4.1., Fig. 6-20). The microstructure consists of major regions with constant chemical composition and a network of chromium and molybdenum-rich precipitates (Figure C9). The EDX mapping (not shown here) shows a higher concentration of carbon in the precipitates network, which suggests that precipitates are carbides. The composition of major regions is $Al_{16}Cr_{26}Fe_{38}Mn_{11}Mo_{9}$, which is assigned as the bcc#2 phase. The significant decrease of manganese content is related to its evaporation during melting. The furnace chamber walls were covered by metallic dust, which was probably the evaporated manganese. The SEM-EDX mapping (Fig. 6-25b) shows chromium and molybdenum-rich carbides in the network. The composition of the chromium-rich carbide (without quantifying carbon) is $Al_{3}Cr_{53}Fe_{21}Mn_{10}Mo_{13.}$ The composition in metallic elements is close to the $M_{23}C_{6}$ carbide in the sintered samples (Subsection 6.2.3.2.) and relatively similar to the chromium-rich carbides found in the sample melted in DSC (Subsection 6.4.1.). Hence, the chromium carbide could be the $M_{23}C_{6}$. The molybdenum-rich precipitates are too small (< 1 µm) to precisely measure the chemical composition. Based on the SEM-EDX mapping (Fig. 6-25b), this carbide is poor in chromium and manganese, which is similar for the $M_{6}C$ carbides in sintered samples. Moreover, some grains of alumina (black spots in Fig. 6-25) were found.

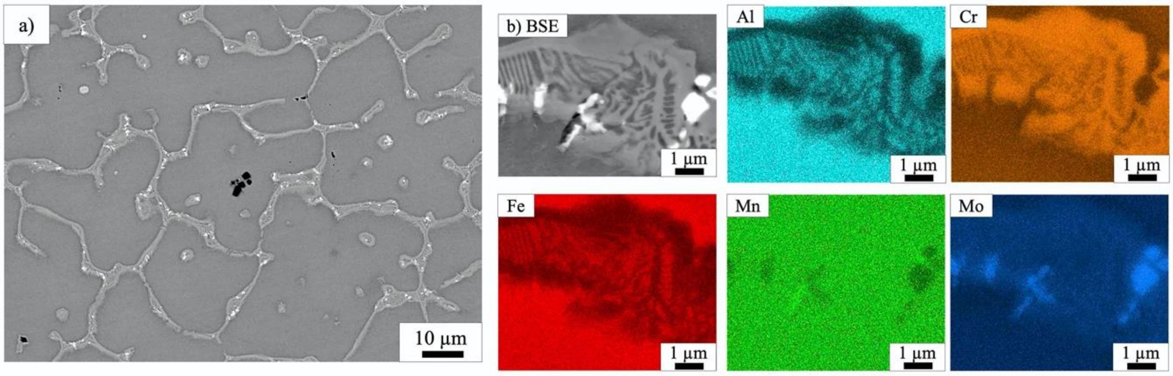

Figure 6-25. SEM analyses of part A of the P-O-S32h powder pre-sintered at 600 °C for 1 h under argon and then arc melted: a) SEM-BSE image showing a general view, b) SEM-BSE image with corresponding EDX mapping of region in the grain boundary.

The part B of the arc melted sample was also investigated by SEM-BSE. The SEM-EDX reveals the composition of the analyzed region as 40 at. % of aluminum and 60 at. % of oxygen, which perfectly corresponds to alumina (Fig. 6-26). The presence of Al_2O_3 explains the decrease in aluminum content in the bcc#2 phase in part A of the arc melted sample. The formation of a small piece of pure alumina is somewhat surprising because, in the sintered samples, only Al_2O_3 nanometric grains form. It is related to residual oxygen in the furnace chamber.

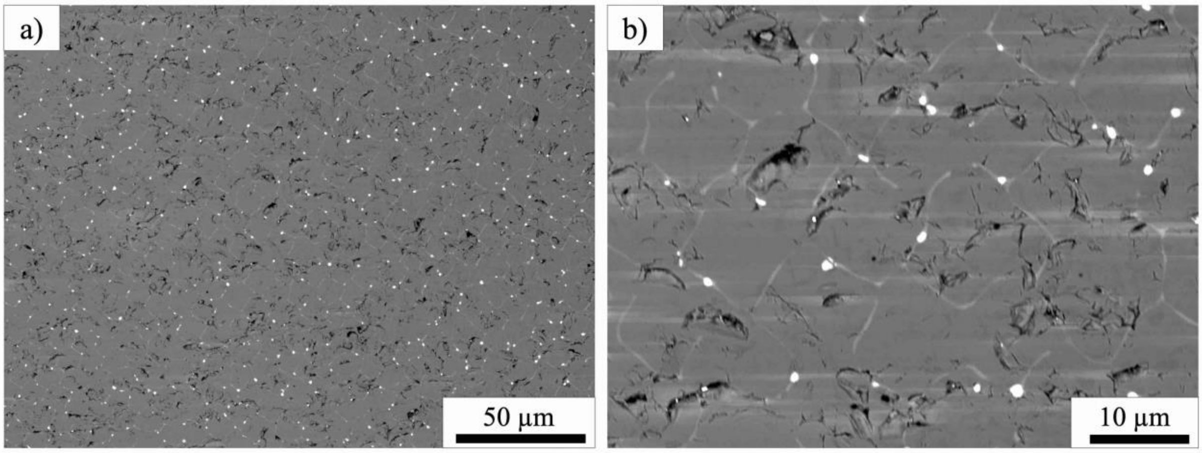

Figure 6-26. SEM-BSE images of part B of the P-O-S32h powder pre-sintered at 600 °C for 1 h under argon and then arc melted: a) low magnification, b) high magnification.

The smallest part C of the arc melted sample was also investigated. The XRD was not performed due to the small size of the sample. The microstructure consists of a major phase with the composition of $Al_{15}Cr_{27}Fe_{45}Mn_{1}Mo_{12}$ and randomly distributed alumina precipitates of a few micrometers size (Fig. 6-27). In opposition to the bcc#2 phase in part A, the major phase in part C contains almost no manganese. Moreover, the network of chromium and molybdenum rich carbides was not found.

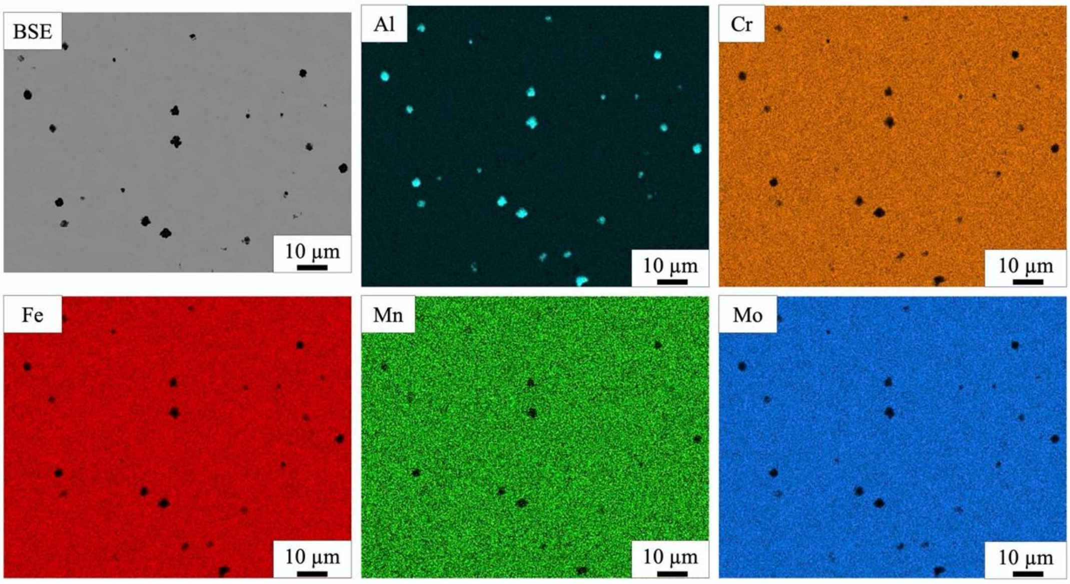

Figure 6-27. SEM-BSE image with corresponding EDX mapping of part C of the P-O-S32h powder pre-sintered at 600 °C for 1 h under argon and then arc melted.

The result of the arc melting confirms the significant evaporation of manganese and the formation of alumina. Similar phenomena occur during sintering, especially at 1250 °C. Nevertheless, during sintering, the loss of manganese is very small, and the volume fraction of alumina is up to 5 %. Hence, it could be concluded that the arc melting is not a suitable route of preparation of bulk samples from the Al-Cr-Fe-Mn-Mo family.

6.6. Results of sintering of equiatomic and experimentally optimized powders

The powders P-EQ-R70hS4h and P-OE-S32h initially (based on annealing results, Subsections 5.2.2. and 5.2.3.) not selected for the consolidation, were also sintered at 950 °C for 1 h under argon. These sintering conditions are the most promising for the P-O-S32h powder. Therefore, similar conditions enable to compare the microstructure of other compositions from the Al-Cr-Fe-Mn-Mo system quickly.

The XRD pattern of the S-EQ-R70hS4h-S950-1hA (Fig. 6-28a) reveals the major bcc#2 phase with a similar lattice parameter (Table 6-10) as for the P-O-S32h powder sintered at 950 °C (Subsection 6.1.). The intensity of the M_6C carbide peaks increases significantly, which shows a higher volume fraction of carbides than for the alloy with lower content of molybdenum. The result is in good agreement with the A-EQ-R70hS4h-950 annealed powder (Subsection 5.2.2.). The increase of the M_6C carbide volume fraction could be the effect of higher molybdenum content in the alloy (M_6C is usually molybdenum-rich) and the higher contamination by carbon due to milling in the planetary mill with the addition of stearic acid as a process control agent. Small peaks of the $M_{23}C_6$ carbide are also present, which is in a good agreement with the results of the optimized alloy (P-O-S32h powder) sintered at 950 °C (Subsection 6.1.).

The XRD pattern of the S-OE-S32h-S950-1hA sample (Fig. 6-28b) reveals the presence of the major multi-element bcc#2 phase with a similar lattice parameter (Table 6-10) as for the sintered optimized alloy (Subsection 6.1.) and the A-OE-S32h-950 annealed powder (Subsection 5.2.3.). The significant presence of the χ phase should be noted. The χ phase is also present in the A-OE-S32h-950 powder as well as after annealing in A-O-S32h-650 and A-O-S32h-800 powders. A slightly different chemical composition could probably shift the disappearance of the χ phase to a higher temperature than for alloys with a higher content of molybdenum. The carbon contamination, which plays a crucial role in carbide formation, could also be slightly lower for the P-OE-S32h powder due to the randomness of the contamination phenomenon and different chemical composition. Small peaks of the $M_{23}C_6$ carbide are present in the pattern. No M_6C carbide peaks were detected; nevertheless, the carbide could be present in a small fraction below the XRD detection limit.

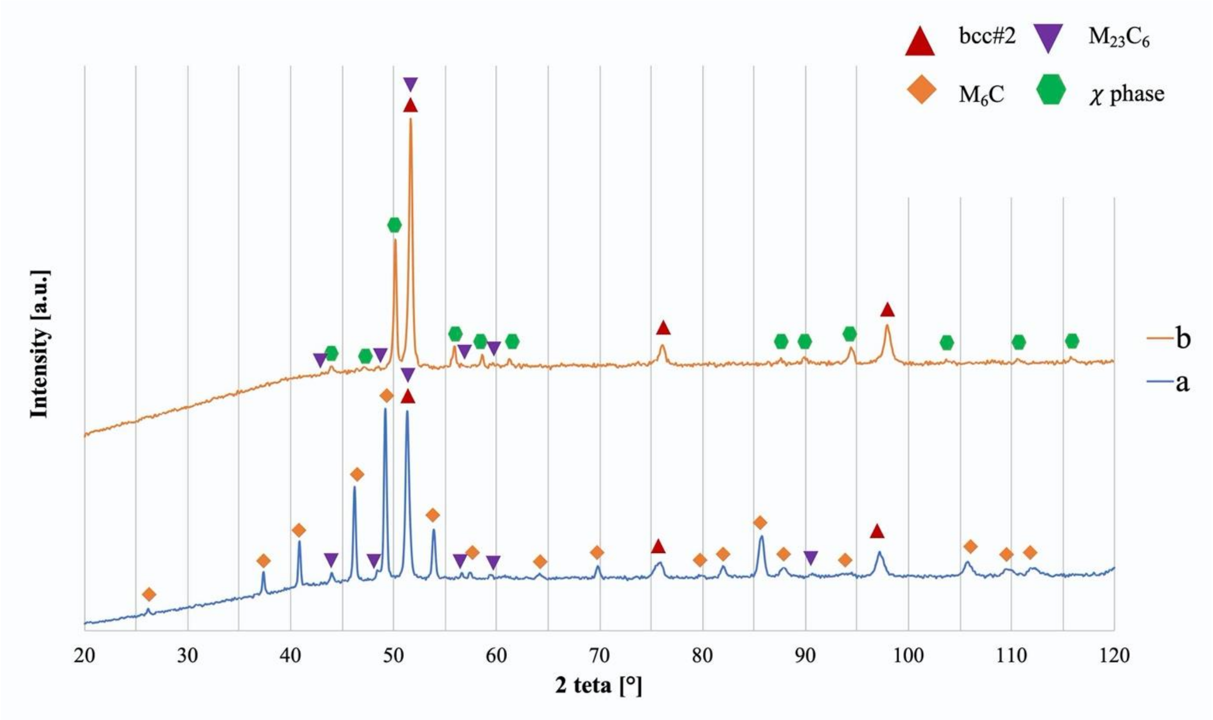

Figure 6-28. XRD patterns of bulk samples: a) S-EQ-R70hS4h-S950-1hA, b) S-OE-S32h-S950-1hA.

Table 6-10. Lattice parameter of bulk samples: S-EQ-R70hS4h-S950-1hA and S-OE-S32h-S950-1hA.

Sample	Lattice parameters [Å]			
	bcc#2	χ phase	M_6C	$M_{23}C_6$
S-EQ-R70hS4h-S950-1hA	2.92	---	11.17	10.66
S-OE-S32h-S950-1hA	2.91	8.96	---	10.69

The SEM-BSE images of the S-EQ-R70hS4h-S950-1hA sample reveal similar microstructure (high content of white precipitates) in the region close to the surface (Fig. 6-29a) and in the center of the sample (Fig. 6-29b). The SEM-EDX (Fig. 6-30) mapping reveals, besides the bcc#2 phase, with the composition of $Al_{19}Cr_{20}Fe_{26}Mn_{24}Mo_{11}$, a very high-volume fraction of molybdenum and chromium rich regions. These regions, based on XRD data (Fig. 6-28), were attributed to the M_6C and $M_{23}C_6$ carbides, respectively. The high-volume fraction of carbides, especially the M_6C, is related to a high-volume fraction of molybdenum in this composition (strong carbide former) and the very significant contamination by carbon from milling media and process control agent (stearic acid). The similar amount of carbides in the center and close to the surface of the sample is unexpected. The result of the sintered P-O-S32h powder shows a higher volume fraction of carbides close to the surface region (Subsection 6.2.1.2.). However, it seems that the amount of carbon introduced from stearic acid (PCA) during milling in the planetary mill is enormous compared to the mechanical alloying in SPEX. Therefore, even important diffusion of carbon from the graphite die during sintering does not significantly change the microstructure in the area close to the sample surface. The very high-volume fraction of carbide could improve hardness or wear resistance of the alloy; however, a significant decrease in ductility seems inevitable. Consequently, the microstructure of the sintered samples from the P-O-S32h powder is much more promising. The density of the sintered S-EQ-R70hS4h-S950-1hA sample is 6.93 g/cm^3, which corresponds to 97.6 % of theoretical density. The measured density is higher than for bulk samples based on the P-O-S32h powder (Table 6-8), mainly due to a high content of molybdenum.

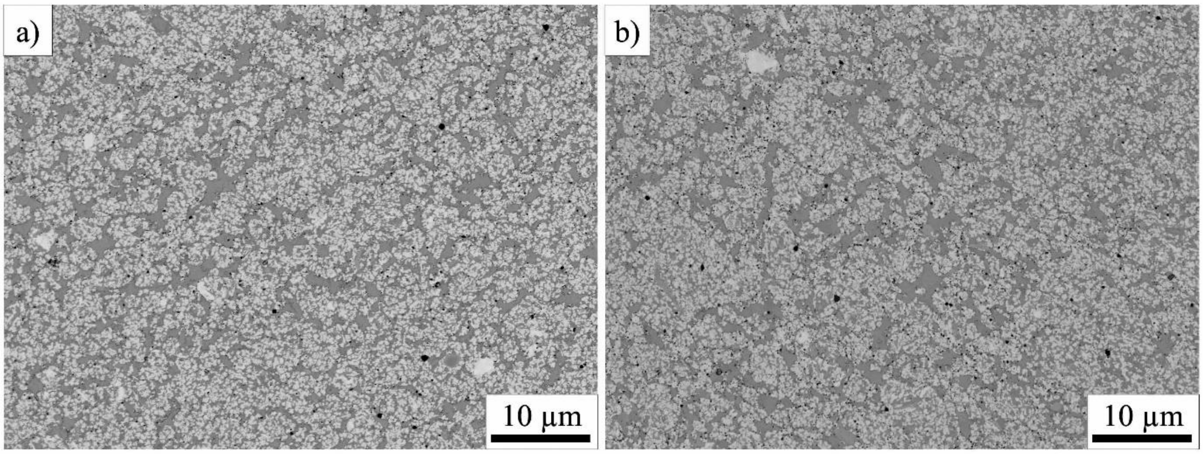

Figure 6-29. SEM-BSE images of the S-EQ-R70hS4h-S950-1hA sample: a) region close to the surface of the sample, b) region in the center of the sample.

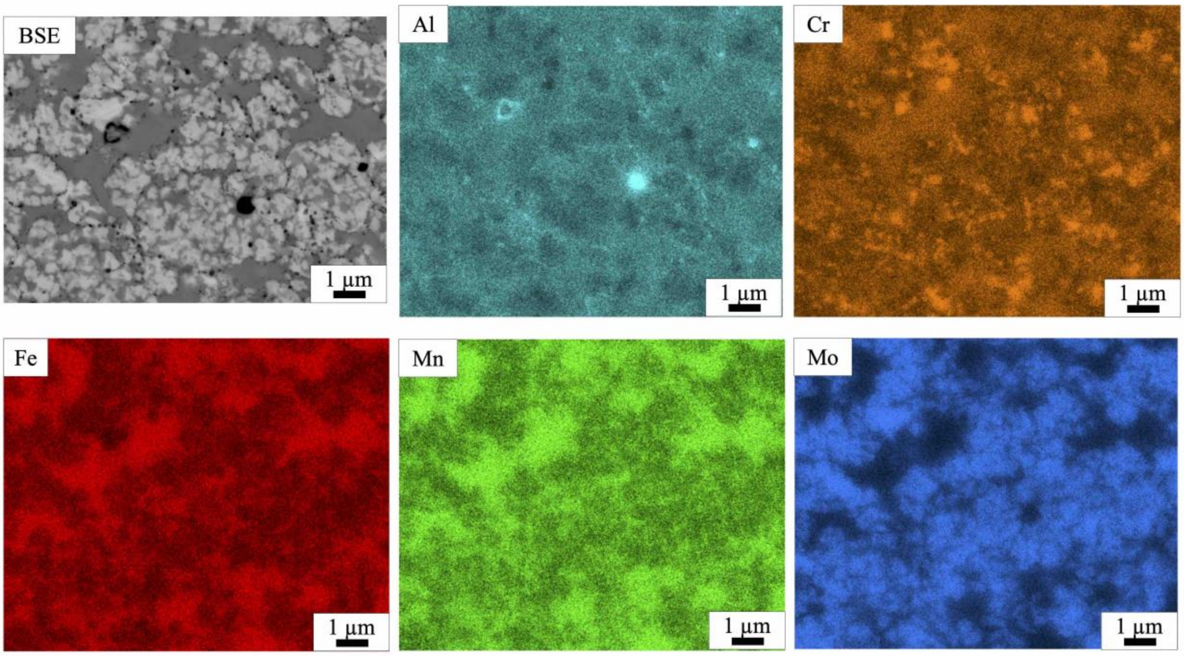

Figure 6-30. SEM-BSE image with corresponding EDX mapping in the center of the S-EQ-R70hS4h-S950-1hA sample.

The SEM-BSE images of the S-OE-S32h-S950-1hA sintered alloy show a significant difference in the microstructure between the areas close to the surface (Fig. 6-31a) and in the sample center (Fig. 6-31b). It should be noted that in both regions (surface and center), the multi-element bcc#2 phase is predominant, which is in good agreement with the XRD (Fig. 6-28, Table 6-10) and results of the A-OE-S32h-950 annealed powder (Subsection 5.2.3.). The SEM-EDX mapping reveals the significant presence of the molybdenum-rich M_6C and chromium-rich $M_{23}C_6$ carbides close to the surface (Fig. C10) while the χ phase is present in a slightly higher distance from the surface towards the center. The SEM-EDX mapping (Fig. 6-32) reveals a high-volume fraction of the χ phase enriched in molybdenum in the sample center, which is also present in the A-OE-S32h-950 annealed powder (Subsection 5.2.3.). The chemical compositions of bcc#2 and χ phases (without quantifying carbon and oxyge) are $Al_{20}Cr_{20}Fe_{38}Mn_{18}Mo_4$ and $Al_{13}Cr_{23}Fe_{34}Mn_{19}Mo_{11}$, respectively. The formation of carbides in the near-surface is certainly related to the high carbon content in this region due to the diffusion from the graphite die during sintering. These results confirm that carbon contamination plays an essential role in the formation of the microstructure after consolidation. As mentioned earlier, the contamination introduced during mechanical alloying can vary depending on milling; however, the variation for the same processing conditions should be small. The more probable reason for the presence of the χ phase in the S-OE-S32h-S950-1hA sintered sample could be a slight difference in the chemical composition compared to the S-O-S32h-S950-1hA. Maybe a slight decrease in molybdenum content could favor the χ phase presence instead of the M_6C carbide. Moreover, the χ phase contains less aluminum than the bcc#2 phase. The content of aluminum in the S-OE-S32h-S950-1hA alloy is lower, compared to the S-O-S32h-S950-1hA alloy. Therefore, relatively small chemical composition changes could significantly affect the final microstructure. The density of the S-OE-S32h-S950-1hA sintered sample is 6.71 g/cm^3, which corresponds to 98.4 % of theoretical density.

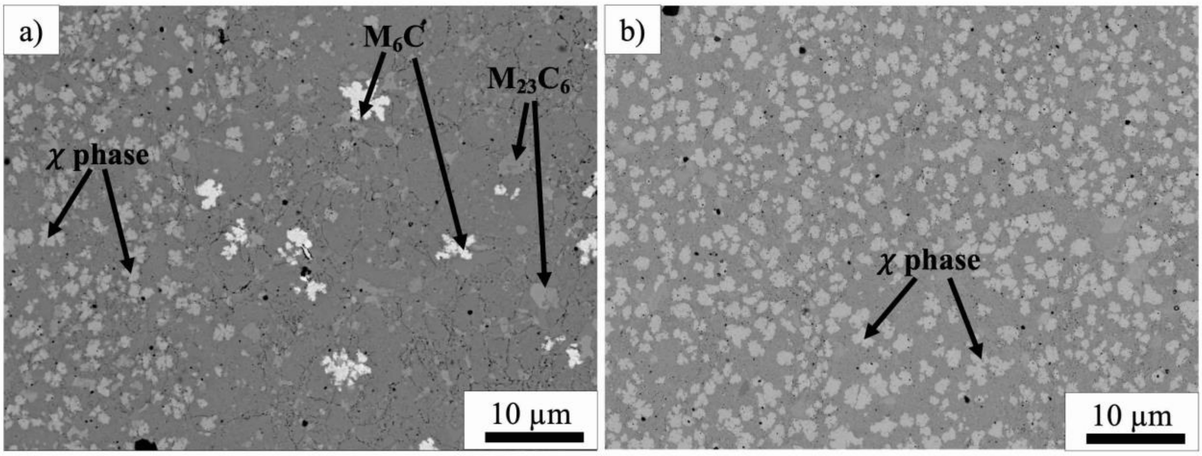

Figure 6-31. SEM-BSE images of the S-OE-S32h-S950-1hA sample: a) region close to the surface of the sample, b) region in the center of the sample.

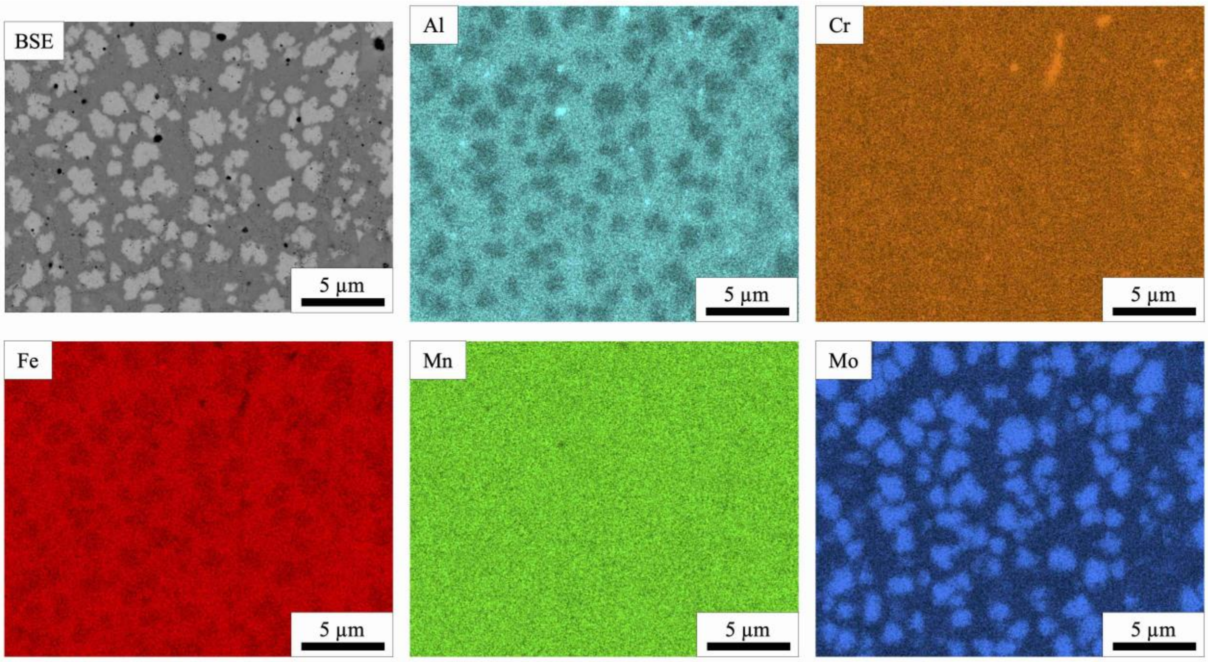

Figure 6-32. SEM-BSE images with corresponding EDX mapping of the center of the S-OE-S32h-S950-1hA sample.

The sintering of the P-EQ-R70hS4h and P-OE-S32h powders shows less promising microstructures than the sample sintered from the P-O-S32h powder. The S-EQ-R70hS4h-S950-1hA alloy, besides the multi-element bcc#2 phase, contains a very high-volume fraction of carbides due to high molybdenum content (carbide former) and significant contamination by carbon during milling (stearic acid). The S-OE-S32h-S950-1hA alloy consists of the bcc#2 phase and χ phase, which could significantly decrease the alloy ductility. The results of sintered samples confirm the good initial choice of the P-O-S32h powder (after annealing of powders, Subsection 5.3.) for further investigations.

6.7. Discussion and summary

The MA powder of the most promising alloy (P-O-S32h) after mechanical alloying and annealing results was sintered under different conditions. The structure and microstructure were carefully analyzed to determine the present phases, their volume fractions, and distribution. The thermal stability was investigated by DSC and annealing experiments. Additionally, arc melting was also performed. Moreover, the P-EQ-R70hS4h and P-OE-S32h powders were sintered to compare the microstructure.

The microstructure of all bulk samples produced from the P-O-S32h powder consists of a predominant multi-element body-centered cubic phase (bcc#2) with a lattice parameter between 2.91-2.93 Å, depending on the sintering conditions, and a small fraction of carbides and oxides. The chemical composition of the multi-element bcc#2 phase varies depending on the consolidation parameters; for the S-O-S32h-S950-1hV sample it is $Al_{19}Cr_{22}Fe_{34}Mn_{19}Mo_6$ and for the S-O-S32h-S1250-2hA sample it is $Al_{18}Cr_{14}Fe_{44}Mn_{19}Mo_5$. The increase in iron content is caused by the decrease of other elements due to manganese sublimation (also found in the literature [131,132]) and the formation of a higher fraction of carbides and oxides. The grain size of the bcc#2 phase increases from 0.22 µm, after sintering at 950 °C (S-O-S32h-S950-2hA), to 0.51 µm after consolidation at 1250 °C (S-O-S32h-S1250-2hA). These findings are consistent with the results of other sintered HEAs that higher sintering temperatures cause an increase in the mean grain size [83]. Therefore, in the purpose to obtain excellent mechanical properties (e.g. high yield strength and hardness), the most promising consolidation temperature is 950 °C. The sintering time (1 or 2 h) and atmosphere (vacuum or argon) at 950 °C seem not to present a significant effect on the microstructure of samples. It should be noted that the brittle intermetallic χ phase found after annealing of MA powder at 600 and 850 °C was not found in the bulk samples. Moreover, the $AlMo_3$ predicted by Senkov *et al.* [22] from CALPHAD calculations for the equiatomic composition, and σ phase or the intermetallic type Cr_3Si (A15) predicted by our CALPHAD calculations, were not found either.

Contamination phenomena commonly occur in powder metallurgy processing [4,21,49]. As mentioned in the Literature review (Chapter 1), contamination could occur during mechanical alloying (Subsection 1.3.2.) and sintering (Subsection 1.3.4.). The results of the bulk samples of sintered P-O-S32h powder reveal the presence of carbides. The carbides were also found in annealed MA powder due to contamination of carbon during milling (Subsection 5.2.1.). Hence, the contamination occurs during mechanical alloying and sintering from graphite die. After sintering at 950 °C, the predominant carbide is the molybdenum-rich M_6C carbide, while only a small fraction of the chromium-rich $M_{23}C_6$ carbide is present. For alloy sintered at 1100 and 1250 °C, the $M_{23}C_6$ is definitely predominant carbide (only a few grains of M_6C were found). Both carbides were found in literature in sintered HEAs: M_6C [87,114] and $M_{23}C_6$ [79,81,82,84,85,113]. The volume fraction of carbides increases with increasing sintering temperature due to easier diffusion of carbon from graphite die into the sample. Moreover, a higher amount of both carbides was found near the surface of the samples, which was in contact with the graphite die. The presence of carbide could have a positive effect on properties such as hardness [51], or it could inhibit grain growth [73]. However, a high carbide phase ratio could cause brittleness. The presence of alumina was also noticed in the sintered samples, especially in the sample consolidated at 1250 °C (S-O-S32h-S1250-2hA) due to the easier formation of Al_2O_3 at higher temperatures. The presence of alumina in sintered HEAs was found in the literature [74,85]. From the point of view to limit the formation of carbides and alumina, the best consolidation temperature is 950 °C.

The S-O-S32h-S950-1hV bulk sample analyzed by differential scanning calorimetry reveals quite similar temperatures of melting of the $M_{23}C_6$ carbide (1297 °C) and the bcc#2 phase (1461 °C) as the P-O-S32h powder. The post-DSC melted sample shows a predominant phase and a network of molybdenum and chromium rich carbides. The major phase is significantly enriched in iron, mainly due to the sublimation of manganese and the formation of the carbides. The annealing for 10 h at 950 °C under argon of the S-O-S32h-S950-1hV bulk sample reveals the stability of the microstructure produced during the sintering (bcc#2 phase, M_6C, $M_{23}C_6$). The grain growth during annealing should be noted.

The arc melted pre-sintered at 600 °C for 1 h under argon P-O-S32h powder presents an interesting microstructure. Three separate parts of the sample were obtained after the experiment. The biggest part reveals structure similar to the sample melted in DSC, i.e., major bcc#2 phase ($a = 2.93$ Å) and a network of chromium and molybdenum rich carbides. The content of manganese is lower than initial due to its significant evaporation. The smaller part consists of pure alumina, which forms due to aluminum and oxygen mutual affinity. The smallest part of the sample consists of a phase significantly enriched in iron and randomly distributed alumina. The results show that the arc melting does not produce a homogeneous single bcc phase from the mechanically alloyed pre-sintered P-O-S32h powder. The substantial loss of manganese and the formation of alumina demonstrate that the arc melting is not a suitable route of fabrication of alloys from the Al-Cr-Fe-Mn-Mo family.

The P-EQ-R70S4h and P-OE-S32h powders were consolidated at 950 °C for 1 h. The microstructure of the S-EQ-R70hS4h-S950-1hA alloy consists of major multi-element bcc#2, similar to found in the bulk samples produced from P-O-S32h powder, and a very high fraction of molybdenum and chromium rich carbides (M_6C and $M_{23}C_6$). It is the effect of the high content of strong carbide former – molybdenum, and high contamination by carbon during mechanical alloying in the planetary mill from milling media and process control agent (stearic acid). The amount of carbides in the center of the sample is so high that the difference between the surface, which was in contact with the graphite die during sintering, and the core could not be seen. The high-volume fraction of carbides could cause brittleness of the material. The microstructure of the S-OE-S32h-S950-1hA sample consists of bcc#2, intermetallic χ phase, and carbides (M_6C and $M_{23}C_6$). The carbides are located mainly close to the surface, which is enriched in carbon due to the diffusion from the graphite die during sintering. In the core region of the sample, the bcc#2 and χ phases are present. The presence of the intermetallic χ phase could be the effect of lower carbon contamination or difference in chemical composition such as lower aluminum contents compared to the S-O-S32h-S950-1hA alloy. The intermetallic χ phase is brittle; therefore, it should be avoided in alloys for structural applications.

The results of the sintering of the P-O-S32h powder show a predominant bcc#2 in all bulk samples consolidated between 950 and 1250 °C. The presence of carbides and oxides depends on the sintering conditions. The consolidation at 950 °C results in the best microstructure for excellent mechanical properties, i.e., a small grain size, limited presence of carbides and oxides. The samples sintered at 950 °C present very good densification (> 98.0 %). The presented findings show the possibility of the preparation of a bulk high entropy alloy with major bcc#2 with a small fraction of carbides and oxides by mechanical alloying and hot press sintering. Moreover, the results showed that arc melting is not a preferred route for the fabrication of alloys from Al-Cr-Fe-Mn-Mo due to significant sublimation or evaporation of manganese and the formation of alumina. Additionally, the S-EQ-R70hS4h-S950-1hA and S-OE-S32h-A950-1hA alloys consist, besides of a predominant bcc#2, of a high-volume fraction of carbides and χ phase, respectively. Hence, the microstructure of these alloys is less promising in terms of potential mechanical properties than the samples sintered form P-O-S32h powder.

Finally, it should be noted that in all bulk samples, the predominant phase is a disordered multi-element body centered cubic phase (bcc#2) with a lattice parameter between 2.91 and 2.93 Å. The composition of this phase varies significantly. The lowest content in iron ($Al_{19}Cr_{20}Fe_{26}Mn_{24}Mo_{11}$) is found in the S-EQ-R70hS4h-S950-1hA sample (the initial composition of the powder is equiatomic). In contrast, the highest content of iron ($Al_{18}Cr_{14}Fe_{44}Mn_{19}Mo_5$) is found in the S-O-S32h-S1250-2hA sample (optimized composition). The lowest content in molybdenum ($Al_{20}Cr_{20}Fe_{38}Mn_{18}Mo_4$) is found in the S-OE-S32h-S950-1hA sample (the initial composition of the powder is 19% Al, 22% Cr, 34% Fe, 19% Mn, 6% Mo), while the highest content of molybdenum

($Al_{19}Cr_{20}Fe_{26}Mn_{24}Mo_{11}$) is found in the S-EQ-R70hS4h-S950-1hA sample (the initial composition of the powder is equiatomic). The initial composition of powder and the contamination (and resulting carbides and oxides or the χ phase) significantly influence the composition of the obtained bcc#2 phase. The above results confirm the good stability of the multi-element bcc#2 phase in all studied bulk high entropy alloys (different chemical compositions and different temperatures of sintering or melting).

7. Mechanical properties

The mechanical properties are essential characteristics of new materials. In this study, mechanical properties were evaluated by means of micro-indentation tests under different loads and by compression at temperatures between room temperature and 800 °C.

7.1. Micro-indentation

The hardness measurements can be divided into three categories: macro-hardness, micro-hardness, and nano-hardness. The applied load in micro-hardness measurements is below 10 N (sometimes below 2 N) and above 10 mN [137]. In this study, the Vickers micro-hardness measurements were performed at load from 0.5 to 9 N, to evaluate the effect of load on the obtained results. The microhardness results are presented in Table 7-1, and selected indentation curves are shown in Figure 7-1. A slight decrease of micro-hardness values was observed with increasing load; however, results stabilize from 2 N. The phenomenon is known as the Indentation Size Effect (ISE) [138]. The indentation depth in this study is between 1.3 and 9.0 μm depending on the sample and applied load.

Table 7-1. Hardness measurement (HV) on the bulk samples for loads from 0.5 N to 9 N.

Sample	0.5 N	0.75 N	1 N	2 N	5 N	9 N
S-O-S32h-S950-1hV	962 ±41	966 ±22	950 ±29	908 ±26	915 ±26	920 ±47
S-O-S32h-S950-1hA	955 ±29	926 ±55	932 ±27	918 ±19	950 ±45	908 ±16
S-O-S32h-S950-2hA	947 ±55	947 ±47	971 ±39	950 ±47	926 ±34	924 ±37
S-O-S32h-S1100-2hA	693 ±30	677 ±35	715 ±23	685 ±23	689 ±15	690 ±20
S-O-S32h-S1250-2hA	531 ±46	504 ±23	491 ±24	475 ±32	453 ±21	487 ±20
S-EQ-R70hS4h-S950-1hA	1176 ±86	1153 ±48	1207 ±85	1223 ±99	1053 ±120	1099 ±133
S-OE-S32h-S950-1hA	934 ±49	910 ±33	948 ±34	958 ±26	932 ±30	903 ±38
P-O-S32h pre-sintered at 650 °C for 1 h, and then arc melting (part A)	562 ±20	548 ±22	541 ±15	536 ±16	521 ±8	510 ±8

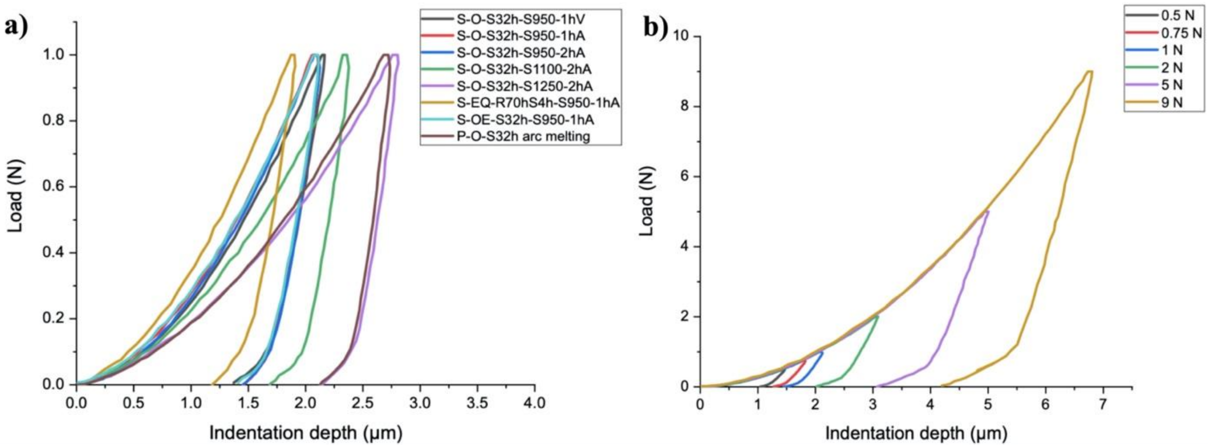

Figure 7-1. Micro-indentation curves: a) all studied samples under a load of 1 N, b) the S-O-S32h-S950-2hA sample under loads between 0.5 N and 9 N.

The results obtained on the sintered samples with the optimized composition (P-O-S32h, initial powder composition of 22.5 at. % Al, 22.5 at. % Cr, 28 at. % Fe, 20 at. % Mn, 7 at. % Mo) show a significant effect of the consolidation temperature on the micro-hardness (Table 7-1). For the samples sintered at 950 °C, no effect of the atmosphere (argon or vacuum in the chamber) was noticed. Both samples present somewhat similar results in the standard deviation margin, which is relatively high, mostly due to not uniformly distributed carbides, oxides, and abnormal grain growth revealed by EBSD results (Subsection 6.2.2). The sintering time (1 or 2 h) does not present a significant effect on hardness either. It is in good agreement with the structure/microstructure investigations (Chapter 6), which did not reveal substantial microstructural differences between samples sintered at 950 °C. The hardness of samples consolidated at 950 °C is very high – about 950 HV_{1N}, which exceeds the values of many sintered HEAs [74,82,83,85,93]. The increase of sintering temperature to 1100 and 1250 °C results in a decrease of the hardness by 25 % and 48 %, respectively. The significant reduction in hardness could be attributed to several coexisting factors revealed by microstructure investigations, such as porosity coalescence (from nanometric size to micrometric size) and grain growth, which according to the Hall-Petch law, decreases the hardness. The carbide transformation from the molybdenum-rich carbide (M_6C) to the chromium-rich carbide ($M_{23}C_6$) seems to play a role in hardness decrease too. The hardness of the M_6C is higher than the one of the $M_{23}C_6$, according to the literature [139,140]. Therefore, the transformation could contribute to the decrease of the hardness of the samples sintered at 1100 and 1250 °C. Nevertheless, it should be noted that the total volume fraction of carbides increases with increasing temperature. The hardness of the arc melted P-O-S32h powder is slightly higher than the powder sintered at 1250 °C. Despite having undeniably larger grains, the lack of porosity compared to the sintered samples contributes to a better hardness level.

Nevertheless, it should be noted that the chemical composition of the major phase in the arc melted sample is depleted in manganese, aluminum, and that some alumina precipitates were found (black spots in Fig.7-2b) (see Subsection 6.5).

The hardness of the bulk S-EQ-R70hS4h-S950-1hA alloy is about 25 % higher than the S-O-S32h-S950-1hA (Table 7-1). It is mainly the effect of a very high-volume fraction of carbides (M_6C and $M_{23}C_6$) showed by XRD and SEM-EDX (Subsection 6.6). The hardness of the S-OE-S32h-S950-1hA alloy is similar to the S-O-S32h-S950-1hA alloy sintered in the same conditions (Table 7-1). Hence, it could be concluded that the presence of the χ phase instead of carbides does not result in the increase of hardness; however, it could increase the brittleness of alloy.

The Young's moduli (elastic moduli, E) of bulk samples were determined from micro-indentation tests. The elastic moduli obtained under loads of 1 N and 2 N are presented in Table 7-2. The moduli values are close between samples of the optimized and experimentally optimized alloys sintered at 950-1100 °C. The optimized powder consolidated at 1250 °C (S-O-S32h-S1250-2hA) reveals a slightly lower elastic modulus, while the sintered equiatomic alloy (S-EQ-R70hS4h-S950-1hA) shows the highest Young's modulus. The results present higher values compared with the value of 213 GPa predicted by Senkov *et al.* [22] for the equiatomic composition. However, it should be noted that Senkov *et al.* evaluated the elastic modulus for the sample without the presence of oxides and carbides.

Table 7-2. Young's modulus (GPa) determined from the micro-indentation curves at load of 1 N and 2 N.

Sample	1 N	2 N
S-O-S32h-S950-1hV	227 ± 6	237 ± 7
S-O-S32h-S950-1hA	249 ± 5	244 ± 6
S-O-S32h-S950-2hA	248 ± 7	243 ± 8
S-O-S32h-S1100-2hA	253 ± 8	235 ± 4
S-O-S32h-S1250-2hA	204 ± 8	193 ± 7
S-EQ-R70hS4h-S950-1hA	287 ± 11	272 ± 11
S-OE-S32h-S950-1hA	245 ± 6	238 ± 4
P-O-S32h pre-sintered at 650 °C for 1 h, and then arc melting (part A)	232 ± 9	226 ± 10

The indentation zones were analyzed by SEM-SE to evaluate the brittleness of the bulk sample. The SEM observations of the indentation sites in the S-O-S32h-S950-2hA alloy reveals small circumferential cracks (Fig. 7-2a). The arc melted sample presents no cracks

(Fig. 7-2b), which shows the best ductility among the bulk samples. However, it should be noted that the arc melted sample reveals significantly lower hardness than samples sintered at 950 °C. The biggest cracks are visible in the S-OE-S32h-S950-1hA sample (Fig. 7-2c), which consists of bcc#2 phase, intermetallic χ phase, and a small volume of carbides. These results confirm that a high-volume fraction of χ phase could manifest in the brittleness of the samples. It is worth to mention that the cracks revealed in Figure 7-2 are not radial cracks present in many brittle materials, e.g., [141]. Therefore, the studied HEA samples could present a certain level of plasticity.

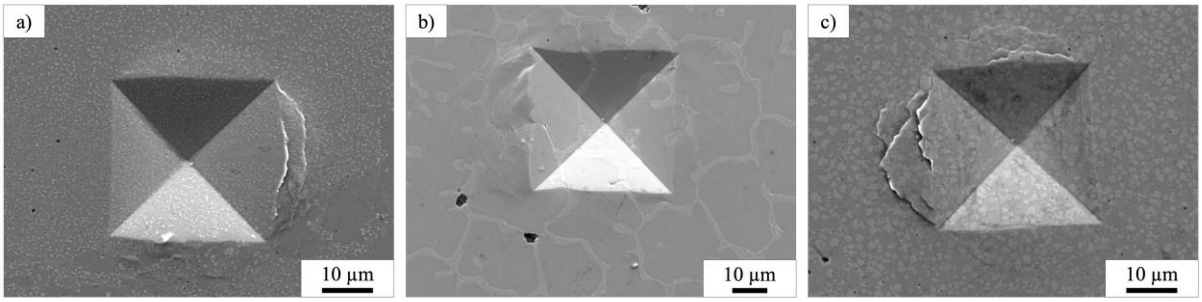

Figure 7-2. SEM-SE images of the indentation sites after micro-hardness measurements with the force of 9 N in samples: a) S-O-S32h-S950-2hA, b) powder P-O-S32h consolidated at 650 °C for 1 h, and then arc melting (part A), c) S-OE-S32h-S950-1hA.

7.2. Compression

The compression tests were carried out on the S-O-S32h-S950-2hA sample. The selected sample presents high hardness (Table 7-1) and promising microstructure, i.e., fine grains of the predominant multi-elemental bcc#2 phase (> 98 vol. %) and a small volume fraction of carbides (M_6C and $M_{23}C_6$) and alumina (Chapter 6).

7.2.1. Compression at room temperature

The compression test at room temperature reveals a very high strength of 2173 MPa; however, the alloy does not show any plastic deformation at this temperature (failure in the elastic region) (Fig. 7-3 and Table 7-3). The sample broke into almost a powder after the compression test (Fig. 7-4). The SEM-SE images of the fracture surface reveal a brittle morphology of the fracture under compression at room temperature (Fig. 7-5). The high compressive strength is the result of different strengthening mechanisms such as grain boundary strengthening (fine grains, the Hall-Petch relation) and solid solution strengthening in the multi-element bcc#2 phase. The grain boundary strengthening can be described by following the Hall-Petch equation [142,143]:

$$\sigma_y = \sigma_0 + k_y d^{-1/2} \tag{7.1}$$

where σ_y is a yield strength, σ_0 is a material constant (the intrinsic strength of the alloy), k_y is the Hall-Petch coefficient, and d is a mean grain size. Moreover, the small fraction of carbides and oxides could increase the strength (particle strengthening). The results of high compressive strength are in good agreement with the high hardness (Subsection 7.1).

The brittle behavior (Figs. 7-3 and 7-5) could be the effect of several factors. The sintering conditions could not be optimal to ensure the cohesion of the grains. The surface of the mechanically alloyed powder is undeniably slightly oxidized, which hinder bonding between particles during sintering. The present porosity contributes to brittle behavior. Moreover, the carbides and alumina present in the sample could cause brittleness. The fine-grain size could also contribute to the lack of plasticity (the Hall-Petch law). Senkov *et al.* [9] suggested that ductile-brittle transition temperature (DBTT) is above room temperature for refractory alloys tested in their study. It could be possible that for the alloy from the Al-Cr-Fe-Mn-Mo family, the DBTT is also above room temperature, which causes failure without plastic deformation.

Table 7-3. Compression properties of the S-O-S32h-S950-2hA alloy.

Temperature	Yield stress [MPa]	Maximum compressive stress [MPa]	Stress at strain of 20 % [MPa]	Strain at complete failure [%]
20 °C	---	2173	---	elastic region
400 °C	---	1680	---	elastic region
500 °C	1941	2100	---	3.0 %
600 °C	1022	1327	1218	21.8 %
650 °C	688	828	808	> 32 %
700 °C	519	664	663	> 32 %
800 °C	240	268	267	> 32 %

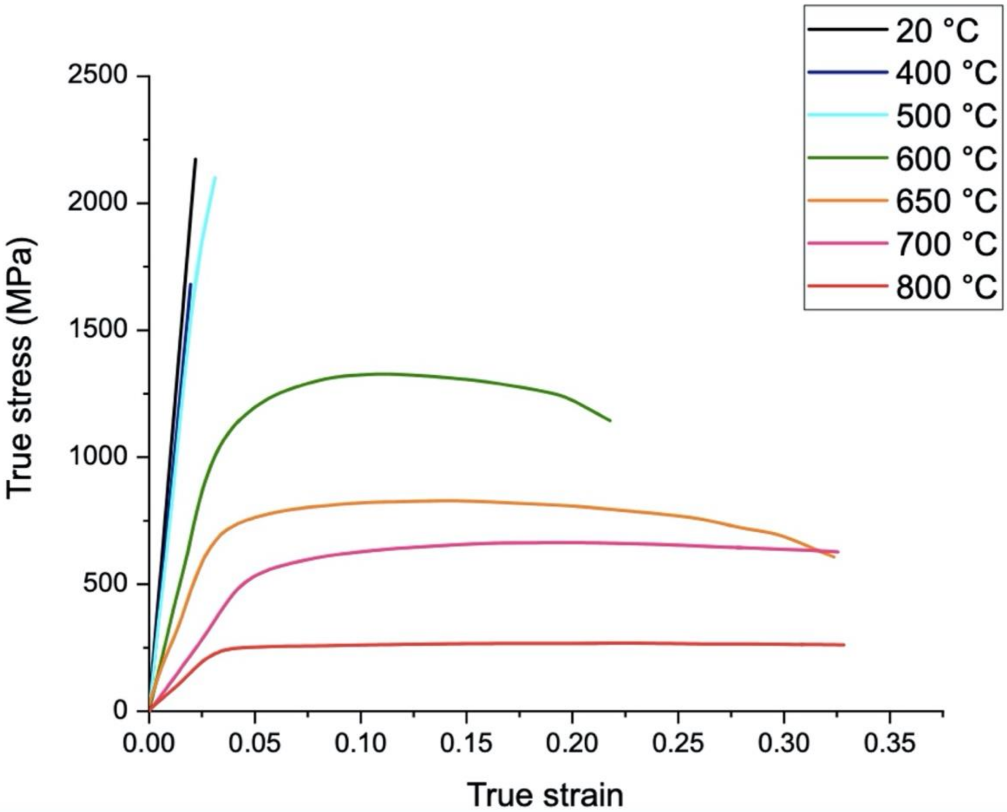

Figure 7-3. Stress-strain compression curves of the S-O-S32h-S950-2hA alloy tested at different temperatures at a strain rate of 10^{-3} s^{-1}.

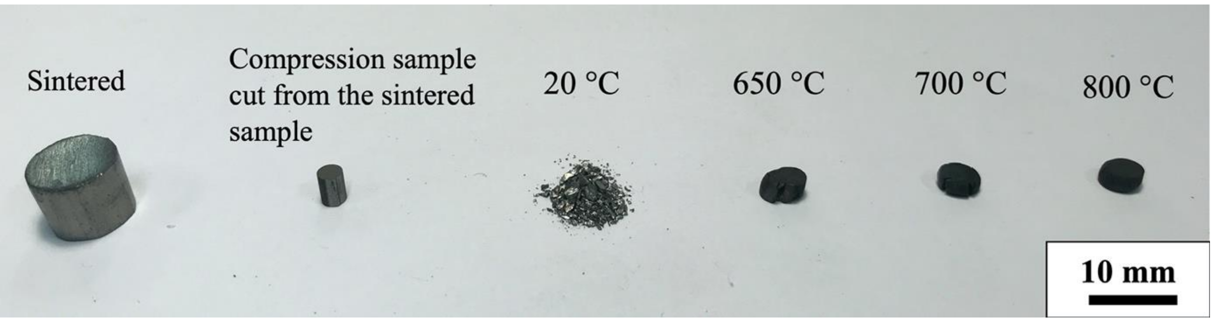

Figure 7-4. Macroscopic image of the sintered and the compressed samples tested at different temperatures.

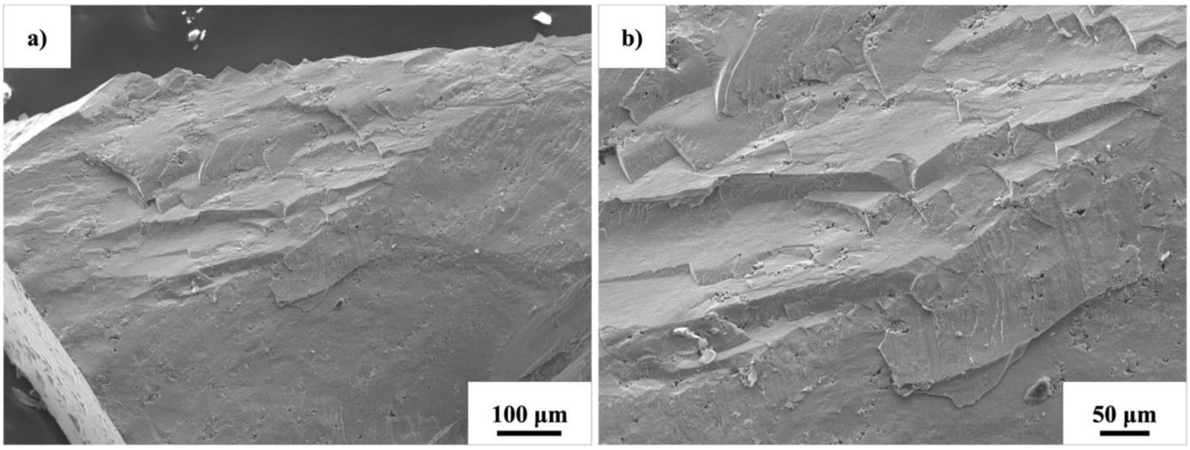

Figure 7-5. SEM-SE images of the fracture surface of the S-O-S32h-S950-2hA sample compressed at room temperature: a) lower magnification, b) higher magnification.

Many HEAs with a bcc structure as a primary phase prepared by powder metallurgy techniques (mechanical alloying followed by sintering) present high compressive strength and very limited plastic deformation at room temperature. The AlCuNiFeCr alloy prepared by mechanical alloying and spark plasma sintering (bcc (B2) + precipitates of fcc phase and $M_{23}C_6$ carbides) presents a yield strength of 1511 MPa, a compressive strength of 1960 MPa, and a plastic deformation of 2.5 % at room temperature [82]. The FeCoCrNiMnAl alloy, prepared by mechanical alloying and hot-press sintering (bcc + fcc structures and M_7C_3 and $M_{23}C_6$ carbides as well as Al_2O_3, which are the result of the contamination), presents a compressive strength of 2406 MPa; however, the alloy does not show any plasticity [85]. The alloy with a slightly lower aluminum content $FeCoCrNiMnAl_{0.7}$ presents a yield strength of 2230 MPa, a compressive strength of 2552 MPa, while the plastic strain is 1.69 % [85]. The $Al_{25}Co_{25}Cr_{25}Fe_{25}$ alloy prepared by mechanical alloying and spark plasma sintering (two bcc phases with partial B2 ordering and a small fraction of $M_{23}C_6$ carbide) presents a compressive yield strength of 3500 MPa, a maximum strength of 3920 MPa, and a plastic strain of 0.7 % [84]. It shows that the compressive properties of the S-O-S32h-S950-2hA sample tested at room temperature are comparable to many other studied HEAs containing bcc phases prepared by powder metallurgy techniques.

7.2.2. Compression at higher temperature

The compression of the produced alloy (S-O-S32h-S950-2hA) shows different behavior depending on the testing temperature (Fig. 7-3 and Table 7-3). The compression test carried out at 400 °C shows similar behavior as at room temperature, i.e., no plastic deformation and brittle fracture. The lower maximum compressive stress than at room temperature is probably caused by the presence of a defect in this particular sample. The fracture at different stress values is common in brittle samples. However, at 500 °C, the alloy starts to show some plastic behavior with small deformation, a very high yield strength of 1941 MPa, and a fracture stress of 2100 MPa. Nevertheless, both samples during compression break into powder (not shown here) similarly to the sample tested at room temperature (Fig. 7-4). The alloy tested at 600 °C reveals a high yield strength and a maximum compressive strength of 1022 MPa and 1327 MPa, respectively. The sample fractures ultimately at the strain of 21.8 %. After yielding, the stress increases due to the work hardening up to the strain of 11.1 % and then decreases due to the appearance of cracks until the complete failure. The fracture surface analyses (Fig. 7-6) reveal mostly intergranular fracture morphology; however, some signs of ductility are visible. An increase of the testing temperature to 650, 700, and

800 °C leads to a significant alloy softening (Figs. 7-3 and 7-7a). The yield strength is 688, 519, and 240 MPa, respectively, while the maximum compressive stress is 828, 664, and 268 MPa. The complete failure does not occur at least until the strain of 32 % for these samples (end of the test at this strain), but cracks and spallation near the edges of samples take place. Some cracks are visible in the macroscopic image of samples after compression at 650-800 °C (Fig. 7-4). This phenomenon is especially visible in the sample tested at 650 °C (less apparent with increasing temperature), which results in a significant decrease of true stress above the true strain of 15 % for this sample (Fig. 7-3). The spallation of the samples, which highlights a certain brittleness, was observed by other authors, e.g., [9]. The samples compressed at 700 and 800 °C present small work hardening capacity. Both samples present steady-state flow stress after reaching maximum compressive stress, which shows that the dynamic softening and work hardening reach a dynamic equilibrium [144].

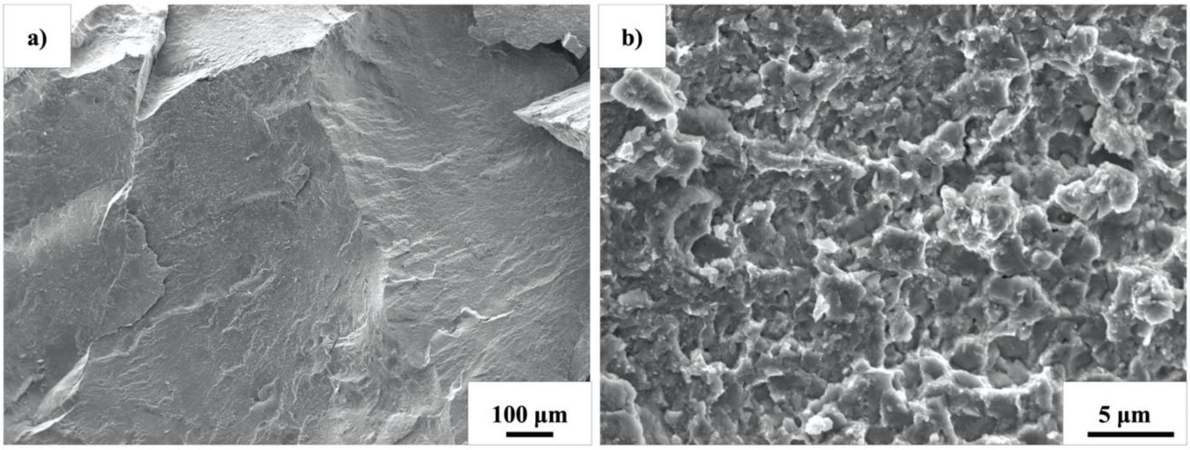

Figure 7-6. SEM-SE images of the fracture surface of the S-O-S32h-S950-2hA sample compressed at 600 °C: a) lower magnification, b) higher magnification.

The hot compression results show similarities with other HEAs prepared by mechanical alloying and sintering. Yurkova *et al.* [82] studied the AlCuNiFeCr alloy prepared by mechanical alloying and spark plasma sintering. They also observed a considerable decrease of the compressive strength from 1960 MPa with a very small plastic deformation at room temperature to 490 and 110 MPa at 600 °C and 800 °C, respectively. The relative deformation at 600 and 800 °C is above 35 %. The authors explain the alloy softening by the much lower melting temperature of a copper-rich fcc phase. The hot compression results of the refractory HfNbTaTiZr alloy prepared by mixing of powder followed by cold isostatic pressing and sintering (two bcc and hcp phases) show the maximum compressive strength of 370 MPa at 800 °C [145]. The authors suggested that fine grain size could lower compressive properties at high temperatures due to grain boundary sliding. The study of compressive properties of AlCrFeTi prepared by mechanical alloying and spark plasma sintering (C14 Laves matrix, and a smaller fraction of bcc and $L1_2$ phases) reveals some similarities with the alloy from the Al-Cr-Fe-Mn-Mo family [146]. The alloy presents high compressive strength of about 1100 MPa at room temperature, but the fracture occurs immediately after yielding. The plastic deformation does not increase significantly up to 700 °C. At a testing temperature of 800 °C, the alloy is ductile (no fracture after deformation of 50 %); nevertheless, the yield strength was 270 MPa, therefore comparable to the HEA investigated in this study. The annealing of the sintered samples at 1000 °C for 24 h increased the ductility considerably at 700 °C due to the grain growth and the increase of the volume bcc phase. The annealing of sintered samples of the Al-Cr-Fe-Mn-Mo alloys should be considered in future studies. The investigation of FeCoNiMnV alloy prepared by mechanical alloying and spark plasma sintering (fcc and two tetragonal phases) revealed a compressive strength of 1470 MPa with almost no plastic deformation at room temperature [147]. Testing at 600 and 800 °C leads to a decrease of the strength to 760 MPa and 170 MPa, respectively, while the plastic deformation increased significantly. The brittleness of the alloy was attributed mainly to the presence of the tetragonal phase. Anyway, many HEAs prepared by powder metallurgy methods show brittle behavior under compression at room temperature. Nevertheless, the refractory $Al_{0.1}$CrNbVMo alloy fabricated by mechanical alloying and spark plasma sintering (bcc and inclusions of alumina), reveal a yield strength of 2863 MPa and an elongation to failure of 8.6 % at room temperature [148]. Moreover, these alloy an exhibits excellent yield strength of 2213 MPa and an elongation to failure of 14.7 % at 800 °C.

In terms of future applications of the studied alloy, the very important parameter is specific yield strength. It allows to compare mechanical properties of materials taking into consideration their densities. The comparison of the specific yield strength of the S-O-S32h-S950-2hA alloy with other HEAs produced by powder metallurgy reveals that alloy from the Al-Cr-Fe-Mn-Mo family exceeds some other HEAs such as AlCuNiFeCr or FeCoNiMnV (Fig. 7-7b). Nevertheless, the $Al_{0.1}$CrNbVMo presents a higher specific yield strength (but the plastic deformation is rather limited). However, the further optimization of sintering conditions could enhance the mechanical properties of studied alloy in the future.

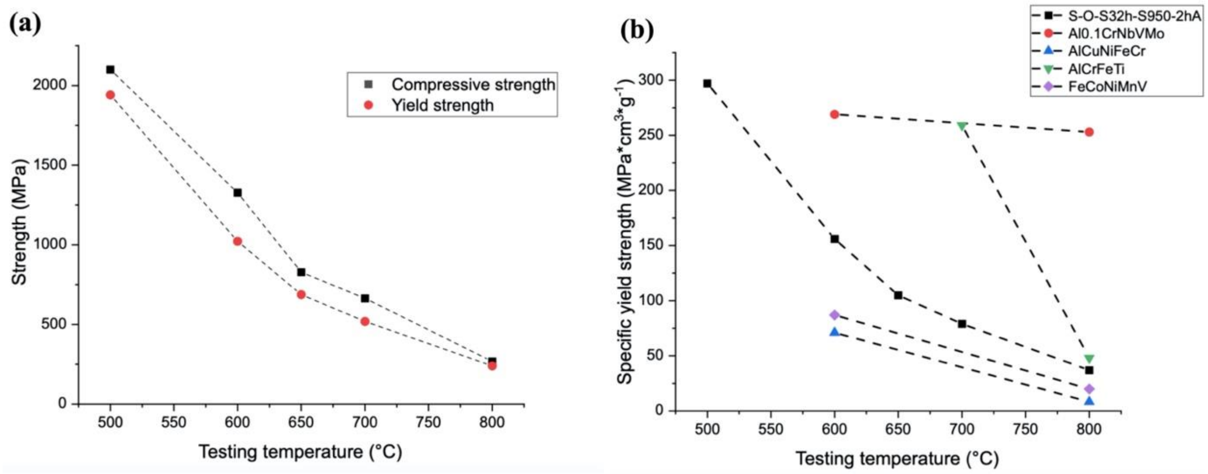

Figure 7-7. Compressive strength and yield strength of the S-O-S32h-S950-2hA alloy as a function of testing temperature (500, 600, 650, 700, 800 °C) (a) and the specific yield strength of the S-O-S32h-S950-2hA alloy compared to other HEAs produced by powder metallurgy (b): Al0.1CrNbVMo [148], AlCuNiFeCr [82], AlCrFeTi [146], FeCoNiMnV [147].

7.3. Summary and perspectives

The micro-indentation and compression tests show a very high strength of bulk samples. The hardness of the sintered optimized powder (P-O-S32h) samples decreases with increasing sintering temperature (from about 950 HV$_{1N}$ after 950 °C to about 490 HV$_{1N}$ after 1250 °C), which is the result mainly of grain growth and coalescence of porosity. It seems that even if carbides and oxides could increase the strength significantly, the multi-element bcc#2 phase presented a good level of hardness due to the solid solution strengthening. The hardness of the S-EQ-R70hS4h-S950-1hA (starting equiatomic composition) is considerably higher than other alloys due to very high M$_6$C carbide fraction. The hardness of the sample containing the χ phase (S-OE-S32h-S950-1hA) is similar to the sample S-O-S32h-S950-1hA containing the major bcc#2 phase and a small fraction of carbides, which confirms the high mechanical resistance of the multi-element bcc#2 phase. The hardness results of the sintered optimized powder (P-O-S32h) are very promising, and thus one of these types of samples, sintered at 950 °C, was chosen for the compression test.

The hot compression test of the S-O-S32h-S950-2hA sample reveals interesting results. The produced alloy shows very high compressive strength (up to 2173 MPa) without showing any plasticity at room temperature and 400 °C. The observations of the fracture surface show brittle morphology at room temperature. The high compressive strength is the result of fine grain size (the Hall–Petch relation), high hardness of the multi-element bcc#2 phase (solid solution strengthening), and the presence of carbides and alumina, which block dislocations movements at grains boundaries. The near-complete lack of plastic deformation, which was also found in other HEAs prepared by powder metallurgy [82,85,146,147], could be related to several coexisting phenomena, i.e., porosity, not complete bonding between particles, small grain size, presence of carbides and alumina. Long-time annealing treatment could be performed in future studies to investigate its effect on the alloy ductility [146]. Moreover, other powder consolidation techniques, such as hot extrusion [66] or high-pressure torsion, followed by annealing [149], which often enable to obtain high strength and ductility, should be performed in the future. The sample compressed at 500 °C starts to reveal small plastic deformation while maintaining high compressive strength. An increase of testing temperature to 600 °C and above leads to the plastic deformation of the samples; however, the decrease of the compressive strength is significant. The rise of plastic deformation with increasing temperature is commonly observed [82,146,147]. Malek *et al.* [145] suggested that fine grain size could not be beneficial for the compressive strength at high temperatures due to grain boundary sliding. Nevertheless, at 650 °C, the alloy exhibits a yield strength of 688 MPa, a compressive strength of 837 MPa, and a sufficient plastic deformation (> 32 %). The results show promising compressive properties of the S-O-S32h-S950-2hA alloy, especially at 600-700 °C. The specific yield in strength at these temperatures exceeds many other HEAs prepared by powder metallurgy techniques.

Conclusions and perspectives

The objective of this work was to prepare a novel high entropy alloy by powder metallurgy techniques with a promising microstructure (body-centered cubic phase) and good mechanical properties. HEAs from the novel Al-Cr-Fe-Mn-Mo family were prepared by mechanical alloying of elemental powders followed by hot press sintering. The chemical composition was optimized by the parametric approach calculations. The microstructure of the powders and bulk samples were investigated by X-Ray Diffraction (XRD), Mössbauer spectrometry, Scanning Electron Microscope (SEM), Transmission Electron Microscope (TEM), both microscopes equipped with Energy-Dispersive X-ray spectroscopy (EDX), and Electron BackScatter Diffraction (EBSD). The phase transformations were studied by Differential Scanning Calorimetry (DSC). The density of the samples was measured by Archimedes' principle. The mechanical properties were evaluated by micro-indentation tests and compression tests of the selected alloy at the temperature range from room temperature to 800 °C.

The chosen Al-Cr-Fe-Mn-Mo HEA family was quickly evaluated by Senkov *et al.* [22] using CALPHAD in thermodynamic equilibrium conditions before this study. The predictions for the equiatomic composition are very promising – major bcc phase and $AlMo_3$ below 1041 °C. The parametric approach calculations for the equiatomic alloy reveal electronegativity difference higher than the value commonly found in the literature for HEAs. The high electronegativity difference could facilitate the formation of intermetallic compounds instead of solid solution phases. The composition was optimized by modifying the content of elements (mainly increasing iron and decreasing molybdenum). The optimized alloy presents all parameters in good range to form HEA. The composition (named experimentally optimized) developed based on the experimental results (i.e., TEM-EDX analysis of the bcc#2 phase composition in the sintered alloy) also reveals good values of all parameters.

The mechanical alloying of raw powders of three different chemical compositions was performed in three different mills: planetary (RETSCH PM-100) and two vibrational (SPEX and CryoMill). The balls-powder-vial shocks in SPEX are more severe than in RETSCH or CryoMill; hence, it enables to produce a powder with better chemical homogeneity. However, the contamination by iron from balls and vial materials occurs. The results reveal that the contamination depends greatly on the chemical composition of the powder. It is the highest for the alloy with the equiatomic content of elements in raw powder, probably due to a high fraction of big and hard particles of molybdenum, which cause significant erosion of balls and vials. Therefore, the milling should be performed in RETSCH (low iron contamination) for a long time (70 h), followed by a short final homogenization in SPEX. The milling of the two other compositions was performed in SPEX because the iron contamination is relatively small (lower erosion due to lower molybdenum content). The optimized mechanical alloying results reveal the formation of two disordered bcc phases – bcc#1 (3.13-3.14 Å) and bcc#2 (2.87-2.93 Å). The powder is homogeneous at the SEM scale. However, in the optimized mechanically alloyed powder, TEM analyses coupled with EDX show a major phase (bcc#2), which contains all elements, and a smaller fraction of a molybdenum rich phase (bcc#1).

In the objective to determine the effect of sintering temperature on the powder microstructure, heat treatment of three compositions of powders milled in the optimized conditions was performed. All powders reveal several phase transformations. The bcc#1 disappears after the annealing above 650 °C. The intermetallic χ phase (8.98 Å, space group: I-43m (217)) appears as a major phase after annealing between 650 and 850 °C, while bcc#2 seems to decrease. The appearance of the χ phase could be the result of a carbon contamination (MA process), which can dissolve and stabilize it. After annealing at 950 °C, the microstructures are more promising, especially the optimized alloy (A-O-S32h-950), for which the predominant phase is the disordered multi-element bcc#2 phase (a =2.91 Å) and a small fraction of carbides (M_6C and $M_{23}C_6$) and oxides (Al_2O_3) was detected. The melting temperature of the bcc#2 was determined at 1445 °C by DSC analysis. The successful fabrication of the annealed powder with a major multi-element disordered body-centered cubic phases and a very small fraction of phases resulting from the contamination is an essential step towards the choice of the sintering conditions. In two other annealed powders at 950 °C, i.e., equiatomic powder (A-EQ-R70hS4h-950) and experimentally optimized powder (A-OE-S32h-950), a high-volume fraction of carbide or χ phase were found, respectively; therefore, the microstructures are not as promising as the optimized powder (A-O-S32h-950).

After sintering, all bulk samples present a major disordered multi-elemental bcc#2 phase (a=2.91-2.92 Å). The most promising sample of the optimized powder sintered at 950 °C (S-O-S32h-S950-2hA) shows a very interesting microstructure, i.e., fine grain size (average about 220 nm), more than 98.0 vol. % of the bcc#2 phase and a small fraction of carbides (M_6C and $M_{23}C_6$) and oxide (Al_2O_3). Sintering at higher temperatures leads to an increase of volume fraction of carbides and oxides as well as average grain size. The other sintered powders equiatomic (S-EQ-R70hS4h-S950-1hA) and experimentally optimized (S-OE-S32h-S950-1hA) show less promising microstructure due to the presence of a high-volume fraction of carbides or χ phase, respectively. All samples present good densification, more than 97 % of the theoretical density. The formation of the major disordered multi-elemental bcc#2 phase is undoubtedly a highlight of this work and shows the achievement of the objectives of the thesis. This phase is stable in the sintered sample after annealing for 10 h at 950 °C. The bcc#2 phase presents a relatively wide range of chemical composition in the produced bulk samples depending on the initial powder composition and consolidation conditions, i.e., Al (16–21 at. %), Cr (14–26 at. %), Fe (26–44 at. %), Mn (11–24 at. %), and (4–11 at. %). Future studies should focus mainly on the bcc#2 phase.

The bulk samples present very high hardness. The hardness is the highest after sintering at 950 °C, for the sintered optimized powders (P-O-S32h), is with a value of about 950 HV_{1N}. The increase of sintering temperature leads to a decrease in the sample hardness (grain growth, coalescence of porosity). The carbides and oxides could increase substantially the mechanical strength. However, the high hardness of the samples is believed to be significantly related to the good strength of the multi-element bcc#2 phase (solid solution strengthening) and fine grain size. The compression test at room temperature of the sample S-O-S32h-S950-2hA reveals a very high compressive strength of 2173 MPa, which is the effect of fine grain size, the good mechanical resistance of bcc#2, and a small presence of alumina and carbides. However, the fracture occurs in the elastic region of the stress-strain curve. Thus, the sample shows no plasticity at room temperature. It could be related to the porosity, the not completed bonding of powder particles during sintering (due to oxide layer on the surface of powders), presence of carbides/oxides, and fine grain size. The alloy starts to show some plastic behavior at 500 °C, but it breaks shortly after yielding at 1941 MPa (maximum strength is 2100 MPa). The increase of testing temperature leads to a decrease of the yield strength and the maximum compressive strength, but the plastic deformation increases significantly (21.8 % at 600 °C, and more than 32 % above 650 °C). The results show that the alloy presents promising compressive properties, especially between 600 and 700 °C, e.g., yield strength of 1022 MPa at 600° C. The specific yield strength values between 600-700 °C are very competitive compared to other HEAs produced by powder metallurgy techniques.

The early stage of the Al-Cr-Fe-Mn-Mo family study does not allow us to identify specific applications for this HEA; however, high hardness and strength reveal a promising future after further investigations. In this thesis, the preparation of samples from the Al-Cr-Fe-Mn-Mo family by powder metallurgy techniques (mechanical alloying and sintering) was presented. Produced samples show a major unique multi-element bcc#2 phase and a small fraction of phases resulting from the contamination (carbides and oxides). Moreover, samples reveal very high hardness and high compressive strength. Nevertheless, different phenomena in the Al-Cr-Fe-Mn-Mo family are not fully understood and demand further research. Especially, the compositional range and thermal stability after a long time annealing of the bcc#2 phase should be studied further. The crucial question arises if the bcc#2 phase can be stable as a single phase in the studied alloys without carbides or oxides. Ideally, the bulk samples without any carbon and oxygen traces should be synthesized to investigate this aspect. The mechanical alloying could be further optimized. It could consist of the use of balls and vials made by different materials, not containing carbon. The sintering by the use of other methods, such as SPS, should be carried out to compare and eventually improve the microstructure and properties or limit contamination. The heat treatment after sintering should be considered. Wear and corrosion resistance could also be evaluated. Moreover, hot extrusion or high-pressure torsion followed by an annealing should be performed to eliminate porosity and increase bonding between powder particles. Then, tensile tests should be carried out to evaluate mechanical properties fully.

References

[1] B. Cantor, I.T.H. Chang, P. Knight, A.J.B. Vincent, Microstructural development in equiatomic multicomponent alloys, Mater. Sci. Eng. A. 375–377 (2004) 213–218. https://doi.org/10.1016/j.msea.2003.10.257.

[2] J.-W. Yeh, S.-K. Chen, S.-J. Lin, J.-Y. Gan, T.-S. Chin, T.-T. Shun, C.-H. Tsau, S.-Y. Chang, Nanostructured High-Entropy Alloys with Multiple Principal Elements: Novel Alloy Design Concepts and Outcomes, Adv. Eng. Mater. 6 (2004) 299–303. https://doi.org/10.1002/adem.200300567.

[3] J.W. Yeh, Alloy design strategies and future trends in high-entropy alloys, JOM. 65 (2013) 1759–1771. https://doi.org/10.1007/s11837-013-0761-6.

[4] M.C. Gao, P.K. Liaw, J.W. Yeh, Y. Zhang, High-entropy alloys: Fundamentals and applications, Springer International Publishing, 2016. https://doi.org/10.1007/978-3-319-27013-5.

[5] E.P. George, D. Raabe, R.O. Ritchie, High-entropy alloys, Nat. Rev. Mater. 4 (2019) 515–534. https://doi.org/10.1038/s41578-019-0121-4.

[6] B. Gludovatz, A. Hohenwarter, D. Catoor, E.H. Chang, E.P. George, R.O. Ritchie, A fracture-resistant high-entropy alloy for cryogenic applications, Science (80-.). 345 (2014) 1153–1158. https://doi.org/10.1126/science.1254581.

[7] T.K. Tsao, A.C. Yeh, C.M. Kuo, K. Kakehi, H. Murakami, J.W. Yeh, S.R. Jian, The High Temperature Tensile and Creep Behaviors of High Entropy Superalloy, Sci. Rep. 7 (2017) 1–9. https://doi.org/10.1038/s41598-017-13026-7.

[8] S. Chen, W. Li, X. Xie, J. Brechtl, B. Chen, P. Li, G. Zhao, F. Yang, J. Qiao, K.A. Dahmen, P.K. Liaw, Nanoscale serration and creep characteristics of Al0.5CoCrCuFeNi high-entropy alloys, J. Alloys Compd. 752 (2018) 464–475. https://doi.org/10.1016/j.jallcom.2018.04.137.

[9] O.N. Senkov, G.B. Wilks, J.M. Scott, D.B. Miracle, Mechanical properties of Nb25Mo25Ta 25W25 and V20Nb20Mo 20Ta20W20 refractory high entropy alloys, Intermetallics. 19 (2011) 698–706. https://doi.org/10.1016/j.intermet.2011.01.004.

[10] S.Q. Xia, X. Yang, T.F. Yang, S. Liu, Y. Zhang, Irradiation Resistance in AlxCoCrFeNi High Entropy Alloys, JOM. 67 (2015) 2340–2344. https://doi.org/10.1007/s11837-015-1568-4.

[11] O. El-Atwani, N. Li, M. Li, A. Devaraj, J.K.S. Baldwin, M.M. Schneider, D. Sobieraj, J.S. Wróbel, D. Nguyen-Manh, S.A. Maloy, E. Martinez, Outstanding radiation resistance of tungsten-based high-entropy alloys, Sci. Adv. 5 (2019) eaav2002. https://doi.org/10.1126/sciadv.aav2002.

[12] S.S. Nene, K. Liu, M. Frank, R.S. Mishra, R.E. Brennan, K.C. Cho, Z. Li, D. Raabe, Enhanced strength and ductility in a friction stir processing engineered dual phase high entropy alloy, Sci. Rep. 7 (2017) 16167. https://doi.org/10.1038/s41598-017-16509-9.

[13] Y.L. Chou, Y.C. Wang, J.W. Yeh, H.C. Shih, Pitting corrosion of the high-entropy alloy Co1.5CrFeNi1.5Ti0.5Mo0.1 in chloride-containing sulphate solutions, Corros. Sci. 52 (2010) 3481–3491. https://doi.org/10.1016/j.corsci.2010.06.025.

[14] Y. Shi, B. Yang, X. Xie, J. Brechtl, K.A. Dahmen, P.K. Liaw, Corrosion of Al xCoCrFeNi high-entropy alloys: Al-content and potential scan-rate dependent pitting behavior, Corros. Sci. 119 (2017) 33–45. https://doi.org/10.1016/j.corsci.2017.02.019.

[15] H. Luo, W. Lu, X. Fang, D. Ponge, Z. Li, D. Raabe, Beating hydrogen with its own weapon: Nano-twin gradients enhance embrittlement resistance of a high-entropy alloy, Mater. Today. 21 (2018) 1003–1009. https://doi.org/10.1016/j.mattod.2018.07.015.

[16] H. Luo, Z. Li, D. Raabe, Hydrogen enhances strength and ductility of an equiatomic high-entropy alloy, Sci. Rep. 7 (2017) 9892. https://doi.org/10.1038/s41598-017-

10774-4.
[17] Y. Zhang, T.T. Zuo, Z. Tang, M.C. Gao, K.A. Dahmen, P.K. Liaw, Z.P. Lu, Microstructures and properties of high-entropy alloys, Prog. Mater. Sci. 61 (2014) 1–93. https://doi.org/10.1016/j.pmatsci.2013.10.001.
[18] H.L. Chen, H. Mao, Q. Chen, Database development and Calphad calculations for high entropy alloys: Challenges, strategies, and tips, Mater. Chem. Phys. 210 (2018) 279–290. https://doi.org/10.1016/j.matchemphys.2017.07.082.
[19] S. Yang, J. Lu, F. Xing, L. Zhang, Y. Zhong, Revisit the VEC rule in high entropy alloys (HEAs) with high-throughput CALPHAD approach and its applications for material design-A case study with Al–Co–Cr–Fe–Ni system, Acta Mater. 192 (2020) 11–19. https://doi.org/10.1016/j.actamat.2020.03.039.
[20] M. Vaidya, G.M. Muralikrishna, B.S. Murty, High-entropy alloys by mechanical alloying: A review, J. Mater. Res. 34 (2019) 664–686. https://doi.org/10.1557/jmr.2019.37.
[21] J.M. Torralba, P. Alvaredo, A. García-Junceda, High-entropy alloys fabricated via powder metallurgy. A critical review, Powder Metall. 62 (2019) 84–114. https://doi.org/10.1080/00325899.2019.1584454.
[22] O.N. Senkov, J.D. Miller, D.B. Miracle, C. Woodward, Accelerated exploration of multi-principal element alloys for structural applications, Calphad Comput. Coupling Phase Diagrams Thermochem. 50 (2015) 32–48. https://doi.org/10.1016/j.calphad.2015.04.009.
[23] D.B. Miracle, O.N. Senkov, A critical review of high entropy alloys and related concepts, Acta Mater. 122 (2017) 448–511. https://doi.org/10.1016/j.actamat.2016.08.081.
[24] R. Kozak, A. Slogubenko, W. Steurer, Single-phase high-entropy alloys – an overview, Zeitschrift Für Krist. . 230 (2015) 55–68.
[25] J.-W. Yeh, Recent Progress in High Entropy Alloys, Ann. Chim. – Sci. Des Matériaux. 31 (2006) 633–648. https://doi.org/doi.org/10.3166/acsm.31.633-648.
[26] D.B. Miracle, High-Entropy Alloys: A Current Evaluation of Founding Ideas and Core Effects and Exploring "Nonlinear Alloys," JOM. 69 (2017) 2130–2136. https://doi.org/10.1007/s11837-017-2527-z.
[27] E.J. Pickering, N.G. Jones, High-entropy alloys: a critical assessment of their founding principles and future prospects, Int. Mater. Rev. 61 (2016) 183–202. https://doi.org/10.1080/09506608.2016.1180020.
[28] E.J. Pickering, R. Muñoz-Moreno, H.J. Stone, N.G. Jones, Precipitation in the equiatomic high-entropy alloy CrMnFeCoNi, Scr. Mater. 113 (2016) 106–109. https://doi.org/10.1016/j.scriptamat.2015.10.025.
[29] K.Y. Tsai, M.H. Tsai, J.W. Yeh, Sluggish diffusion in Co-Cr-Fe-Mn-Ni high-entropy alloys, Acta Mater. 61 (2013) 4887–4897. https://doi.org/10.1016/j.actamat.2013.04.058.
[30] J. Dąbrowa, M. Zajusz, W. Kucza, G. Cieślak, K. Berent, T. Czeppe, T. Kulik, M. Danielewski, Demystifying the sluggish diffusion effect in high entropy alloys, J. Alloys Compd. 783 (2019) 193–207. https://doi.org/10.1016/j.jallcom.2018.12.300.
[31] S. Ranganathan, Alloyed pleasures: Multimetallic cocktails, Curr. Sci. 85 (2003) 1404–1406.
[32] S. Gorsse, D.B. Miracle, O.N. Senkov, Mapping the world of complex concentrated alloys, Acta Mater. 135 (2017) 177–187. https://doi.org/10.1016/j.actamat.2017.06.027.
[33] S. Varalakshmi, M. Kamaraj, B.S. Murty, Synthesis and characterization of nanocrystalline AlFeTiCrZnCu high entropy solid solution by mechanical alloying, J.

Alloys Compd. 460 (2008) 253–257. https://doi.org/10.1016/j.jallcom.2007.05.104.
[34] Y. Ma, B. Jiang, C. Li, Q. Wang, C. Dong, P. Liaw, F. Xu, L. Sun, The BCC/B2 Morphologies in AlxNiCoFeCr High-Entropy Alloys, Metals (Basel). 7 (2017) 57. https://doi.org/10.3390/met7020057.
[35] T. Yang, S. Xia, S. Liu, C. Wang, S. Liu, Y. Fang, Y. Zhang, J. Xue, S. Yan, Y. Wang, Precipitation behavior of AlxCoCrFeNi high entropy alloys under ion irradiation, Sci. Rep. 6 (2016) 32146. https://doi.org/10.1038/srep32146.
[36] M. Li, J. Gazquez, A. Borisevich, R. Mishra, K.M. Flores, Evaluation of microstructure and mechanical property variations in AlxCoCrFeNi high entropy alloys produced by a high-throughput laser deposition method, Intermetallics. 95 (2018) 110–118. https://doi.org/10.1016/j.intermet.2018.01.021.
[37] J.W. Qiao, M.L. Bao, Y.J. Zhao, H.J. Yang, Y.C. Wu, Y. Zhang, J.A. Hawk, M.C. Gao, Rare-earth high entropy alloys with hexagonal close-packed structure, J. Appl. Phys. 124 (2018) 195101. https://doi.org/10.1063/1.5051514.
[38] K.M. Youssef, A.J. Zaddach, C. Niu, D.L. Irving, C.C. Koch, A Novel Low-Density, High-Hardness, High-entropy Alloy with Close-packed Single-phase Nanocrystalline Structures, Mater. Res. Lett. 3 (2015) 95–99. https://doi.org/10.1080/21663831.2014.985855.
[39] K.J. Laws, C. Crosby, A. Sridhar, P. Conway, L.S. Koloadin, M. Zhao, S. Aron-Dine, L.C. Bassman, High entropy brasses and bronzes - Microstructure, phase evolution and properties, J. Alloys Compd. 650 (2015) 949–961. https://doi.org/10.1016/j.jallcom.2015.07.285.
[40] F. Thiel, D. Geissler, K. Nielsch, A. Kauffmann, S. Seils, M. Heilmaier, D. Utt, K. Albe, M. Motylenko, D. Rafaja, J. Freudenberger, Origins of strength and plasticity in the precious metal based high-entropy alloy AuCuNiPdPt, Acta Mater. 185 (2020) 400–411. https://doi.org/10.1016/j.actamat.2019.12.020.
[41] F. Otto, A. Dlouhý, K.G. Pradeep, M. Kuběnová, D. Raabe, G. Eggeler, E.P. George, Decomposition of the single-phase high-entropy alloy CrMnFeCoNi after prolonged anneals at intermediate temperatures, Acta Mater. 112 (2016) 40–52. https://doi.org/10.1016/j.actamat.2016.04.005.
[42] Z. Wu, H. Bei, G.M. Pharr, E.P. George, Temperature dependence of the mechanical properties of equiatomic solid solution alloys with face-centered cubic crystal structures, Acta Mater. 81 (2014) 428–441. https://doi.org/10.1016/j.actamat.2014.08.026.
[43] Y. Deng, C.C. Tasan, K.G. Pradeep, H. Springer, A. Kostka, D. Raabe, Design of a twinning-induced plasticity high entropy alloy, Acta Mater. 94 (2015) 124–133. https://doi.org/10.1016/j.actamat.2015.04.014.
[44] Z. Li, K.G. Pradeep, Y. Deng, D. Raabe, C.C. Tasan, Metastable high-entropy dual-phase alloys overcome the strength-ductility trade-off, Nature. 534 (2016) 227–230. https://doi.org/10.1038/nature17981.
[45] M.H. Tsai, J.W. Yeh, High-entropy alloys: A critical review, Mater. Res. Lett. 2 (2014) 107–123. https://doi.org/10.1080/21663831.2014.912690.
[46] I. Kunce, M. Polanski, K. Karczewski, T. Plocinski, K.J. Kurzydlowski, Microstructural characterisation of high-entropy alloy AlCoCrFeNi fabricated by laser engineered net shaping, J. Alloys Compd. 648 (2015) 751–758. https://doi.org/10.1016/j.jallcom.2015.05.144.
[47] A. Gali, E.P. George, Tensile properties of high- and medium-entropy alloys, Intermetallics. 39 (2013) 74–78. https://doi.org/10.1016/j.intermet.2013.03.018.
[48] O.N. Senkov, G.B. Wilks, D.B. Miracle, C.P. Chuang, P.K. Liaw, Refractory high-entropy alloys, Intermetallics. 18 (2010) 1758–1765.

https://doi.org/10.1016/j.intermet.2010.05.014.
[49] B.S. Murty, J.W. Yeh, S. Ranganathan, High Entropy Alloys, Elsevier, 2014. https://doi.org/10.1016/C2013-0-14235-3.
[50] J.S. Benjamin, Dispersion strengthened superalloys by mechanical alloying, Metall. Trans. 1 (1970) 2943–2951. https://doi.org/10.1007/BF03037835.
[51] Y.B. Peng, W. Zhang, X.L. Mei, H.J. Wang, M.Y. Zhang, L. Wang, X.F. Li, Y. Hu, Microstructures and mechanical properties of FeCoCrNi-Mo High entropy alloys prepared by spark plasma sintering and vacuum hot-pressed sintering, Mater. Today Commun. 24 (2020) 101009. https://doi.org/10.1016/j.mtcomm.2020.101009.
[52] A.S. Sharma, S. Yadav, K. Biswas, B. Basu, High-entropy alloys and metallic nanocomposites: Processing challenges, microstructure development and property enhancement, Mater. Sci. Eng. R Reports. 131 (2018) 1–42. https://doi.org/10.1016/j.mser.2018.04.003.
[53] C.C. Koch, Nanocrystalline high-entropy alloys, J. Mater. Res. 32 (2017) 3435–3444. https://doi.org/10.1557/jmr.2017.341.
[54] C.S. Chen, C.C. Yang, H.Y. Chai, J.W. Yeh, J.L.H. Chau, Novel cermet material of WC/multi-element alloy, Int. J. Refract. Met. Hard Mater. 43 (2014) 200–204. https://doi.org/10.1016/j.ijrmhm.2013.11.005.
[55] P.K. Huang, J.W. Yeh, Inhibition of grain coarsening up to 1000 °C in (AlCrNbSiTiV)N superhard coatings, Scr. Mater. 62 (2010) 105–108. https://doi.org/10.1016/j.scriptamat.2009.09.015.
[56] K. von Fieandt, E.M. Paschalidou, A. Srinath, P. Soucek, L. Riekehr, L. Nyholm, E. Lewin, Multi-component (Al,Cr,Nb,Y,Zr)N thin films by reactive magnetron sputter deposition for increased hardness and corrosion resistance, Thin Solid Films. 693 (2020) 137685. https://doi.org/10.1016/j.tsf.2019.137685.
[57] D.-S. Chen, M.-K. Chen, S.-Y. Chang, Multiprincipal-Element AlCrTaTiZr-Nitride Nanocomposite Film of Extremely High Thermal Stability as Diffusion Barrier for Cu Metallization, in: ECS Trans., The Electrochemical Society, 2009: pp. 751–762. https://doi.org/10.1149/1.3122130.
[58] S. Guo, C.T. Liu, Phase stability in high entropy alloys: Formation of solid-solution phase or amorphous phase, Prog. Nat. Sci. Mater. Int. 21 (2011) 433–446. https://doi.org/10.1016/S1002-0071(12)60080-X.
[59] Y. Zhang, Y.J. Zhou, J.P. Lin, G.L. Chen, P.K. Liaw, Solid-Solution Phase Formation Rules for Multi-component Alloys, Adv. Eng. Mater. 10 (2008) 534–538. https://doi.org/10.1002/adem.200700240.
[60] X. Yang, S.Y. Chen, J.D. Cotton, Y. Zhang, Phase Stability of Low-Density, Multiprincipal Component Alloys Containing Aluminum, Magnesium, and Lithium, JOM. 66 (2014) 2009–2020. https://doi.org/10.1007/s11837-014-1059-z.
[61] S. Guo, C. Ng, J. Lu, C.T. Liu, Effect of valence electron concentration on stability of fcc or bcc phase in high entropy alloys, in: J. Appl. Phys., American Institute of Physics, 2011: p. 103505. https://doi.org/10.1063/1.3587228.
[62] S. Gorsse, F. Tancret, Current and emerging practices of CALPHAD toward the development of high entropy alloys and complex concentrated alloys, J. Mater. Res. 33 (2018) 2899–2923. https://doi.org/10.1557/jmr.2018.152.
[63] M. Eumann, G. Sauthoff, M. Palm, Re-evaluation of phase equilibria in the Al-Mo system, Int. J. Mater. Res. 97 (2006) 1502–1511. https://doi.org/10.3139/146.101412.
[64] S. Riva, S.G.R. Brown, N.P. Lavery, A. Tudball, K. V. Yusenko, Spark Plasma Sintering of High Entropy Alloys, in: Spark Plasma Sinter. Mater., Springer International Publishing, 2019: pp. 517–538. https://doi.org/10.1007/978-3-030-05327-7_18.

[65] J. Málek, J. Zýka, F. Lukáč, M. Vilémová, T. Vlasák, J. Čížek, O. Melikhova, A. Macháčková, H.-S. Kim, The Effect of Processing Route on Properties of HfNbTaTiZr High Entropy Alloy, Materials (Basel). 12 (2019) 4022. https://doi.org/10.3390/ma12234022.

[66] B. Liu, J. Wang, Y. Liu, Q. Fang, Y. Wu, S. Chen, C.T. Liu, Microstructure and mechanical properties of equimolar FeCoCrNi high entropy alloy prepared via powder extrusion, Intermetallics. 75 (2016) 25–30. https://doi.org/10.1016/j.intermet.2016.05.006.

[67] D. Yim, W. Kim, S. Praveen, M.J. Jang, J.W. Bae, J. Moon, E. Kim, S.J. Hong, H.S. Kim, Shock wave compaction and sintering of mechanically alloyed CoCrFeMnNi high-entropy alloy powders, Mater. Sci. Eng. A. 708 (2017) 291–300. https://doi.org/10.1016/j.msea.2017.09.132.

[68] S. Chen, Y. Tong, P. Liaw, Additive Manufacturing of High-Entropy Alloys: A Review, Entropy. 20 (2018) 937. https://doi.org/10.3390/e20120937.

[69] J. Li, Y. Huang, X. Meng, Y. Xie, A Review on High Entropy Alloys Coatings: Fabrication Processes and Property Assessment, Adv. Eng. Mater. 21 (2019) 1900343. https://doi.org/10.1002/adem.201900343.

[70] M. Sherif El-Eskandarany, Mechanical Alloying, Elsevier, 2015. https://doi.org/10.1016/C2012-0-06192-3.

[71] Y. Xu, S. Zhou, B. Liao, S. Zhao, X. Dai, D. Chen, Effect of milling time on the microstructure and magnetic properties of amorphous Ti50Fe50 alloys prepared by mechanical alloying, J. Mater. Res. Technol. 8 (2019) 3929–3935. https://doi.org/10.1016/j.jmrt.2019.07.001.

[72] K.G. Pradeep, N. Wanderka, P. Choi, J. Banhart, B.S. Murty, D. Raabe, Atomic-scale compositional characterization of a nanocrystalline AlCrCuFeNiZn high-entropy alloy using atom probe tomography, Acta Mater. 61 (2013) 4696–4706. https://doi.org/10.1016/j.actamat.2013.04.059.

[73] S.H. Joo, H. Kato, M.J. Jang, J. Moon, E.B. Kim, S.J. Hong, H.S. Kim, Structure and properties of ultrafine-grained CoCrFeMnNi high-entropy alloys produced by mechanical alloying and spark plasma sintering, J. Alloys Compd. 698 (2017) 591–604. https://doi.org/10.1016/j.jallcom.2016.12.010.

[74] I. Moravcik, J. Cizek, P. Gavendova, S. Sheikh, S. Guo, I. Dlouhy, Effect of heat treatment on microstructure and mechanical properties of spark plasma sintered AlCoCrFeNiTi0.5 high entropy alloy, Mater. Lett. 174 (2016) 53–56. https://doi.org/10.1016/j.matlet.2016.03.077.

[75] I. Moravcik, J. Cizek, J. Zapletal, Z. Kovacova, J. Vesely, P. Minarik, M. Kitzmantel, E. Neubauer, I. Dlouhy, Microstructure and mechanical properties of Ni1,5Co1,5CrFeTi0,5 high entropy alloy fabricated by mechanical alloying and spark plasma sintering, Mater. Des. 119 (2017) 141–150. https://doi.org/10.1016/j.matdes.2017.01.036.

[76] P. Wang, H. Cai, S. Zhou, L. Xu, Processing, microstructure and properties of Ni1.5CoCuFeCr0.5−xVxhigh entropy alloys with carbon introduced from process control agent, J. Alloys Compd. 695 (2017) 462–475. https://doi.org/10.1016/j.jallcom.2016.10.288.

[77] S. Thangaraju, E. Bouzy, A. Hazotte, Phase Stability of a Mechanically Alloyed CoCrCuFeNi High Entropy Alloy, Adv. Eng. Mater. 19 (2017) 1700095. https://doi.org/10.1002/adem.201700095.

[78] Y. Long, K. Su, J. Zhang, X. Liang, H. Peng, X. Li, Enhanced Strength of a Mechanical Alloyed NbMoTaWVTi Refractory High Entropy Alloy, Materials (Basel). 11 (2018) 669. https://doi.org/10.3390/ma11050669.

[79] H. CHENG, Y.C. XIE, Q.H. TANG, C. RAO, P.Q. DAI, Microstructure and mechanical properties of FeCoCrNiMn high-entropy alloy produced by mechanical alloying and vacuum hot pressing sintering, Trans. Nonferrous Met. Soc. China (English Ed. 28 (2018) 1360–1367. https://doi.org/10.1016/S1003-6326(18)64774-0.

[80] D. Oleszak, A. Antolak-Dudka, T. Kulik, High entropy multicomponent WMoNbZrV alloy processed by mechanical alloying, Mater. Lett. 232 (2018) 160–162. https://doi.org/10.1016/j.matlet.2018.08.060.

[81] S. Praveen, A. Anupam, R. Tilak, R.S. Kottada, Phase evolution and thermal stability of AlCoCrFe high entropy alloy with carbon as unsolicited addition from milling media, Mater. Chem. Phys. 210 (2018) 57–61. https://doi.org/10.1016/j.matchemphys.2017.10.040.

[82] A.I. Yurkova, V. V. Cherniavsky, V. Bolbut, M. Krüger, I. Bogomol, Structure formation and mechanical properties of the high-entropy AlCuNiFeCr alloy prepared by mechanical alloying and spark plasma sintering, J. Alloys Compd. 786 (2019) 139–148. https://doi.org/10.1016/j.jallcom.2019.01.341.

[83] X. Liu, H. Cheng, Z. Li, H. Wang, F. Chang, W. Wang, Q. Tang, P. Dai, Microstructure and mechanical properties of FeCoCrNiMnTi0.1C0.1 high-entropy alloy produced by mechanical alloying and vacuum hot pressing sintering, Vacuum. 165 (2019) 297–304. https://doi.org/10.1016/j.vacuum.2019.04.043.

[84] Ł. Rogal, Z. Szklarz, P. Bobrowski, D. Kalita, G. Garzeł, A. Tarasek, M. Kot, M. Szlezynger, Microstructure and Mechanical Properties of Al–Co–Cr–Fe–Ni Base High Entropy Alloys Obtained Using Powder Metallurgy, Met. Mater. Int. 25 (2019) 930–945. https://doi.org/10.1007/s12540-018-00236-5.

[85] H. Cheng, X. Liu, Q. Tang, W. Wang, X. Yan, P. Dai, Microstructure and mechanical properties of FeCoCrNiMnAlx high-entropy alloys prepared by mechanical alloying and hot-pressed sintering, J. Alloys Compd. 775 (2019) 742–751. https://doi.org/10.1016/j.jallcom.2018.10.168.

[86] M. Vaidya, A. Karati, A. Marshal, K.G. Pradeep, B.S. Murty, Phase evolution and stability of nanocrystalline CoCrFeNi and CoCrFeMnNi high entropy alloys, J. Alloys Compd. 770 (2019) 1004–1015. https://doi.org/10.1016/j.jallcom.2018.08.200.

[87] C. Sun, P. Li, S. Xi, Y. Zhou, S. Li, X. Yang, A new type of high entropy alloy composite Fe18Ni23Co25Cr21Mo8WNb3C2 prepared by mechanical alloying and hot pressing sintering, Mater. Sci. Eng. A. 728 (2018) 144–150. https://doi.org/10.1016/j.msea.2018.05.022.

[88] F.J. Baldenebro-Lopez, J.M. Herrera-Ramírez, S.P. Arredondo-Rea, C.D. Gómez-Esparza, R. Martínez-Sánchez, Simultaneous effect of mechanical alloying and arc-melting processes in the microstructure and hardness of an AlCoFeMoNiTi high-entropy alloy, J. Alloys Compd. 643 (2015) S250–S255. https://doi.org/10.1016/j.jallcom.2014.12.059.

[89] C.D. Gómez-Esparza, F. Baldenebro-López, L. González-Rodelas, J. Baldenebro-López, R. Martínez-Sánchez, Series of nanocrystalline NiCoAlFe(Cr, Cu, Mo, Ti) high-entropy alloys produced by mechanical alloying, in: Mater. Res., Universidade Federal de Sao Carlos, 2016: pp. 39–46. https://doi.org/10.1590/1980-5373-MR-2015-0668.

[90] Y.L. Chen, Y.H. Hu, C.A. Hsieh, J.W. Yeh, S.K. Chen, Competition between elements during mechanical alloying in an octonary multi-principal-element alloy system, J. Alloys Compd. 481 (2009) 768–775. https://doi.org/10.1016/j.jallcom.2009.03.087.

[91] M.A. Avila-Rubio, J.A. Baldenebro-Lopez, R. Soto-Rojo, L.G. Ceballos-Mendivil, Carreño-Gallardo, N.F. Garza-Montes-de-Oca, F.J. Baldenebro-Lopez, Effect of Mo and Ti on the microstructure and microhardness in AlCoFeNiMoTi high entropy alloys

prepared by mechanical alloying and conventional sintering, Adv. Powder Technol. 31 (2020) 1693–1701. https://doi.org/10.1016/j.apt.2020.02.008.
[92] Z. Fu, W. Chen, Z. Jiang, B.E. MacDonald, Y. Lin, F. Chen, L. Zhang, E.J. Lavernia, Influence of Cr removal on the microstructure and mechanical behaviour of a high-entropy Al0.8Ti0.2CoNiFeCr alloy fabricated by powder metallurgy, Powder Metall. 61 (2018) 106–114. https://doi.org/10.1080/00325899.2018.1427662.
[93] A. Fourmont, S. Le Gallet, O. Politano, C. Desgranges, F. Baras, Effects of planetary ball milling on AlCoCrFeNi high entropy alloys prepared by Spark Plasma Sintering: Experiments and molecular dynamics study, J. Alloys Compd. 820 (2020) 153448. https://doi.org/10.1016/j.jallcom.2019.153448.
[94] R.M. Pohan, B. Gwalani, J. Lee, T. Alam, J.Y. Hwang, H.J. Ryu, R. Banerjee, S.H. Hong, Microstructures and mechanical properties of mechanically alloyed and spark plasma sintered Al0.3CoCrFeMnNi high entropy alloy, Mater. Chem. Phys. 210 (2018) 62–70. https://doi.org/10.1016/j.matchemphys.2017.09.013.
[95] V.K. Portnoi, A. V. Leonov, S.E. Filippova, A.N. Streletskii, A.I. Logacheva, Mechanochemical synthesis and heating-induced transformations of a high-entropy Cr-Fe-Co-Ni-Al-Ti alloy, Inorg. Mater. 50 (2014) 1202–1211. https://doi.org/10.1134/S0020168514120188.
[96] W. Ge, Y. Wang, C. Shang, Z. Zhang, Y. Wang, Microstructures and properties of equiatomic CuZr and CuZrAlTiNi bulk alloys fabricated by mechanical alloying and spark plasma sintering, J. Mater. Sci. 52 (2017) 5726–5737. https://doi.org/10.1007/s10853-017-0808-0.
[97] F. Thummler, R. Oberacker, Introduction to Powder Metallurgy, Institute of Materials, London, 1993.
[98] C.C. Yang, J.L. Hang Chau, C.J. Weng, C.S. Chen, Y.H. Chou, Preparation of high-entropy AlCoCrCuFeNiSi alloy powders by gas atomization process, Mater. Chem. Phys. 202 (2017) 151–158. https://doi.org/10.1016/j.matchemphys.2017.09.014.
[99] D. Yim, M.J. Jang, J.W. Bae, J. Moon, C.H. Lee, S.J. Hong, S.I. Hong, H.S. Kim, Compaction behavior of water-atomized CoCrFeMnNi high-entropy alloy powders, Mater. Chem. Phys. 210 (2018) 95–102. https://doi.org/10.1016/j.matchemphys.2017.06.013.
[100] D. Yang, H. Jiang, Y. Liu, Z. Lai, M. Liao, N. Qu, Y. Han, J. Zhu, Parameters prediction of hot-pressing sintering of high entropy alloys using numerical modeling and simulation, in: Procedia Manuf., Elsevier B.V., 2019: pp. 529–536. https://doi.org/10.1016/j.promfg.2019.12.084.
[101] S. Moustafa, W. Daoush, A. Ibrahim, E. Neubaur, Hot Forging and Hot Pressing of AlSi Powder Compared to Conventional Powder Metallurgy Route, Mater. Sci. Appl. 02 (2011) 1127–1133. https://doi.org/10.4236/msa.2011.28152.
[102] R.F. Zhao, B. Ren, B. Cai, Z.X. Liu, G.P. Zhang, J. jian Zhang, Corrosion behavior of CoxCrCuFeMnNi high-entropy alloys prepared by hot pressing sintered in 3.5% NaCl solution, Results Phys. 15 (2019) 102667. https://doi.org/10.1016/j.rinp.2019.102667.
[103] N.T.B.N. Koundinya, C. Sajith Babu, K. Sivaprasad, P. Susila, N. Kishore Babu, J. Baburao, Phase evolution and thermal analysis of nanocrystalline AlCrCuFeNiZn high entropy alloy produced by mechanical alloying, J. Mater. Eng. Perform. 22 (2013) 3077–3084. https://doi.org/10.1007/s11665-013-0580-5.
[104] Z. Fu, W. Chen, H. Wen, Z. Chen, E.J. Lavernia, Effects of Co and sintering method on microstructure and mechanical behavior of a high-entropy Al0.6NiFeCrCo alloy prepared by powder metallurgy, J. Alloys Compd. 646 (2015) 175–182. https://doi.org/10.1016/j.jallcom.2015.04.238.
[105] A. Takeuchi, A. Inoue, Calculations of Mixing Enthalpy and Mismatch Entropy for

Ternary Amorphous Alloys, Mater. Trans. JIM. 41 (2000) 1372–1378. https://doi.org/10.2320/matertrans1989.41.1372.
[106] O.N. Senkov, D.B. Miracle, Effect of the atomic size distribution on glass forming ability of amorphous metallic alloys, Mater. Res. Bull. 36 (2001) 2183–2198. https://doi.org/10.1016/S0025-5408(01)00715-2.
[107] S. Fang, X. Xiao, L. Xia, W. Li, Y. Dong, Relationship between the widths of supercooled liquid regions and bond parameters of Mg-based bulk metallic glasses, J. Non. Cryst. Solids. 321 (2003) 120–125. https://doi.org/10.1016/S0022-3093(03)00155-8.
[108] B. Beausir, J.-J. Fundenberger, Analysis Tools for Electron and X-ray diffraction, ATEX- software, (2017). www.atex-software.eu.
[109] W.C. Oliver, G.M. Pharr, An improved technique for determining hardness and elastic modulus using load and displacement sensing indentation experiments, J. Mater. Res. 7 (1992) 1564–1583. https://doi.org/10.1557/JMR.1992.1564.
[110] S.N. Kumaran, Mechanical Alloying of Powders of High-Entropy Alloys, IMT Atlantique and Université de Lille 1, 2017.
[111] N. Derimow, T. Clark, C. Roach, S. Mathaudhu, R. Abbaschian, Processing pathway effects in CoCrCuNi+X (Fe, Mn) high-entropy alloys, Philos. Mag. 99 (2019) 1899–1913. https://doi.org/10.1080/14786435.2019.1616121.
[112] K. Edalati, Z. Horita, Correlations between hardness and atomic bond parameters of pure metals and semi-metals after processing by high-pressure torsion, Scr. Mater. 64 (2011) 161–164. https://doi.org/10.1016/j.scriptamat.2010.09.034.
[113] Y. Xie, D. Zhou, Y. Luo, T. Xia, W. Zeng, C. Li, J. Wang, J. Liang, D. Zhang, Fabrication of CoCrFeNiMn high entropy alloy matrix composites by thermomechanical consolidation of a mechanically milled powder, Mater. Charact. 148 (2019) 307–316. https://doi.org/10.1016/j.matchar.2019.01.002.
[114] S. Praveen, B.S. Murty, R.S. Kottada, Effect of molybdenum and niobium on the phase formation and hardness of nanocrystalline CoCrFeNi high entropy alloys, J. Nanosci. Nanotechnol. 14 (2014) 8106–8109. https://doi.org/10.1166/jnn.2014.9441.
[115] K.B. Zhang, Z.Y. Fu, J.Y. Zhang, J. Shi, W.M. Wang, H. Wang, Y.C. Wang, Q.J. Zhang, Nanocrystalline CoCrFeNiCuAl high-entropy solid solution synthesized by mechanical alloying, J. Alloys Compd. 485 (2009) L31–L34. https://doi.org/10.1016/j.jallcom.2009.05.144.
[116] B. Gwalani, A. V. Ayyagari, D. Choudhuri, T. Scharf, S. Mukherjee, M. Gibson, R. Banerjee, Microstructure and wear resistance of an intermetallic-based Al0.25Ti0.75CoCrFeNi high entropy alloy, Mater. Chem. Phys. 210 (2018) 197–206. https://doi.org/10.1016/j.matchemphys.2017.06.034.
[117] N. Llorca-Isern, H. López-Luque, I. López-Jiménez, M.V. Biezma, Identification of sigma and chi phases in duplex stainless steels, Mater. Charact. 112 (2016) 20–29. https://doi.org/10.1016/j.matchar.2015.12.004.
[118] J. Michalska, M. Sozańska, Qualitative and quantitative analysis of σ and χ phases in 2205 duplex stainless steel, Mater. Charact. 56 (2006) 355–362. https://doi.org/10.1016/j.matchar.2005.11.003.
[119] W. Xu, D. San Martin, P.E.J. Rivera Díaz del Castillo, S. van der Zwaag, Modelling and characterization of chi-phase grain boundary precipitation during aging of Fe-Cr-Ni-Mo stainless steel, Mater. Sci. Eng. A. 467 (2007) 24–32. https://doi.org/10.1016/j.msea.2007.02.071.
[120] V.G. Gavriljuk, H. Berns, High Nitrogen Steels: Structure, Properties, Manufacture, Applications, Springer-Verlag, Berlin Heidelberg, 1999. https://doi.org/doi.org/10.1007/978-3-662-03760-7.

[121] M.J. Duarte, A. Kostka, J.A. Jimenez, P. Choi, J. Klemm, D. Crespo, D. Raabe, F.U. Renner, Crystallization, phase evolution and corrosion of Fe-based metallic glasses: An atomic-scale structural and chemical characterization study, Acta Mater. 71 (2014) 20–30. https://doi.org/10.1016/j.actamat.2014.02.027.

[122] K.W. Andrews, A new intermetallic phase in alloy steels [25], Nature. 164 (1949) 1015. https://doi.org/10.1038/1641015a0.

[123] M. Vaidya, A. Karati, K. Guruvidyathri, M. Nagini, K.G. Pradeep, B.S. Murty, Suppression of σ-phase in nanocrystalline CoCrFeMnNiV high entropy alloy by unsolicited contamination during mechanical alloying and spark plasma sintering, Mater. Chem. Phys. 255 (2020) 123558. https://doi.org/10.1016/j.matchemphys.2020.123558.

[124] P.L. Jain, Principles of Foundry Technology, McGraw Hill Education, 2014.

[125] S. Praveen, J. Basu, S. Kashyap, R.S. Kottada, Exceptional resistance to grain growth in nanocrystalline CoCrFeNi high entropy alloy at high homologous temperatures, J. Alloys Compd. 662 (2016) 361–367. https://doi.org/10.1016/j.jallcom.2015.12.020.

[126] M.J. Donachie, S.J. Donachie, Superalloys: A Technical Guide, Second Edi, ASM International, 2002.

[127] I.M. Makena, M.B. Shongwe, M.M. Ramakokovhu, M.L. Lethabane, Influence of Temperature on Microstructure and Mechanical Properties of Ni-40Fe-10Co Alloy Consolidated by Spark Plasma Sintering, Procedia Manuf. 7 (2017) 708–713. https://doi.org/10.1016/j.promfg.2016.12.105.

[128] J.-P. Morniroli, Atlas of electron diffreaction zone-axis patterns, Bouvines, 2015.

[129] J.P. Morniroli, G. Ji, D. Jacob, A systematic method to identify the space group from PED and CBED patterns part I - theory, Ultramicroscopy. 121 (2012) 42–60. https://doi.org/10.1016/j.ultramic.2012.04.008.

[130] D. Jacob, G. Ji, J.P. Morniroli, A systematic method to identify the space group from PED and CBED patterns part II - practical examples, Ultramicroscopy. 121 (2012) 61–71. https://doi.org/10.1016/j.ultramic.2012.04.015.

[131] A. Šalak, M. Selecká, Manganese in powder metallurgy steels, Cambridge International Science Publishing, 2012. https://doi.org/10.1007/978-1-907343-75-9.

[132] E. Hryha, E. Dudrova, The Sintering Behaviour of Fe-Mn-C Powder System, Correlation between Thermodynamics and Sintering Process, Manganese Distribution and Microstructure Composition, Effect of Alloying Mode, in: M. Tadashi (Ed.), Appl. Thermodyn. to Biol. Mater. Sci., InTech, 2011: pp. 573–602. https://doi.org/10.5772/13735.

[133] M. Li, Y. Guo, H. Wang, J. Shan, Y. Chang, Microstructures and mechanical properties of oxide dispersion strengthened CoCrFeNi high-entropy alloy produced by mechanical alloying and spark plasma sintering, Intermetallics. 123 (2020) 106819. https://doi.org/10.1016/j.intermet.2020.106819.

[134] J.R. Davis, Heat-Resistant Materials, ASM International, Materials Park, 1997.

[135] F. Hanning, A.K. Khan, J. Steffenburg-Nordenström, O. Ojo, J. Andersson, Investigation of the Effect of Short Exposure in the Temperature Range of 750–950 °C on the Ductility of Haynes® 282® by Advanced Microstructural Characterization, Metals (Basel). 9 (2019) 1357. https://doi.org/10.3390/met9121357.

[136] G. Qin, R. Chen, H. Zheng, H. Fang, L. Wang, Y. Su, J. Guo, H. Fu, Strengthening FCC-CoCrFeMnNi high entropy alloys by Mo addition, J. Mater. Sci. Technol. 35 (2019) 578–583. https://doi.org/10.1016/j.jmst.2018.10.009.

[137] Y. Zhou, L. Yang, Y. Huang, Micro- and Macromechanical Properties of Materials, 1st ed., CRC Press Taylor & Francis Group, 2013.

[138] J. Gong, Y. Li, Energy-balance analysis for the size effect in low-load hardness testing,

J. Mater. Sci. 35 (2000) 209–213. https://doi.org/10.1023/A:1004777607553.
[139] C.P. Tabrett, I.R. Sare, M.R. Ghomashchi, Microstructure-property relationships in high chromium white iron alloys, Int. Mater. Rev. 41 (1996) 59–82. https://doi.org/10.1179/imr.1996.41.2.59.
[140] G. Laird, R. Gundlach, K. Rohrig, Abrasion-resistant cast iron handbook, American Foundry Society, Des Plaines, 2000.
[141] L. Dobrzański, B. Dołżańska, Hardness to toughness relationship on WC-Co tool gradient materials evaluated by Palmqvist method, Arch. Mater. Sci. Eng. Vol. 43 (2010) 87–93.
[142] E.O. Hall, The deformation and ageing of mild steel: III Discussion of results, Proc. Phys. Soc. Sect. B. 64 (1951) 747–753. https://doi.org/10.1088/0370-1301/64/9/303.
[143] N.J. Petch, The Cleavage Strength of Polycrystals, J. Iron Steel Inst. 174 (1953) 25–28.
[144] J. Wang, Y. Liu, B. Liu, Y. Wang, Y. Cao, T. Li, R. Zhou, Flow behavior and microstructures of powder metallurgical CrFeCoNiMo0.2 high entropy alloy during high temperature deformation, Mater. Sci. Eng. A. 689 (2017) 233–242. https://doi.org/10.1016/j.msea.2017.02.064.
[145] J. Málek, J. Zýka, F. Lukáč, J. Čížek, L. Kunčická, R. Kocich, Microstructure and Mechanical Properties of Sintered and Heat-Treated HfNbTaTiZr High Entropy Alloy, Metals (Basel). 9 (2019) 1324. https://doi.org/10.3390/met9121324.
[146] D. Shaysultanov, A. Nepapushev, S. Zherebtsov, D. Moskovskikh, N. Stepanov, Structure and mechanical properties of a low-density AlCrFeTi medium entropy alloy produced by spark plasma sintering, Mater. Sci. Eng. A. 795 (2020) 140018. https://doi.org/10.1016/j.msea.2020.140018.
[147] F. Alijani, M. Reihanian, K. Gheisari, H. Miyamoto, Microstructure and high-temperature deformation behavior of FeCoNiMnV high entropy alloy, Mater. Chem. Phys. 256 (2020) 123675. https://doi.org/10.1016/j.matchemphys.2020.123675.
[148] B. Kang, J. Lee, H.J. Ryu, S.H. Hong, Microstructure, mechanical property and Hall-Petch relationship of a light-weight refractory Al0.1CrNbVMo high entropy alloy fabricated by powder metallurgical process, J. Alloys Compd. 767 (2018) 1012–1021. https://doi.org/10.1016/j.jallcom.2018.07.145.
[149] P. Asghari-Rad, P. Sathiyamoorthi, N.T.C. Nguyen, A. Zargaran, T.S. Kim, H.S. Kim, A powder-metallurgy-based fabrication route towards achieving high tensile strength with ultra-high ductility in high-entropy alloy, Scr. Mater. 190 (2021) 69–74. https://doi.org/10.1016/j.scriptamat.2020.08.038.

Research Outputs

Publications

[1] T. Stasiak, M.A. Sow, A. Addad, M. Touzin, F. Béclin, C. Cordier, Processing and characterization of a mechanically alloyed and hot press sintered high entropy alloy from the Al-Cr-Fe-Mn-Mo family, in preparation.

[2] T. Stasiak, S.N. Kumaran, M. Touzin, F. Béclin, C. Cordier, Novel Multicomponent Powders from the AlCrFeMnMo Family Synthesized by Mechanical Alloying, Advanced Engineering Materials 21 (2019) 1900808.
http://doi.org/10.1002/adem.201900808

Conference Proceedings

[1] T. Stasiak, S.N. Kumaran, M. Touzin, F. Béclin, C. Cordier, Powder metallurgy processing of a novel massive AlCrFeMnMo High Entropy Alloy: a comparative study of the mechanical alloying techniques, Proceedings of the Euro PM2018 International Powder Metallurgy Congress & Exhibition, ISBN: 978-1-899072-50-7.

Conference Presentations

[1] T. Stasiak, A. Addad, M. Touzin, F. Béclin, C. Cordier, "Phase analysis and mechanical properties of the new Al-Cr-Fe-Mn-Mo high entropy alloy family prepared by powder metallurgy route", Euromat 2019: European Conference and Exhibition on Advanced Materials and Processes, Stockholm, Sweden, 1-5 September 2019.

[2] C. Cordier, F. Béclin, M. Touzin, M.A. Sow, T. Stasiak, "Des alliages Al-Cr-Fe-Mn-Mo en poudre aux revêtements et massifs de type HEA ou CCA", Premières Journées Annuelles du GDR HEA, Nantes, France, 25-26 June 2019.

[3] T. Stasiak, M. Touzin, F. Béclin, C. Cordier, "Elaboration d’un alliage à haute entropie $Al_{22.5}Cr_{22.5}Fe_{28}Mn_{20}Mo_7$ par métallurgie des poudres", Premières Journées Annuelles du GDR HEA, Nantes, France, 25-26 June 2019.

[4] T. Stasiak, A. Addad, M. Touzin, F. Béclin, C. Cordier, "Elaboration d’un alliage à haute entropie de la famille AlCrFeMnMo par métallurgie des poudres", Poudres 2019: Matériaux frittés et fabrication additive, Grenoble, France, 22-24 May 2019.

[5] C. Cordier, F. Béclin, M. Touzin, T. Stasiak, "Mössbauer characterization of HEA-CCA alloys during development", Mediterranean Conference on the Applications of the Mössbauer Effect, Montpellier, France, 19-23 may 2019.

[6] T. Stasiak, S.N. Kumaran, M. Touzin, F. Béclin, C. Cordier, "Elaboration d’alliages HEA de la famille AlCrFeMnMo par mécano-synthèse : influence du type de broyeur", Conférence Matériaux 2018, Strasbourg, France, 19-23 November 2018.

[7] T. Stasiak, S. N. Kumaran, M. Touzin, F. Béclin, C. Cordier, "Powder metallurgy processing of a novel massive AlCrFeMnMo High Entropy Alloy: a comparative study of the mechanical alloying techniques", Euro PM2018 International Powder Metallurgy Congress & Exhibition, Bilbao, Spain, 14-18 October 2018.

Appendix A

Results of mechanically alloyed powders

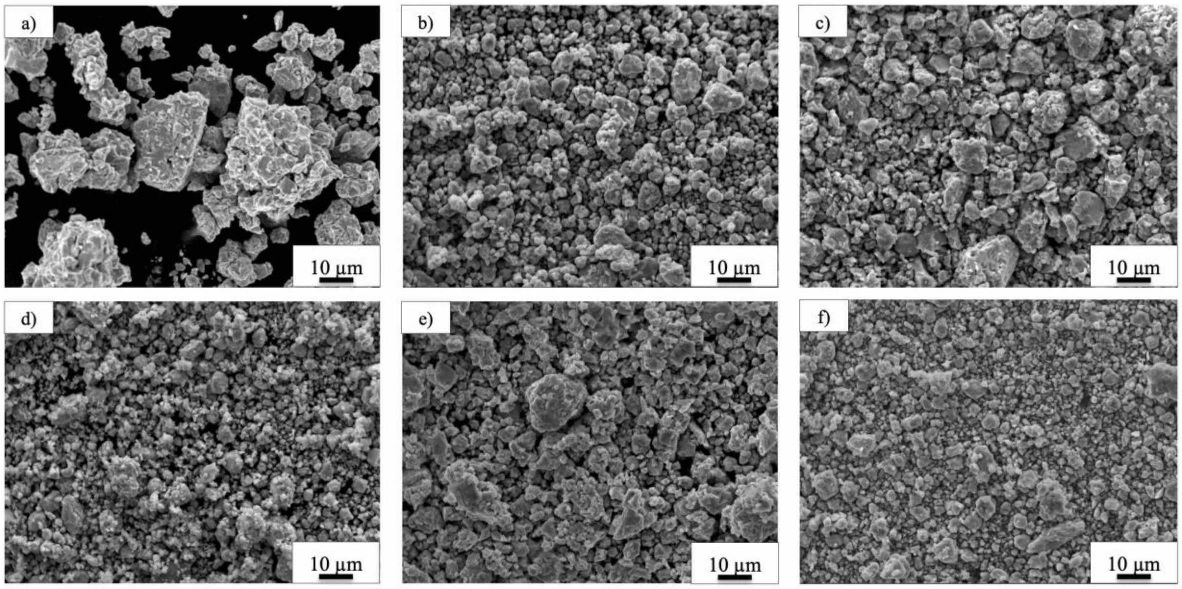

Figure A1. SEM-SE images of non-polished milled powders: a) P-EQ-S32h, b) P-EQ-R70h, c) P-EQ-R70hS4h, d) P-EQ-C32h, e) P-O-S32h, f) P-O-C32h.

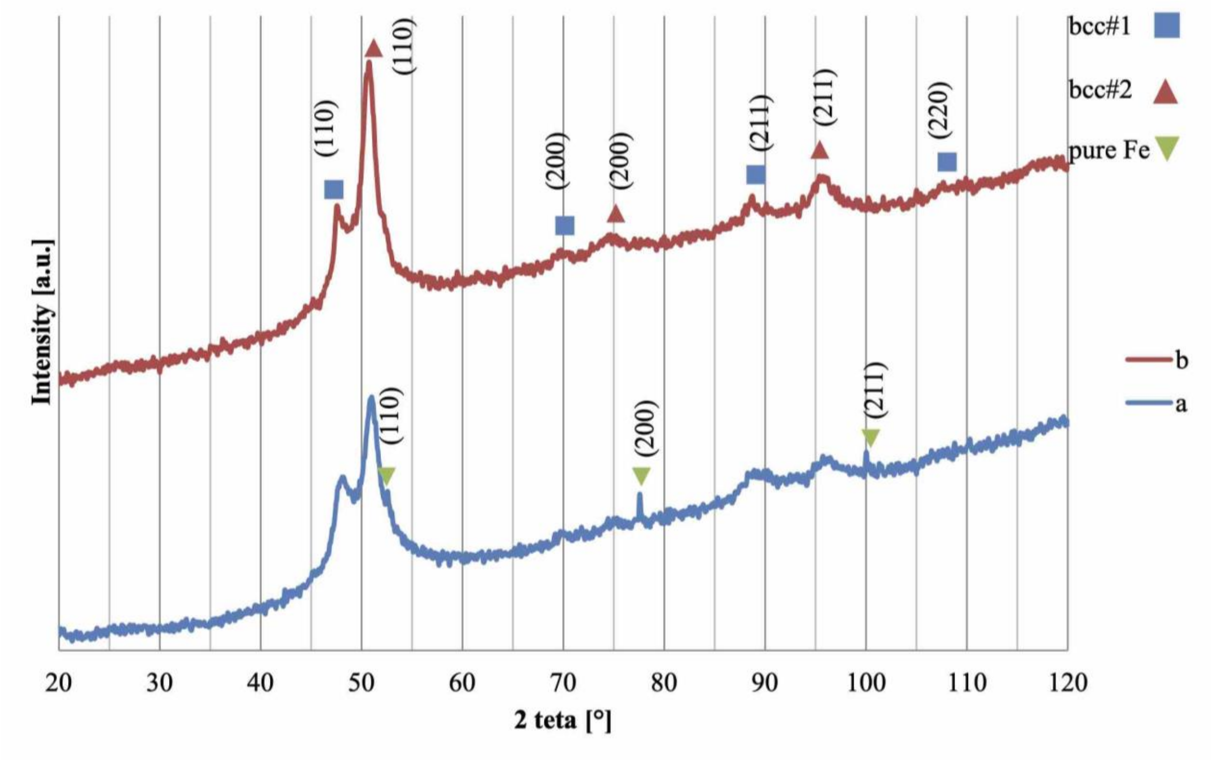

Figure A2. XRD patterns of P-EQ-RFe-S32h (a) and P-EQ-NFe-S32h (b) powders after milling.

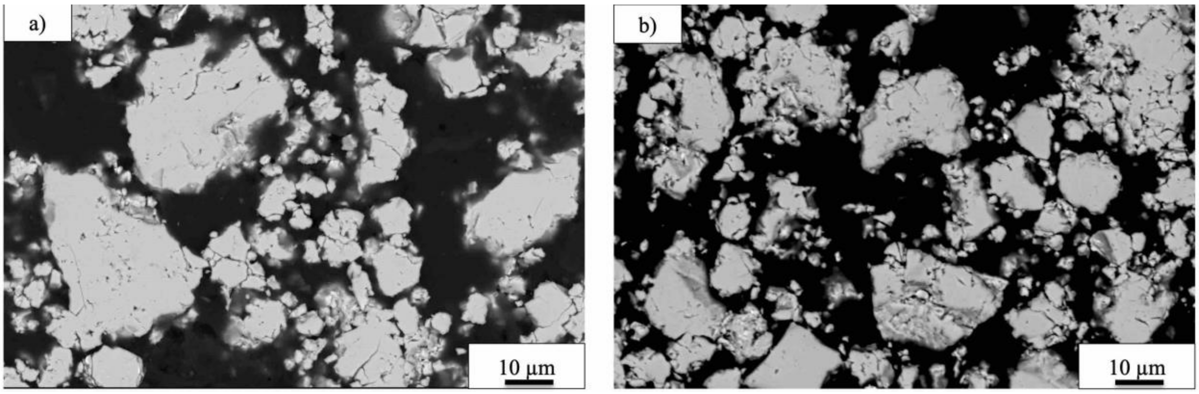

Figure A3. SEM-BSE images of P-EQ-RFe-S32h (a) and P-EQ-NFe-S32h (b) powders after milling.

Table A1. Summary of results of P-EQ-RFe-S32h and P-EQ-NFe-S32h powders after milling SPEX.

Sample	Final composition and homogeneity	Phase composition	
		Bcc#1	Bcc#2
P-EQ-RFe-S32h	17% Al, 20% Cr, 28% Fe, 17% Mn, 18% Mo (homogeneous + Fe particles)	3.12 Å	2.95 Å
P-EQ-NFe-S32h	17% Al, 22% Cr, 24% Fe, 18% Mn, 19% Mo (homogeneous)	3.14 Å	2.95 Å

Table A2 Mössbauer hyperfine parameters of iron environments in P-EQ-RFe-S32h, P-EQ-NFe-S32h, P-EQ-S32h powders mechanically alloyed in SPEX for 32h. Effect of the iron amount in powder initially introduced in vial before milling. (Hyperfine parameters are calculated by comparison with iron reference).

Sample	**Iron site**	**H (T)**	**IS (mm/s)**	**QS (mm/s)**	**W (mm/s)**	**A (%)**	**Magnetic properties**
P-EQ-NFe-S32h	Sites 2+3	28.2 ±1	0.05±0.05	-0.06±0.05	0.25±0.02	14.50±4.50	**Magnetic:** 14.50 ±4.50% **Non-magnetic:** 85.50±4.50%
	Site 5	-	-0.03±0.01	0.81±0.02	0.25±0.01	9.90±0.40	
	Site 6	-	-0.08±0.02	0.61±0.01	0.25±0.01	19.09±0.79	
	Site 7	-	-0.08±0.01	0.34±0.03	0.25±0.01	25.96±1.26	
	Site 12	-	-0.01±0.05	0.16±0.01	0.25±0.01	18.51±1.21	
	Site 8	-	-0.08±0.03	0	0.24±0.01	12.04±0.84	
P-EQ-RFe-S32h	Sites 2+3	30.1 ±2	-0.61±0.50	-0.20±0.50	0.25±0.01	3.84±0.39	**Magnetic:** 5.52±2.25% **Non-magnetic:** 94.48±2.25%
	Sites 4+5	-	-0.04±0.03	0.98±0.11	0.25±0.01	3.36±0.16	
	Site 5	-	-0.06±0.02	0.83±0.05	0.25±0.01	9.80±0.47	
	Site 6	-	-0.09±0.01	0.59±0.02	0.25±0.01	22.17±0.41	
	Site 7	-	-0.11±0.01	0.36±0.04	0.25±0.01	24.95±0.50	
	Site 9	-	-0.06±0.03	0.26±0.05	0.25±0.01	20.81±1.14	
	Site 8	-	-0.08±0.02	0	0.24±0.01	15.0±0.03	
P-EQ-S32h	Sites 2+3	29.6 ±1	-0.03±0.05	-0.38±0.05	0.25±0.01	5.77±1.49	**Magnetic:** 7.38±3.14% **Non-magnetic:** 92.62±3.14%
	Sites 4+5	-	-0.06±0.01	0.92±0.06	0.25±0.01	3.22±0.04	
	Site 5	-	-0.05±0.01	0.83±0.04	0.25±0.01	9.23±0.11	
	Site 6	-	-0.08±0.01	0.59±0.03	0.25±0.01	21.44±1.34	
	Site 7	-	-0.11±0.02	0.36±0.04	0.25±0.01	26.06±3.28	
	Sites 9+12	-	-0.05±0.04	0.24±0.04	0.25±0.01	22.68±2.30	
	Site 8	-	-0.07±0.01	0	0.25±0.01	11.60±2.60	

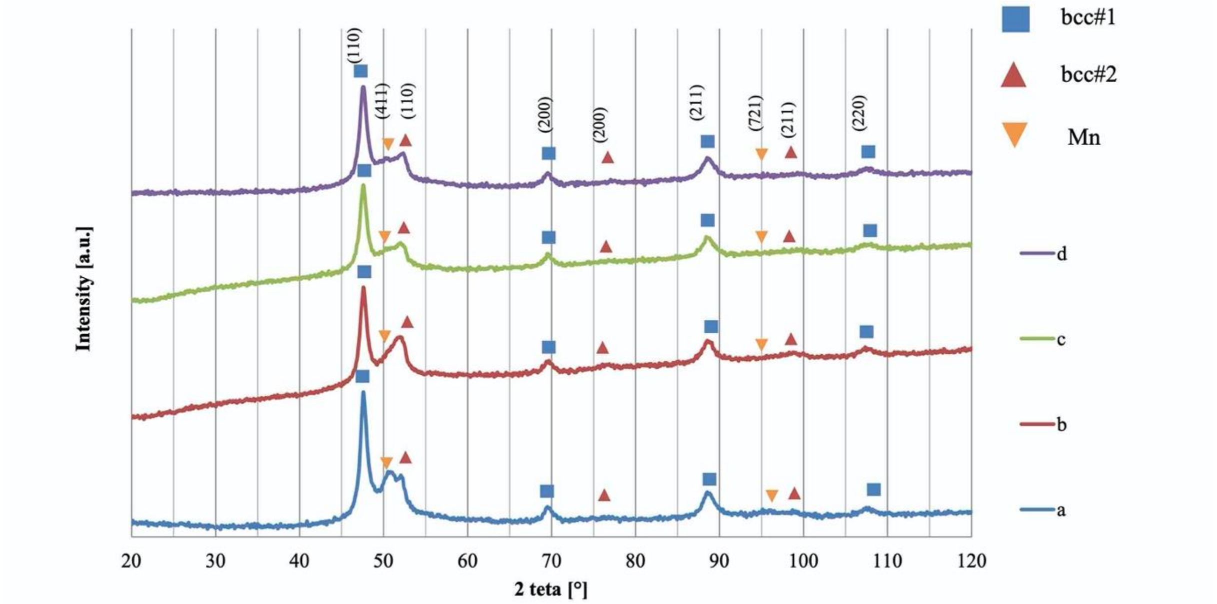

Figure A4. XRD patterns of powders: a) P-EQ-R70h, b) P-EQ-R70hS1h, c) P-EQ-R70hS2h, d) P-EQ-R70hS4h.

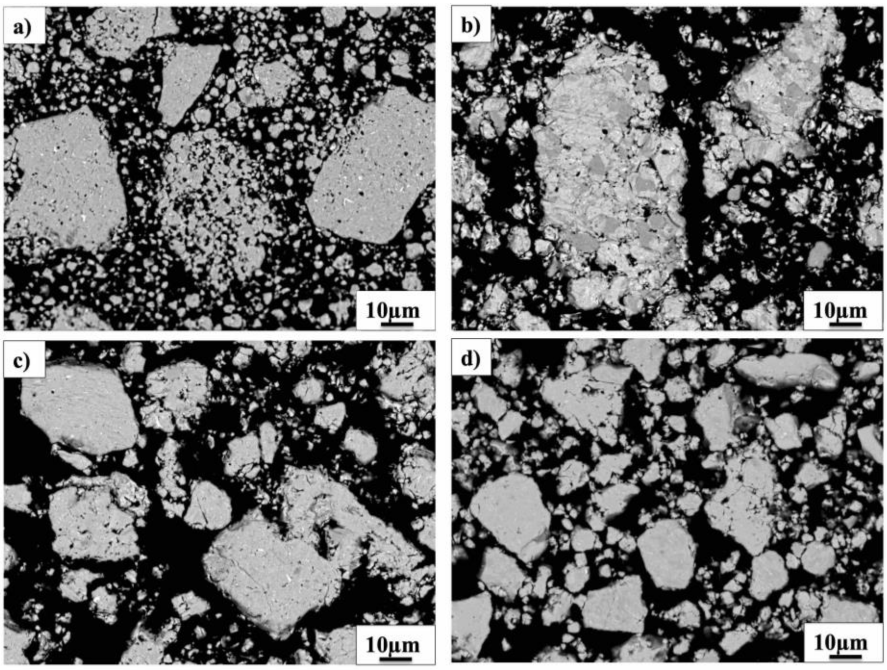

Figure A5. SEM images of: a) P-EQ-R70h, b) P-EQ-R70hS1h, c) P-EQ-R70hS2h, d) P-EQ-R70hS4h.

Table A3. Summary of results of powders with the starting equiatomic composition.

Sample	Final composition and homogeneity	Lattice parameters		
		Bcc#1	Bcc#2	Mn bbc
P-EQ-R70h	19% Al, 20% Cr, 22% Fe, 19% Mn, 20% Mo (heterogeneous)	3.14 Å	2.90 Å	8.91 Å
P-EQ-R70hS1h	20% Al, 21% Cr, 23% Fe, 19% Mn, 17% Mo (heterogeneous)	3.14 Å	2.89 Å	8.90 Å
P-EQ-R70hS2h	19% Al, 20% Cr, 23% Fe, 19% Mn, 19% Mo (heterogeneous)	3.14 Å	2.89 Å	8.89 Å
P-EQ-R70hS4h	18% Al, 20% Cr, 24% Fe, 19% Mn, 19% Mo (homogeneous)	3.14 Å	2.87 Å	8.92 Å

Table A4 Mössbauer hyperfine parameters of iron environments in P-EQ-R70hS4h and P-EQ-R70h powders.

Sample	**Iron site**	**H (T)**	**IS (mm/s)**	**QS (mm/s)**	**W (mm/s)**	**A (%)**	**Magnetic properties**
P-EQ-R70hS4h	Sites 2+3	30.1±1	0.08±0.05	0.12±0.05	0.28±0.03	9.40±0.41	**Magnetic:** 9.40±0.41% **Non-magnetic:** 90.60±0.41 %
	Sites 4+5	-	0.02±0.01	0.85±0.01	0.24±0.02	21.24±0.92	
	Site 6	-	0.00±0.01	0.59±0.02	0.24±0.02	28.32±2.27	
	Sites 9+7	-	-0.02±0.01	0.31±0.01	0.24±0.02	27.32±0.59	
	Site 8	-	-0.01±0.01	0	0.24±0.02	13.72±0.35	
P-EQ-R70h	Site 1	34.4±1	0.03±0.05	-0.11±0.05	0.26±0.02	2.73±0.30	**Magnetic:** 16.23±1.81 % **Non-magnetic:** 83.77±1.81 %
	Site 2	31.2±1	-0.08±0.05	-0.08±0.05	0.26±0.02	6.91±0.67	
	Site 3	28.7±1	-0.15±0.05	-0.06±0.05	0.26±0.02	2.06±0.83	
	Site 4	-	0.11±0.01	1.29±0.22	0.26±0.02	4.53±0.31	
	Site 5	-	0.08±0.01	0.87±0.01	0.26±0.02	18.08±0.05	
	Site 6	-	0.06±0.01	0.59±0.01	0.26±0.02	30.05±0.06	
	Sites 9+7	-	0.05±0.01	0.32±0.01	0.26±0.02	24.08±0.52	
	Site 8	-	0.05±0.01	0	0.27±0.02	11.56±0.27	

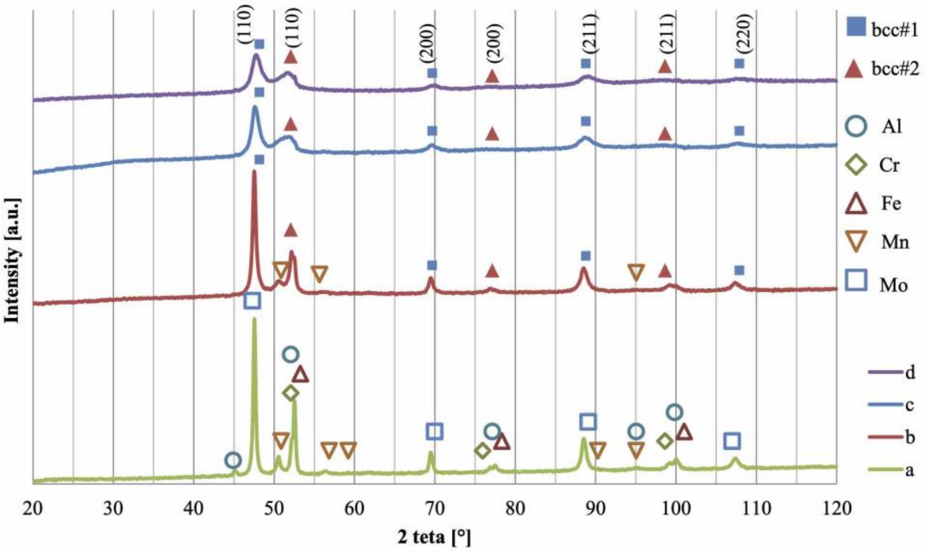

Figure A6. XRD patterns of powders: a) P-EQ-C32h-15Hz, b) P-EQ-C32h-20Hz, c) P-EQ-C32h, and d) P-EQ-C64h.

Table A5. Summary of results of the powders with the starting equiatomic composition,

Sample	Final composition and homogeneity	Lattice parameters [Å]		
		Bcc#1	Bcc#2	Mn (bbc)
P-EQ-C32h-15Hz	(areas of elemental powders)	Peaks of pure elements		
P-EQ-C32h-20Hz	19% Al, 21% Cr, 20% Fe, 20% Mn, 20% Mo (heterogeneous)	3.14	2.88	8.92
P-EQ-C32h	19% Al, 21% Cr, 20% Fe, 19% Mn, 21% Mo (heterogeneous)	3.13	2.88	---
P-EQ-C64h	19% Al, 18% Cr, 21% Fe, 21% Mn, 21% Mo (heterogeneous)	3.13	2.89	---

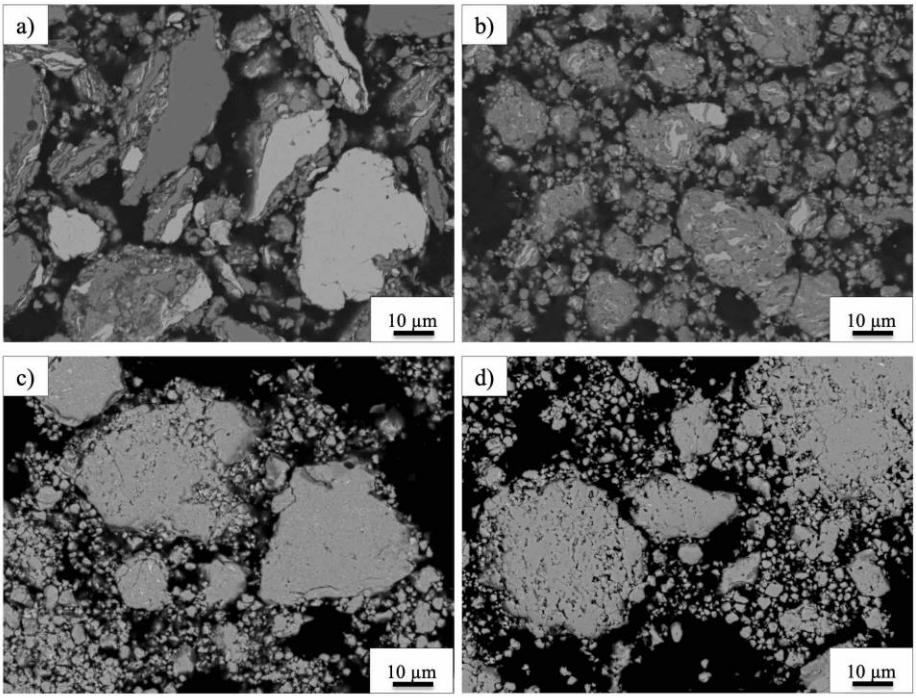

Figure A7. SEM-BSE images of powders: a) P-EQ-C32h-15Hz, b) P-EQ-C32h-20Hz, c) P-EQ-C32h, and d) P-EQ-C64h.

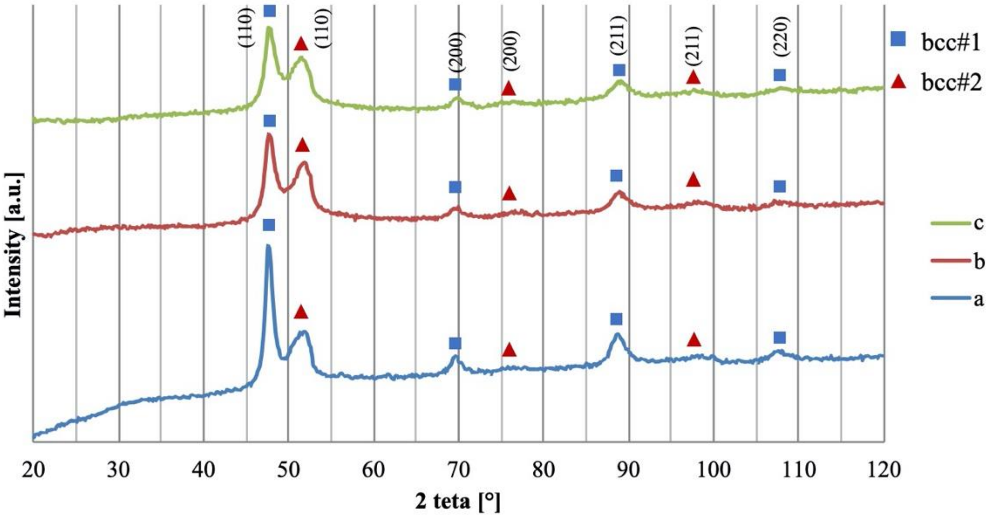

Figure A8. XRD patterns of powders after milling a) P-EQ-C32h, b) P-EQ-C32h8h, and c) P-EQ-RFe-C32h8h.

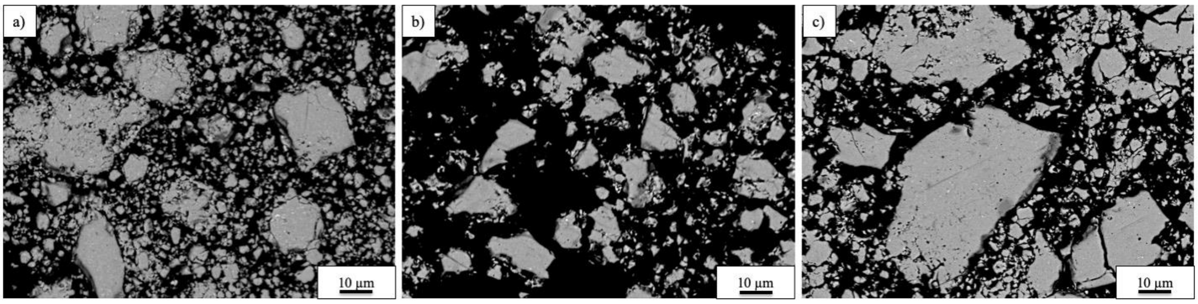

Figure A9. SEM-BES images of powders after milling: a) P-EQ-C32h, b) P-EQ-C32h8h, and c) P-EQ-RFe-C32h8h.

Table A6. Summary of results of powders (P-EQ-C32h, P-EQ-C32h8h, and P-EQ-RFe-C32h8h)

Sample	Final composition and homogeneity	Lattice parameters	
		Bcc#1	Bcc#2
P-EQ-C32h	19% Al, 21% Cr, 20% Fe, 19% Mn, 21% Mo (heterogenous)	3.13 Å	2.88 Å
P-EQ-C32h8h	17% Al, 20% Cr, 27% Fe, 18% Mn, 18% Mo (homogeneous)	3.13 Å	2.90 Å
P-EQ-RFe-C32h8h	19% Al, 20% Cr, 21% Fe, 20% Mn, 20% Mo (homogeneous)	3.13 Å	2.90 Å

Table A7. Mössbauer hyperfine parameters of iron environments in powders: P-EQ-C32h, P-EQ-C32h8h, and P-EQ-RFe-C32h8h.

Sample	**Iron site**	**H (T)**	**IS (mm/s)**	**QS (mm/s)**	**W (mm/s)**	**A (%)**	**Magnetic properties**
P-EQ-RFe-C32h8h	Site1	34.21±1	0.14 ±0.05	-0.16±0.05	0.26±0.02	10.61±1.36	**Magnetic:** 25.54 ±2.42% **Non-magnetic:** 74.46 ±2.42%
	Site2	31.77±1	-0.14±0.05	0.20±0.05	0.26±0.02	6.86±0.49	
	Site 3	28.54±1	0.29±0.05	-0.15±0.05	0.26±0.02	8.07±0.57	
	Site 5	-	-0.05±0.02	0.78±0.02	0.25±0.01	14.19±0.49	
	Site 6	-	-0.07±0.04	0.53±0.03	0.25±0.01	17.52±0.67	
	Site 7	-	-0.10±0.02	0.39±0.05	0.25±0.01	15.13±3.06	
	Sites 9+12	-	-0.07±0.02	0.22±0.02	0.25±0.01	16.51±0.81	
	Site 8	-	-0.07±0.02	0	0.24±0.01	11.11±1.02	
P-EQ-C32h8h	Site1	34.02±1	-0.03±0.05	-0.08±0.05	0.27±0.03	7.90±1.94	**Magnetic:** 25.00 ±5.79% **Non-magnetic** 75.00 ±5.79 %
	Site 2	30.69±1	-0.00±0.05	-0.08±0.05	0.29±0.05	17.10±3.85	
	Site 5	-	-0.05±0.01	0.84±0.02	0.25±0.01	12.16±0.02	
	Site 6	-	-0.08±0.01	0.58±0.04	0.25±0.01	15.79±0.40	
	Site 7	-	-0.12±0.02	0.38±0.02	0.25±0.01	13.15±0.34	
	Site 9	-	-0.09±0.01	0.29±0.03	0.25±0.01	14.15±0.69	
	Site 12	-	-0.07±0.03	0.15±0.07	0.25±0.01	11.49±0.69	
	Site 8	-	-0.09±0.01	0	0.25±0.01	8.25±1.20	
P-EQ-C32h	Site 1	33.4±1	0.01±0.05	0.03±0.05	0.26±0.02	11.78±0.75	**Magnetic:** 30.54 ±3.93% **Non-magnetic:** 69.46 ±3.93 %
	Site 3	29.5±1	-0.11±0.05	0.09±0.05	0.26±0.03	8.89±1.51	
	Site 11	26.5±1	0.08±0.05	-0.09±0.05	0.26±0.02	9.87±1.67	
	Site 5	-	0.01±0.01	0.87±0.01	0.25±0.01	11.99±0.57	
	Site 6	-	-0.01±0.01	0.61±0.01	0.25±0.01	16.89±0.10	
	Site 7	-	-0.02±0.01	0.37±0.01	0.24±0.01	15.55±1.43	
	Sites 9+12	-	0.01±0.01	0.19±0.04	0.24±0.02	17.47±2.71	
	Site 8	-	-0.01±0.01	0	0.23±0.01	7.56±4.56	

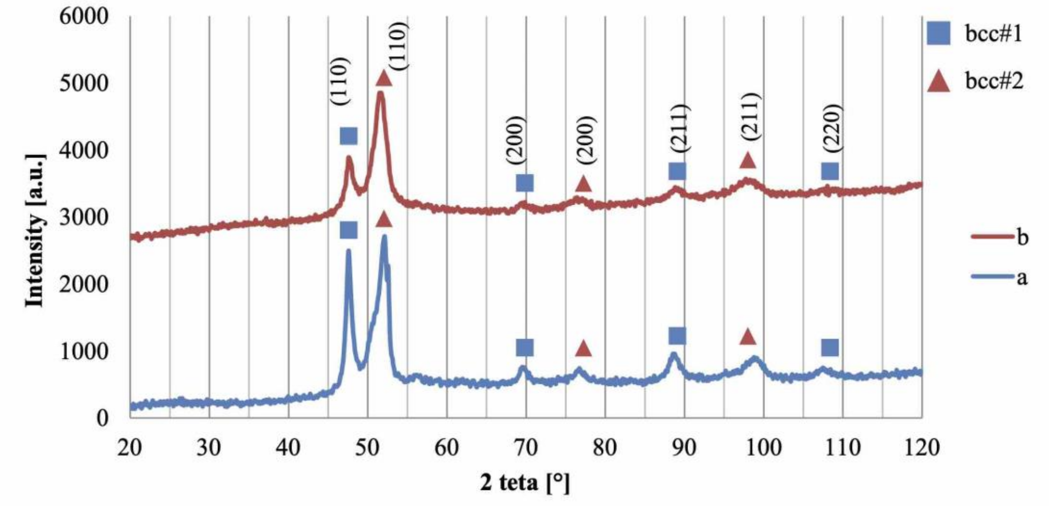

Figure A10. XRD patterns of powders after milling: a) P-O-C32h and b) P-O-C32hS8h.

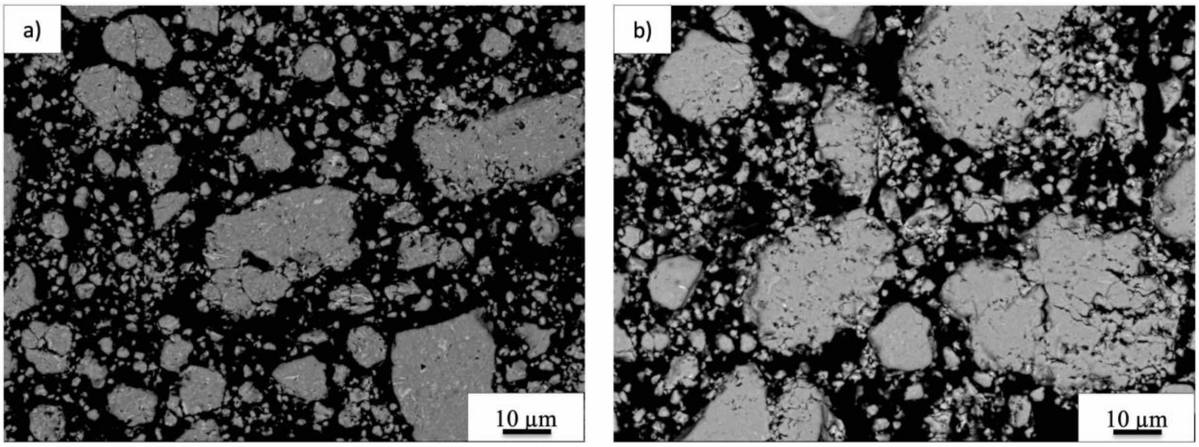

Figure A11. SEM images of powders after milling: a) P-O-C32h and b) P-O-C32hS8h.

Table A8. Summary of results of the powder after milling

Sample	Final composition and homogeneity	Phase composition	
		Bcc#1	Bcc#2
P-O-C32h	22% Al, 23% Cr, 28% Fe, 20% Mn, 7% Mo (heterogenous)	3.14 Å	2.88 Å
P-O-C32hS8h	20% Al, 22% Cr, 30% Fe, 20% Mn, 8% Mo (homogeneous)	3.13 Å	2.90 Å

Table A9. Mössbauer hyperfine parameters of iron environments in the P-O-C32h and P-O-S32h.

Sample	**Iron site**	**H (T)**	**IS (mm/s)**	**QS (mm/s)**	**W (mm/s)**	**A (%)**	**Magnetic properties**
P-O-C32h	Site 1	32.84±1	-0.03±0.05	0.02±0.05	0.32±0.03	21.64±2.33	**Magnetic:** 54.45 ±4.52% **Non-magnetic:** 45.55 ±4.52%
	Site 3	29.13±1	-0.02±0.05	0.03±0.05	0.37±0.03	14.30±1.89	
	Site 11	25.02±1	-0.11±0.05	0.00±0.05	0.43±0.03	12.73±1.68	
	Site 4	-	0.05±0.03	1.22±0.21	0.27±0.04	5.78±0.40	
	Site 6	-	0.03±0.01	0.61±0.41	0.25±0.02	11.08±0.33	
	Sites 7	-	0.04±0.01	0.49±0.25	0.25±0.02	12.55±0.19	
	Site 9	-	0.03±0.01	0.27±0.03	0.24±0.02	7.65±0.95	
	Site 12		0.04±0.01	0.16±0.02	0.23±0.02	7.21±2.17	
	Site 8	-	0.04±0.01	0	0.23±0.01	7.06±0.88	
P-O-S32h	Site 1	33.53±1	0.04±0.05	0.12±0.05	0.28±0.05	4.61±0.60	**Magnetic:** 12.89 ±4.73% **Non-magnetic:** 87.11 ±4.73%
	Site 3	29.13±1	-0.07±0.05	0.09±0.05	0.30±0.07	3.55±2.08	
	Site 11	25.22±0.5	-0.07±0.05	-0.08±0.05	0.33±0.10	3.26±1.92	
	Site 4	-	0.04±0.03	1.34±0.06	0.27±0.04	1.47±0.13	
	Site 5	-	-0.03±0.03	0.80±0.05	0.25±0.01	14.01±1.97	
	Site 6	-	-0.06±0.02	0.51±0.06	0.25±0.01	20.81±0.03	
	Sites 7+9	-	-0.05±0.01	0.31±0.03	0.25±0.01	19.96±1.21	
	Site 12	-	-0.03±0.01	0.17±0.02	0.24±0.02	23.26±5.20	
	Site 8	-	-0.04±0.02	0	0.23±0.01	9.07±2.53	

Table A10. Mössbauer hyperfine parameters of iron environments in the experimentally optimized powder after mechanical alloying (P-OE-S32h).

Sample	**Iron site**	**H (T)**	**IS (mm/s)**	**QS (mm/s)**	**W (mm/s)**	**A (%)**	**Magnetic properties**
P-OE-S32h	Sites 2+3	30.5±1	-0.08±0.05	0.46±0.05	0.39±0.05	6.44±1.03	**Magnetic:** 9.41 ±4.00 % **Non-magnetic:** 93.56 ±4.00 %
	Sites 4+5	-	0.02±0.01	1.02±0.08	0.26±0.03	5.94±1.05	
	Site 6	-	-0.00±0.01	0.64±0.03	0.25±0.02	19.48±0.86	
	Site 7	-	0.00±0.01	0.37±0.02	0.25±0.02	26.19±0.36	
	Site 12	-	0.01±0.01	0.16±0.02	0.25±0.02	29.61±0.04	
	Site 8	-	0.01±0.01	0	0.25±0.02	12.34±0.16	

Appendix B

Results of the thermal stability of mechanically alloyed powders

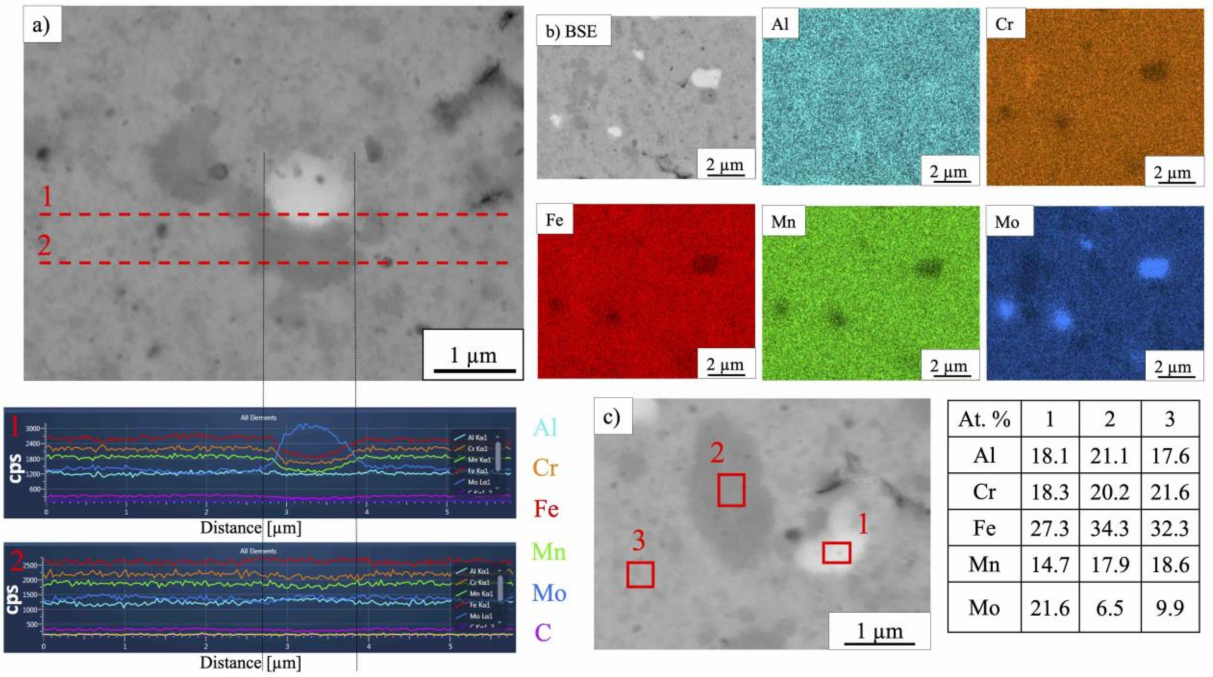

At. %	1	2	3
Al	18.1	21.1	17.6
Cr	18.3	20.2	21.6
Fe	27.3	34.3	32.3
Mn	14.7	17.9	18.6
Mo	21.6	6.5	9.9

Figure B1. Results of the A-O-S32h-800 powder a) SEM-BSE image with line scans revealing zones enriched in molybdenum, b) SEM-EDX mapping, c) SEM-EDX compositions of molybdenum-rich carbide (1), bcc#2 phase (2), chi phase (3).

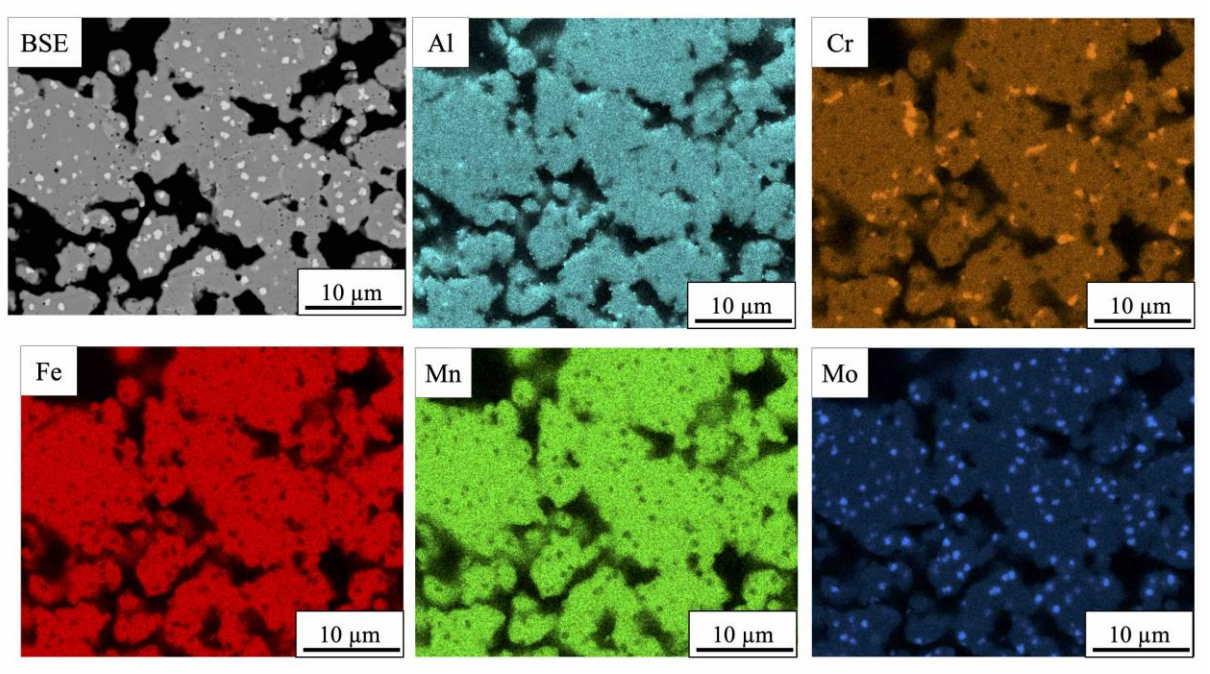

Figure B2. SEM-EDX mapping of the A-O-S32h-950 powder.

Table B1. Mössbauer hyperfine parameters of iron sites in the optimized powders: P-O-S32h, A-O-S32h-500, A-O-S32h-950.

Sample	Iron site	IS (mm/s)	QS (mm/s)	A (%)	Phase amount
A-O-S32h-950	Site 13 – χ phase	0.02 ± 0.02	0.95 ± 0.04	0.47 ± 1	**χ phase:** 4.82%
	Site 14 – χ phase	-0.00 ± 0.02	0.70 ± 0.04	4.35 ± 1	
	Site 7 – bcc#2	0.05 ± 0.02	0.42 ± 0.04	21.73 ± 1	**bcc#2:** 70.84 – 95.18% **carbides:** 24.34 – 0%
	Site 9 – bcc#2	0.06 ± 0.02	0.20 ± 0.04	34.77 ± 1	
	Site 8 – bcc#2	0.06 ± 0.02	0 ± 0.04	14.34 ± 1	
	Site 12 – bcc#2 or carbides	0.05 ± 0.02	0.12 ± 0.04	24.34± 1	
A-O-S32h-500	Site 1+2 – residual	-0.02 ± 0.02	1.56 ± 0.04	0.87 ± 1	**Residual iron environments:** 1.49%
	Sites 3+4 – residual	0.02 ± 0.02	1.21 ± 0.04	0.62 ± 1	
	Site 5 – bcc#1	-0.04 ± 0.02	0.82 ± 0.04	14.30 ± 1	**bcc#1:** 17.92%
	Site 6 – bcc#1	-0.12 ± 0.02	0.65 ± 0.04	3.62 ± 1	
	Site 7 – bcc#2	-0.09 ± 0.02	0.47 ± 0.04	26.35 ± 1	**bcc#2:** 80.58%
	Sites 9+12 – bcc#2	-0.02 ± 0.02	0.21 ± 0.04	33.09 ± 1	
	Site 8 – bcc#2	-0.03 ± 0.02	0 ± 0.04	21.14 ± 1	
P-O-S32h	Site 1 – residual	-0.20 ± 0.02	1.81 ± 0.04	0.75 ± 1	**Residual iron environments:** 3.14%
	Site 2 – residual	-0.07 ± 0.02	1.41 ± 0.04	1.07 ± 1	
	Sites 3+4 – residual	0.02 ± 0.02	1.21 ± 0.04	1.32 ± 1	
	Site 5 – bcc#1	-0.02±0.02	0.83 ± 0.04	12.91 ± 1	**bcc#1:** 34.43%
	Site 6 – bcc#1	-0.04 ± 0.02	0.56 ± 0.04	21.52 ± 1	
	Site 7 – bcc#2	-0.04 ± 0.02	0.35 ± 0.04	24.53 ± 1	**bcc#2:** 62.42%
	Site 12 – bcc#2	-0.02 ± 0.02	0.15 ± 0.04	29.90 ± 1	
	Site 8 – bcc#2	-0.02 ± 0.02	0 ± 0.04	7.99 ± 1	

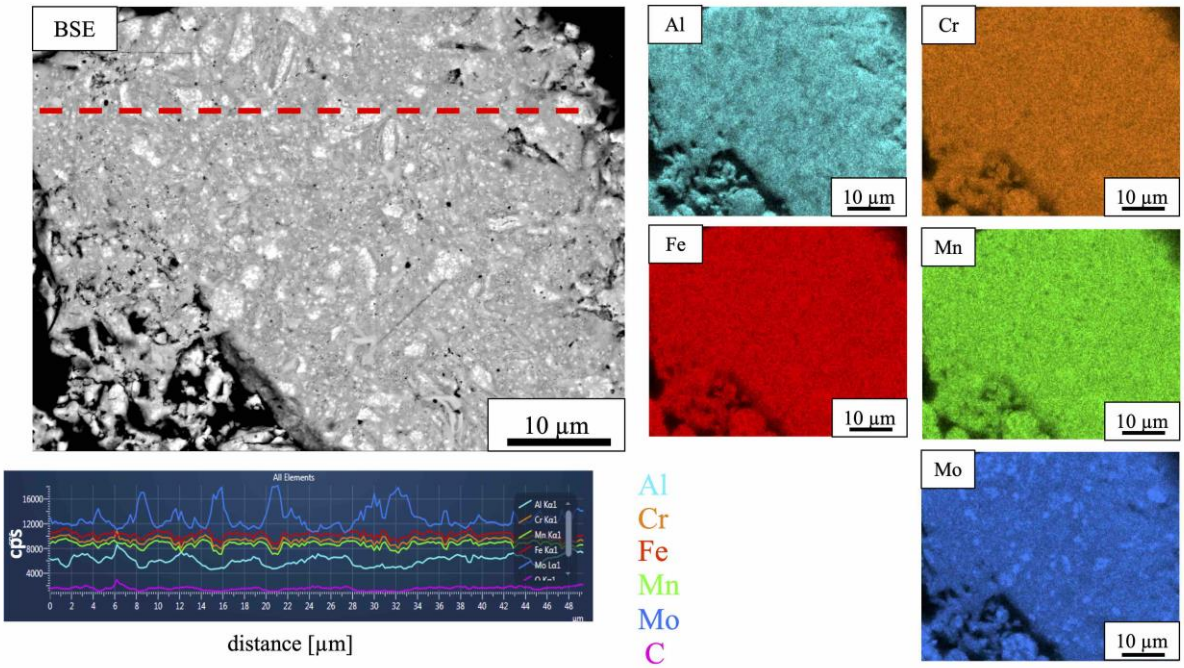

Figure B3. SEM-BSE image of the A-EQ-R70hS4h-850 powder with corresponding line scan and EDX mapping.

Table B2. Mössbauer hyperfine parameters of iron environments in the P-EQ-R70hS4h and A-EQ-R70hS4h-850.

Sample	Iron site	H (T)	IS (mm/s)	QS (mm/s)	W (mm/s)	A (%)	Magnetic Properties
P-EQ-R70hS4h	Sites 2+3	30.1±1	0.08±0.05	0.12±0.05	0.28±0.03	9.40±0.41	**Magnetic:** 9.40±0.41% **Non-magnetic:** 90.60±0.41%
	Sites 4+5	-	0.02±0.01	0.85±0.01	0.24±0.02	21.24±0.92	
	Site 6	-	0.00±0.01	0.59±0.01	0.24±0.02	28.32±2.27	
	Sites 7+9	-	-0.02±0.01	0.31±0.01	0.24±0.02	27.32±0.59	
	Site 8	-	-0.02±0.01	0	0.24±0.02	13.72±0.35	
A-EQ-R70hS4h-850	Site 5	-	-0.06±0.02	0.82±0.03	0.24±0.02	7.32±0.56	**Magnetic:** 0±2% **Non-magnetic:** 100±2%
	Site 6	-	-0.13±0.01	0.53±0.01	0.24±0.02	26.98±0.74	
	Site 7+9	-	-0.15±0.01	0.32±0.01	0.24±0.02	31.10±0.01	
	Site 12	-	-0.15±0.01	0.14±0.01	0.24±0.02	31.97±0.48	
	Site 8	-	-0.11±0.01	0	0.23±0.01	2.63±0.65	

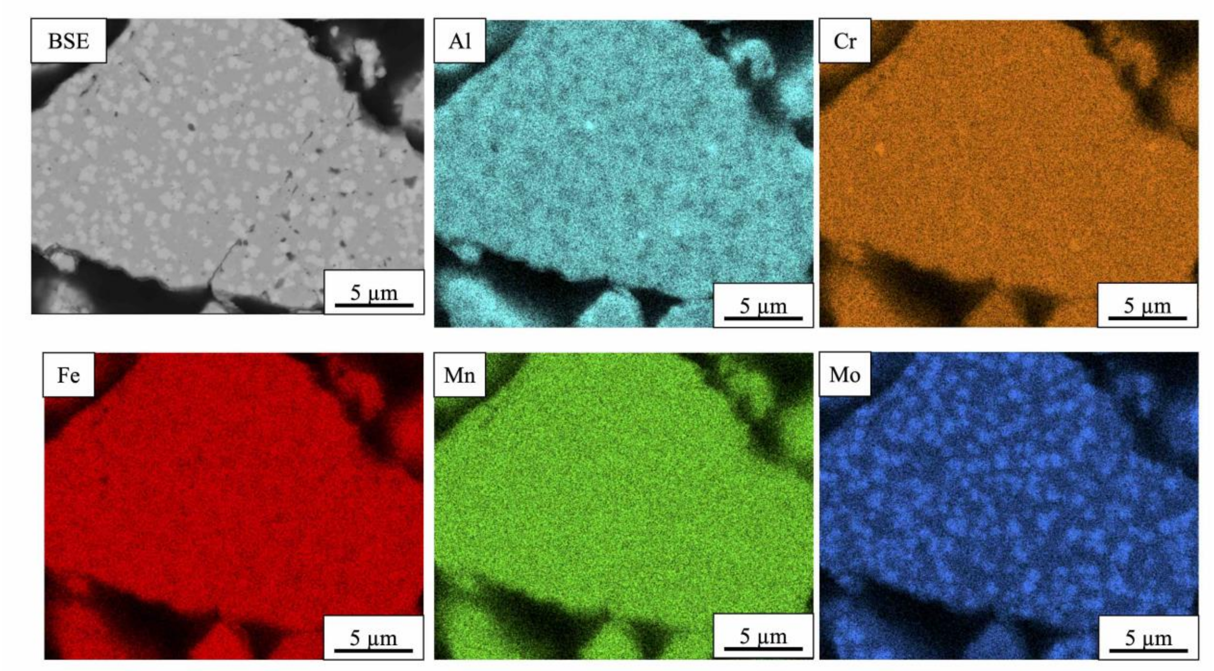

Figure B4. SEM-BSE and corresponding EDX mapping of the A-OE-S32h-950 powder.

Table B3. Mössbauer hyperfine parameters of iron environments in the P-OE-S32h and A-OE-S32h-950.

Sample	Iron site	H (T)	IS (mm/s)	QS (mm/s)	W (mm/s)	A (%)	Magnetic properties
A-OE-S32h-950	Site 1	33.6±1	0.03±0.08	0.28±0.08	0.32±0.08	5.75±0.65	**Magnetic:** 29.82 ±1.79% **Non-magnetic:** 70.18 ±1.79 %
	Site 10	13.5±1	-0.19±0.02	-0.12±0.02	0.34±0.09	17.60±1.02	
	Site 11	-	-0.08±0.11	1.46±0.36	0.29±0.04	6.47±0.12	
	Site 5	-	0.02±0.04	0.77±0.31	0.26±0.02	13.55±0.04	
	Site 6	-	-0.07±0.01	0.56±0.01	0.26±0.02	21.44±1.11	
	Sites 9+12	-	-0.04±0.01	0.21±0.01	0.26±0.01	22.91±0.47	
	Site 8	-	-0.02±0.01	0	0.26±0.01	12.28±0.02	
P-OE-S32h	Sites 2+3	30.5±1	-0.08±0.08	0.46±0.15	0.39±0.04	6.44±1.03	**Magnetic:** 9.93 ±4.53% **Non-magnetic:** 90.07% ± 4.53%
	Sites 4+5	-	0.02±0.01	1.02±0.08	0.26±0.03	5.94±1.05	
	Site 6	-	-0.01±0.01	0.64±0.03	0.25±0.02	19.48±0.86	
	Site 7	-	0.01±0.01	0.37±0.02	0.25±0.02	26.19±0.36	
	Site 12	-	0.01±0.01	0.16±0.02	0.25±0.02	29.61±0.04	
	Site 8	-	0.01±0.01	0	0.25±0.02	12.34±1.06	

Appendix C

Results of sintered samples

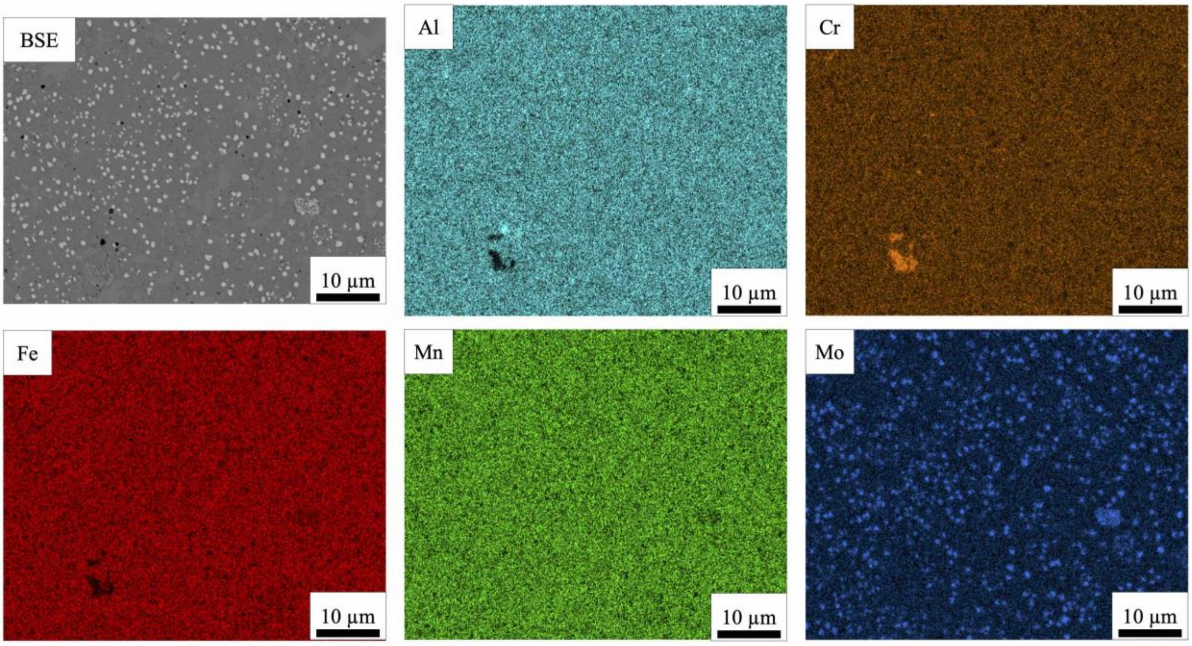

Figure C1. SEM-BSE image with corresponding EDX mapping in the central area of the sample S-O-S32h-S950-1hV.

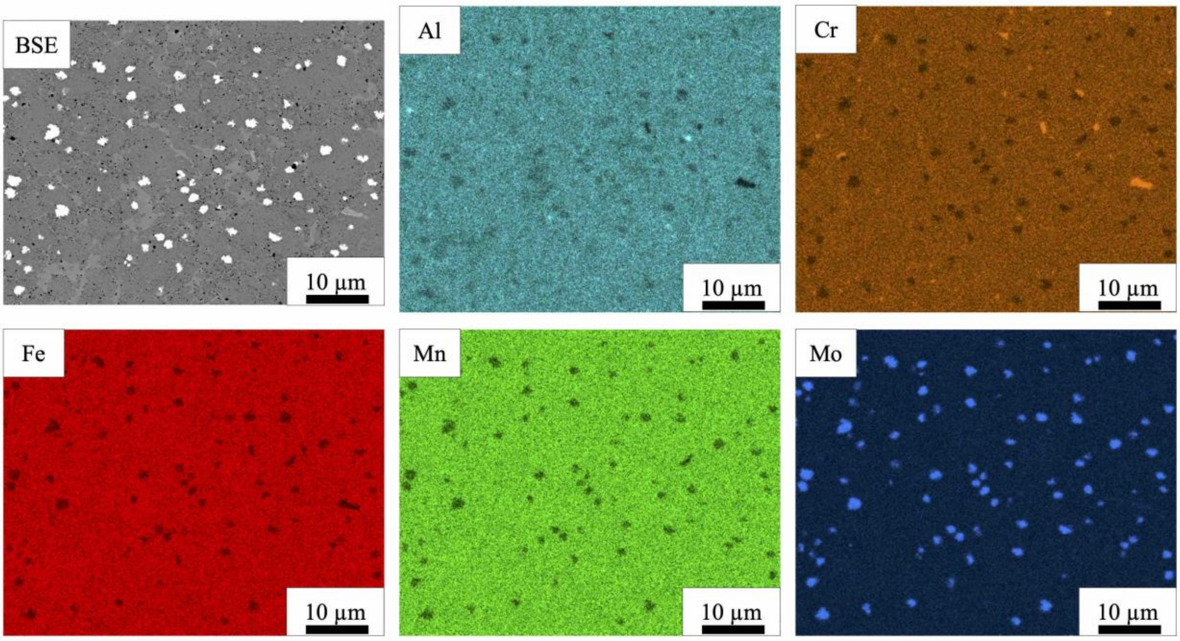

Figure C2. SEM-BSE image with corresponding EDX mapping in the central area of the sample S-O-S32h-S950-1hA.

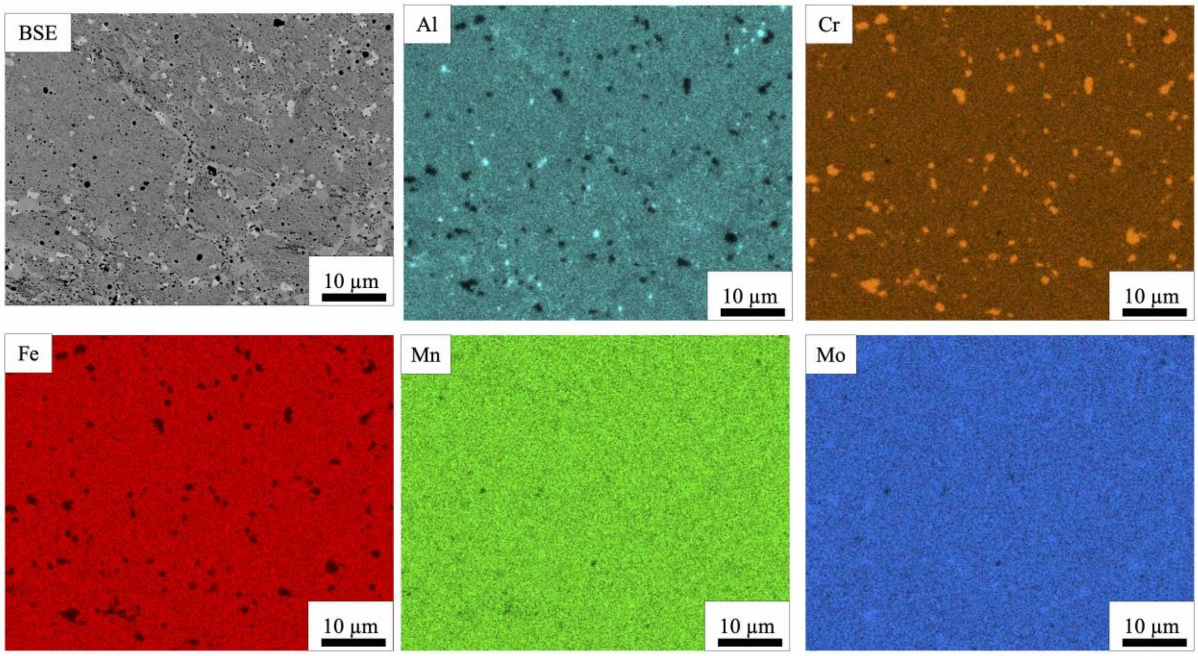

Figure C3. SEM-BSE image with corresponding EDX mapping in the central area of the sample S-O-S32h-S1100-2hA.

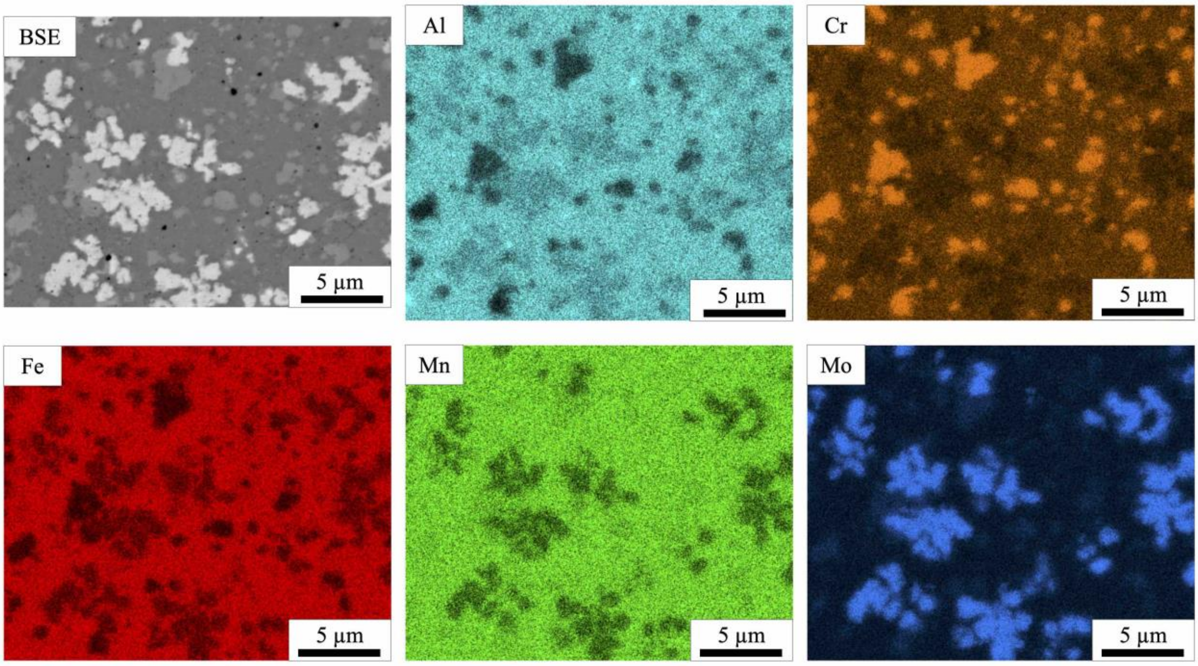

Figure C4. SEM-BSE image with corresponding EDX mapping showing region close to the surface of the S-O-S32h-S950-1hV sample.

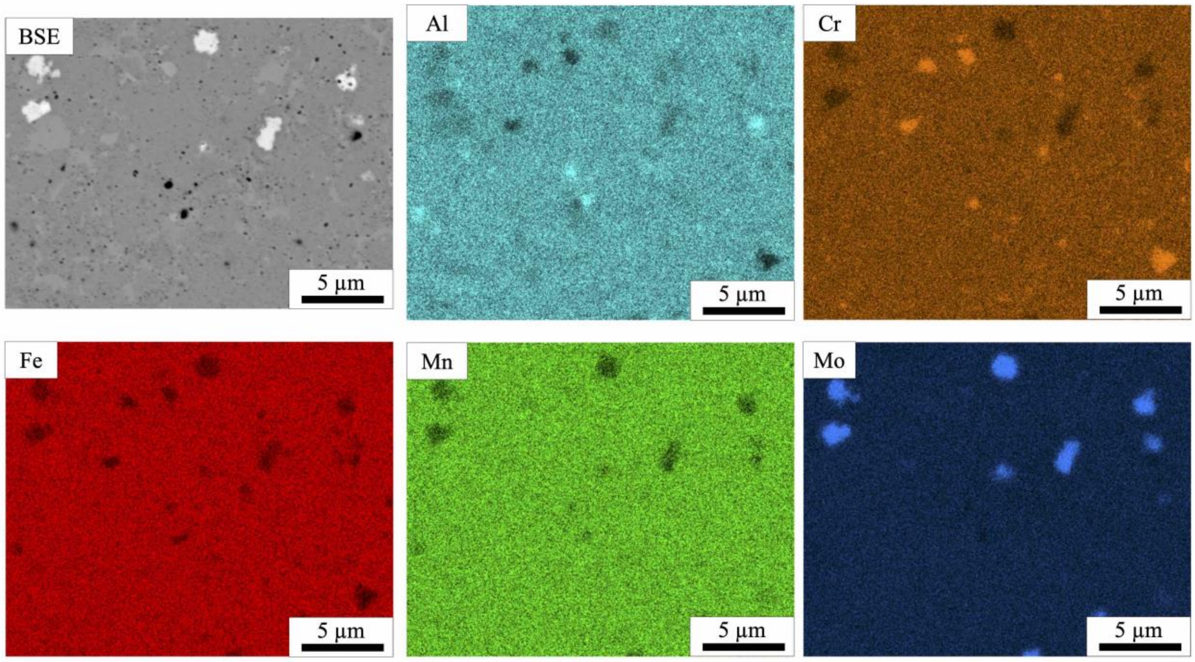

Figure C5. SEM-BSE image with corresponding EDX mapping showing region close to the surface of the S-O-S32h-S950-1hA sample.

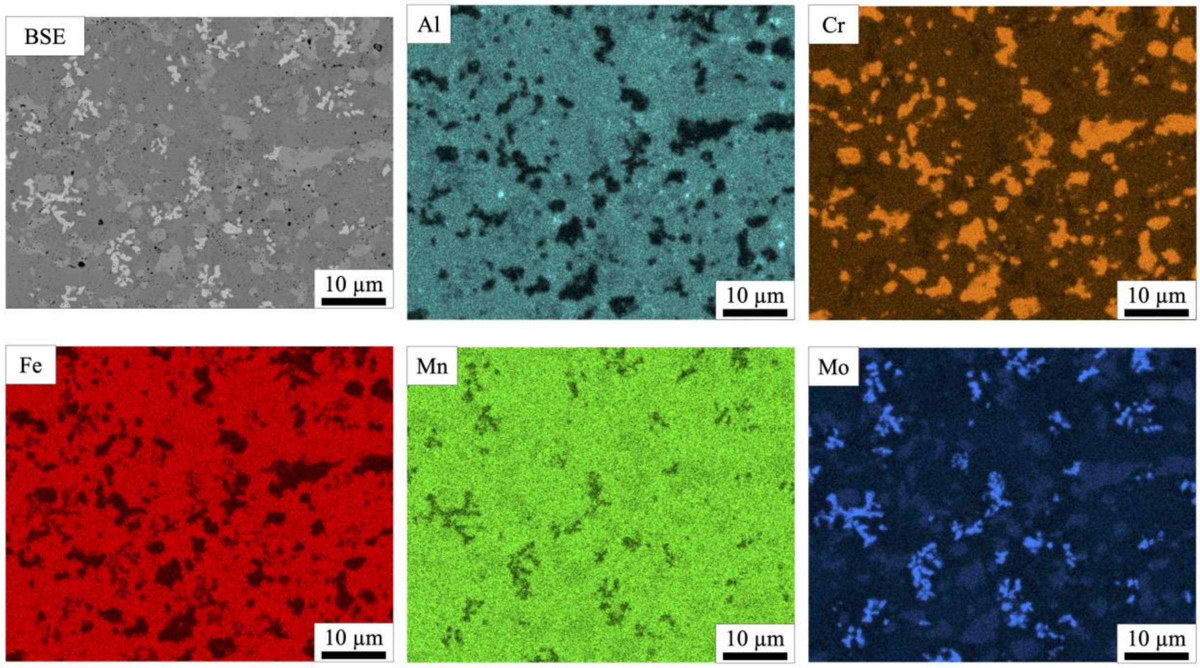

Figure C6. SEM-BSE image with corresponding EDX mapping showing region close to the surface of the S-O-S32h-S1100-2hA sample.

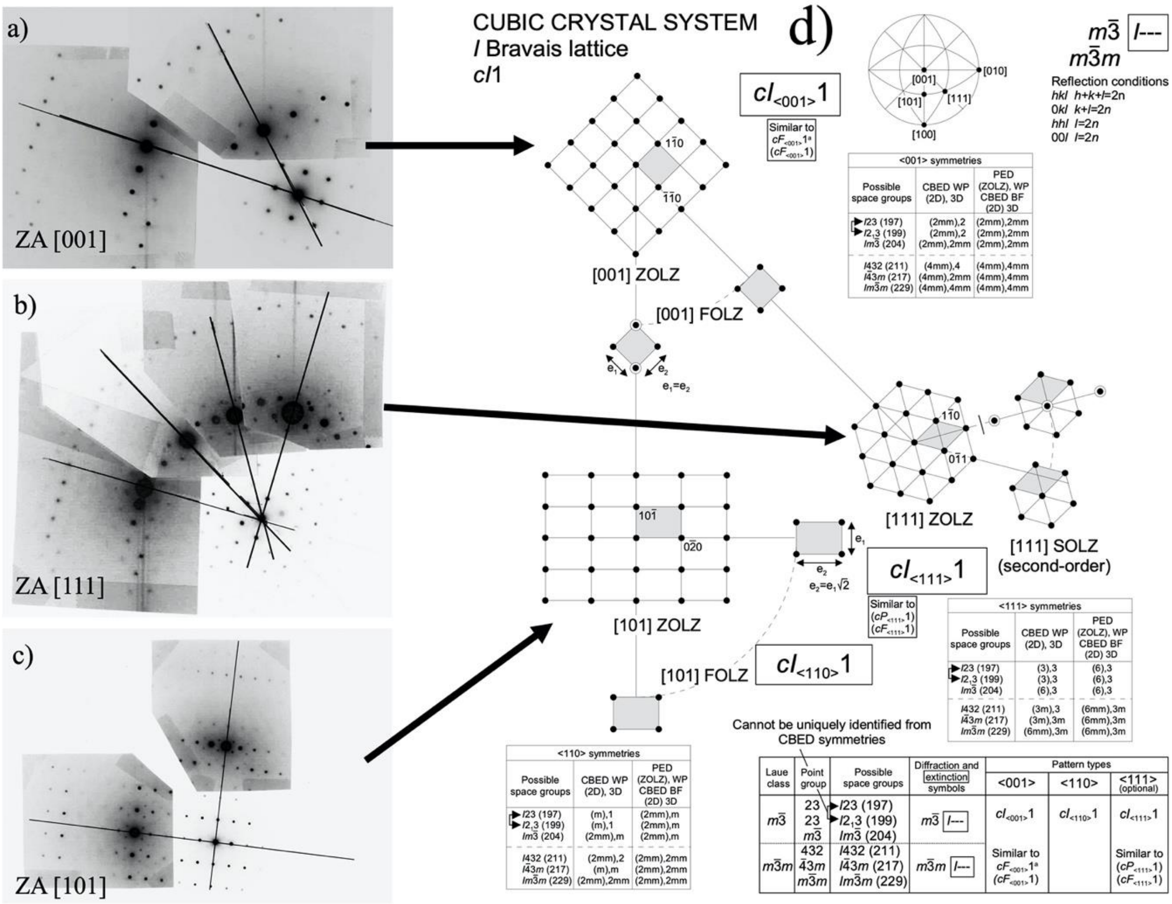

Figure C7. SAED patterns of the S-O-S32h-S950-1hV revealing Zero-order Laue Zone (ZOLZ) and First-order Laue zone (FOLZ) in three zone axis a) [001] b) [111] c) [101]; d) data from “Atlas of Electron Diffraction Zone-Axis Patterns” [128] of bcc phase.

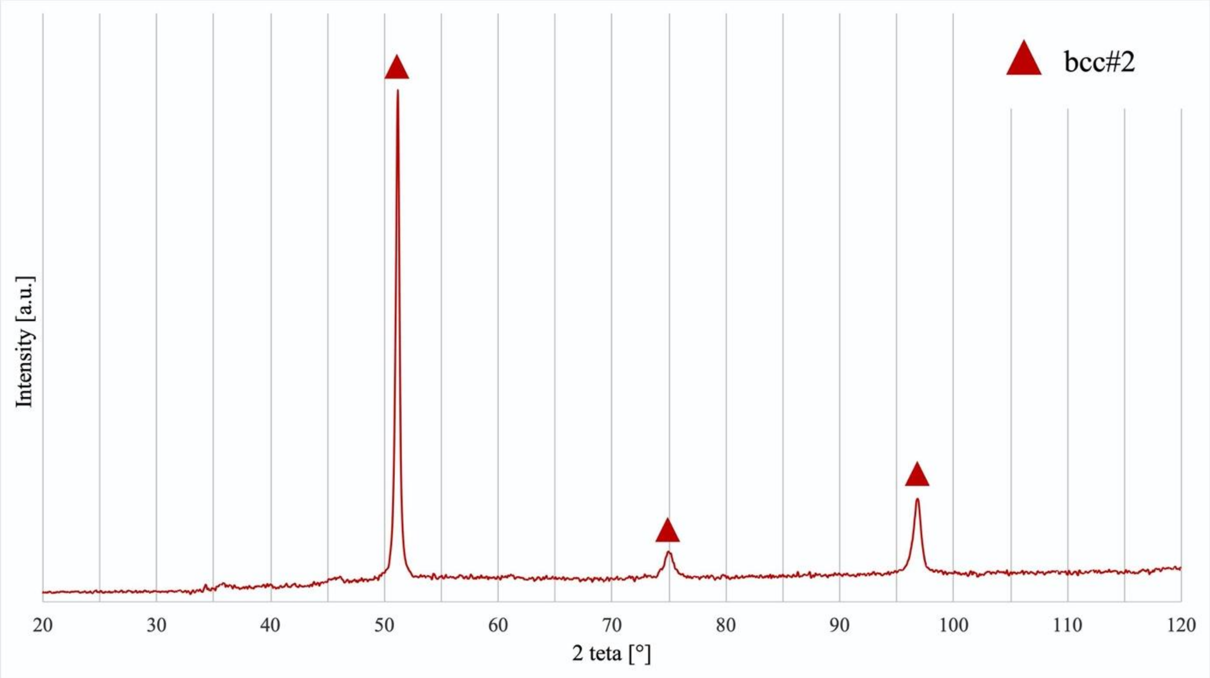

Figure C8. XRD pattern of part A of the P-O-S32h powder pre-sintered at 600 °C for 1 h under argon and then arc melted.

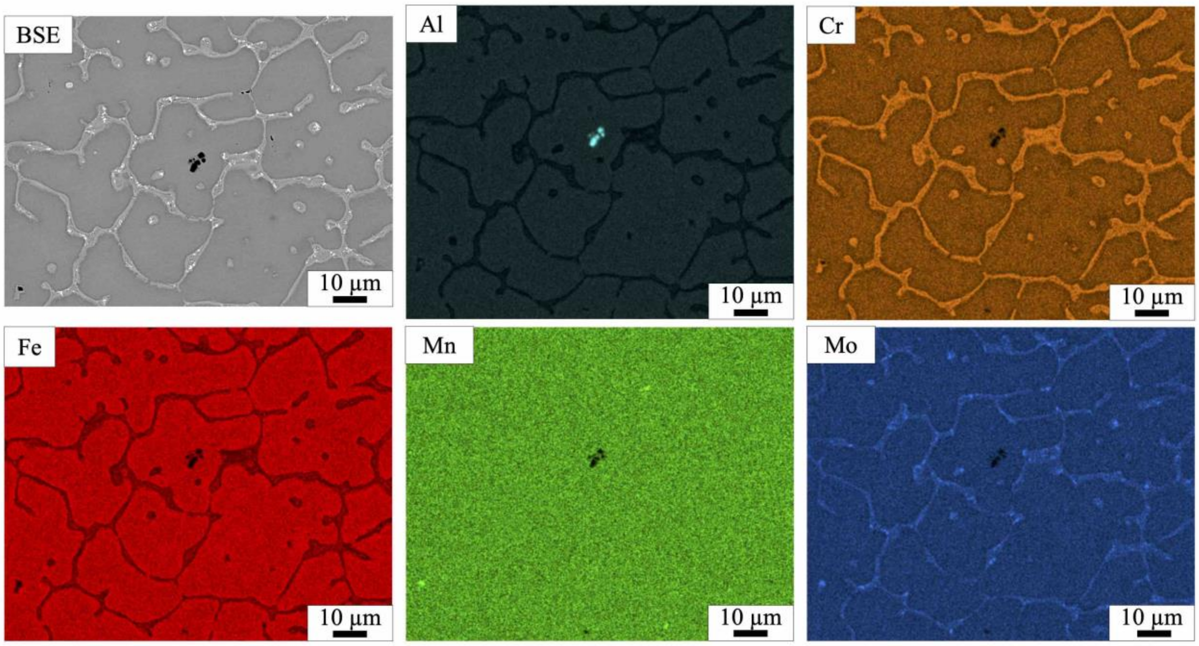

Figure C9. SEM-BSE with corresponding EDX mapping of part A of the P-O-S32h powder pre-sintered at 600 °C for 1 h under argon and then arc melted.

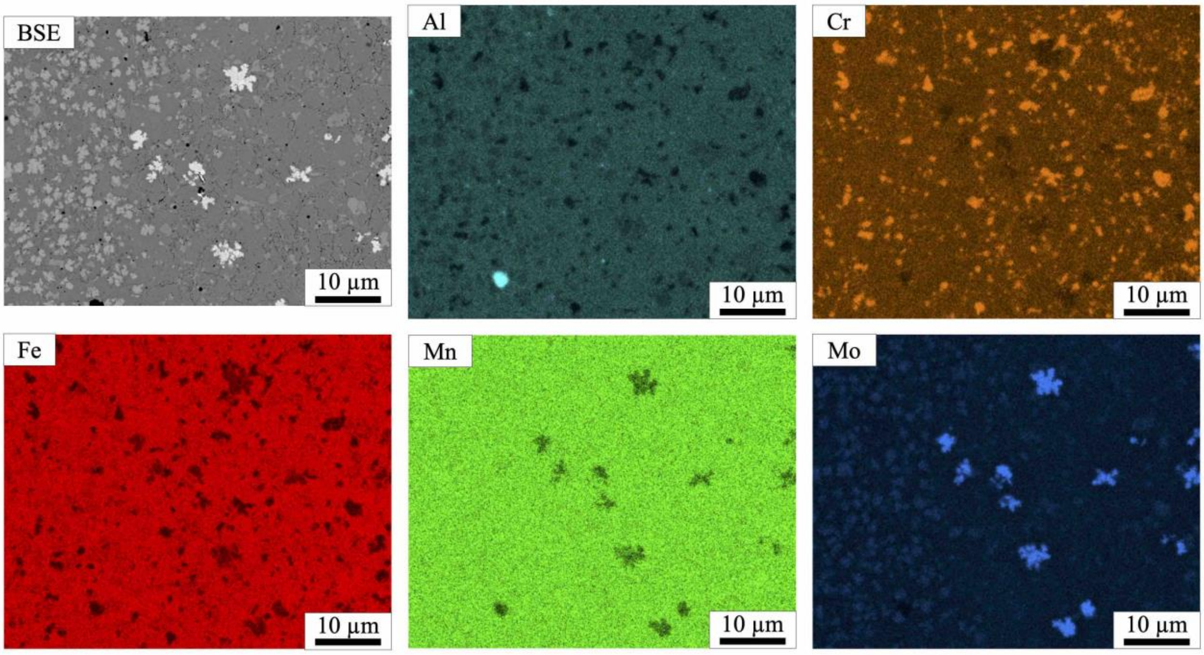

Figure C10. SEM-BSE with corresponding EDX mapping of region close to the surface of the S-OE-S32h-S950-1hA sample.

Appendix - Names of samples

The system of names of samples was created to present all results clearly. It is explained below in Figure N1. The list of samples is also shown in Tables N1-N3.

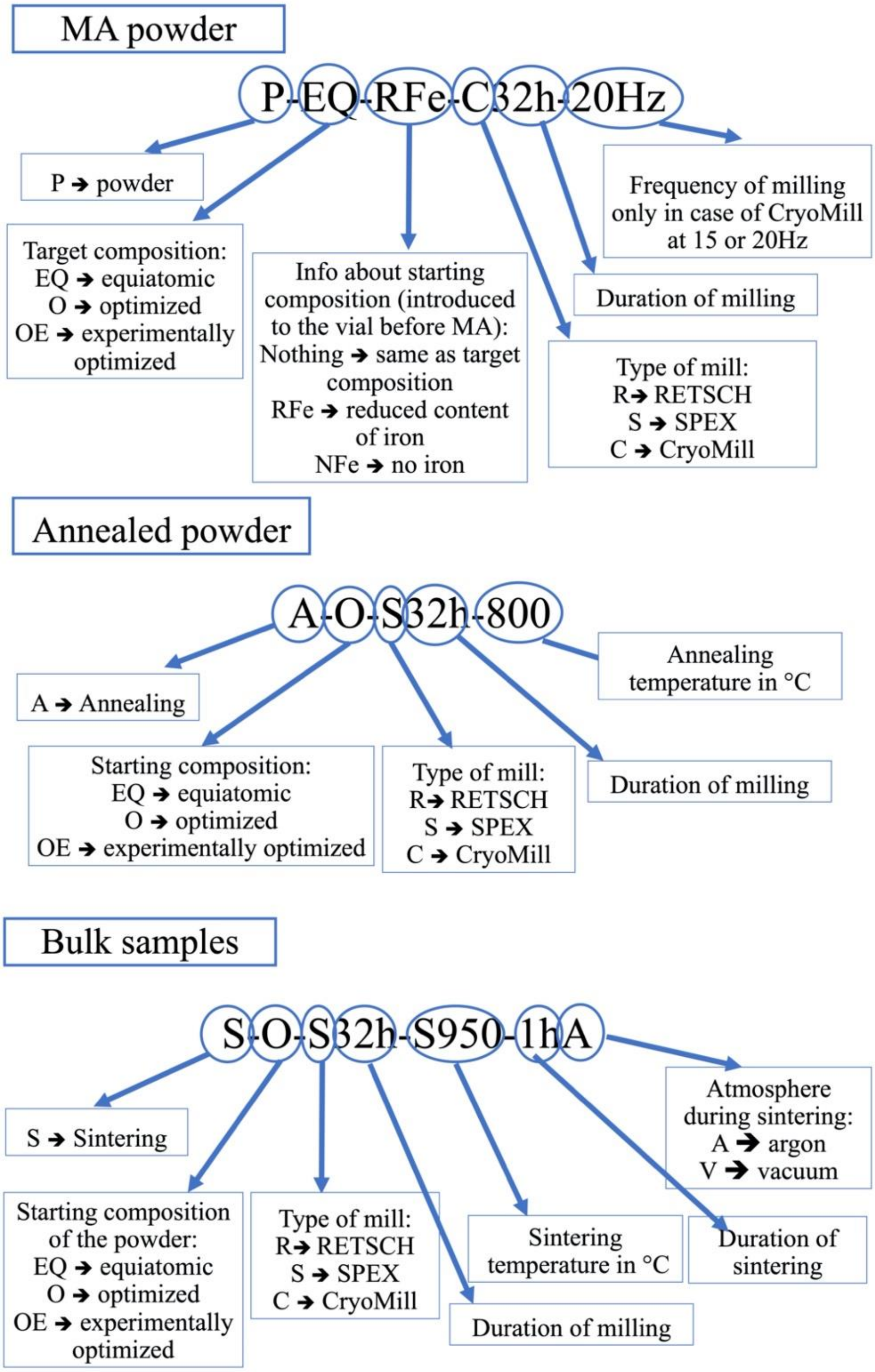

Figure N1. Explanation of names of samples: MA powder, annealed powder, bulk samples.

Table N1. List of powder samples prepared by mechanical alloying.

Name of sample	Initial composition of powder (at. %)	Milling conditions
P-EQ-S16h	20% Al, 20% Cr, 20% Fe, 20% Mn, 20% Mo	SPEX 16 h
P-EQ-S32h	20% Al, 20% Cr, 20% Fe, 20% Mn, 20% Mo	SPEX 32 h
P-EQ-S64h	20% Al, 20% Cr, 20% Fe, 20% Mn, 20% Mo	SPEX 64 h
P-EQ-RFe-S32h	22.2% Al, 22.2% Cr, 11.2% Fe, 22.2% Mn, 22.2% Mo	SPEX 32 h
P-EQ-NFe-S32h	25% Al, 25% Cr, 25% Mn, 25% Mo	SPEX 32 h
P-EQ-R70h	20% Al, 20% Cr, 20% Fe, 20% Mn, 20% Mo	RETSCH 70 h
P-EQ-R70hS1h	20% Al, 20% Cr, 20% Fe, 20% Mn, 20% Mo	RETSCH 70 h + SPEX 1 h
P-EQ-R70hS2h	20% Al, 20% Cr, 20% Fe, 20% Mn, 20% Mo	RETSCH 70 h + SPEX 2 h
P-EQ-R70hS4h	20% Al, 20% Cr, 20% Fe, 20% Mn, 20% Mo	RETSCH 70 h + SPEX 4 h
P-EQ-C32h-15Hz	20% Al, 20% Cr, 20% Fe, 20% Mn, 20% Mo	CryoMill (15 Hz) 32 h
P-EQ-C32h-20Hz	20% Al, 20% Cr, 20% Fe, 20% Mn, 20% Mo	CryoMill (20 Hz) 32 h
P-EQ-C32h	20% Al, 20% Cr, 20% Fe, 20% Mn, 20% Mo	CryoMill (25 Hz) 32 h
P-EQ-C64h	20% Al, 20% Cr, 20% Fe, 20% Mn, 20% Mo	CryoMill (25 Hz) 64 h
P-EQ-C32hS8h	20% Al, 20% Cr, 20% Fe, 20% Mn, 20% Mo	CryoMill (25 Hz) 32 h + SPEX 8 h
P-EQ-RFe-C32hS8h	22.2% Al, 22.2% Cr, 11.2% Fe, 22.2% Mn, 22.2% Mo	CryoMill (25 Hz) 32 h + SPEX 8 h
P-O-S32h	22.5% Al, 22.5% Cr, 28% Fe, 20% Mn, 7% Mo	SPEX 32 h
P-O-C32h	22.5% Al, 22.5% Cr, 28% Fe, 20% Mn, 7% Mo	CryoMill (25 Hz) 32 h
P-O-C32hS8h	22.5% Al, 22.5% Cr, 28% Fe, 20% Mn, 7% Mo	CryoMill (25 Hz) 32 h + SPEX 8 h
P-OE-S32h	19% Al, 22% Cr, 34% Fe, 19% Mn, 6% Mo	SPEX 32 h

Table N2. List of the powder samples annealed under vacuum.

Name of the annealed powder	Name of the MA powder	Annealing conditions
A-O-S32h-500	P-O-S32h	500 °C for 1 h
A-O-S32h-650		650 °C for 1 h
A-O-S32h-800		800 °C for 1 h
A-O-S32h-950		950 °C for 1 h
A-EQ-R70hS4h-850	P-EQ-R70hS4h	850 °C for 1 h
A-EQ-R70hS4h-950		950 °C for 1 h
A-OE-S32h-950	P-OE-S32h	950 °C for 1 h

Table N3. List of sintered samples.

Name of sintered samples	Name of MA powder	Sintering conditions
S-O-S32h-S950-1hV	P-O-S32h	950 °C for 1 h under vacuum
S-O-S32h-S950-1hA		950 °C for 1 h under argon
S-O-S32h-S950-2hA		950 °C for 2 h under argon
S-O-S32h-S1100-2hA		1100 °C for 2 h under argon
S-O-S32h-S1250-2hA		1250 °C for 2 h under argon
S-EQ-R70hS4h-S950-1hA	P-EQ-R70hS4h	950 °C for 1 h under argon
S-OE-S32h-S950-1hA	P-OE-S32h	950 °C for 1 h under argon